

# **Strain Fields in Crystalline Solids**

*Prediction and Measurement of X-Ray Diffraction Patterns  
and Electron Diffraction-Contrast Images*

## **Proefschrift**

ter verkrijging van de graad van doctor  
aan de Technische Universiteit Delft,  
op gezag van de Rector Magnificus prof.ir. K.F. Wakker,  
in het openbaar te verdedigen ten overstaan van een commissie,  
door het College voor Promoties aangewezen,  
op dinsdag 16 mei 2000 te 16.00 uur

door

Teunis Cornelis BOR

materiaalkundig ingenieur  
geboren te Schoonrewoerd

Dit proefschrift is goedgekeurd door de promotoren:

Prof.dr.ir. E.J. Mittemeijer  
Prof.dr.ir. E. van der Giessen

Samenstelling promotiecommissie:

Rector Magnificus	voorzitter
Prof.dr.ir. E.J. Mittemeijer	Technische Universiteit Delft, promotor
Prof.dr.ir. E. van der Giessen	Technische Universiteit Delft, promotor
Prof.dr.ir. P. van Houtte	Katholieke Universiteit Leuven, België
Prof.dr. J.Th.M. de Hosson	Rijksuniversiteit Groningen
Prof.dr. H.W. Zandbergen	Technische Universiteit Delft
Dr. I. Groma	Eötvös University Budapest, Hongarije
Dr.ir. R. Delhez	Technische Universiteit Delft

Dr.ir. R. Delhez en dr.ir. Th.H. de Keijser hebben als begeleider in belangrijke mate aan de totstandkoming van het proefschrift bijgedragen.

The work described in this thesis was made possible by financial support from the Foundation for Fundamental Research of Matter (FOM) and partly by financial support from the Netherlands Technology Foundation (STW).

# Contents

<b>1. General Introduction</b>	<b>1</b>
<b>2. X-Ray Diffraction Line Shift and Broadening of Precipitating Alloys;</b>	
<b>Part I: Model Description and Study of "Size" Broadening Effects</b>	<b>7</b>
1. Introduction .....	7
2. The line-profile simulation model .....	9
2.1. The strain field of the particle-arrangement unit cell .....	9
2.2. Method of line-profile calculations .....	12
2.2.1. Sampling of displacement field .....	12
2.2.2. Intensity distribution of a single crystal .....	12
2.2.3. Intensity distribution of a polycrystalline powder; sampling in reciprocal space .....	16
2.2.4. Computing time considerations .....	16
2.3. Characterization of line profiles .....	17
3. The interpretation of "size broadening" .....	18
3.1. Introduction .....	18
3.2. Centroid and variance; numerical results .....	18
3.3. Relation between particle fraction and line width .....	20
3.4. Relation between particle number density and line width; variance-range plots .....	22
3.5. Effect of particle clustering .....	25
4. "Size-strain separation" .....	27
5. Conclusions .....	28
<i>Appendix A: Interpolation of displacement field within an element</i> .....	29
<i>Appendix B: Calculation of the structure factor using the Fast Fourier         Transform algorithm</i> .....	30
<i>Appendix C: Influence of the rotation procedure on the centroid and variance         of the {hk} powder diffraction line profile</i> .....	36
<i>Appendix D: Calculation of the size Fourier coefficients of a p.a.-unit cell         containing clustered particles</i> .....	38
References .....	40
<b>3. X-Ray Diffraction Line Shift and Broadening of Precipitating Alloys;</b>	
<b>Part II: Study of "Strain" Broadening Effects</b>	<b>41</b>
1. Introduction .....	41
2. Basis of micromechanical and diffraction calculations .....	42
3. Characterization of strain fields and line profiles .....	43

4. Analysis of misfit-strain fields .....	45
4.1. Role of particle fraction; orientation dependence of strain parameters ...	45
4.2. Role of particle/matrix misfit; scaling properties .....	50
4.3. Role of particle clustering.....	50
5. Line-profile calculations .....	53
5.1. Role of mechanical properties .....	53
5.2. Role of particle fraction .....	56
5.3. Role of p.a.-unit cell size .....	56
5.4. Role of clustering.....	59
5.5. Concluding remarks on line profile centroid and variance.....	59
6. Conclusions .....	62
<i>Appendix A: Directional independence of mean matrix strain <math>\langle e_{hk} \rangle_{p.a.}</math> .....</i>	<i>63</i>
<i>Appendix B: Strain field for circular inclusion in circular matrix .....</i>	<i>65</i>
References .....	66

#### **4. Diffraction Contrast Analysis of Misfit Strains around Inclusions**

<b>in a Matrix; VN Particles in <math>\alpha</math>-Fe</b> .....	<b>67</b>
1. Introduction .....	68
2. Calculated BF and DF diffraction contrast images.....	69
2.1. Theoretical background .....	69
2.1.1. Dynamical theory of electron diffraction.....	69
2.1.2. Displacement field of a misfitting particle .....	71
2.1.3. Procedures of strain field contrast image calculation .....	72
2.2. Results of BF and DF diffraction-contrast calculations .....	73
2.2.1. Characterization of the contrast image; the image width .....	73
2.2.2. Parameters determining the image width .....	74
2.2.2.1. Foil thickness .....	75
2.2.2.2. Particle radius.....	76
2.2.2.3. Particle Burgers vector .....	76
2.2.2.4. Particle position .....	78
2.2.2.5. Neighbouring particle; overlapping strain fields.....	79
3. Specimen preparation .....	81
4. Fitting calculated diffraction contrast images to experimental diffraction contrast images of VN in $\alpha$ -Fe .....	83
4.1. Selection of experimental diffraction contrast images of misfitting particles .....	83
4.2. Fitting of particle Burgers vector and foil thickness .....	87
5. Additional results and discussion .....	93

5.1. Particle size and visibility of strain contrast .....	93
5.2. Platelet thickness .....	93
5.3. Occurrence of misfit dislocations; lattice plane imaging .....	94
5.4. X-ray diffraction line-shift and -broadening.....	96
6. Conclusions .....	99
<i>Appendix: Rearrangement of Howie-Whelan equations for a four beam case..</i>	100
References .....	102
<b>5. A Method to Determine the Volume Fraction of a Separate Component in a Diffracting Volume</b> .....	<b>105</b>
1. Introduction .....	105
2. Theoretical basis .....	106
3. Experimental.....	107
4. Results and discussion.....	108
5. Conclusions .....	112
References .....	112
<b>6. Analysis of Ball Milled Mo Powder using X-ray Diffraction</b> .....	<b>115</b>
1. Introduction .....	115
2. Theoretical basis .....	116
2.1. Description of diffraction-line profiles in real space and Fourier space	116
2.2. Deconvolution with prior normalization .....	118
2.3. Deconvolution without prior normalization .....	119
3. Experimental.....	120
4. Evaluation of X-ray diffraction data.....	122
5. Results and discussion.....	125
5.1. Morphology of ball milled powder.....	125
5.2. Volume fraction of undeformed powder particles in ball milled powder .....	127
5.3. Deformation texture.....	129
5.4. Evolution of structural imperfection.....	131
5.4.1. Integral breadth as function of ball milling time .....	131
5.4.2. Integral breadth as function of diffraction-vector length.....	132
5.5. Interpretation of microstrain; determination of dislocation density .....	136
6. Conclusions .....	141
<i>Appendix: Relation between <math>T^{HKL}</math> and <math>a^{HKL}</math></i> .....	142
References .....	143

<b>Summary</b>	<b>145</b>
<b>Samenvatting</b>	<b>149</b>
<b>Nawoord</b>	<b>153</b>
<b>Curriculum Vitae</b>	<b>155</b>

# *Chapter 1*

## ***General introduction***

Nowadays, the search for new, better, stronger and lighter materials has become a field of large interest, both from a scientific and an economical point of view [1-3]. Development of new and/or improved materials is considered to be essential in, for example, semi-conductor, aircraft and space industries [3]. Such a development requires fundamental knowledge of materials behaviour on all relevant length scales, such as the (mis)arrangement of atoms at a nanometer scale and the orientation, distribution and behaviour of grains and grain boundaries at the micrometer scale in order to understand and predict the behaviour of macro-sized products [4].

The prediction of the overall (mechanical) behaviour is possible using micromechanics [5]. A small volume, which is representative of the microstructure of the material, is used to model and calculate the materials behaviour on a local (mesoscopic) scale using continuum mechanics. Subsequently, the behaviour of the representative element is used to calculate the overall materials properties. In this respect characterization of materials through experimental techniques, such as light microscopy, X-ray diffraction (XRD), Scanning Electron Microscopy (SEM) and Transmission Electron Microscopy (TEM) [6], plays an essential role. These techniques do not only contribute to the qualitative, theoretical understanding of materials behaviour, but they also serve as tools to obtain quantitative input for materials modelling. It is the combination of the powers of micromechanics and X-ray diffraction for the understanding and prediction of materials properties and behaviour that forms the incentive for this thesis.

### **Scope of thesis**

The main part of this thesis is concerned with X-ray powder diffraction, i.e. the line profile analysis of polycrystalline specimens for the characterization and investigation of materials. Powder diffraction is non-destructive in nature and enables structural information to be obtained over a moderately large (sample) volume ( $\sim 1 \text{ mm}^3$ ) [7]. A powder diffraction-line profile contains a wealth of information yielding many characteristics from the same measured data (of which); some characteristics cannot be obtained from other analysis methods [8, 9, 10].

The positions of the line profiles enable phase and structure identification and the determination of (macro) strain (i.e. average strain over the length scale of diffracting crystallites). From the integrated intensities, the amount of phases present

can be determined and preferential orientation of crystals (i.e. texture) can be established. The analysis of the shape (broadening) of the line profiles enables the determination of the (finite) size of the diffracting crystallites, of the presence of all kinds of lattice imperfections that cause microstrains (i.e. strains varying over the length scale of the diffracting crystallites), of stacking and twin faults and of compositional inhomogeneities.

Examples of lattice imperfections causing microstrains are dislocations and (small) misfitting particles/precipitates, see Fig. 1. These imperfections cause the atomic lattice to be deformed, i.e. locally the atomic spacing is increased or decreased. In the absence of such lattice imperfections (and employing a perfect measurement instrument with a single wavelength) the XRD line profiles would resemble sharp, delta-function like, peaks. The peak position follows directly from the use of Bragg's law, which relates the lattice spacing to the diffraction angle(s). Hence, it is understandable that lattice imperfections induce line broadening: small variations in the (local) atomic spacing correspondingly cause small variations in the diffraction angles.

Lattice imperfections have a large influence on the (mechanical and other) properties of crystalline materials. The motion of dislocations facilitates the deformation of crystalline materials and therefore, mechanical properties, such as the hardness and the yield strength, are improved greatly by hindering the dislocation motion [9]. One way to block or obstruct dislocation motion is the introduction of small (nanometer sized), misfitting precipitates/particles in the (matrix) material. Another way to impede dislocation motion reveals itself during (cold) deformation: dislocations hinder each other, leading to a dramatic increase of the dislocation density (strain hardening). Further, the presence of dislocations is important for the recrystallisation behaviour of (deformed) materials [11].

From the above it follows that since the presence and properties of lattice imperfections largely determine both (i) the behaviour and properties of materials and (ii) the shift and broadening of XRD line profiles, a potential route to the direct understanding of materials behaviour from the analysis of XRD line shift and broadening is conceivable. Hence, it is important to establish sound relationships between the line shift and broadening measured and the type and amounts of lattice imperfections present.

However, the analysis of line broadening is not straightforward [7 - 10, 13]. Within a single specimen several types of lattice imperfections may occur and cause line broadening (structural line broadening). Moreover, the measured line broadening is augmented by additional broadening due to the measurement instrument and the spectral distribution of the X-rays (instrumental line broadening) [9, 10], see Fig. 1.



Fortunately, the instrumental line broadening can be separated from the total line broadening with the aid of a suitable reference specimen that is practically free of lattice imperfections [9, 10].

In a line-broadening analysis the respective contributions of the sources of structural line broadening are to be identified. With the aid of certain assumptions and often using several orders of reflection, the structural broadening is usually separated into a contribution due to size (the finite size of the diffracting crystallites) and a contribution due to strain (including all microstrain sources). Examples of such size-strain analysis methods are the Williamson-Hall analysis [14], the Warren-Averbach analysis [9] and an alternative analysis by Van Berkum et al. [15]. Although these types of analysis can be performed in a relatively straightforward manner and are applicable independent of the types of lattice imperfections present, they suffer from at least two drawbacks. Firstly, the assumptions underlying the methods are not always verified or even correct, leading to unreliable outcomes [15], and secondly, the interpretation of the size and strain contributions in terms of the microstructural features (e.g. dislocations, precipitates) of the polycrystalline material considered is very often difficult [15].

Recently a novel way of line-profile analysis has been proposed which is the main theme of this thesis [16]. On the basis of an adequate physical/micromechanical model of the lattice imperfections within a representative volume of the crystalline material, XRD line profiles are calculated. The calculated line profiles are matched to the experimental line profiles by changing (a limited number of) model parameters that are directly related to the type and distribution of the lattice imperfections. In this way the values of relevant physical parameters are determined directly. Evidently, their accuracy/reliability depends upon the adequacy of the physical model.

In addition to a proper determination of the relevant physical parameters another (fruitful) outcome of this methodology is the elimination of so-called truncation errors. In diffraction-line broadening analysis, one practically never obtains the full line profile due to overlap with line profiles of neighbouring reflections and the presence of a background intensity. Each measurement of a line profile suffers therefore from truncation both vertically (finite measurement range) and horizontally (subtraction of background), which affects the results of all subsequent analysis [7, 9, 10, 17]. However, if an appropriate description of the structural broadening is available and the instrumental line broadening is known, the entire diffraction-line profile, or even the *complete* diffraction pattern, could be calculated and fitted at once.

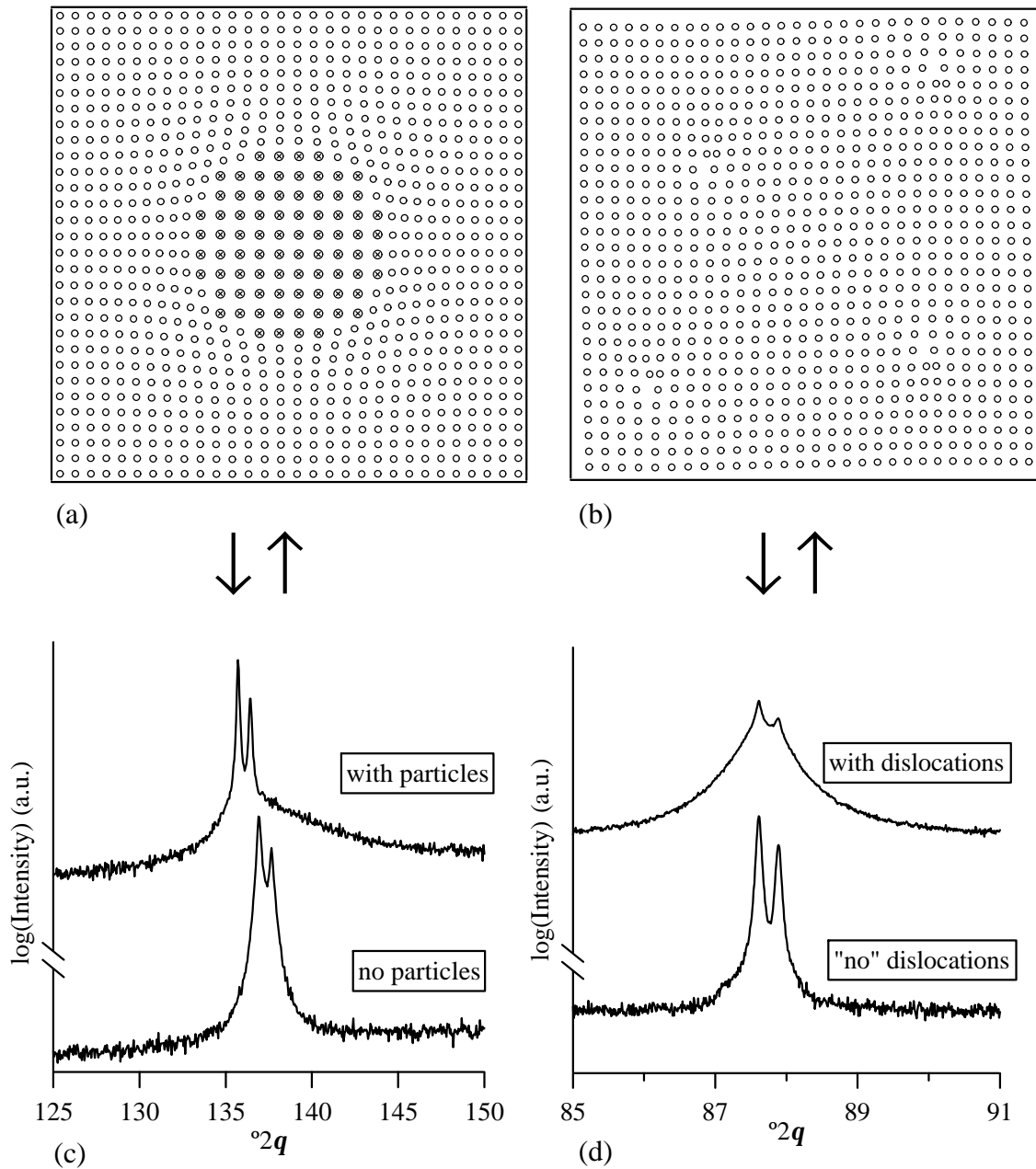


**Fig. 1.** Atomic representation of model materials containing misfitting particles (a) or (edge) dislocations (b) for interpretation and generation (illustrated by the  $\uparrow\downarrow$ -symbols) of X-ray diffraction-line profiles. The distortion of the lattice due to the strain fields of the lattice imperfections cause broadening of the X-ray diffraction line profiles (structural broadening). Examples of experimental line profiles are displayed for a VN precipitates containing  $\alpha$ -Fe matrix (c) (see also Chapter 4) and a cold deformed, ball milled, Mo powder (d) (see also Chapters 5 and 6). The structural line broadenings are obtained by elimination of the line broadenings in absence of lattice imperfections (instrumental line broadening).

The outcomes of the diffraction-line profile calculation and fitting methodology must, of course, be verified. Even in the case of just a single solution for the model parameters, the physical relevance of the micromechanical model must be checked. In this respect the following sources of errors should be recognised. Firstly, the measurement of experimental line profiles is always hindered by (counting) statistical intensity variations. Secondly, a relatively simple micromechanical model can describe the important features of the experimental material successfully, but it will not be capable of capturing all details.

An obvious route to check the validity of the parameters determined from XRD is to study the same material using a different experimental technique. Transmission Electron Microscopy serves as an excellent candidate in this respect, since it enables a detailed study of very small volumes containing the lattice imperfections causing broadening of X-ray diffraction-line profiles [18].

### **Contents of thesis**

This thesis contains three parts. In the first part, chapters II and III, the novel XRD methodology is explained and studied in full detail for the case of misfitting particles/precipitates in a matrix. Both the broadening due to finite size effects (chapter II) and due to microstrains (chapter III) are considered and a simple method of separating both broadenings is proposed. The broadening due to microstrains is studied in two steps. First the relations between model parameters, such as the particle size, the particle fraction, the particle-matrix misfit and the distribution of particles within the matrix, and characteristic values of the strain within the matrix, such as the mean strain and the root mean square strain, are investigated in detail. Subsequently, the relations between the values that characterize the matrix strains and the shift and width of calculated line profiles are analysed.

In the second part, chapter IV, a particle-matrix model system is studied using Transmission Electron Microscopy to enable verification of the results of the simulation methodology. A model system, consisting of an  $\alpha$ -Fe matrix filled with small, misfitting VN precipitates is studied in detail. A new method of determining the particle-matrix misfit from TEM micrographs is proposed.

In the last part, attention is paid to ball milling/mechanical alloying [19]. In a ball milling device, small amounts of elementary and/or alloyed powder particles can be deformed severely using one or more vibrating balls. The deformation process induces large numbers of lattice imperfections, such as dislocations and grain boundaries. In chapters V and VI the first stages of the ball milling of elementary Mo powder in a low-impact ball milling device are studied. Special attention is devoted to

the determination of the fractions of powder particles that remain undeformed for relatively short milling times.

### *references*

- [1] P. Ball, *Made to Measure, New Materials for the 21<sup>st</sup> Century*, Princeton University Press, Princeton, New Jersey, 1997.
- [2] M. Schwartz, *Emerging Engineering Materials: Design, Processes, Applications*, Technomic Publishing Company, Inc., Lancaster, 1996.
- [3] M.C. Flemings, *Ann. Rev. Mater. Sci.* **29** (1999), 1 - 23.
- [4] E. Lifshin (ed.), *Materials Science and Technology 2A, part I*, Weinheim, 1992.
- [5] S. Nemat-Nasser, M. Hori, *Micromechanics: Overall Properties of Heterogeneous Materials*, Elsevier, Amsterdam, 1999.
- [6] F.H. Chung, D.K. Smith, (eds), *Industrial Applications of X-Ray Diffraction*, Marcel Dekker, Inc, New York, 2000.
- [7] R. Delhez, Th.H. de Keijser, E.J. Mittemeijer, *Fres. Z. Anal. Chem* **312** (1982), 1 - 16.
- [8] H.P. Klug, L.E. Alexander, *X-Ray Diffraction Procedures*, John Wiley, New York, 1974.
- [9] B.E. Warren, *X-ray Diffraction*, Reading, Massachusetts: Addison-Wesley, 1969.
- [10] R.L. Snyder, J. Fiala, H.J. Bunge, *Defect and Microstructure Analysis by Diffraction*, Oxford University Press, New York, 1999.
- [11] G.E. Dieter, *Mechanical Metallurgy*, McGraw-Hill, Singapore, 1987.
- [12] J.W. Christian, *The Theory of Transformations in Metals and Alloys*, Pergamon, Oxford, 1965.
- [13] J.G.M. van Berkum, R. Delhez, Th.H. de Keijser, E.J. Mittemeijer, *Acta Cryst.* **A52** (1996), 730 - 747.
- [14] G.K. Williamson, W.H. Hall, *Acta Metall.* **1** (1953), 22 - 31.
- [15] J.G.M. van Berkum, A.C. Vermeulen, R. Delhez, Th.H. de Keijser, E.J. Mittemeijer, *J. Appl. Cryst.* **27** (1994), 345 - 357.
- [16] J.G.M. van Berkum, R. Delhez, Th.H. de Keijser, E.J. Mittemeijer, P. van Mourik, *Scripta Metall. Mater.* **25** (1991), 2255 - 2258.
- [17] A.C. Vermeulen, R. Delhez, Th.H. de Keijser, E.J. Mittemeijer, *J. Appl. Phys.* **71** (1992), 5303 - 5309.
- [18] P.B. Hirsch, A. Howie, R.B. Nicholson, D.W. Pashley, *Electron microscopy of thin crystals*, Butterworths, London, 1967.
- [19] C. Suryanarayana (ed.), *Non-Equilibrium Processing of Materials*, Pergamon, Amsterdam, 1999.

## Chapter 2

# X-Ray Diffraction Line Shift and Broadening of Precipitating Alloys *Part I: Model Description and Study of "Size" Broadening Effects*

T.C. Bor<sup>1,2</sup>, R. Delhez<sup>1</sup>, E.J. Mittemeijer<sup>1,3</sup> and E. Van der Giessen<sup>2</sup>

<sup>1</sup>Laboratory of Materials Science, Delft University of Technology,  
Rotterdamseweg 137, 2628 AL Delft, The Netherlands

<sup>2</sup>Koiter Institute Delft, Delft University of Technology,  
Mekelweg 2, 2628 CD Delft, The Netherlands

<sup>3</sup>Max Planck Institute for Metals Research,  
Seestraße 92, 70174 Stuttgart, Germany

### ***Abstract***

A new diffraction-line profile simulation approach is presented that is based on a micromechanical model of the crystalline material considered. It uses the kinematical theory of diffraction and is, in principle, valid for any three-dimensional crystal. The approach is demonstrated for a two-dimensional model material containing a periodic distribution of equal sized, circular, non-diffracting, misfitting particles. In this first paper, the line shift and broadening in absence of misfit between particles and matrix is studied in detail with an emphasis on the role of the particle fraction, the particle size and the particle clustering on the line profile position and width. Further, the separation of broadening due to "size" and "strain" effects is discussed.

### ***1. Introduction***

Precipitation in alloys can induce pronounced mechanical strengthening. The volume misfit of the precipitate particles with the matrix is associated with the introduction of strain fields surrounding the precipitate particles which can hinder dislocation movement and thus enhance the mechanical strength [1]. To understand material behaviour it is of crucial importance to establish which are the key parameters of the strain distribution in the material considered and to determine their values experimentally.

X-ray diffraction is one of the few methods enabling the non-destructive and quantitative measurement of macroscopic strains, i.e. strains which are constant on the length scale of a grain in the specimen, as well as microscopic strains, i.e. strains which are varying over atomic distances. A macroscopic strain is observed as a shift of a diffraction-line profile from its strain-free position and microscopic strains are observed through broadening of the diffraction-line profile. The interpretation of this diffraction-line broadening in terms of local strain fields, however, is not straightforward [2] since diffraction-line broadening can be caused also by, for instance, the finite size of the diffracting crystals (size broadening). Until now, methods used for line-profile decomposition (i.e. separation of the "size and strain broadened" parts) rely on specific assumptions made for the order dependences of "size" and "strain" broadenings, leading to "size" and "strain" parameters that are difficult to interpret [2 - 4].

Recently, a different approach has been proposed: line-profile simulation on the basis of an appropriate model for the occurring strain field [4]. Such line profiles can be matched with experimental ones, thereby determining values for strain-field parameters that can be interpreted easily. Earlier treatments (e.g. [5 - 8]) for the effect of misfitting particles on line broadening are based on a description of the particle induced misfit-strain field in the matrix according to a formalism originally presented by Eshelby [9] for misfitting point defects. In this way, the influence on the simulated line profiles of the particle-matrix misfit and the particle volume fraction could be modelled quite readily. However, these simulations pertain to randomly distributed particles within a matrix for which the interaction of the strain fields due to the individual particles is accounted for in an approximate way. To eliminate these limitations and to accurately calculate the displacement and the strain field within a material containing misfitting particles a micromechanical description is adopted here. The power of the proposed methodology can be well demonstrated by considering an infinitely large two-dimensional model system of misfitting, circular particles distributed in a matrix. It will be shown here that the results obtained for this simple system already have a direct bearing on the diffraction line shift and broadening observed in practice.

In this first paper a full description of this new approach is given. It is applied to various cases of particles in a matrix. In the absence of particle-matrix misfit, the so-called size broadening is analysed. In the presence of particle-matrix misfit, the way how to separate size and strain broadening effects is discussed. In the second paper the occurring strain broadening is analysed in detail.

## 2. The line-profile simulation model

### 2.1 The strain field of the particle-arrangement unit cell

Although the approach is quite general, it will be demonstrated for a two-dimensional model material. For convenience, the second-phase particles considered have a circular shape and are distributed periodically in an infinitely large crystal (the matrix). The particles exhibit a certain volume misfit with respect to the matrix. Such a misfit can be due to differences in specific volume of atoms of the constituting elements upon precipitation and/or can arise due to different thermal expansion coefficients of matrix and particles during cooling of the material from the processing, precipitation temperature to room temperature. It is assumed that all misfit is accommodated elastically.

Due to the particle ordering, a unit cell can be defined such that its deformation due to the precipitates fully characterizes the entire particle-matrix composite. This unit cell will be called "particle arrangement unit cell" or p.a.-unit cell. A schematic drawing of the (primitive) p.a.-unit cell considered here as an example is given in Fig. 1. The particle with radius  $R_p$  is placed in the center of a square matrix of size  $2L \times 2L$  at the origin of a Cartesian coordinate system with the  $x$  and  $y$ -axes parallel to the sides of the p.a.-unit cell. The particle area fraction  $c$  is defined as  $c = \pi R_p^2 / 4L^2$ . Each phase exhibits linear elastic behaviour and is assumed to possess isotropic elastic properties: Young's moduli  $E_m$  ("m" denotes matrix) and  $E_p$  ("p" denotes particle) and Poisson ratios  $\nu_m$  and  $\nu_p$ . The particle-matrix misfit is characterized by the linear misfit parameter  $\epsilon$ .

The displacement field and the corresponding strain field are calculated from the governing elasticity equations, assuming plane strain in the out-of-plane direction. Since the p.a.-unit cell exhibits mirror symmetry about the lines  $x = 0$  and  $y = 0$ , the displacement and strain fields need only be calculated in a quarter of the p.a.-unit cell. The boundary conditions required to solve the elasticity problem are implied by the periodic arrangement of p.a.-unit cells and the symmetry properties of the p.a.-unit cell. Denoting the displacements parallel to the  $x$ -axis and the  $y$ -axis by  $u$  and  $v$ , respectively, and with  $t$  as the in-plane shear stress, the boundary conditions can be written as

$$\begin{aligned} u(0, y) = 0, v(x, 0) = 0, u(L, y) = U, v(x, L) = V; \\ t(0, y) = t(x, 0) = t(L, y) = t(x, L) = 0. \end{aligned} \quad (1)$$

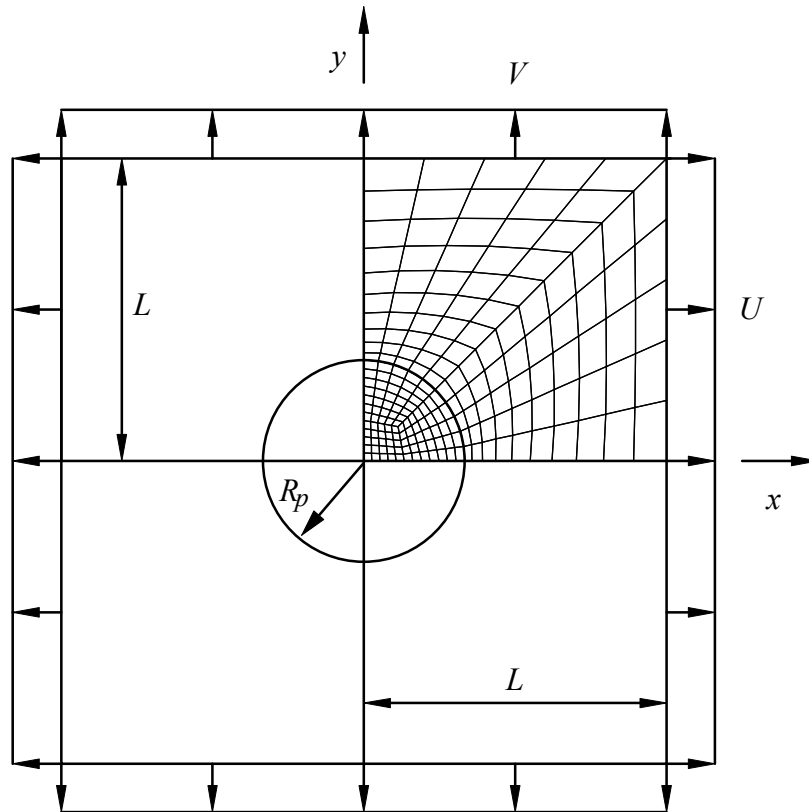


**Fig. 1.** Schematic drawing of the square p.a.-unit cell of size  $2L \times 2L$  containing a single centered particle of radius  $R_p$  at the origin of the  $x$ - $y$ -coordinate system. The overall expansion of the p.a.-unit cell in  $x$ - and  $y$ -direction is denoted by  $U$  and  $V$ , respectively. Due to symmetry properties of this p.a.-unit cell the displacement and strain fields are calculated only for a quarter of the cell. The type of mesh is shown, but the actual mesh used contains many more elements.

The cell boundary displacements  $U$  and  $V$  are determined such that the *average* normal stresses at the p.a.-unit cell boundaries in the  $x$ -direction and the  $y$ -direction vanish in order to maintain a globally stress-free state. Because of the symmetry and elastic isotropy of matrix and particle, the p.a.-unit cell will only exhibit overall dilation, i.e.  $U = V$ .

No closed-form analytical solution exists for this elastic problem and therefore the solution is obtained numerically using a finite element method [10]. This solution is accurate to a desired level of accuracy by choosing a sufficiently fine mesh of elements. In this work this mesh is constructed from approximately  $35 \times 35$  four noded elements, somewhat depending on the particle fraction  $c$ . The size of the



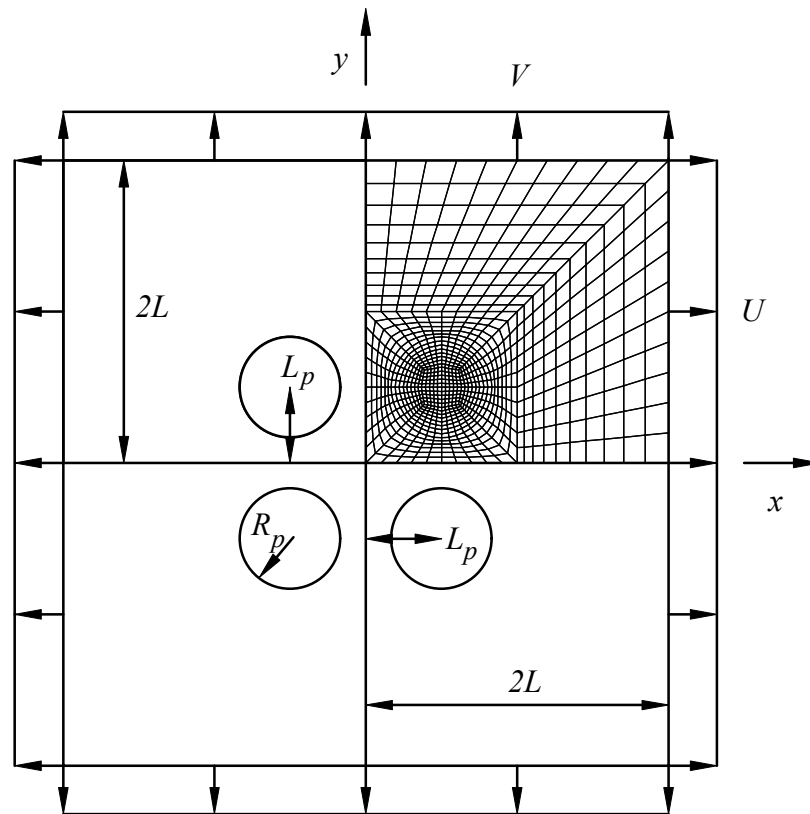


**Fig. 2.** Schematic drawing of square p.a.-unit cell of size  $4L \times 4L$  containing four clustered particles of equal radius  $R_p$  located at  $(\pm L_p, \pm L_p)$ . See also caption of Fig. 1.

elements in the neighbourhood of the particle-matrix interface is intentionally reduced to capture the relatively steep strain gradient (cf. Fig. 1).

The displacement and strain fields computed in this way duly account for "interaction" of the particles. Obviously, the displacement field reflects the periodicity of the particle distribution. Hence, the displacement and strain field are distinctly anisotropic.

To study the influence of non-periodic distributions of second-phase particles, local deviations of the periodic distribution of particles are considered: a p.a.-unit cell is taken which contains four identical particles that are clustered near the origin and located on the cell diagonals (see Fig. 2). The size of the p.a.-unit cell now is  $4L \times 4L$ ; the distance between neighbouring circular particles in the p.a.-unit cell is equal to  $2L_p$ . The degree of clustering can be denoted by the dimensionless cluster factor  $C_f = 1 - L_p/L$ . If  $C_f = 0$ , there is no clustering and the cell is equivalent to the p.a.-unit cell of Fig. 1. If  $C_f = 1$ , the four particles in the p.a.-unit cell overlap fully at  $x = y = 0$ . If

the particles touch but do not overlap, the utmost clustered state is reached when  $L_p = R_p$ ; then  $C_f^{max} = 1 - 2\sqrt{c/p}$ . This large p.a.-unit cell shows the same symmetry as the small p.a.-unit cell of Fig. 1 and therefore the displacement field and strain field calculations can again be restricted to a quarter of this cell.

Since the displacement field and the strain field in matrix and particle are calculated using linear continuum elasticity, they do not have the sizes of the p.a.-unit cell and of the particle as independent variables: the displacements and the strains are fully characterized by their ratio  $R_p/L$  or by the particle fraction  $c$ . Physically this means that no length scale related to, for example, the atomic distance is introduced.

## 2.2 Method of line-profile calculation

### 2.2.1 Sampling of displacement field

The p.a.-unit cell is filled with a square array of  $2N \times 2N$  atoms divided over matrix and particle such that the filled p.a.-unit cell is symmetric about the lines  $x = 0$ ,  $y = 0$  and  $x = |y|$  as shown schematically in Fig. 3a. This 2D array can be described by vectors  $\mathbf{a}_1$  and  $\mathbf{a}_2$  that are related to the vectors describing the p.a.-unit cell,  $\tilde{\mathbf{a}}_1$  and  $\tilde{\mathbf{a}}_2$ , by  $\tilde{\mathbf{a}}_i = 2N\mathbf{a}_i$  ( $i = 1, 2$ ). The atomic distance is  $|\mathbf{a}_1| = |\mathbf{a}_2| = a$ . Note that  $\mathbf{a}_i$ , and thus  $\tilde{\mathbf{a}}_i$ , change in proportion to the overall dilatation of the p.a.-unit cell in the strained condition. The radius of the misfitting particle can also be expressed as an integer number of atoms,  $N_R$ , as  $N_R = \text{mod}(R_p/a)$ .

The continuous displacement field, as calculated according to Section 2.1, is sampled at the original, reference positions of the atoms, rendering the displacement of the atoms from their reference position. The values of the atomic displacements are obtained by bilinear interpolation between the displacements of the four nodes forming the element in which a particular atom is located [10]; see Appendix A.

### 2.2.2 Intensity distribution of a single crystal

According to the kinematical theory of diffraction, the  $\{hk\}$  intensity distribution of a single (here two-dimensional) crystal in reciprocal space is given by [11]

$$I(h, k) = F(h, k)F^*(h, k)G(h, k)G^*(h, k) \quad (2)$$

where  $I(h, k)$  is expressed in electron units,  $F(h, k)$  denotes the structure factor,  $G(h, k)$  represents the crystal factor, and "\*" indicates the complex conjugate. The structure

factor  $F(h,k)$  comprises the contribution to the scattering amplitude of all atoms within a single unit cell; the crystal factor  $G(h,k)$  accounts for the spatial distribution of all unit cells making up the crystal.

If the vector  $\mathbf{r}_{mn}$  indicates the position of an atom  $(m,n)$  with respect to the origin of the p.a.-unit cell (see Fig. 3) and  $f_{mn}$  is its scattering factor, then the structure factor of a p.a.-unit cell containing  $2N \times 2N$  atoms is given by

$$F(\tilde{h}, \tilde{k}) = \sum_{m=0}^{2N-1} \sum_{n=0}^{2N-1} f_{mn} e^{2\pi i \mathbf{H} \cdot \mathbf{r}_{mn}} \quad (3)$$

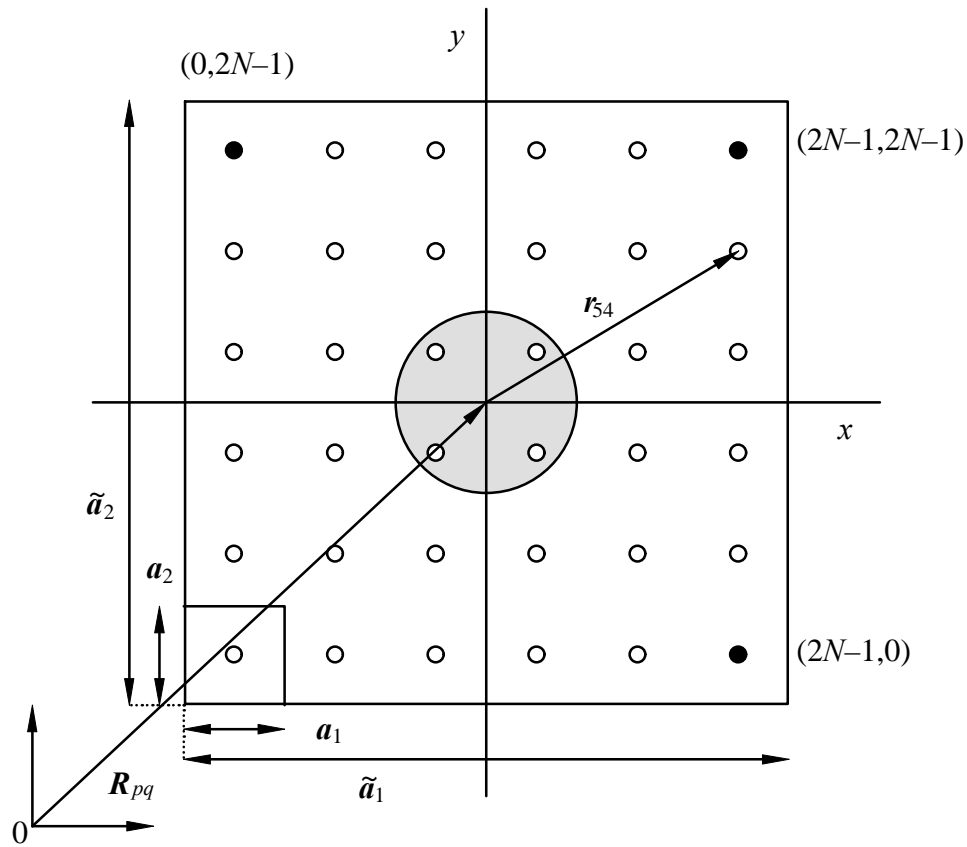


**Fig. 3a.** The  $(p,q)$  particle arrangement unit cell defined by  $\tilde{a}_1$  and  $\tilde{a}_2$  positioned in global space by  $\mathbf{R}_{pq}$ . The p.a.-unit cell contains  $2N \times 2N = 6 \times 6$  atoms and a single circular particle at the origin of an  $x$ - $y$ -coordinate system. In the p.a.-unit cell one matrix unit cell defined by  $a_1$  and  $a_2$  has been indicated and an example of  $\mathbf{r}_{mn}$  for  $m = 5$  and  $n = 4$  is shown.

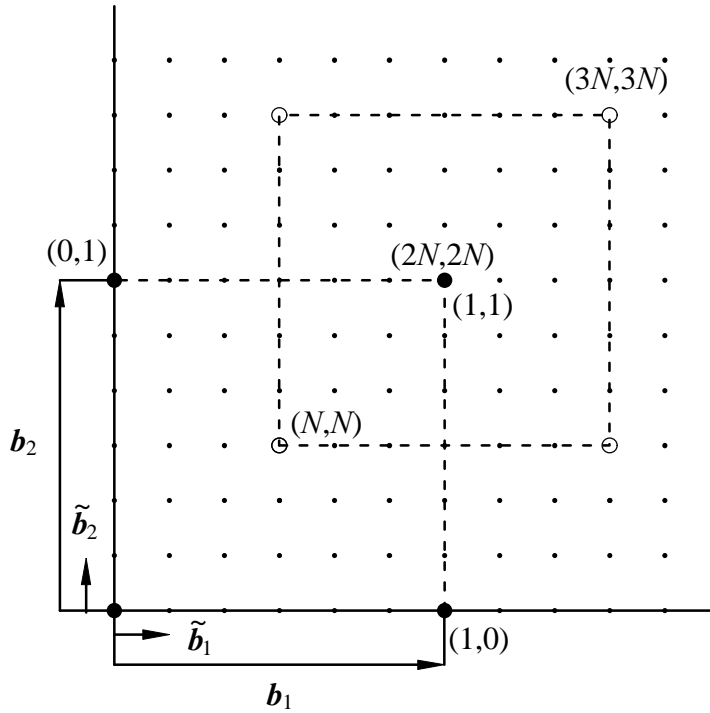


**Fig. 3b.** Representation of the reciprocal space pertaining to the p.a.-unit cell, defined by reciprocal vectors  $\tilde{\mathbf{b}}_1$  and  $\tilde{\mathbf{b}}_2$  (cf. Fig. 3a). The dashed square section surrounding the  $(1,1)$  matrix reflection ( $\tilde{h}_B = 2N, \tilde{k}_B = 2N$ ) is taken to comprise the intensity distribution of the  $(1,1)$  matrix reflection. Reciprocal lattice vectors of the matrix unit cell description,  $\mathbf{b}_1$  and  $\mathbf{b}_2$ , are indicated.

Here, the diffraction vector  $\mathbf{H} = \tilde{h}\tilde{\mathbf{b}}_1 + \tilde{k}\tilde{\mathbf{b}}_2$  is expressed in terms of real-valued variables  $\tilde{h}$  and  $\tilde{k}$ , and reciprocal lattice vectors  $\tilde{\mathbf{b}}_j$ , that are associated with  $\tilde{\mathbf{a}}_i$  according to  $\tilde{\mathbf{a}}_i \cdot \tilde{\mathbf{b}}_j = \mathbf{d}_{ij}$ , with  $\mathbf{d}_{ij}$  the Kronecker delta. The "~" symbol is used to mark all variables directly related to p.a.-unit cell vectors  $\tilde{\mathbf{a}}_1$  and  $\tilde{\mathbf{a}}_2$ .

Each vector  $\mathbf{r}_{mn}$  is expressed in terms of components along  $\tilde{\mathbf{a}}_1$  and  $\tilde{\mathbf{a}}_2$  by means of fractional coordinates  $\tilde{X}_{mn}$  and  $\tilde{Y}_{mn}$  ( $-\frac{1}{2} \leq \tilde{X}_{mn}, \tilde{Y}_{mn} \leq \frac{1}{2}$ ), i.e.  $\mathbf{r}_{mn} = \tilde{X}_{mn}\tilde{\mathbf{a}}_1 + \tilde{Y}_{mn}\tilde{\mathbf{a}}_2$ . In the deformed state,  $|\tilde{\mathbf{a}}_1|$  and  $|\tilde{\mathbf{a}}_2|$  are equal to the sum of the strain-free length,  $2L = 2Na$ , and the p.a.-unit cell dilatations  $2U$  and  $2V$ , respectively; cf. Fig. 1 (here  $U = V$ ; see below Eq. (1)). The atom  $(m,n)$  is displaced from its strain-free reference position  $([m + \frac{1}{2} - N]a, [n + \frac{1}{2} - N]a)$  (cf. Fig. 3a)<sup>1</sup> by a displacement  $(u_{mn}, v_{mn})$ . Thus,

<sup>1</sup> Note that the indices  $m$  and  $n$  start at the lower left corner of the p.a.-unit cell (with  $m = n = 0$ ). The choice of the position of the origin within the p.a.-unit cell is inconsequential for the corresponding intensity distribution in reciprocal space.

$$\tilde{X}_{mn} = \frac{(m + \frac{1}{2} - N)a + u_{mn}}{2Na + 2U}, \quad \tilde{Y}_{mn} = \frac{(n + \frac{1}{2} - N)a + v_{mn}}{2Na + 2V}. \quad (4)$$

The crystal factor  $G(\tilde{h}, \tilde{k})$  is defined as

$$G(\tilde{h}, \tilde{k}) = \sum_p \sum_q e^{2\pi i \mathbf{H} \cdot \mathbf{R}_{pq}} \quad (5)$$

with  $\mathbf{R}_{pq} = p\tilde{\mathbf{a}}_1 + q\tilde{\mathbf{a}}_2$  the vector indicating the position of the  $(p,q)$  unit cell with respect to a global origin (see Fig. 3a). Two limiting cases for the crystal size can be considered for  $G(\tilde{h}, \tilde{k})$ . Firstly, consider an imaginary, small crystal consisting of one p.a.-unit cell only. Then, it follows that  $G(\tilde{h}, \tilde{k})G^*(\tilde{h}, \tilde{k})=1$  and the intensity distribution in reciprocal space of the imaginary small crystal,  $I(\tilde{h}, \tilde{k})$ , equals  $F(\tilde{h}, \tilde{k})F^*(\tilde{h}, \tilde{k})$  and is continuous in  $\tilde{h}$  and  $\tilde{k}$  (cf. Eqs. (2) and (3)). Secondly, consider the infinitely large crystal studied so far, consisting of an infinite number of p.a.-unit cells that are exactly equal (i.e. there is no microstrain among the p.a.-unit cells; only within a p.a.-unit cell microstrain occurs). For this crystal it follows from Eq. (5) that  $G(\tilde{h}, \tilde{k})$  has only non-zero values for integer values of  $\tilde{h}$  and  $\tilde{k}$ . Then, the intensity distribution of the infinitely large crystal follows from sampling the intensity distribution of the imaginary small crystal at integer values of  $\tilde{h}$  and  $\tilde{k}$  (cf. Eqs. (2) and (3)). Hence, each  $(\tilde{h}, \tilde{k})$  line profile is a line intensity and the distribution of intensity in reciprocal space is not continuous but discrete.

The same particle-matrix system can also be described in terms of a matrix unit cell, containing one atom at its center and defined by the vectors  $\mathbf{a}_1$  and  $\mathbf{a}_2$ , as indicated in Fig. 3a. The corresponding reciprocal matrix lattice vectors,  $\mathbf{b}_1$  and  $\mathbf{b}_2$ , are defined in the usual way and the diffraction vector  $\mathbf{H}$  can be expressed as,  $\mathbf{H} = h\mathbf{b}_1 + k\mathbf{b}_2$ , with the real-valued variables  $h$  and  $k$  (see below Eq. (3)). Since  $\mathbf{H} = h\mathbf{b}_1 + k\mathbf{b}_2 = \tilde{h}\tilde{\mathbf{b}}_1 + \tilde{k}\tilde{\mathbf{b}}_2$  and  $\tilde{\mathbf{a}}_i = 2N\mathbf{a}_i$ , it follows  $\tilde{h} = 2Nh$  and  $\tilde{k} = 2Nk$ . Hence, the  $\{h,k\}$  line intensity in terms of the matrix unit cell description is the  $(2Nh, 2Nk)$  line intensity in terms of the p.a.-unit cell description (cf. Fig. 3b). The periodic arrangement of particles causes the presence of  $\{\tilde{h}, \tilde{k}\}$  satellites at both sides of the  $\{h,k\}$  reflections<sup>2</sup>.

Now, consider the presence of a microstrain field so that the matrix unit cells are strained differently. The p.a.-unit cells remain identical (see above) and again

<sup>2</sup> Since  $|\tilde{\mathbf{a}}_i|$  depends on the state of deformation it follows for a given reflection  $\{\tilde{h}, \tilde{k}\}$ , with  $\tilde{h}$  and  $\tilde{k}$  integers, that  $|\mathbf{H}|$ , with  $\mathbf{H} = \tilde{h}\tilde{\mathbf{b}}_1 + \tilde{k}\tilde{\mathbf{b}}_2$  and  $|\tilde{\mathbf{b}}_i| = 1/|\tilde{\mathbf{a}}_i|$ , also depends on the overall state of deformation.

$G(\tilde{h}, \tilde{k})$  has only non zero values for integer values of  $\tilde{h}$  and  $\tilde{k}$ ; however,  $F(\tilde{h}, \tilde{k})$  changes. Now, by the introduction of microstrains the  $\{hk\}$  line profile does not broaden in the usual sense: the "broadened"  $\{hk\}$  line profile is made up by a series of  $\{\tilde{h}\tilde{k}\}$  line intensities around the position of the ideal  $\{hk\}$  line intensity, due to the periodicity of the misfitting particle distribution. Therefore, in this work the  $\{hk\}$ -reflection is described by all  $\{\tilde{h}\tilde{k}\}$  line intensities within a square section of reciprocal space, in accordance with the symmetry of the reciprocal lattice. Using a subscript "B" to denote the values of  $h, k, \tilde{h}$  and  $\tilde{k}$  at a Bragg position according to the matrix unit cell description, this section is bounded by  $h_B-1/2 \leq h \leq h_B+1/2$  and  $k_B-1/2 \leq k \leq k_B+1/2$  in terms of the matrix unit cell description or by  $2(h_B-1/2)N \leq \tilde{h} \leq 2(h_B+1/2)N$  and  $2(k_B-1/2)N \leq \tilde{k} \leq 2(k_B+1/2)N$  in terms of the p.a.-unit cell description.

### 2.2.3 Intensity distribution of a polycrystalline powder; sampling in reciprocal space

Consider a powder composed of "infinitely large" powder particles, each of which is identical to the infinitely large single crystal considered above. The orientation distribution of the powder particles is assumed to be perfectly random. Then, the intensity of the  $\{hk\}$  powder diffraction-line profile at a specified length of the diffraction vector,  $|\mathbf{H}|$ , can be obtained from the intensity distribution in reciprocal space for a single crystal as considered above, through integration along a circle with radius equal to  $|\mathbf{H}|$  (for the case of 3D crystals, see Ref. 11) as illustrated in Fig. 4. The full  $\{hk\}$  powder diffraction-line profile is obtained by repeating this procedure for an appropriate range of diffraction vector lengths. This sampling procedure will be referred to as the "rotation procedure".

In powder-diffraction analysis usually the so-called "tangent plane approximation" is applied [11, 12]. In this case, the intensity distribution for a powder is obtained from the intensity distribution for the single crystal through integration in reciprocal space along a line *perpendicular* to  $\mathbf{H}_B$ , at a specified length of the diffraction vector,  $|\mathbf{H}|$  (cf. Fig. 4). The full  $\{hk\}$  powder diffraction-line profile is then obtained by repeating this procedure for an appropriate range of diffraction vector lengths. This sampling procedure will be referred to as the "tangent procedure".

### 2.2.4 Computing time considerations

It follows from Eqs. (2) and (3) that the number of steps in a straightforward calculation of the intensity distribution of an  $\{hk\}$ -matrix line profile is dependent on the square of the number of atoms in the p.a.-unit cell: (i) each  $\{\tilde{h}\tilde{k}\}$  intensity requires

the summation of the contribution of all atoms within the p.a.-unit cell ( $= 4N^2$ ) and (ii) each square section of reciprocal space to be considered for an  $\{hk\}$  matrix line profile (cf. Section 2.2.2) consists of  $4N^2 \{\tilde{h}\tilde{k}\}$  line intensities (cf. Fig. 4b). However, based on a Fast Fourier Transform and a special reformulation of the displacement field, a fast method of calculation has been developed (see Appendix B), with a computation time that is roughly linearly dependent on the number of atoms in the p.a.-unit cell.

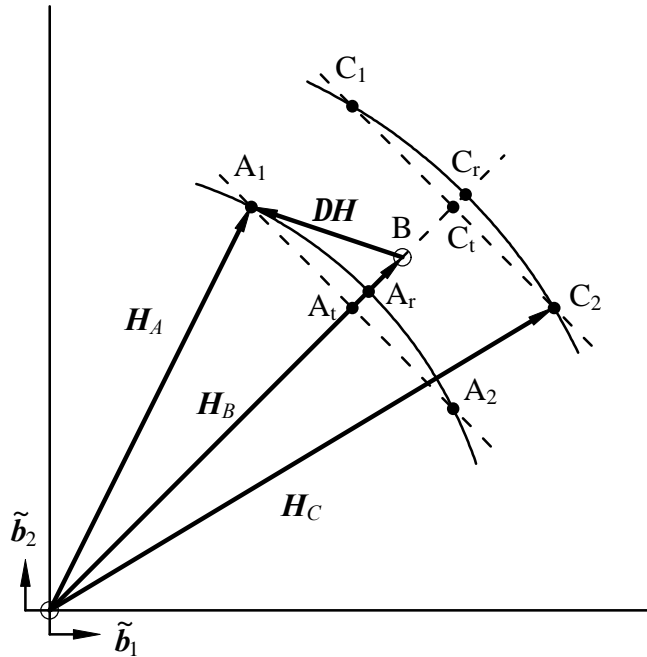


**Fig. 4.** Comparison of two procedures to obtain a powder diffraction-line profile from the intensity distribution in reciprocal space of an "infinitely large" single powder particle. (i) The rotation procedure is represented by the solid arcs that depict parts of the circles through all line intensities at equal distance to the origin of reciprocal space. (ii) The tangent procedure is represented by the dashed lines. All line intensities located at the dashed lines perpendicular to the diffraction vector  $\mathbf{H}_B$  are projected onto the diffraction vector at the same distance from the origin of reciprocal space.

### 2.3 Characterization of line profiles

As demonstrated in Section 2.2.2 the  $\{hk\}$  powder diffraction line profile consists of a series of line intensities. The  $\{hk\}$  line profile will be characterized by its centroid  $H_c^{hk}$ , as a measure of profile position, and its standard deviation  $S^{hk}$ , as a measure of profile width. The centroid of an  $\{hk\}$  powder diffraction-line profile is obtained from

$$H_c^{hk} = \frac{\sum_{\tilde{h}} \sum_{\tilde{k}} |\mathbf{H}(\tilde{h}, \tilde{k})| I(\tilde{h}, \tilde{k})}{\sum_{\tilde{h}} \sum_{\tilde{k}} I(\tilde{h}, \tilde{k})} \quad (6)$$

where the summations over  $\tilde{h}$  and  $\tilde{k}$  are limited to these reflections of the p.a.-unit cell that contribute to the  $\{hk\}$  reflection (see Section 2.2.2) and with  $|\mathbf{H}(\tilde{h}, \tilde{k})|$  as the distance from the origin of reciprocal space to a specific  $\{\tilde{h}\tilde{k}\}$  line intensity *after* projection onto the diffraction vector by either the tangent procedure or the rotation procedure (cf. Fig. 4). The standard deviation of the  $\{hk\}$  diffraction-line profile equals the square root of its variance,  $S^{hk} = \sqrt{Var^{hk}}$ . The latter is defined with respect to the centroid position  $H_c^{hk}$  as

$$Var^{hk} = \frac{\sum_{\tilde{h}} \sum_{\tilde{k}} (|\mathbf{H}(\tilde{h}, \tilde{k})| - H_c^{hk})^2 I(\tilde{h}, \tilde{k})}{\sum_{\tilde{h}} \sum_{\tilde{k}} I(\tilde{h}, \tilde{k})}. \quad (7)$$

### 3. The interpretation of "size broadening"

#### 3.1 Introduction

Even in the absence of misfit at the particle-matrix interfaces ( $\mathbf{e} = 0$ ), broadening of  $\{hk\}$  line profiles occurs, if the particles do not contribute to the diffraction process, i.e.  $f_{mn} = 0$  for a particle atom and  $f_{mn} = 1$  for a matrix atom (see Eq. (3)). This type of broadening is not always recognized for precipitating systems. It is due to finite distances within the matrix between the particles; it is order independent and called "size"-broadening; it should not be confused with the usual "size" broadening due to the finite, outer size of the matrix.

#### 3.2 Centroid and variance; numerical results

The centroid and the variance of a  $\{10\}$ -reflection,  $H_c^{10}$  and  $Var^{10}$ , respectively, are plotted in Figs. 5a and b as a function of  $c/(1-c)$  for different particle radii,  $R_p = N_R a$ , for the unclustered state (and obviously with  $\mathbf{e} = 0$ ) and with  $a = 1$ . Both the shift of the centroid and the variance increase with  $c/(1-c)$  at constant  $2N_R$  and decrease with increasing particle size  $2N_R$  at constant  $c/(1-c)$ .



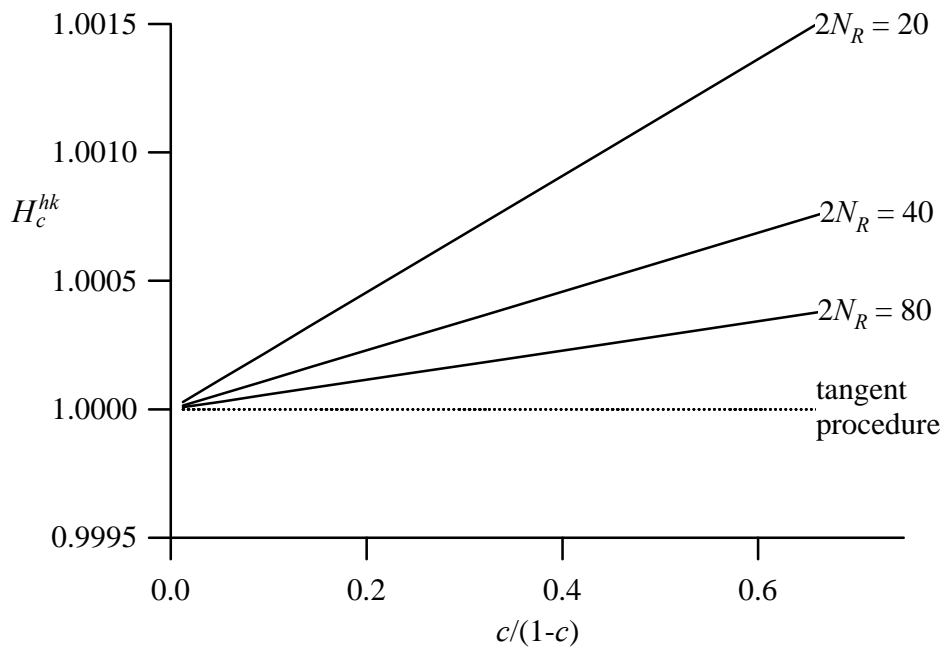


**Fig. 5a.** Centroids of size broadened  $\{10\}$  line profiles as a function of particle fraction  $c/(1-c)$  for particle size  $2N_R = 20, 40$  and  $80$  ( $2N \times 2N$  is changed correspondingly). Solid lines represent results of rotation procedure to obtain  $\{10\}$  powder diffraction-line profile and dashed lines represent results of tangent procedure.

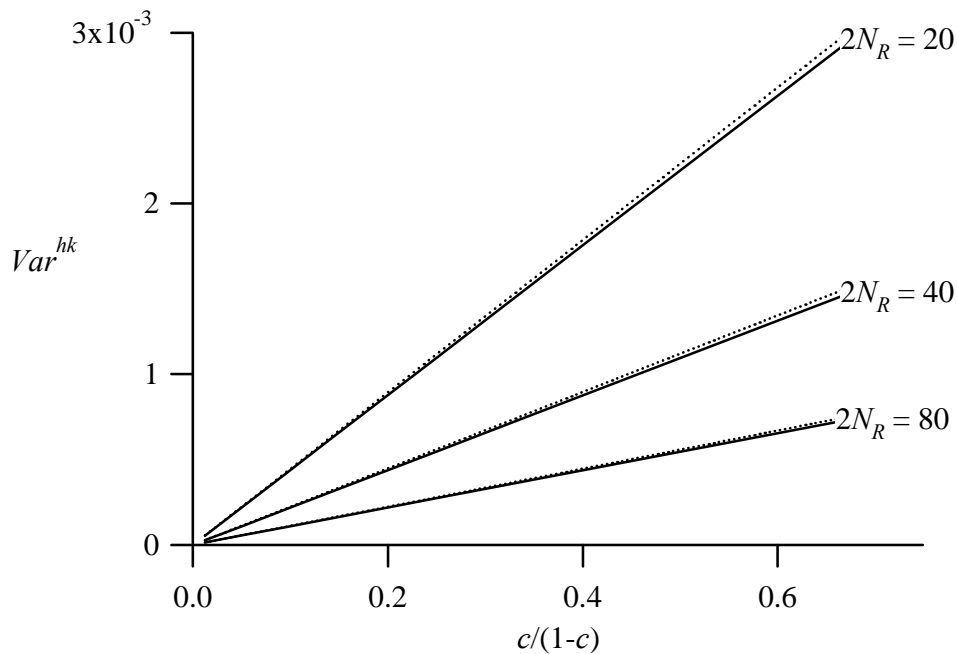


**Fig. 5b.** Variances of size broadened  $\{10\}$  line profiles as a function of particle fraction  $c/(1-c)$  for particle size  $2N_R = 20, 40$  and  $80$  ( $2N \times 2N$  is changed correspondingly). Solid lines represent results of rotation procedure to obtain  $\{10\}$  powder diffraction-line profile and dashed lines represent results of tangent procedure.

The influence of the type of sampling in reciprocal space is only distinct for the centroid shift: line profiles obtained using the tangent procedure exhibit even no centroid shift at all, contrary to those obtained using the exact, rotation procedure. The observation of an, albeit very small, centroid shift in a case of pure "size broadening" is counter-intuitive. In fact, the line shift observed for the exact sampling procedure is physically genuine, but it is entirely due to the way the powder diffraction measurement is performed in practice, as described by the exact sampling (of reciprocal space) procedure. This can be shown with the aid of Fig. 4 as follows.

In Fig. 4 a Bragg reflection is considered with a maximum denoted by  $B$ , along with equal intensities symmetrically placed around  $B$  (belonging to the reflection considered):  $A_1$ ,  $A_2$ ,  $C_1$  and  $C_2$ . The powder diffraction measurement implies projection on the diffraction vector  $\mathbf{H}$  (of variable length but fixed position; cf. Section 2.2.3). In the approximate, tangent procedure, the intensities  $A_1$  and  $A_2$  are projected onto the diffraction vector at  $A_t$ ; the intensities  $C_1$  and  $C_2$  are projected onto  $C_t$ . The distance from  $A_t$  to  $B$  equals the distance from  $C_t$  to  $B$ , so that the powder diffraction-line profile is symmetric with respect to  $B$  also after projection. However, using the exact, rotation procedure, the line intensities  $A_1$  and  $A_2$  are projected on the diffraction vector according to radius  $|\mathbf{H}_A|$  and the intensities  $C_1$  and  $C_2$  are projected according to radius  $|\mathbf{H}_C|$ . As a consequence, the distance from  $B$  to the projected line intensities  $A_r$  is smaller than to  $C_r$ , so that the powder diffraction-line profile according to the rotation procedure is asymmetric. Apparently, in Fig. 5a a positive centroid shift (towards higher  $|\mathbf{H}|$ ) occurs. Detailed analysis reveals that this shift is proportional to the variance of the powder-diffraction line profile; see Appendix C.

The variance of the profiles is not significantly affected by the sampling procedure in reciprocal space and is a clear indication of the "size broadening", as is discussed next.

### 3.3 Relation between particle fraction and line width

The shape of the intensity distribution is largely determined by the shape and size of the particle. This follows from the calculation of the structure factor of the p.a.-unit cell (cf. Eq. (3)) when applying Babinet's principle [13]. Consider the p.a.-unit cell depicted in Fig. 3a containing an array of atoms divided over matrix *and* particle. For the structure factor  $F(\tilde{h}, \tilde{k})$ , the sum over the *matrix* atoms can be written as the sum over the matrix *and* particle atoms in the p.a.-unit cell minus the sum over the *particle* atoms. If the scattering factors of matrix and hypothetical particle atoms are taken equal, the sum over all matrix *and* particle atoms yields the structure factor of a particle free, p.a.-unit cell, further denoted by  $F_{pf}$ , and the sum over all *particle* atoms

yields the structure factor of a p.a.-unit cell containing a hypothetical diffracting particle of matrix material only, denoted by  $F_p$ . Thus

$$F(\tilde{h}, \tilde{k}) = \sum_{m=0}^{2N-1} \sum_{n=0}^{2N-1} f_{mn} e^{2\pi i \mathbf{H} \cdot \mathbf{r}_{mn}} = F_{pf} - F_p = \sum_{m=0}^{2N-1} \sum_{n=0}^{2N-1} e^{2\pi i \mathbf{H} \cdot \mathbf{r}_{mn}} - \sum_{particle} \sum e^{2\pi i \mathbf{H} \cdot \mathbf{r}_{mn}} \quad (8)$$

It can be shown that  $F_{pf}$  equals zero at every position in reciprocal space except for the Bragg positions of the matrix according to the matrix unit cell description if the crystal consists of an infinite number of p.a.-unit cells,  $F_{pf}(h_B, k_B) = 4N^2$  (for  $f_{mn} = 1$ ). Thus at non-Bragg positions in reciprocal space,  $F(\tilde{h}, \tilde{k}) = F_p(\tilde{h}, \tilde{k})$ .

Calculation of  $I(\tilde{h}, \tilde{k})$  for an infinitely large single crystal composed of identical p.a.-unit cells at integer values of  $\tilde{h}$  and  $\tilde{k}$  (see Section 2.2.2) by multiplication of  $F(\tilde{h}, \tilde{k})$  with its complex conjugate yields intensity at non-Bragg positions from the product  $F_p F_p^* = I_p(\tilde{h}, \tilde{k})$  only. Hence the intensity distribution at non-Bragg positions is equal to the intensity distribution that would have been obtained if only atoms of the hypothetical particle of matrix material had diffracted. The shape of the intensity distribution at non-Bragg positions is thus determined by the size and shape of the particle. At the Bragg position  $(h_B, k_B)$  the intensity equals the square of the number of matrix atoms,  $I(h_B, k_B) = (4N^2 - N_p)^2 = N_m^2$  for  $f_{mn} = 1$  and with  $N_m$  as the number of matrix atoms and  $N_p$  as the number of atoms per particle. On this basis, the dependence of the variance on particle fraction  $c$  can be understood as follows.

The calculation of the variance according to Eq. (7) indicates that  $\{\tilde{h}, \tilde{k}\}$  line intensities are sampled in reciprocal space at  $(\tilde{h}, \tilde{k})$  positions defined by the size and number of atoms of the p.a.-unit cell. If the density of these sampling locations is sufficiently large (i.e.  $|\tilde{b}_1| = |\tilde{b}_2| = 1/2N$  is sufficiently small), Eq. (7) can be replaced by:

$$Var^{hk} = \frac{\iint_{\tilde{h}, \tilde{k}} (|\mathbf{H}(\tilde{h}, \tilde{k})| - H_c^{hk})^2 I(\tilde{h}, \tilde{k}) d\tilde{h} d\tilde{k}}{\iint_{\tilde{h}, \tilde{k}} I(\tilde{h}, \tilde{k}) d\tilde{h} d\tilde{k}} \quad (9)$$

with  $\tilde{h}$  and  $\tilde{k}$  now as real-valued variables. Then the following approximations can be made. First, the factor  $I(\tilde{h}, \tilde{k})$  in the numerator on the right hand side of Eq. (9) can be replaced by  $I_p(\tilde{h}, \tilde{k})$  away from the Bragg position  $(h_B, k_B)$  since at and near

the Bragg position  $(|H(\tilde{h}, \tilde{k})| - H_c^{hk})^2$  is very small. Similarly, the denominator of the right hand side of Eq. (9) can be rewritten as

$$\int \int_{\tilde{h} \tilde{k}} I(\tilde{h}, \tilde{k}) d\tilde{h} d\tilde{k} = \int \int_{\tilde{h} \tilde{k}} I_p(\tilde{h}, \tilde{k}) d\tilde{h} d\tilde{k} - I_p(h_B, k_B) + I(h_B, k_B). \quad (10)$$

Obviously,  $\int \int_{\tilde{h} \tilde{k}} I_p(\tilde{h}, \tilde{k}) d\tilde{h} d\tilde{k} = N_p$ , with  $N_p$  the number of atoms per particle (e.g. Ref. 11)<sup>3</sup>. Further,  $I_p(\tilde{h}_B, \tilde{k}_B) = N_p^2 = (4N^2c)^2$  and  $I(\tilde{h}_B, \tilde{k}_B) = N_m^2 = (4N^2(1-c))^2$  (see above discussion). Substitution of all this in Eq. (10) leads to

$$Var^{hk} = \frac{1}{N_p} \frac{c}{1-c} \int \int_{\tilde{h} \tilde{k}} (|\mathbf{H}(\tilde{h}, \tilde{k})| - H_c^{hk})^2 I_p(\tilde{h}, \tilde{k}) d\tilde{h} d\tilde{k}. \quad (11)$$

At constant particle size, and thus constant  $N_p$ ,  $I_p(\tilde{h}, \tilde{k})$  is constant and then  $Var^{hk}$  is approximately proportional to  $c/(1-c)$ , as indeed observed in Fig. 5b. Hence, recognizing that  $S^{hk} = \sqrt{Var^{hk}}$  and for  $c \ll 1$ , the line width is proportional to square root of the particle fraction  $c$ .

### 3.4 Relation between particle number density and line width; variance-range plots

A change of  $2N$  and thereby the p.a.-unit cell size  $2L = 2Na$  can be interpreted as a change of the size and the number density of precipitate particles  $p$ , with  $p = 1/(4N^2)$ . As pointed out in Section 3.1, "size broadening" of matrix reflections is due to the presence of non-diffracting parts (the particles) in this matrix. According to [11], the size of the diffracting crystallite leads to line broadening that is inversely proportional to that size. A possible "size parameter" in the present case is the inter particle distance, which is proportional to  $2N$  at constant particle fraction. However, it follows from Fig. 6a that a plot of  $S^{hk}$  vs  $1/2N$  does not yield a straight line. Rather  $S^{hk}$  appears to be proportional to  $1/\sqrt{2N}$  according to Fig. 6b. These phenomena can be explained as follows.

Variance-range plots can be used to characterize line broadening [14-16]. Let  $s$  denote the distance along  $\mathbf{H}$  to the origin (e.g. the centroid/maximum) of the powder diffraction line profile. Starting at the origin ( $s = 0$ ) the variance is calculated for

<sup>3</sup>  $N_p$  is related to  $N_R$  (see Section 2.2.1) by  $N_p \approx pN_R^2$ . Note that both  $N_p$  and  $N_R$  are integer.

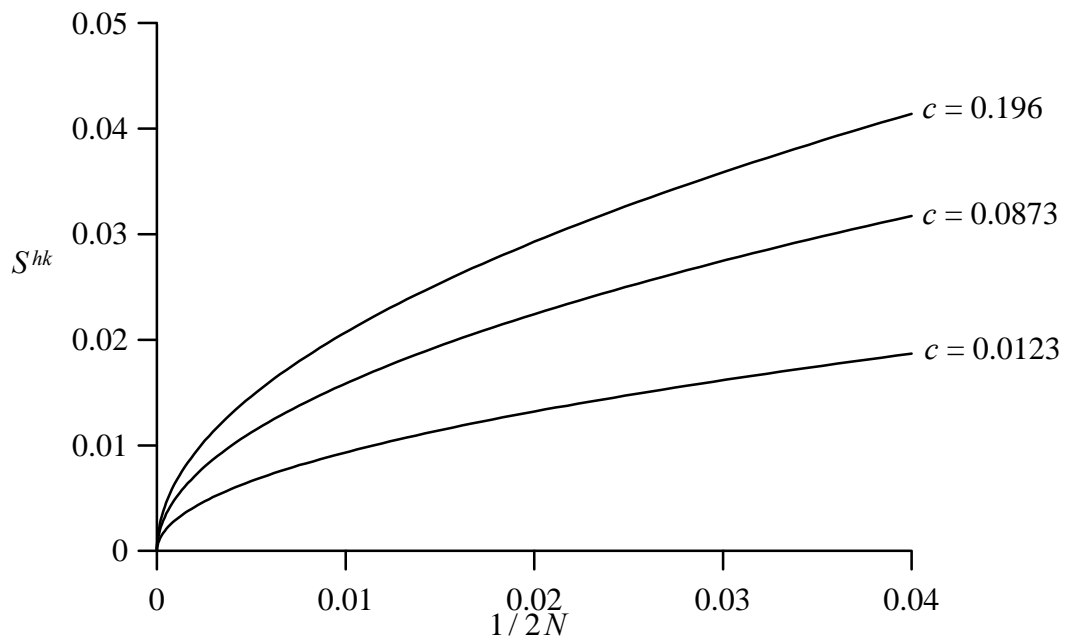


**Fig. 6a.** Standard deviation of size broadened  $\{10\}$  line profile as a function of the reciprocal of the size of the p.a.-unit cell,  $2N$ , for  $c = 0.0123$ ,  $0.0873$  and  $0.196$ .

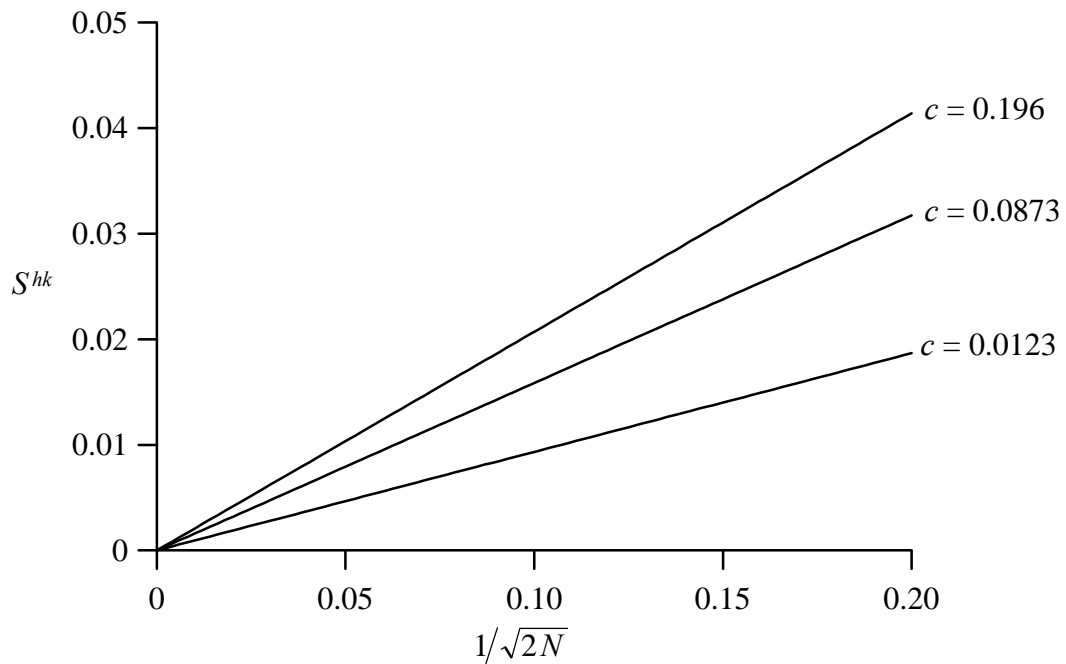


**Fig. 6b.** Standard deviation of size broadened  $\{10\}$  line profile as a function of the reciprocal of the square root of the size of the p.a.-unit cell,  $2N$ , for  $c = 0.0123$ ,  $0.0873$  and  $0.196$ .

increasing lengths of the range  $-s_1$  to  $s_2$  on either side of the peak maximum (cf. Eqs. (7) and (9)). Examples of such plots are given in Fig. 7 for the  $\{10\}$  diffraction line profile for a p.a.-unit cell with  $c = 0.087$  and  $N_R = 20, 40$  or  $80$ , respectively, corresponding to  $2N \times 2N = 120 \times 120, 240 \times 240$  or  $480 \times 480$ , respectively. Clearly, apart from very close to the origin ( $s \downarrow 0$ ), the variance scales linearly with  $s = s_1 + s_2$  over a considerable range of values<sup>4</sup>. This reflects the recognition that in case of "size broadening" the tails of a profile fall off inversely proportional to  $s^2$  [14-16]. The slope of this linear part of the plot,  $C$ , is a measure for "size".

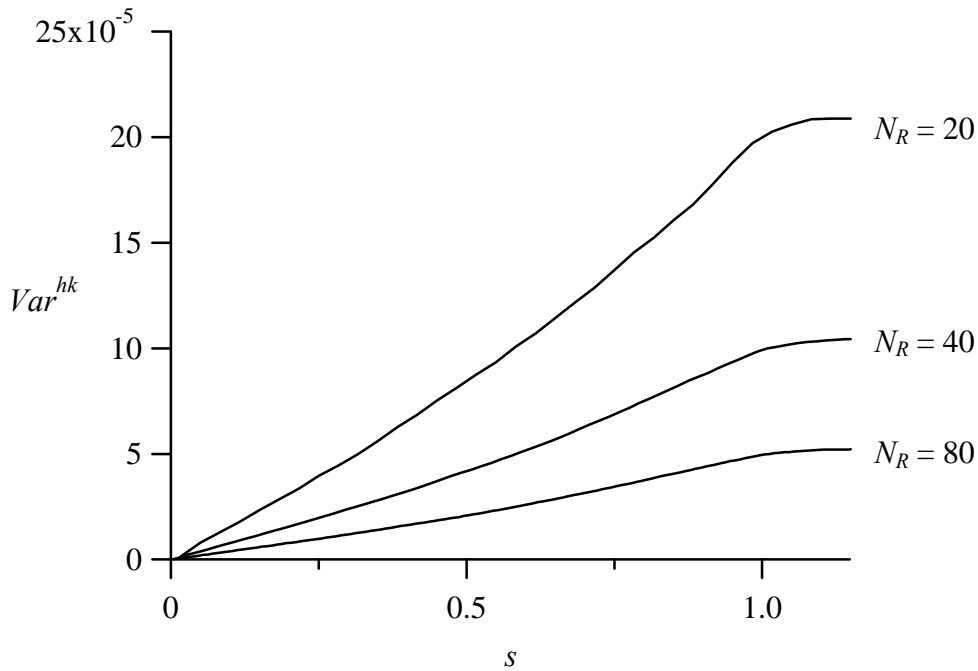


**Fig. 7.** Variance-range plots for  $\{10\}$  diffraction line profile of a p.a.-unit cell containing one misfitting particle with  $c = 0.087$  and  $E_p/E_m = 1$  for various particle sizes:  $N_R = 20, 40$  or  $80$ , respectively, corresponding to  $2N \times 2N = 120 \times 120, 240 \times 240$  or  $480 \times 480$ , respectively. The centroid of the diffraction line profile corresponds with  $s = 0$  and the range is taken symmetrical with respect to the centroid.

Now consider, at constant  $c$ , a p.a. unit cell of size  $2N_1$  and one of size  $2N_2 = a2N_1$ . Because all dimensions of the matrix (including the interparticle distance) scale with  $2N$  and the width of the size broadening in reciprocal space is

<sup>4</sup> At the end of the range the intensity distributions of neighbouring reflections overlap. Consequently, the intensity distribution does not fall off inversely proportional to  $s^2$  in this region and the linear character of the variance-range diagram is disturbed.

proportional with  $1/2N$  [11], one can write  $I_{2N_1}(\mathbf{as}) = I_{2N_2}(s)$  with  $I$  the intensity distribution along  $\mathbf{H}$ . Thus

$$\begin{aligned} Var_{2N_2}^{hk} &= \frac{\int_{-s_1}^{s_2} s^2 I_{2N_2}(s) ds}{\int_{-s_1}^{s_2} I_{2N_2}(s) ds} = \frac{\int_{-s_1}^{s_2} s^2 I_{2N_1}(\mathbf{as}) ds}{\int_{-s_1}^{s_2} I_{2N_1}(\mathbf{as}) ds} = \frac{1}{\mathbf{a}^2} \frac{\int_{-\mathbf{as}_1}^{\mathbf{as}_2} (\mathbf{as})^2 I_{2N_1}(\mathbf{as}) d(\mathbf{as})}{\int_{-\mathbf{as}_1}^{\mathbf{as}_2} I_{2N_1}(\mathbf{as}) d(\mathbf{as})} \equiv \\ &\equiv \frac{1}{\mathbf{a}^2} C(\mathbf{as}_1 + \mathbf{as}_2) = \frac{1}{\mathbf{a}} C(s_1 + s_2) = \frac{1}{\mathbf{a}} Var_{2N_1}^{hk} \end{aligned} \quad (12)$$

Here the approximation  $\int_{-\mathbf{as}_1}^{\mathbf{as}_2} I_{2N_2}(\mathbf{as}) d(\mathbf{as}) \equiv \int_{-s_1}^{s_2} I_{2N_2}(s) ds$  has been applied, which is justified when the tails of the intensity distribution have a negligible contribution to the integrated intensity. It immediately follows from Eq. (12) that  $S^{hk} (= \sqrt{Var^{hk}})$  is inversely proportional to  $\sqrt{2N}$ , as observed (Fig. 6). Hence the line width is proportional to  $(p)^{1/4}$ .

The reason for  $S^{hk}$  being related inversely proportional to  $\sqrt{2N}$  instead of  $2N$  is a direct consequence of the variance being defined to include *all* line intensities of the  $\{hk\}$  reflection (see Eqs. 7 and 9), so that the length of the range,  $s_1 + s_2$ , is independent of the width and the shape of the line profile. Had the lengths of the ranges of  $I_{2N_1}$  and  $I_{2N_2}$  been scaled according to  $(s_1 + s_2)_{2N_1} = \mathbf{a}(s_1 + s_2)_{2N_2}$ , then the calculation of the corresponding variances would have yielded the  $1/2N$ -dependence.

### 3.5 Effect of particle clustering

The simulations show that, although the  $\{hk\}$  diffraction line profiles of the matrix are dependent on the state of particle clustering, for the case of pure "size broadening" the centroid and the variance of these diffraction line profiles are practically unaffected by clustering (see also discussion in Section 3.2 and footnote 4). Only for the utmost clustered state when particles touch, the variance changes abruptly.

The effect of particle clustering can be clarified by comparing the Fourier coefficients of the diffraction-line profiles for different states of clustering. As an example, the real and imaginary parts of the Fourier coefficients, normalised by the first Fourier coefficient and obtained using the tangent procedure (cf. Section 2.2.3), have been plotted in Fig. 8 for  $C_f$ -values ranging from the unclustered state ( $C_f = 0$ ) to

the (utmost) clustered state where particles touch (with  $c = 0.087$  it follows  $C_f^{\max} = 0.67$ , see Section 2.1) and  $4N \times 4N = 240 \times 240$ .

The imaginary parts of the Fourier coefficients of the  $\{10\}$  powder diffraction line profile are zero independent of the state of particle clustering: the line profile remains symmetric with respect to its origin as there is no shift of the centroid.

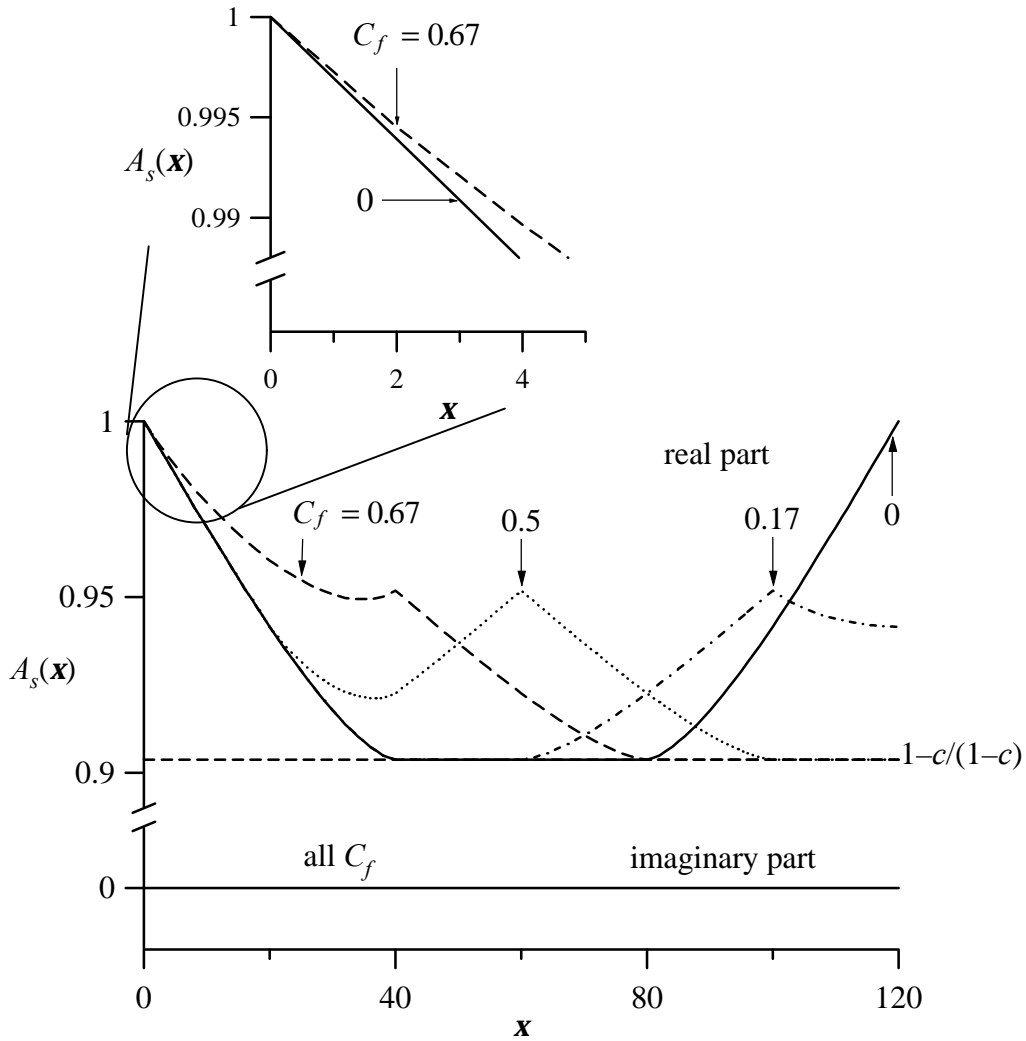


**Fig. 8.** Real and imaginary parts of Fourier coefficients  $A_s(\mathbf{z})$  of  $\{10\}$  powder diffraction line profile, obtained using the tangent procedure, of a large p.a.-unit cell containing  $4N \times 4N = 240 \times 240$  atoms and four non diffracting particles of radius  $N_R = 20$  ( $c = 0.0873$ ) located at  $(x,y) = (\pm L_p, \pm L_p) = (\pm N_c a, \pm N_c a)$ , with  $N_c = 60$  ( $C_f = 0$ ),  $N_c = 50$  ( $C_f = 0.17$ ),  $N_c = 30$  ( $C_f = 0.50$ ) and  $N_c = 20$  ( $C_f = C_f^{\max} = 0.67$ ).



The real parts of the Fourier coefficients of the  $\{10\}$  powder diffraction line profiles are clearly dependent on the state of clustering. It can be shown (see Appendix D) that the "size Fourier coefficients" can be regarded as being the sum of a constant level,  $A_s(\mathbf{x}) = 1-c/(1-c)$  ( $A_s(\mathbf{x}) \approx 0.9$  here), and the size Fourier coefficients of the particles if they diffract and consist of matrix material. For  $C_f = 0$  the large p.a.-unit cell is in its unclustered state and  $A_s(\mathbf{x})$  is periodic with period  $2N$  ( $2N = 120$  here). If  $C_f > 0$  the peak at  $\mathbf{x} = 2N$  separates into two equal peaks of half height that move either towards  $\mathbf{x} = 0$  or to  $\mathbf{x} = 4N$  with a shift directly related to the state of clustering.

According to a result of Fourier theory [17] the variance of the  $\{hk\}$  powder diffraction line profile can be calculated from the curvature of the  $A_s(\mathbf{x})$ -curve at the origin

$$Var^{hk} = -\frac{1}{4p^2 A_s(0)} \frac{d^2 A_s}{dx^2}(0). \quad (13)$$

Since the curvature of the  $A_s(\mathbf{x})$ -curve at the origin (Fig. 8) does not change significantly with clustering, the variance remains constant for almost all values of  $C_f$ . However, as soon as particles touch, i.e.  $C_f = C_f^{max}$ , the curvature at the origin changes, so that the variance changes. Physically this means that the clustered particles cannot be considered as separate particles anymore.

#### 4. "Size-strain separation"

If "size" and "(micro)strain" both contribute to line broadening, the problem arises how to separate both contributions.

For the present case of misfitting particles in a matrix a series of variance-range plots (calculated from the corresponding intensity distributions; cf. Section 3.4 and Fig. 7) is shown in Fig. 9 for a range of values for the misfit parameter  $\epsilon$ . As discussed in connection with Fig. 7 (where  $\epsilon = 0$ : only "size" broadening") the slope of the linear part of the curve with  $\epsilon = 0$  in Fig. 9 is representative of the "size broadening": tails of the intensity distribution decay with  $1/s^2$  [14-16]. It follows from the results shown in Fig. 9 that (i) a linear part in the variance-range plots also occurs for  $\epsilon > 0$ , and (ii) that this slope is independent of  $\epsilon$ . When one recognizes that "size" dominates the tails of the intensity distribution at large values of  $s$  [14-16], these results suggest that the variance of the "size broadening" occurring in all cases ( $\epsilon > 0$ )

is the same. This is compatible with the supposition that the full line profile can be conceived as the convolution of the "size-" and "strain-broadened" parts [2, 11].

It is concluded that in the analysis of line width due to "strain" in a system of misfitting particles in a matrix (see part II), the variance due to "size" only (the case with  $\mathbf{e} = 0$ ) can be subtracted straightforwardly from the variance for a case with  $\mathbf{e} > 0$  in order to obtain the variance due to "strain" only.

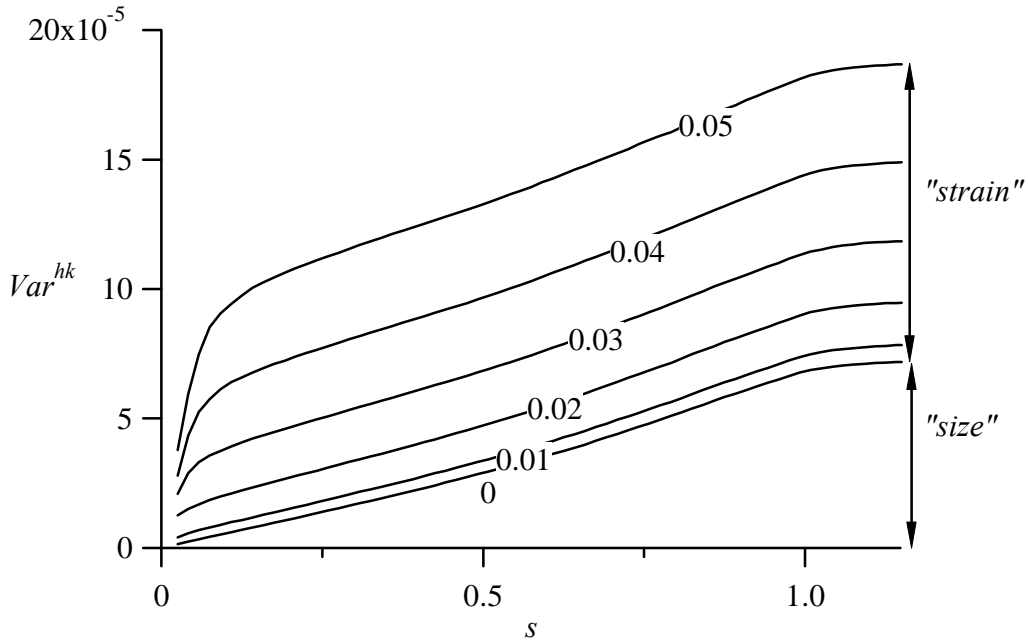


**Fig. 9.** Variance-range plots for  $\{10\}$  diffraction line profile of a p.a.-unit cell containing one misfitting particle with  $c = 0.087$ ,  $E_p/E_m = 1$  and p.a.-unit cell size  $2N \times 2N = 240 \times 240$  for various values of the particle matrix misfit:  $\mathbf{e} = 0, 0.01, \dots, 0.05$ . The contribution of "size" and "strain" to the total broadening is indicated.

## 5. Conclusions

- (i) Diffraction-line broadening due to misfitting particles in a matrix can be described appropriately using a micromechanical model, introducing the concept of a particle-arrangement unit cell and a suitable procedure for calculation of its structure factor.
- (ii) "Size broadening" of matrix reflections arises due to finite interparticle distances in the matrix between the particles.
- (iii) The line width due to "size broadening" (expressed as standard deviation of the intensity profile) is proportional to  $\sqrt{c/(1-c)}$ , with  $c$  the particle fraction, and to  $(p)^{1/4}$ , with  $p$  the particle number density. The line width at constant  $c$  is proportional to  $1/\sqrt{2R}$ , with  $R$  the particle radius.

(iv) Clustering of particles does affect the powder diffraction line profiles, but it does not affect the centroid and the variance due to "size" broadening as long as the particles do not touch.

(v) For the case of misfitting particles in a matrix, the variances of the "size-" and "strain-broadened" parts of the intensity distribution can be regarded as being additive to a high accuracy. This implies that the variance of the "strain-broadened part" can be obtained by subtraction of the variance observed in the case of pure "size broadening".

### ***Acknowledgement***

This work has been part of the research program of the Foundation for Fundamental Research on Matter (Stichting FOM), The Netherlands.

### *Appendix A*

#### ***Interpolation of displacement field within an element***

The displacement of an arbitrary point  $P$  in a quadrilateral element can be obtained by bilinear interpolation between the displacements of its four nodes. First, the so-called natural coordinates of  $P$  in a reference, square element are determined. Then, bilinear interpolation of the displacements of each node using the natural coordinates yields the displacement at  $P$ .

The natural coordinates  $(\mathbf{x}, \mathbf{h})$  of  $P(x, y)$  are found from solving the following matrix equation [10] for  $\mathbf{x}$  and  $\mathbf{h}$

$$\begin{bmatrix} 1 \\ x \\ y \end{bmatrix} = \begin{bmatrix} 1 & 1 & 1 & 1 \\ x_1 & x_2 & x_3 & x_4 \\ y_1 & y_2 & y_3 & y_4 \end{bmatrix} \begin{bmatrix} \frac{1}{4}(1-\mathbf{x})(1-\mathbf{h}) \\ \frac{1}{4}(1-\mathbf{x})(1+\mathbf{h}) \\ \frac{1}{4}(1+\mathbf{x})(1-\mathbf{h}) \\ \frac{1}{4}(1+\mathbf{x})(1+\mathbf{h}) \end{bmatrix}. \quad (\text{A. 1})$$

with  $(x_i, y_i)$  the coordinates of the four nodes of the quadrilateral element. Working out the matrix product of Eq. (A. 1), two non linear coupled equations are obtained

$$\begin{bmatrix} 4x \\ 4y \end{bmatrix} = \begin{bmatrix} a_1 + a_2\mathbf{x} + a_3\mathbf{h} + a_4\mathbf{hx} \\ b_1 + b_2\mathbf{x} + b_3\mathbf{h} + b_4\mathbf{hx} \end{bmatrix} \quad (\text{A. 2})$$

with  $a_i$  and  $b_i$  given by

$$\begin{bmatrix} 1 & 1 & 1 & 1 \\ -1 & -1 & 1 & 1 \\ 1 & -1 & -1 & 1 \\ -1 & 1 & -1 & 1 \end{bmatrix} \begin{bmatrix} x_1 y_1 \\ x_2 y_2 \\ x_3 y_3 \\ x_4 y_4 \end{bmatrix} = \begin{bmatrix} a_1 b_1 \\ a_2 b_2 \\ a_3 b_3 \\ a_4 b_4 \end{bmatrix}. \quad (\text{A. 3})$$

After elimination of the term  $\mathbf{xh}$  in Eq. (A. 2),  $\mathbf{x}$  can be expressed in  $\mathbf{h}$  as

$$\mathbf{x} = c_1 + c_2 \mathbf{h} \quad (\text{A. 4})$$

with

$$c_1 = \frac{4(b_4 x - a_4 y) - (a_1 b_4 - a_4 b_1)}{a_2 b_4 - a_4 b_2}; \quad c_2 = -\frac{a_3 b_4 - a_4 b_3}{a_2 b_4 - a_4 b_2} \quad (\text{A. 5})$$

Subsequently, the relation between  $\mathbf{x}$  and  $\mathbf{h}$  is used in Eq. (A. 2) to obtain a quadratic equation in  $\mathbf{h}$  of the type  $e_1 \mathbf{h}^2 + e_2 \mathbf{h} + e_3 = 0$ , with  $e_1$ ,  $e_2$  and  $e_3$  as known constants, which can be readily solved. Two solutions  $\mathbf{h}_1$  and  $\mathbf{h}_2$  are obtained that correspond with  $\mathbf{x}_1$  and  $\mathbf{x}_2$ , respectively, using Eq. (A. 4). However, since  $\mathbf{x}$  and  $\mathbf{h}$  are defined such that  $-1 \leq \xi, \eta \leq 1$  only one set of coordinates  $(\mathbf{x}, \mathbf{h})$  is found.

The displacements  $(u, v)$  at  $P$  are finally calculated by means of the same interpolation as in Eq. (A.1) [10]

$$\begin{bmatrix} 1 \\ u \\ v \end{bmatrix} = \begin{bmatrix} 1 & 1 & 1 & 1 \\ u_1 & u_2 & u_3 & u_4 \\ v_1 & v_2 & v_3 & v_4 \end{bmatrix} \begin{bmatrix} \frac{1}{4}(1-\mathbf{x})(1-\mathbf{h}) \\ \frac{1}{4}(1-\mathbf{x})(1+\mathbf{h}) \\ \frac{1}{4}(1+\mathbf{x})(1-\mathbf{h}) \\ \frac{1}{4}(1+\mathbf{x})(1+\mathbf{h}) \end{bmatrix} \quad (\text{A. 6})$$

with  $u_i, v_i$  the displacements of the four nodes of the quadrilateral element.

## *Appendix B*

### ***Calculation of the structure factor using the Fast Fourier Transform algorithm***

The calculation of the structure factor of the p.a.-unit cell can be carried out straightforwardly using Eqs. (3) and (4) (cf. Section 2.2.2). To improve the speed of this calculation, these formulae are rewritten in a form that enables the use of a Fast Fourier Transform algorithm. The discussion in this appendix is limited to a one-

dimensional case, although the method can be adapted easily and straightforwardly to two and three dimensional cases.

### B. 1. One-dimensional particle arrangement unit cell

The one-dimensional analogon of the two-dimensional p.a.-unit cell is displayed in Fig. B1. It consists of a row of  $2N$  atoms with a one-dimensional (misfitting) "particle" at the center (origin of  $x$ -axis). This one-dimensional p.a. unit cell is described in analogy with the two-dimensional p.a.-unit cell by a p.a.-unit cell vector  $\tilde{\mathbf{a}}$ , which is equal to  $\tilde{\mathbf{a}} = 2N\mathbf{a}$  with  $\mathbf{a}$  the matrix unit-cell vector and  $|\mathbf{a}| = a$  the atomic distance. The structure factor of this p.a.-unit cell, with  $\mathbf{r}_n$  the position of atom ( $n$ ) with respect to the origin of the p.a.-unit cell and  $f_n$  the scattering factor of atom ( $n$ ), is given by (cf. Eq. (3))

$$F(\tilde{\mathbf{h}}) = \sum_{n=0}^{2N-1} f_n e^{2\pi i \tilde{\mathbf{H}} \cdot \mathbf{r}_n} . \quad (\text{B. 1})$$

The one-dimensional diffraction vector  $\mathbf{H} = \tilde{\mathbf{h}}\tilde{\mathbf{b}}$  is expressed in terms of the real-valued variable  $\tilde{h}$  and the reciprocal lattice vector  $\tilde{\mathbf{b}}$ , ( $\tilde{\mathbf{a}} \cdot \tilde{\mathbf{b}} = 1$ ). The "~" symbol is used to mark all variables directly related to the p.a.-unit cell vector  $\tilde{\mathbf{a}}$ .

Each vector  $\mathbf{r}_n$  is expressed by means of a fractional coordinate  $\tilde{X}_n$ , i.e.  $\mathbf{r}_n = \tilde{X}_n \tilde{\mathbf{a}}$ . In the deformed state, the fractional coordinates are written as (cf. Eq. (4))

$$\tilde{X}_n = \frac{(n + \frac{1}{2} - N)a + u_n}{2Na + 2U} \quad (\text{B. 2})$$

with  $u_n$  the displacement of atom  $n$  from its undeformed position  $(n + \frac{1}{2} - N)a$ . Combining Eqs. (B. 1) and (B. 2), the one dimensional p.a.-unit cell structure factor is given by

$$F(\tilde{\mathbf{h}}) = \sum_{n=0}^{2N-1} f_n e^{2\pi i \tilde{h} \frac{(n + \frac{1}{2} - N)a + u_n}{2Na + 2U}} \quad (\text{B. 3})$$

As explained in Section 2.2.2,  $F(\tilde{\mathbf{h}})$  for an infinitely large crystal needs only be calculated at integer positions within the range  $2(h_B - 1/2)N \leq \tilde{h} \leq 2(h_B + 1/2)N$ , where  $h_B$  denotes the value of  $h$  at a Bragg position according to the one-dimensional matrix unit cell description.

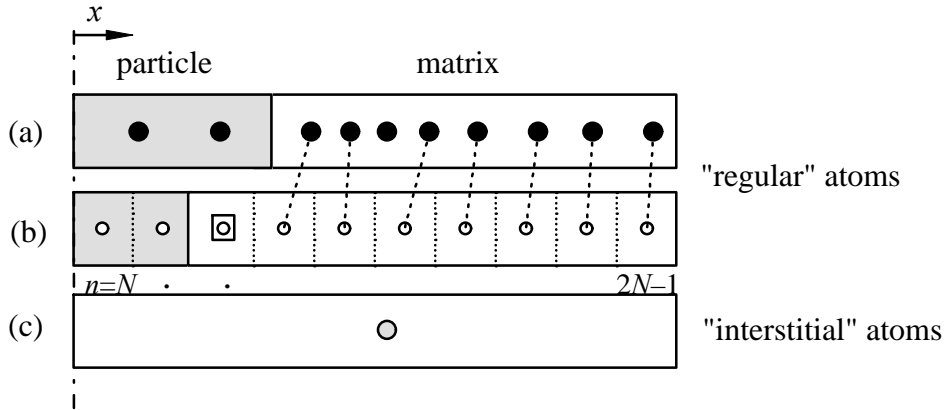


**Fig. B.1.** Schematic presentation of the redefinition of the displacement field of (particle and) matrix atoms in a one-dimensional p.a.-unit cell of  $2N = 20$  and  $N_R = 2$ ; only the right half of the p.a.-unit cell is shown. In (a) the positions of the atoms in the deformed state are shown. In (b) the reference lattice positions are shown. The displacement of a matrix atom from its strain free, reference lattice, position is redefined as the displacement from the nearest reference lattice position. This is indicated in (a) and (b) by the dotted lines that connect the displaced atoms with the nearest reference lattice position. These atoms are denoted "regular" atoms. If no matrix atom is close enough to a specific reference lattice point then that reference lattice point is conceived as a vacancy, indicated by the " $\square$ "-symbol in (b). If more than one atom is close to the same reference lattice point the one closest to this lattice point is selected. The remaining one is considered an "interstitial" type of atom (see (c)). The calculation of the structure factor is performed in two parts: one part uses the FFT-method of Eq. (B. 10) which includes all regular atoms and the local vacancies and the other part uses the fundamental description (Eq. (B. 9)) for the "interstitial" type of atoms.

The total number of calculations necessary to calculate the intensity distribution of an  $\{h_B\}$  reflection is dependent on the *square* of the number of atoms within the p.a.-unit cell: for every single line intensity,  $2N$  summations have to be carried out in Eq. (B. 3) and every  $\{h_B\}$  reflection consists of the same number of line intensities.

## B. 2. Calculation of the structure factor using the discrete Fourier transform

The discrete Fourier transform  $P(t)$  of an arbitrary discrete function  $p(m)$  of period  $M$  is given by [17]

$$P(t) = \frac{1}{M} \sum_{m=0}^{M-1} p(m) e^{2\pi i t \frac{m}{M}} \quad (\text{B. 4})$$

where both the real space variable,  $m$ , and the Fourier space variable,  $t$ , are integers, here. Comparing this equation with Eq. (B. 3) ( $M = 2N$ ), we see that Eq. (B. 3) cannot be considered a discrete Fourier transform due to the contribution of the displacement field in the numerator and denominator of the exponent of Eq. (B. 3). However, Eq. (B. 3) can be rewritten such that an equation similar to Eq. (B. 4) is obtained.

Firstly, a new lattice constant is defined for the *deformed* p.a.-unit cell. In the deformed state, the length of the p.a.-unit cell vector equals  $|\tilde{\mathbf{a}}| = 2Na + 2U$ . A new (average) lattice constant  $a_d$  is defined such that  $|\tilde{\mathbf{a}}| = 2Na_d$  and  $a_d = a + U/N$ . Then, the displacement  $u_n^d$  of an atom from its undeformed position given by the new lattice constant can be expressed as

$$u_n^d = u_n - (n + \frac{1}{2} - N) \frac{U}{N}. \quad (\text{B. 5})$$

The structure factor according to Eq. (B. 3) can now be rewritten as

$$F(\tilde{h}) = \sum_{n=0}^{2N-1} f_n e^{2\pi i \tilde{h} \frac{(n + \frac{1}{2} - N) + u_n^d / a_d}{2N}}. \quad (\text{B. 6})$$

Secondly, the diffraction vector is expressed in terms of the deviation from the Bragg position (in terms of the p.a.-unit cell description: at the Bragg position  $\tilde{h}_B = 2Nh_B$ ; see at the end of Section 2.2.2):  $\mathbf{H} = \tilde{h} \tilde{\mathbf{b}} = (2Nh_B + \Delta\tilde{h}) \tilde{\mathbf{b}}$ , or  $\tilde{h} = 2Nh_B + \Delta\tilde{h}$ . Note that since  $\tilde{h}$  and  $2Nh_B$  are integers,  $\Delta\tilde{h}$  is integer too.

Now Eq. (B. 6) can be split up into a displacement-dependent part and a displacement-independent part:

$$F(\tilde{h}) = \sum_{n=0}^{2N-1} f_n e^{2\pi i h_B u_n^d / a_d} e^{2\pi i \frac{\Delta \tilde{h} u_n^d / a_d}{2N}} e^{2\pi i \frac{\Delta \tilde{h} n}{2N}} \quad (\text{B. 7})$$

where the term  $(n+1/2-N)$  has been reduced to  $n$  as this leaves the value of  $F(\tilde{h})F^*(\tilde{h})$  unaffected. Although the third exponential on the right hand side of Eq. (B. 7) is similar to the exponential given in Eq. (B. 4), Eq. (B. 7) is not a discrete Fourier transform since the second exponential on the right hand side of Eq. (B. 7) depends on  $\Delta \tilde{h}$ .

Next, the second exponential on the right hand side of Eq. (B. 7) is written as a Taylor series expansion leading to

$$F(\tilde{h}) = \sum_{t=0}^{\infty} \frac{(2\pi i \Delta \tilde{h} / 2N)^t}{t!} \left\{ \sum_{n=0}^{2N-1} \left[ f_n (u_n^d / a_d)^t e^{2\pi i h_B u_n^d / a_d} \right] e^{2\pi i \frac{\Delta \tilde{h} n}{2N}} \right\} \quad (\text{B. 8})$$

The term within braces represents the discrete Fourier transform of the function in square brackets (cf. Eq. (B. 4)). The structure factor is computed by a finite sum of such Fourier transforms. For the 2D case considered in this work Eq. (B. 8) has been summed up to  $t = 8$ , leading to a relative error in the value of the variance smaller than  $10^{-4}$  %.

The number of terms of the Taylor series expansion necessary to calculate accurately the structure factor is limited only if the displacements are small compared to  $a_d$ . However, in the immediate neighbourhood of misfitting particles, displacements of the order of several atomic distances can occur. This may seriously destroy the convergence of the series, especially for large deviations from the Bragg position. This can be remedied in the following way.

For the calculation of the structure factor the locations of all atoms in the *deformed* state are considered and therefore it is *not* important from which reference lattice points the atoms were displaced (cf. Fig. B1). Thus, the displacement of an atom over several atomic distances can also be conceived as a displacement from a different reference lattice point over a distance smaller than the atomic distance. In this way the displacement of all atoms is redefined as the displacement from the nearest reference lattice point. Thus, all atomic displacements remain smaller than half of the atomic distance and only a few terms of the Taylor series expansion (B. 8) need to be taken into account. Following this procedure, only one atom is allocated to most reference lattice points; these atoms are denoted "regular" atoms from now on. However, two special cases need to be considered: (i) two or more atoms are close to



the same reference lattice point and (ii) no atom is close enough to a specific reference lattice point (see Fig. B1).

In the first case, only one atom can be assigned to the reference lattice point. The contributions to the structure factor of the remaining, "interstitial" type of atoms (see Fig. B1) cannot be calculated by the discrete Fourier transform method but requires application of the fundamental equation, similar to Eq. (B. 3):

$$F_{int}(\tilde{h}) = \sum_{n_{int}=1}^{N_{int}} f_n e^{2\pi i \mathbf{H} \cdot \mathbf{r}_n} \quad (\text{B. 9})$$

with  $N_{int}$  the total number of "interstitials".

In the second case, no atom is close enough to a specific reference lattice point and, consequently, there is no contribution of this reference lattice point to the structure factor. Hence it can be treated as a vacancy. In the calculation of the structure factor this is handled by setting the atomic scattering factor  $f_n$  for this reference lattice point equal to zero. (Since the total number of atoms remains unchanged it is clear that the number of "vacancies" equals the number of "interstitial" type atoms).

Finally, the structure factor of the p.a.-unit cell in the deformed state equals the sum of the contribution of all "regular" atoms and all "interstitial" atoms, i.e.

$$F(\tilde{h}) = \sum_{t=0}^{\infty} \frac{(2\pi i \Delta \tilde{h} / 2N)^t}{t!} \left\{ \sum_{n=0}^{2N-1} \left[ \hat{f}_n \left( \hat{u}_n^d / a_d \right)^t e^{2\pi i h_B \hat{u}_n^d / a_d} \right] e^{2\pi i \frac{\Delta \tilde{h} n}{2N}} \right\} + \sum_{n_{int}=1}^{N_{int}} f_n e^{2\pi i \mathbf{H} \cdot \mathbf{r}_n} \quad (\text{B.10})$$

where  $\hat{f}_n$  indicates the atomic scattering factor ( $\hat{f}_n = f_n$  for an atom and  $\hat{f}_n = 0$  for a vacancy) and  $\hat{u}_n^d$  indicates the redefined displacement field that assigns to each reference lattice points a displacement smaller than half of the atomic distance.

The calculation of the structure factor using Eq. (B. 10) is much faster than that using Eq. (B. 3): the calculation on the basis of Eq. (B. 3) increases *quadratically* with the number of atoms (cf. Section B.1), whereas the calculation on the basis of Eq. (B. 10) increases approximately *linearly* with the number of atoms. The total number of calculations on the basis of Eq. (B. 10) can be assessed as follows. The contribution of the majority of atoms to the structure factor is calculated using a Fast Fourier Transform algorithm. The calculation of the discrete Fourier transform of  $2N$  datapoints is proportional to  $2N \log(2N)$  [17]. If the number of terms used in the Taylor series expansion equals  $t_{max}$ , the total number of calculations for the "regular" atoms thus scale as  $2N t_{max} \log(2N)$ . The number of calculations for the "interstitial"

type atoms scale as  $N_{int}2N$  (see discussion below Eq. (B. 3)). Thus, the total number of calculations for the structure factor on the basis of Eq. (B. 10) scale as  $2N(t_{max}\log(2N)+N_{int})$  with  $N_{int} \ll 2N$ , which shows that for large values of  $2N$  this number increases approximately linearly with  $2N$ .

### B. 3. Simplified calculation of the structure factor

If  $\Delta\tilde{h}$  is small ( $\Delta\tilde{h} \ll N$ ) the second exponential on the right hand side of Eq. (B. 7) can be neglected, which is equivalent to a maximum value of  $t$  in Eq. (B. 7) of  $t = 0$ , and a simplified, approximate, again discrete Fourier transform expression for the structure factor results

$$F_{approx}(\tilde{h}) = \sum_{n=0}^{2N-1} f_n e^{2\pi i h_B u_n^d / a_d} e^{2\pi i \frac{\Delta\tilde{h} n}{2N}} \quad (\text{B. 11})$$

The simplification is equivalent to replacing  $\mathbf{H} \cdot \mathbf{r}$  in Eq. (B. 1) by  $\mathbf{H}_B \cdot \mathbf{r}$ . In standard treatments of X-ray diffraction (e.g. Warren [11]) this same approximation is carried out in the calculation of line profiles. The real-valued variable  $h_3$  in reciprocal space is replaced by the order of reflection  $l$  of a  $\{00l\}$ -type reflection and only the component of displacement of unit cell  $m$  along the  $h_3$ -axis,  $Z_m$ , is considered.

## Appendix C

### ***Influence of the rotation procedure on the centroid and variance of the $\{hk\}$ powder diffraction line profile***

A powder diffraction line profile can be obtained from the intensity distribution in reciprocal space of a single powder particle using the rotation procedure (cf. Section 2.3). This procedure causes an intensity distribution of a single powder particle that is symmetrical in reciprocal space to become slightly asymmetrical after projection onto the diffraction vector. The asymmetry leads to an additional shift of the centroid (cf. Fig. 5a) which is proportional to the variance of the powder diffraction line profile as is proven here.

The position of an  $\{\tilde{h}\tilde{k}\}$  line intensity in reciprocal space,  $\mathbf{H}(\tilde{h}, \tilde{k})$ , is described as the sum of the vector indicating the Bragg position of the reflection considered,  $\mathbf{H}_B$ , and a vector describing the deviation from the Bragg position,  $\Delta\mathbf{H}(\tilde{h}, \tilde{k})$

$$\mathbf{H}(\tilde{h}, \tilde{k}) = \mathbf{H}_B + \Delta\mathbf{H}(\tilde{h}, \tilde{k}) \quad (\text{C. 1})$$

The distance of the  $\{\tilde{h}\tilde{k}\}$  line intensity to the origin of reciprocal space,  $|\mathbf{H}(\tilde{h}, \tilde{k})|$ , follows from Eq. (C. 1) as

$$|\mathbf{H}(\tilde{h}, \tilde{k})| = |\mathbf{H}_B| \sqrt{1 + 2 \frac{\mathbf{H}_B \cdot \Delta\mathbf{H}(\tilde{h}, \tilde{k})}{|\mathbf{H}_B|^2} + \frac{|\Delta\mathbf{H}(\tilde{h}, \tilde{k})|^2}{|\mathbf{H}_B|^2}} \quad (\text{C. 2})$$

Since in Eq. (C. 2) the second and third term inside the square root are small compared to the first one, the square root can be approximated by a Taylor series. Using the first term of the Taylor series expansion only, Eq. (C. 2) can be simplified to

$$|\mathbf{H}(\tilde{h}, \tilde{k})| \cong |\mathbf{H}_B| + \Delta\mathbf{H}(\tilde{h}, \tilde{k}) \cdot \frac{\mathbf{H}_B}{|\mathbf{H}_B|} + \frac{1}{2} \frac{|\Delta\mathbf{H}(\tilde{h}, \tilde{k})|^2}{|\mathbf{H}_B|} \quad (\text{C. 3})$$

Using this equation to calculate the centroid position according to Eq. (6) (cf. Section 2.3) in case of the rotation procedure yields

$$H_{c,rot}^{hk} = |\mathbf{H}_B| + \frac{1}{|\mathbf{H}_B|} \frac{\sum \sum I(\tilde{h}, \tilde{k}) \Delta\mathbf{H}(\tilde{h}, \tilde{k}) \cdot \mathbf{H}_B}{\sum \sum I(\tilde{h}, \tilde{k})} + \frac{1}{2|\mathbf{H}_B|} \frac{\sum \sum I(\tilde{h}, \tilde{k}) \Delta\mathbf{H}(\tilde{h}, \tilde{k})^2}{\sum \sum I(\tilde{h}, \tilde{k})} \quad (\text{C. 4})$$

with the subscript "rot" denoting the rotation procedure. The second term on the right hand side of Eq. (C. 4) expresses the projection of  $\Delta\mathbf{H}(\tilde{h}, \tilde{k})$  perpendicularly onto the diffraction vector  $\mathbf{H}_B$  as is the case applying the tangent procedure. Thus, the sum of the first and the second term corresponds exactly to the centroid that would have been obtained if the tangent procedure had been used. Consequently, the third term expresses the difference between the tangent and the rotation procedure. This term is proportional to the square of the distance of the matrix Bragg reflection  $\mathbf{H}_B$  to the  $\{\tilde{h}\tilde{k}\}$  line intensity,  $\Delta\mathbf{H}(\tilde{h}, \tilde{k})^2$ , and can be interpreted in terms of the variance of this line profile.

The variance of the  $\{hk\}$  line profile is calculated with respect to the centroid position using Eq. (8) (cf. Section 2.3). If the centroid of the  $\{hk\}$  line profile is shifted from  $H_c^{hk} = |\mathbf{H}_B|$  by an amount  $\mathbf{dh}$  then the variance according to the rotation procedure is equal to

$$Var_{rot}^{hk} = \frac{\sum \sum I(\tilde{h}, \tilde{k}) \Delta \mathbf{H}(\tilde{h}, \tilde{k})^2}{\sum \sum I(\tilde{h}, \tilde{k})} + (\mathbf{dh})^2. \quad (\text{C. 5})$$

From a comparison of the size of the shift of the centroid in Fig. 5a,  $\mathbf{dh} \approx 10^{-3}$ , and the size of the related variance of the corresponding line profile in Fig. 5b for the case of the rotation procedure,  $Var_{rot}^{hk} \approx 10^{-3}$ , it can be concluded that the contribution of  $(\mathbf{dh})^2$  to  $Var_{rot}^{hk}$  is negligible. Then combining Eqs. (C. 4) and (C. 5) the centroid shift according to the rotation procedure can be written as

$$H_{c,rot}^{hk} = H_{c,tan}^{hk} + \frac{Var_{rot}^{hk}}{2|\mathbf{H}_B|} \quad (\text{C. 6})$$

where the subscript "tan" denotes the tangent procedure. From this equation it is concluded that the additional centroid shift of the powder diffraction-line profile due to the rotation procedure is proportional to its variance and inversely proportional to the (relative) length of the diffraction vector indicating the Bragg position of the  $\{hk\}$  reflection.

### Appendix D

#### ***Calculation of the size Fourier coefficients of a p.a.-unit cell containing clustered particles***

The structure factor of a large p.a.-unit cell containing four particles shifted from the center to locations given by  $(x,y) = (\pm L_p, \pm L_p) = (\pm N_c a, \pm N_c a)$  is written, in analogy with Section 3.3, as the difference of two terms (see Fig. 2). The first term involves a sum over all matrix *and* hypothetical particle atoms,  $F_{pf}$  (the case of a particle free p.a.-unit cell). The second term involves a summation over all atoms of the particles only, assuming that the particles consist of matrix material. If  $F_p$  represents the structure factor of one such particle located at the center of the large p.a.-unit cell, then for each particle, located at  $(x,y) = (\pm N_c a, \pm N_c a)$  its contribution to the structure factor is obtained by the product of  $F_p$  and a phase factor  $e^{2\pi i(\pm h N_c \pm k N_c)/4N}$ . Thus, the

structure factor of the p.a.-unit cell containing all four particles,  $F(\tilde{h}, \tilde{k})$ , can be expressed as (cf. Eq. (8))

$$F(\tilde{h}, \tilde{k}) = F_{pf} - \mathbf{a}F_p \quad (\text{D. 1})$$

with

$$\mathbf{a} = 4 \cos\left(\frac{2\mathbf{p}\tilde{h}N_c}{4N}\right) \cos\left(\frac{2\mathbf{p}\tilde{k}N_c}{4N}\right) \quad (\text{D. 2})$$

The intensity distribution in reciprocal space of a single crystal composed of an infinite number of p.a.-unit cells equals, according to Section 2.2.2,  $I(\tilde{h}, \tilde{k}) = F(\tilde{h}, \tilde{k})F^*(\tilde{h}, \tilde{k})$  at integer values of  $\tilde{h}$  and  $\tilde{k}$ . Writing  $F_p(\tilde{h}, \tilde{k})F_p^*(\tilde{h}, \tilde{k}) = I_p(\tilde{h}, \tilde{k})$ , it follows that (cf. Eq. (10))

$$I(\tilde{h}, \tilde{k}) = \mathbf{a}^2 I_p(\tilde{h}, \tilde{k}) - I_p(h_B, k_B) + I(h_B, k_B). \quad (\text{D. 3})$$

The intensity distribution has two contributions: (i) at the Bragg position  $I(\tilde{h}_B, \tilde{k}_B) = (16N^2(1-c))^2$  (see below Eq. (10)) and (ii) at non-Bragg positions the intensity distribution in reciprocal space equals the intensity distribution that would have been obtained if only particles made of matrix materials had diffracted,  $I(\tilde{h}, \tilde{k}) = \mathbf{a}^2 I_p(\tilde{h}, \tilde{k})$ , where  $\mathbf{a}^2$  can be expressed as

$$\mathbf{a}^2 = 4 \left[ 1 + \cos(4\mathbf{p}\tilde{h}N_c/4N) + \cos(4\mathbf{p}\tilde{k}N_c/4N) + \cos(4\mathbf{p}(\tilde{h} + \tilde{k})N_c/4N) + \cos(4\mathbf{p}(\tilde{h} - \tilde{k})N_c/4N) \right] \quad (\text{D. 4})$$

Now, on the basis of Eqs. (D.3) and (D. 4) the (2D) size Fourier coefficients of  $I(\tilde{h}, \tilde{k})$ , normalised by the first Fourier coefficient,  $A_s(\mathbf{x}, \mathbf{z})$ , consist of the sum of the Fourier coefficients of two contributions. The normalised Fourier coefficients of the first contribution can be expressed as  $A_s^{(i)}(\mathbf{x}, \mathbf{z}) = 1 - c / (1 - c)$ , i.e. a constant level independent of the degree of clustering.

The Fourier coefficients of the second contribution,  $A_s^{(ii)}(\mathbf{x}, \mathbf{z})$ , represent the Fourier coefficients of the hypothetically diffracting particles made of matrix material; they can be calculated in the following way (see Eq. (D. 4)). If the Fourier coefficients

of  $I_p(\tilde{h}, \tilde{k})$  equal  $A_s^P(\mathbf{x}, \mathbf{z})$ , with  $\mathbf{x}$  and  $\mathbf{z}$  as the (harmonic) numbers, then according to Fourier theory [17], the Fourier coefficients of  $I_p(\tilde{h}, \tilde{k}) \cos(4p\tilde{w}\tilde{h}/4N)$  equal  $[A_s^P(\mathbf{x} + N_c, \mathbf{z}) + A_s^P(\mathbf{x} - N_c, \mathbf{z})] / 2$ , i.e. the Fourier coefficients consist of half the sum of two replicas of  $A_s^P(\mathbf{x}, \mathbf{z})$  shifted by an amount of  $\pm N_c$  along  $\tilde{b}_1$ . In the same way, the contribution of other terms of  $\mathbf{a}^2$  to  $A_s^{(ii)}$  can be calculated giving rise to an unshifted replica of  $A_s^P(\mathbf{x}, \mathbf{z})$  located at the origin of reciprocal space and shifted replicas displaced by amounts  $(0, \pm N_c)$  and  $(\pm N_c, \pm N_c)$ , respectively.

Thus, the size Fourier coefficients of the intensity distribution of a p.a.-unit cell containing four non-diffracting particles clustered along  $x = \pm y$  can be conceived as the sum of a constant level and unshifted replica of the size Fourier coefficients of hypothetically diffracting particles made of matrix material and four pairs of shifted replicas.

## References

- [1] G.E. Dieter, Mechanical Metallurgy, McGraw-Hill, Singapore, 1987.
- [2] R. Delhez, Th.H. de Keijser and E.J. Mittemeijer, Fresenius Z. anal. Chem. **312** (1982) 1 - 16.
- [3] J.G.M. van Berkum, A.C. Vermeulen, R. Delhez, Th.H. de Keijser and E.J. Mittemeijer, J. Appl. Cryst. **27** (1994) 345 - 357.
- [4] J.G.M. van Berkum, R. Delhez, Th.H. de Keijser and E.J. Mittemeijer, Acta Cryst. **A52** (1996) 730 - 747.
- [5] P. van Mourik, Th.H. de Keijser, N.M. van der Pers and E.J. Mittemeijer, Scripta Metall. **22** (1988) 1547 - 1551.
- [6] S. Iida, B.C. Larson, J.Z. Tischler, J. Mater. Res. **3**(2), (1988), 267 - 273.
- [7] J.G.M. van Berkum, R. Delhez, Th.H. de Keijser, E.J. Mittemeijer, P. van Mourik, Scripta Metall. Mater. **25** (1991), 2255 - 2258.
- [8] C.R. Houska, Acta Cryst. **A49** (1993), 771 - 781.
- [9] J.D. Eshelby, Solid State Phys. **3** (1956), 79 - 144.
- [10] O.C. Zienkiewics, The Finite Element Method in Engineering Science, McGraw-Hill, London, 1971.
- [11] B.E. Warren, X-ray Diffraction, Reading, Massachusetts: Addison-Wesley, 1969.
- [12] Von Laue, Z. Kristallogr. **64** (1926) 115 - 142.
- [13] M.A. Krivoglaz, X-ray and Neutron Diffraction in Nonideal Crystals, Springer, Berlin, 1996.
- [14] A.J.C. Wilson, Proc. Phys. Soc. **80**, 286 - 294, 1962.
- [15] A.J.C. Wilson, Proc. Phys. Soc. **81**, 41 - 46, 1963.
- [16] J.I. Langford, A.J.C. Wilson, In: Crystallography and Crystal Perfection, ed. G.N. Ramachandran, Academic Press, 207 - 222, London, 1963.
- [17] R.N. Bracewell, The Fourier Transform and its Applications, McGraw-Hill, Tokyo, 1978.

## Chapter 3

# X-Ray Diffraction Line Shift and Broadening of Precipitating Alloys

## *Part II: Study of "Strain" Broadening Effects*

T.C. Bor<sup>1,2</sup>, R. Delhez<sup>1</sup>, E.J. Mittemeijer<sup>1,3</sup> and E. Van der Giessen<sup>2</sup>

<sup>1</sup>Laboratory of Materials Science, Delft University of Technology,  
Rotterdamseweg 137, 2628 AL Delft, The Netherlands

<sup>2</sup>Koiter Institute Delft, Delft University of Technology,  
Mekelweg 2, 2628 CD Delft, The Netherlands

<sup>3</sup>Max Planck Institute for Metals Research,  
Seestraße 92, 70174 Stuttgart, Germany

### ***Abstract***

The effects of misfitting precipitates in a polycrystalline matrix on the shift and broadening of diffraction-line profiles are investigated applying a novel approach to the simulation and interpretation of diffraction line profiles. The strain fields are calculated in two ways by using (i) a numerical analysis for a unit cell containing one or a few precipitates and (ii) an analytical, Eshelby-type approximation. The diffraction-line profiles are computed as a function of the precipitate-matrix misfit, the elastic moduli of precipitates and matrix, the volume fraction of precipitates and the degree of precipitate clustering. The relations between the characteristics of the strain fields and the shifts and broadenings of the diffraction-line profiles are established. Against this background, the approximations traditionally applied in X-ray diffraction analysis are critically analyzed.

### ***1. Introduction***

X-ray diffraction measurements of materials containing a dispersion of particles exhibit shift and broadening of diffraction-line profiles, as compared to the particle-free situation [1, 2]. The line shift can be caused by a change of the overall lattice parameter, caused for instance by a change of composition upon precipitation, or, less obviously, by the development of a hydrostatic (macroscopic) stress component [3]. The line broadening can be caused by "size" and "microstrain" effects.

This study has been initiated to find out how key parameters characterizing the strain fields in a precipitating system can be determined by (X-ray) diffraction measurements. In part I of this work, it has been shown for a micromechanical 2D model how a continuum strain field can be effectively used to simulate the diffracted intensity distributions directly from the kinematic diffraction theory. The "size broadening", in the absence of "strain" (i.e. no misfit between the particle and matrix), due to the finite spacing between particles, was analysed in detail. Furthermore, it was shown how the "size broadening" can be separated from the "strain broadening".

In this paper, attention is focussed subsequently on the analysis of "strain broadening" solely. In particular the relations between the line width and strain-field parameters such as the mean square strain, and the (misfitting) particle size, density and distribution are investigated.

The strain fields considered here include effects due to the interaction of strain fields of neighbouring particles. Results obtained are compared with those from a simple Eshelby-type approximation. Attention is paid to the directional dependence of strain fields as well as to line-profile shifts and broadenings, proceeding from explorative work conducted earlier [4, 5].

## ***2. Basis of micromechanical and diffraction calculations***

A two-dimensional model material with a doubly periodic arrangement of circular misfitting particles in an elastic matrix is considered (see Part I). Due to the particle ordering, a square unit cell can be defined such that its deformation due to the particles fully characterizes the entire particle-matrix composite: i.e. the particle-arrangement unit cell ("p.a.-unit cell"). The particle with radius  $R_p$  is located in the centre of the cell, which has size  $2L \times 2L$ . The particle area fraction  $c$  is  $c = \pi R_p^2 / 4L^2$ . Each phase exhibits linear elastic, isotropic behaviour with Young's moduli  $E_m$  ("m" denotes matrix) and  $E_p$  ("p" denotes particle), and Poisson ratios  $\nu_m$  and  $\nu_p$ . The particle-matrix misfit is characterized by the linear misfit parameter  $\epsilon$ . To study the influence of non-periodic distributions of second-phase particles, local deviations of the periodic distribution of particles are considered: a p.a.-unit cell is taken which contains four identical circular particles that are clustered near the centre of the p.a.-unit cell and are located on the cell diagonals (see Fig. 2 in part I). The degree of clustering is measured by the dimensionless cluster factor  $C_f = 1 - L_p/L$ , with  $2L_p$  the distance between neighbouring circular particles in the p.a.-unit cell. Stress, strain and displacement fields inside the p.a.-unit cell can be routinely obtained by finite element methods. Results of this description will be identified with subscript "p.a." further on.



In the case that the p.a.-unit cell contains a single particle, an approximate solution can be obtained, following a suggestion by Eshelby [6]. First the  $2L \times 2L$  matrix is replaced by a circular matrix with an effective radius of  $R_m^{eff} = 2L/\sqrt{p}$ , so that the particle fraction is the same. Then, the classical Eshelby solution is used for a misfitting particle in an infinite matrix, corrected so that the traction at the matrix outer radius  $R_m^{eff}$  vanishes. The solution is given in Appendix A. Due to the finite radius of the matrix, some elastic interaction between particles is accounted for effectively, but, obviously, the directionality of the strain field due to the specific distribution of the precipitates is absent in this approximate description. Results of this approximate description will be identified with subscript "Esh" further on.

The calculation of a powder diffraction line profile is briefly summarized here; see part I for a full discussion. The p.a.-unit cell is filled with a square grid of atoms at an atomic distance  $a$  in the undeformed state. The displacement field, induced by the misfitting particle in the matrix, is sampled at the locations of the atoms. The kinematic diffraction theory is then used to calculate the intensity distribution in reciprocal space from the position of the displaced atoms in the p.a.-unit cell. Powder diffraction line profiles are obtained by projecting the line intensities in reciprocal space onto the diffraction vector by either an exact, rotation procedure or by an approximative, yet commonly applied, procedure, called the tangent procedure.

The "size" contribution to the intensity distribution is eliminated by means of the method discussed in part I.

### **3. Characterization of strain fields and line profiles**

The  $\{hk\}$ -powder diffraction-line profile contains information on strain components  $e_{hk}$  in the  $\langle hk \rangle$ -directions only [1]. Therefore, the matrix-strain field is characterized in  $\langle hk \rangle$ -directions by the probability distribution of matrix strains,  $P(e_{hk})$ , the average local strain  $\langle e_{hk} \rangle$  and the root mean squared local strain  $\sqrt{\langle e_{hk}^2 \rangle}$ . The last measure is defined here with respect to  $\langle e_{hk} \rangle$  as

$$\sqrt{\langle e_{hk}^2 \rangle} = \frac{\iint_{A_m} (e_{hk} - \langle e_{hk} \rangle)^2 dx dy}{\iint_{A_m} dx dy}, \quad (1)$$

where  $A_m$  is the matrix part of the p.a.-unit cell and where  $x$  and  $y$  denote Cartesian coordinates with the origin at the centre of the p.a.-unit cell, (cf. Fig. 1 in part I). In the

finite element solution the contribution of a finite element is obtained from the average of the values at the four integration points of that element [7].

Due to the symmetry of the p.a.-unit cell it can be proven that  $\langle e_{hk} \rangle$  is independent of the  $\langle hk \rangle$ -directions and hence it represents the hydrostatic strain (see Appendix B). Therefore the subscript "hk" will be omitted for the average strain  $\langle e \rangle$  in remainder of this paper.

Obviously, the Eshelby-type approximate solution is inherently independent of the  $\langle hk \rangle$ -directions because of the circular symmetry.

The  $\{hk\}$  powder diffraction-line profile consists of a series of  $\{\tilde{h}\tilde{k}\}$  line intensities,  $I(\tilde{h}, \tilde{k})$ . It is characterized by its centroid  $H_c^{hk}$ , as a measure of profile position, and its standard deviation  $S^{hk}$ , as a measure of profile width. Here,

$$H_c^{hk} = \frac{\sum_{\tilde{h}} \sum_{\tilde{k}} |\mathbf{H}(\tilde{h}, \tilde{k})| I(\tilde{h}, \tilde{k})}{\sum_{\tilde{h}} \sum_{\tilde{k}} I(\tilde{h}, \tilde{k})}, \quad (2)$$

with  $|\mathbf{H}(\tilde{h}, \tilde{k})|$  the distance from the origin of reciprocal space to a specific  $\{\tilde{h}\tilde{k}\}$  line intensity obtained by projection onto the diffraction vector by either the tangent procedure or the rotation procedure (cf. part I), and

$$(S^{hk})^2 = Var^{hk} = \frac{\sum_{\tilde{h}} \sum_{\tilde{k}} (|\mathbf{H}(\tilde{h}, \tilde{k})| - H_c^{hk})^2 I(\tilde{h}, \tilde{k})}{\sum_{\tilde{h}} \sum_{\tilde{k}} I(\tilde{h}, \tilde{k})} \quad (3)$$

with  $Var^{hk}$  as the variance of the profile considered (defined with respect to  $H_c^{hk}$ ).

Diffraction estimates for  $\langle e \rangle$  and  $\sqrt{\langle e_{hk}^2 \rangle}$  can be obtained from  $H_c^{hk}$  and  $Var^{hk}$  as follows. The centroid of a (strain broadened) line-profile,  $H_c^{hk}$ , is indicative of the average lattice spacing in the diffracting material. Thus, with  $d_{hk}$  and  $d_{hk}^0$  as the (average) lattice spacings for the strained and strain-free material, and  $H_c^{hk}$  and  $H_{c,0}^{hk}$  as the corresponding centroids in reciprocal space, it follows

$$\langle e_{hk} \rangle_{XRD} = \frac{d_{hk} - d_{hk}^0}{d_{hk}^0} = \frac{1/H_c^{hk} - 1/H_{c,0}^{hk}}{1/H_{c,0}^{hk}}. \quad (4)$$

where the subscript "XRD" is used to indicate that the concerned measure for strain is derived from the diffraction-line profiles. A prerequisite for the above is that the relative displacements of adjacent unit cells are small compared to the unit cell

dimensions [8-10]. This will reasonably be the case if the linear misfit parameter is not chosen larger than, say,  $\epsilon = 5\%$ . Even in the case of incompressible misfitting particles ( $E_p/E_m \rightarrow \infty$ ), it can be shown with the aid of Appendix B, that the strains in the matrix at the particle/matrix interface ( $r = R_p$ ) are of the same order of magnitude as  $\epsilon$ .

The variance of the strain broadened profile,  $Var_{\epsilon}^{hk}$ , is obtained by subtraction of the variance of the merely size broadened profile,  $Var_{\epsilon=0}^{hk} = (S_e^{hk})^2$ . According to [8-10], this variance is a measure of the root mean squared strain,

$$\sqrt{\langle e_{hk}^2 \rangle}_{XRD} = \frac{1}{H_{c,0}^{hk}} S_e^{hk}. \quad (5)$$

## 4. Analysis of misfit-strain fields

### 4.1. Role of particle fraction; orientation dependence of strain parameters

The average local matrix strain  $\langle e \rangle$  has been calculated as a function of the particle fraction  $c$  for values of  $E_p/E_m$  equal to 0.1, 1 and 10, in the unclustered state. Throughout this work the Poisson ratios of particle and matrix have been taken equal:  $\nu_m = \nu_p = 0.3$ . The results for  $\langle e \rangle$  are shown in Fig. 1 both for the numerical p.a.-unit cell analysis ("p.a.") and the analytical Eshelby-type analysis ("Esh"). The average local matrix strains  $\langle e \rangle_{Esh}$  and  $\langle e \rangle_{p.a.}$  obviously increase with the particle fraction  $c$  (exactly linearly for  $E_p/E_m = 1$  in the "Esh"-approximation; see Appendix B), with the increase being larger for larger ratio  $E_p/E_m$ . This reflects the fact that a larger part of the misfit has to be accommodated by the matrix if the particle becomes relatively more rigid. The differences between the "p.a." and the "Esh" results are very small up to large particle fractions and for a wide range of  $E_p/E_m$ . In Fig. 1, differences become visible only for particle fractions above  $c = 0.25$  at  $E_p/E_m = 10$ . So, the average matrix strain obtained from the direction-independent "Esh"-model provides a very good approximation of the actual average matrix strain obtained from the p.a.-unit cell description.

The mean squared local matrix strain  $\langle e_{hk}^2 \rangle$  in the  $\langle 10 \rangle$  and the  $\langle 11 \rangle$  directions of the matrix is shown for the "p.a." and "Esh" descriptions in Fig. 2. The respective values  $\langle e_{hk}^2 \rangle_{p.a.}$  and  $\langle e_{hk}^2 \rangle_{Esh}$  also increase with the particle fraction  $c$  and Young's modulus ratio  $E_p/E_m$  (exactly linearly only for  $E_p/E_m = 1$  in case of the "Esh"-description). However, a distinct difference between the results from both descriptions occurs:  $\langle e_{hk}^2 \rangle_{p.a.}$  clearly shows direction dependence whereas  $\langle e_{hk}^2 \rangle_{Esh}$ , of course, does not. Also note that (i)  $\langle e_{10}^2 \rangle_{p.a.}$  is always larger than  $\langle e_{11}^2 \rangle_{p.a.}$ , (ii) their difference

increases with particle fraction  $c$  and  $E_p/E_m$ , and (iii)  $\langle e_{hk}^2 \rangle_{Esh}$  is always in between both.

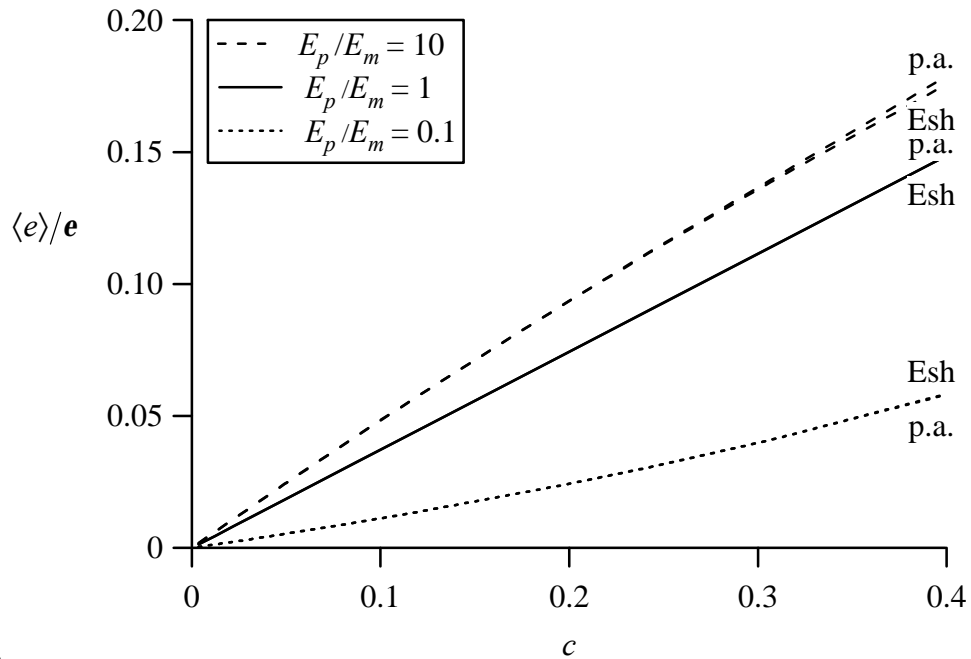


**Fig. 1.** Normalised average strain  $\langle e \rangle / \mathbf{e}$  in the matrix, according to the p.a.-unit cell description and according to the Eshelby-type description, versus particle fraction  $c$  for different  $E_p/E_m$ .

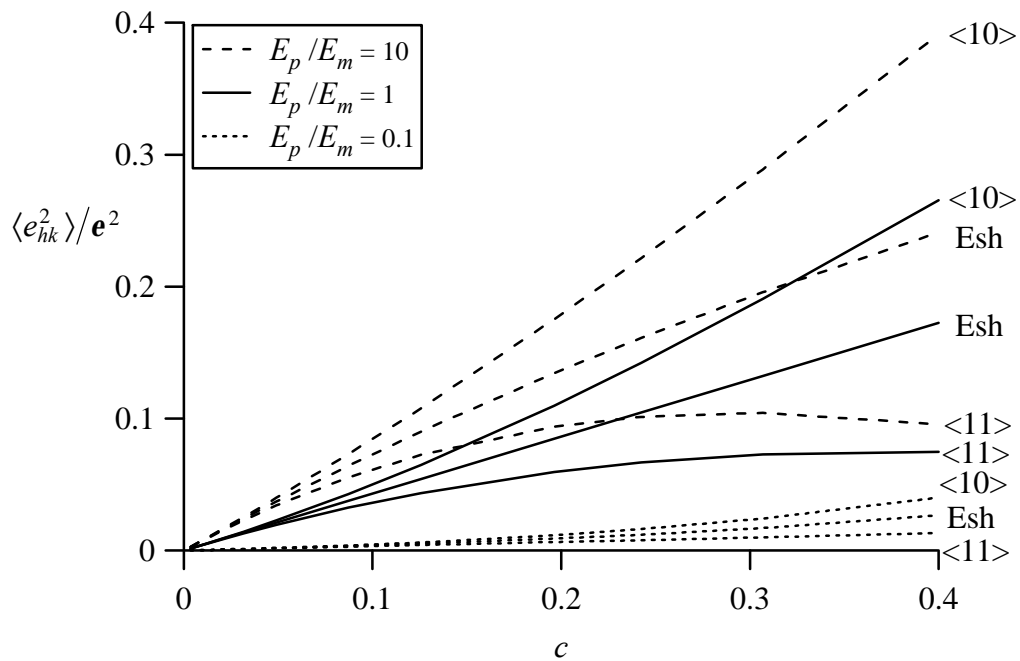


**Fig. 2.** Normalised mean square strain  $\langle e_{hk}^2 \rangle / \mathbf{e}^2$  in the matrix, according to the p.a.-unit cell description and according to the Eshelby-type description, versus particle fraction  $c$  for different  $E_p/E_m$  in two crystallographic directions  $\langle 10 \rangle$  and  $\langle 11 \rangle$ .

The directional dependence of the strain field according to the "p.a." description is revealed also in the probability distribution of matrix strains,  $P(e_{hk}/\mathbf{e})_{p.a.}$ : the width of this probability distribution can be characterized by its variance  $\langle e_{hk}^2 \rangle_{p.a.}$  according to Eq. (1). Probability distributions of matrix strains in the  $\langle 10 \rangle$  and the  $\langle 11 \rangle$  directions are shown in Fig. 3 for  $c = 0.087$  with  $E_p/E_m = 1$ . Each probability distribution is symmetric about the average local matrix strain  $\langle e \rangle$ . The shapes and the widths of the probability distributions, however, differ strongly:  $P(e_{11}/\mathbf{e})_{p.a.}$  is relatively narrow, whereas  $P(e_{10}/\mathbf{e})_{p.a.}$  is much broader and, additionally, has satellite peaks at both sides of the main peak. Consequently the variance of  $P(e_{10}/\mathbf{e})_{p.a.}$  is larger than that of  $P(e_{11}/\mathbf{e})_{p.a.}$  (cf. Fig. 2).

The probability distribution of matrix strains according to the "Esh" description has also been calculated using the area-weighted procedure as described in Section 3. The probability distribution so obtained is symmetric about the average matrix strain and exhibits two equally high maxima for small values of the strain (for the case shown in Fig. 3 at  $|e|/\mathbf{e} \approx 0.1$ ). Hence,  $P(e_{hk}/\mathbf{e})_{Esh}$  cannot be considered at all as some average of  $P(e_{10}/\mathbf{e})_{p.a.}$  and  $P(e_{11}/\mathbf{e})_{p.a.}$ , as can be anticipated on the basis of the  $\langle e_{hk}^2 \rangle$  data shown in Fig. 2.

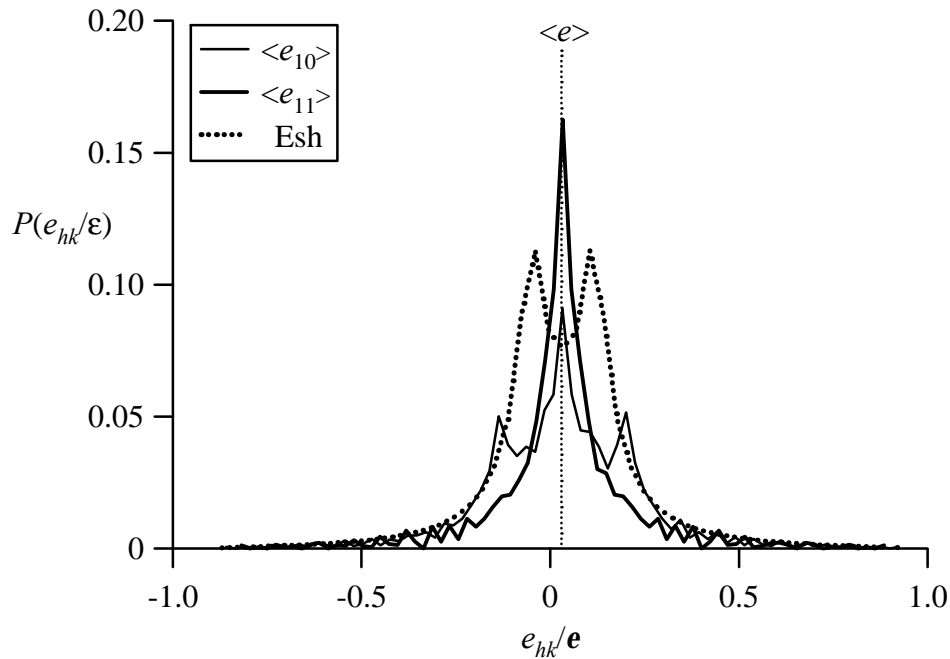


**Fig. 3.** Probability distributions of matrix strains  $P(e_{hk}/\mathbf{e})$  in the  $\langle 10 \rangle$  and  $\langle 11 \rangle$  directions of normalised strain  $e_{hk}/\mathbf{e}$ , according to the p.a.-unit cell description and according to the Eshelby-type description, for a particle fraction of  $c = 0.087$  with  $E_p/E_m = 1$  in the unclustered state,  $C_f = 0$ . The average matrix strain is  $\langle e \rangle_{p.a.}/\mathbf{e} \cong \langle e \rangle_{Esh}/\mathbf{e} = 0.032$ .

The probability distributions of matrix strains shown in Fig. 3 differ especially for the moderate and small strain values ( $|e|/e < 0.2$ ), and the differences reduce with higher strains. This can be understood by recognizing that the largest strains are confined to a small region near the particle/matrix interface and therefore are not influenced much by the presence of neighbouring misfitting particles. Hence, the directional dependence of  $\langle e_{hk}^2 \rangle_{p.a.}$  is due in particular to the region (with large area fraction) away from the particle/matrix interface, in between the particles.

The origins of the differences seen in Fig. 3 can be demonstrated in terms of the iso-strain contours around a misfitting particle as shown in Figs. 4a-d. The contours show the distribution of deviatoric strains, i.e.: the hydrostatic strain has been subtracted

$$e'_{ij} = e_{ij} - 1/3 e_{kk} \mathbf{d}_{ij}. \quad (6)$$

In this case, by construction of the solution (cf. Section 2.1), the iso-strain contours of the Eshelby-type approach are exactly equal to those of a single misfitting particle in an *infinitely large* matrix.

Now, suppose two equal misfitting particles, with identical mechanical properties (so that fields can be superimposed) as the matrix, are brought together from infinity along, for example, the  $x$ -axis until their centres are a distance  $2L$  apart. The  $\langle 10 \rangle$ -strains of a single particle exhibit mirror symmetry with respect to the  $x$ -axis and the  $y$ -axis. Therefore, starting at infinite interparticle distance, the  $\langle 10 \rangle$  deviatoric strains on the  $x$ -axis on both sides of the particles are negative (see Fig. 4c) and thus it follows directly upon decreasing the interparticle distance along the  $x$ -axis that for the region in between both particles the sum of the strain fields of the two particles becomes more negative than the corresponding values for the individual particles: compare the  $e'_{10}/e = -0.1$ - and  $e'_{10}/e = -0.2$ -iso-strain contours of the "p.a." description and the "Esh" description in Figs. 4a and 4c, respectively. Thus, particle interaction explains the origin of the satellite maxima in  $P(e_{10}/e)_{p.a.}$  at  $e_{10}/e \approx -0.2$ . (Similar reasoning for the satellite maximum at  $e_{10}/e \approx +0.2$ ).

The  $\langle 11 \rangle$ -strains of the "Esh" description of a single particle also exhibit mirror symmetry, but with respect to the lines  $x = |y|$ . Then, the  $\langle 11 \rangle$  deviatoric strains of the particles above the  $x$ -axis are of opposite sign, and similarly also below the  $x$ -axis. Hence, upon bringing together two equal particles from infinity along the  $x$ -axis, the sum of the strain fields of the two particles becomes less positive and less negative, respectively, than the corresponding values for the individual particles. Consequently, the  $|e'_{11}/e| = 0.1$ - and  $|e'_{11}/e| = 0.2$ -iso-strain contours of the p.a.-unit

cell description are confined more to the particle than those of the Eshelby-type description; cf. Figs. 4b and 4d. Therefore, the fraction of the p.a.-unit cell with  $\langle 11 \rangle$  strains deviating only slightly from the average matrix strain (say,  $|e'_{11}/e| < 0.1$ ) is larger than for the "Esh" description. As a result, satellite maxima are absent for  $P(e_{11})_{p.a.}$ .

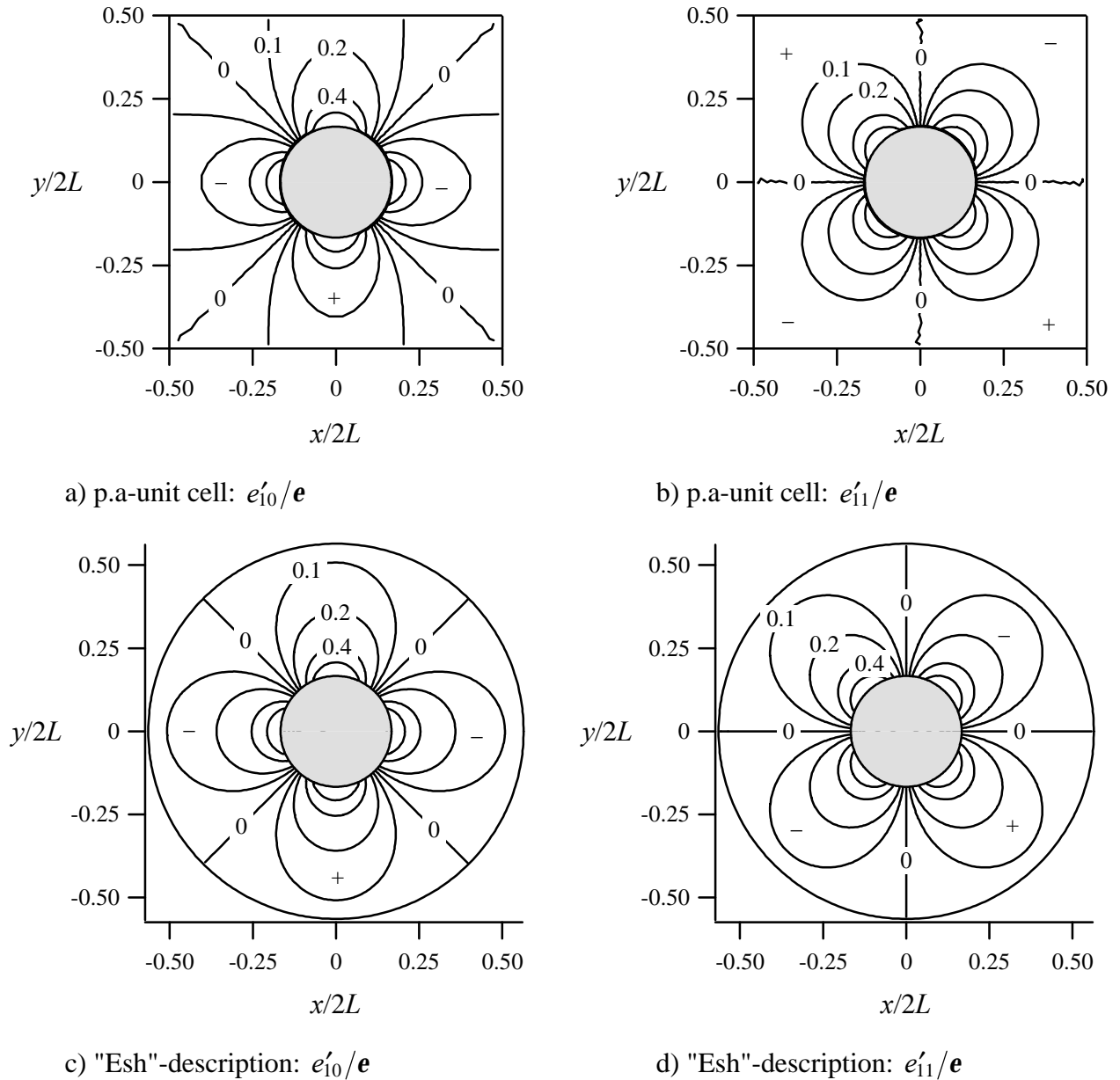


**Fig. 4.** Comparison between the iso-strain contour plots of the  $\langle 10 \rangle$  and  $\langle 11 \rangle$  strain distributions at a particle fraction  $c = 0.087$ , according to the p.a.-unit cell description (Figs. a and b, respectively) and according to the Eshelby-type description (Figs. c and d, respectively). Contour levels are  $|e'/e| = 0, 0.1, 0.2, 0.4$  and  $0.6$  with signs as indicated. These figures show the deviatoric strains, see Eq. (6).

## 4.2 Role of particle/matrix misfit; scaling properties

The calculated local strain scales linearly with the particle/matrix misfit  $\mathbf{e}$ , since linear elasticity theory has been applied. Therefore, the probability distribution of matrix strains,  $P(e_{hk}/\mathbf{e})$ , is independent of  $\mathbf{e}$  and the average strains or the root mean squared strains,  $\sqrt{\langle e_{hk}^2 \rangle}$ , depend linearly on  $\mathbf{e}$  with proportionality factors determined by  $c$ ,  $E_p/E_m$ ,  $\mathbf{n}_m$  and  $\mathbf{n}_p$ .

For equal Poisson ratios of particle and matrix ( $\mathbf{n}_m = \mathbf{n}_p = \mathbf{n}$ ) the strain fields in matrix and precipitate according to the Eshelby-type description are completely given by a combination of  $\mathbf{e}$  and  $E_p/E_m$  through an effective misfit strain  $\mathbf{e}_{eff} = \mathbf{e}Q(E_p/E_m, c)$  (see appendix B). Hence  $\langle e \rangle_{Esh}$ ,  $\sqrt{\langle e_{hk}^2 \rangle_{Esh}}$  and the shape of the probability distribution of matrix strains  $P(e_{hk}/\mathbf{e})_{Esh}$  depend on  $\mathbf{e}_{eff}$  only. Such kind of scaling of the strain field (measures) also holds for the p.a.-unit cell description as long as  $\langle e \rangle_{Esh} \cong \langle e \rangle_{p.a.}$  (see Fig. 1).

## 4.3 Role of particle clustering

The effect of clustering of misfitting particles on the strain parameters is analysed for two different particle fractions,  $c = 0.031$  and  $c = 0.087$ , corresponding to cases with a relatively weak and relatively strong orientation dependence, respectively.

The strain fields of the large ( $4L \times 4L$ ; cf. Fig. 2 in part I) p.a.-unit cells have been calculated for cluster factors  $0 \leq C_f \leq 0.5$  for  $c = 0.087$ , and  $0 \leq C_f \leq 0.7$  for  $c = 0.031$  with  $E_p/E_m = 0.1, 1, \text{ and } 10$  (for definition of  $C_f$ , see Section 2.1 in part I). Note that for any value of  $c$  there is an upper bound for  $C_f$ , recognizing impenetrable particles: with  $L_p \geq 2R_p$  it follows  $C_f \leq 1 - 2c/\sqrt{p}$ . Obviously, the strain field according to the "Esh" description is independent of the cluster factor  $C_f$  (see Section 2.2). The p.a.-unit cell containing four particles exhibits the same symmetry properties as the p.a.-unit cell containing a single particle and therefore the mean matrix strain of the large p.a.-unit cell is also independent of direction (see Section 3). The average matrix strain  $\langle e \rangle_{p.a.}$  exhibits a very weak dependence on the cluster factor  $C_f$  for both particle fractions. The relative difference between  $\langle e \rangle_{p.a.}$  in the unclustered state ( $C_f = 0$ ) (practically equal to  $\langle e \rangle_{Esh}$ ; see Section 4.1) and  $\langle e \rangle_{p.a.}$  in the strongly clustered state ( $C_f = 0.5$  for  $c = 0.087$  or  $C_f = 0.7$  for  $c = 0.031$ ) remains smaller than 0.2 % for  $E_p/E_m = 0.1$  and  $E_p/E_m = 1$ , and increases to about 1 % if  $E_p/E_m = 10$ . Therefore, it is concluded that the influence of clustering of misfitting particles on the average matrix strain remains small.



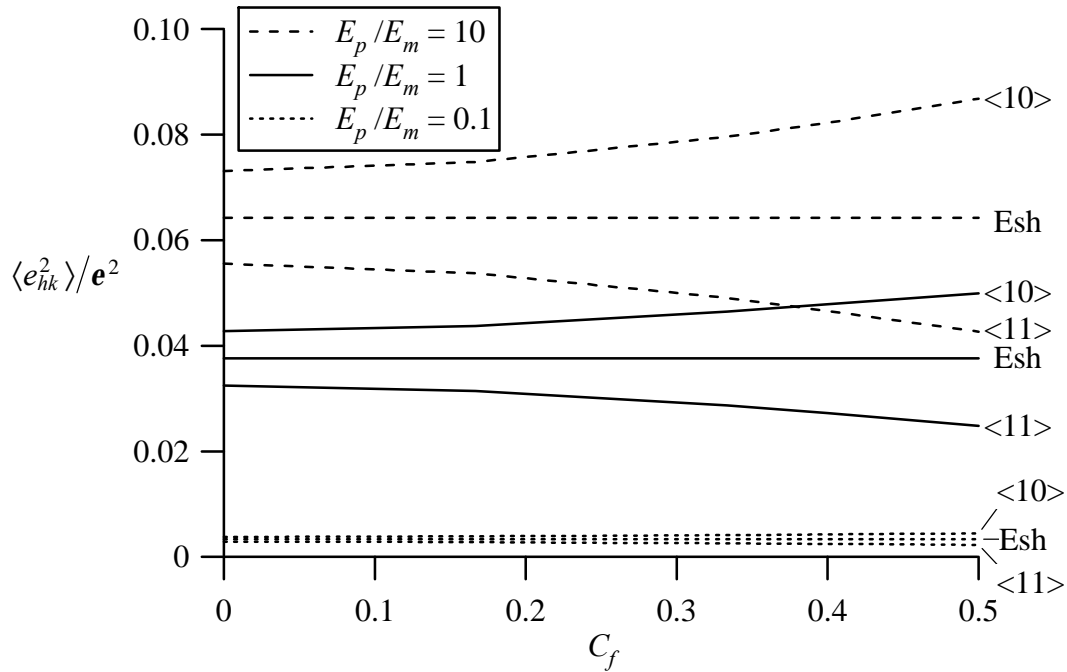


**Fig. 5.** Normalised mean square strain  $\langle e_{hk}^2 \rangle / e^2$  in the matrix, according to the p.a.-unit cell description and according to the Eshelby-type description, versus clusterfactor  $C_f$  for different values of  $E_p/E_m$  in two crystallographic directions,  $\langle 10 \rangle$  and  $\langle 11 \rangle$ , at constant  $c = 0.087$ .

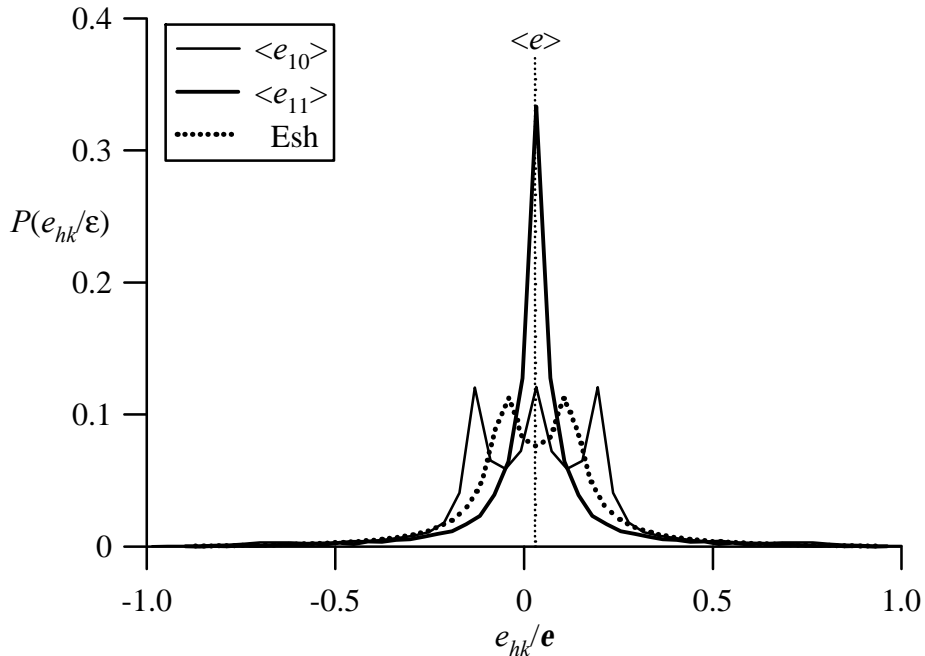


**Fig. 6.** Probability distributions of matrix strains  $P(e_{hk}/e)$  in the  $\langle 10 \rangle$  and  $\langle 11 \rangle$  directions of normalised strain  $e_{hk}/e$ , according to the p.a.-unit cell description and according to the Eshelby-type description, for a particle fraction of  $c = 0.087$  with  $E_p/E_m = 1$  in the most clustered state considered,  $C_f = 0.5$ . The average matrix strain is  $\langle e \rangle_{p.a.}/e \cong \langle e \rangle_{Esh}/e = 0.032$ .

The mean squared strains are depicted in Fig. 5 as a function of the cluster factor  $C_f$  for the case of  $c = 0.087$  and  $E_p/E_m = 0.1, 1$  and  $10$ . As clustering becomes more pronounced  $\langle e_{10}^2 \rangle_{p.a.}$  increases, whereas  $\langle e_{11}^2 \rangle_{p.a.}$  decreases (with approximately the same amount). Similar behaviour is observed for  $c = 0.031$ , but less distinct. The increase of the difference between  $\langle e_{10}^2 \rangle_{p.a.}$  and  $\langle e_{11}^2 \rangle_{p.a.}$  implies that the orientation dependence becomes more pronounced for increasing clustering. This can also be seen in the probability distribution of matrix strains that is shown for  $c = 0.087$  and  $C_f = 0.5$  in Fig. 6. As compared to the unclustered state (cf. Fig. 3), for  $P(e_{11}/\mathbf{e})_{p.a.}$  the contribution of the strains close to zero has increased significantly, and the probability distribution has become narrower as exhibited by the smaller value for the variance  $\langle e_{11}^2 \rangle_{p.a.}$  (see Fig. 5). As compared to the unclustered state  $P(e_{10}/\mathbf{e})_{p.a.}$  has become broader, since the contribution of the shoulder at  $|e|/e \approx 0.3$  has become more pronounced; see also the increase of  $\langle e_{10}^2 \rangle_{p.a.}$  with increasing  $C_f$  (Fig. 5).

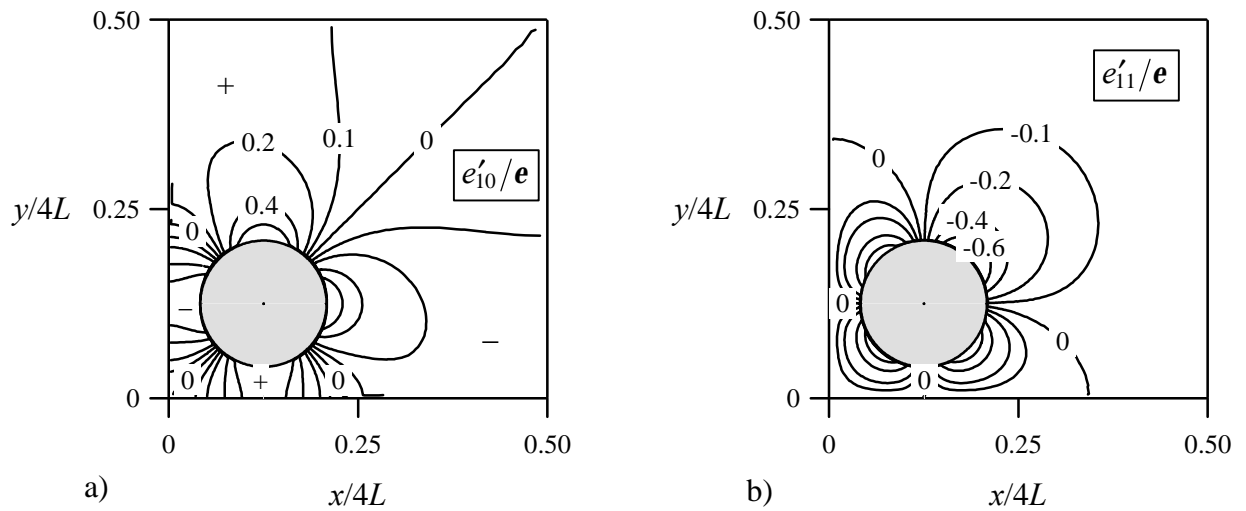


**Fig. 7.** Comparison between the iso-strain contour plots of the  $\langle 10 \rangle$  and  $\langle 11 \rangle$  strain distributions with  $C_f = 0.5$  at a particle fraction  $c = 0.087$  for a quarter of a p.a.-unit cell. Contour levels are  $|e'/e| = 0, 0.1, 0.2, 0.4$  and  $0.6$  with signs as indicated. These figures show the deviatoric strains, see Eq. (6).

The  $\langle 10 \rangle$  and  $\langle 11 \rangle$  iso-strain contour plots for a quarter of the large p.a.-unit cell ( $4L \times 4L$ ; cf. part I) in the most clustered state considered,  $C_f = 0.5$  with  $c = 0.087$ , are presented in Figs. 7a and 7b. The effects of clustering are clearly visible upon comparing these figures with Figs. 4a and b for the unclustered state. Due to clustering, the shape and symmetry properties of the strain field change. In particular, in between the clustered particles, significant interaction distorts the strain distribution.

## 5. Line-Profile Calculations

In line with the previous discussion of the strain distributions  $\{h0\}$  and  $\{hh\}$  matrix diffraction line profiles have been computed for values of the particle-matrix misfit  $\mathbf{e}$  between 0 % and 5 %. For each series of line-profile simulations, line profiles have been calculated for three orders of reflection (i.e.  $\{10\}$ ,  $\{20\}$ ,  $\{30\}$  and  $\{11\}$ ,  $\{22\}$ ,  $\{33\}$ ).

### 5.1 Role of mechanical properties

The effect of the mechanical properties of particle and matrix on  $\langle e_{hk} \rangle_{XRD}$  and  $S_e^{hk}$  has been studied by varying  $\mathbf{e}$  for constant values of  $E_p/E_m$  ( $= 0.1, 1$  and  $10$ ) and  $c = 0.087$ . The simulations have used  $2N \times 2N = 240 \times 240$  atoms per p.a.-unit cell, which corresponds to a particle radius of  $N_R = 40$  (cf. Section 2.2.1 of part I).

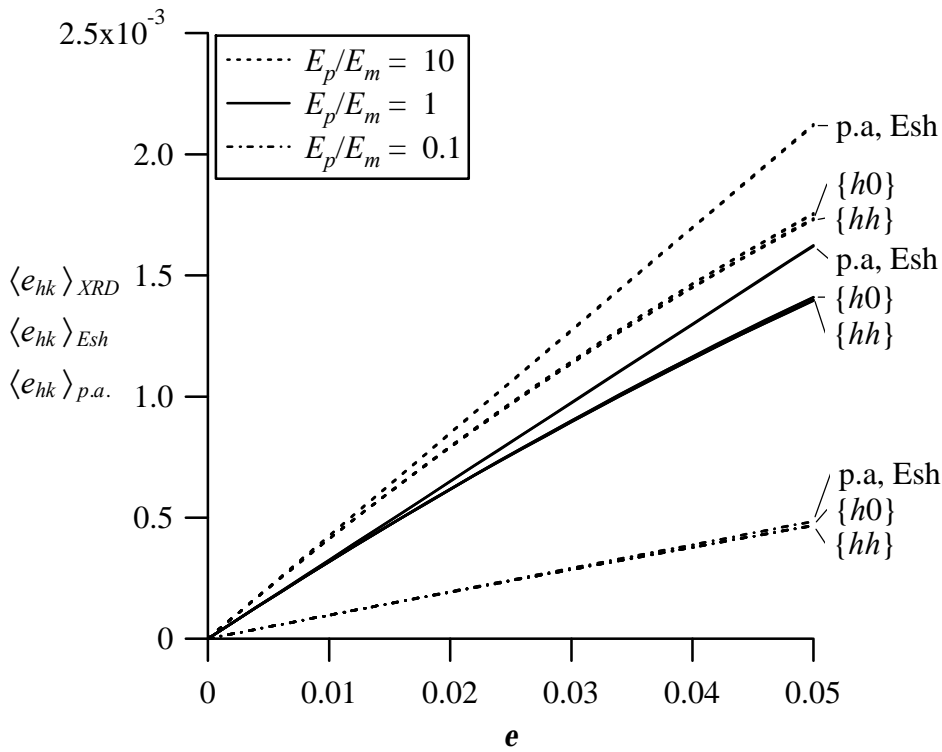


**Fig. 8a.** The average matrix strains as a function of  $\mathbf{e}$  for the three values of  $E_p/E_m$  for  $c = 0.0873$  and  $2N \times 2N = 240 \times 240$ . The average strains  $\langle e_{hk} \rangle_{XRD}$  have been calculated from the centroid shift of the  $\{hk\}$  reflections. These strains can be compared with  $\langle e \rangle_{p.a.}$  calculated from the p.a.-unit cell strain field, and with  $\langle e \rangle_{Esh}$  calculated from the approximate analytical strain field. The mean strains  $\langle e \rangle_{p.a.}$  and  $\langle e \rangle_{Esh}$  are independent of  $\{hk\}$  and practically equal (see text).

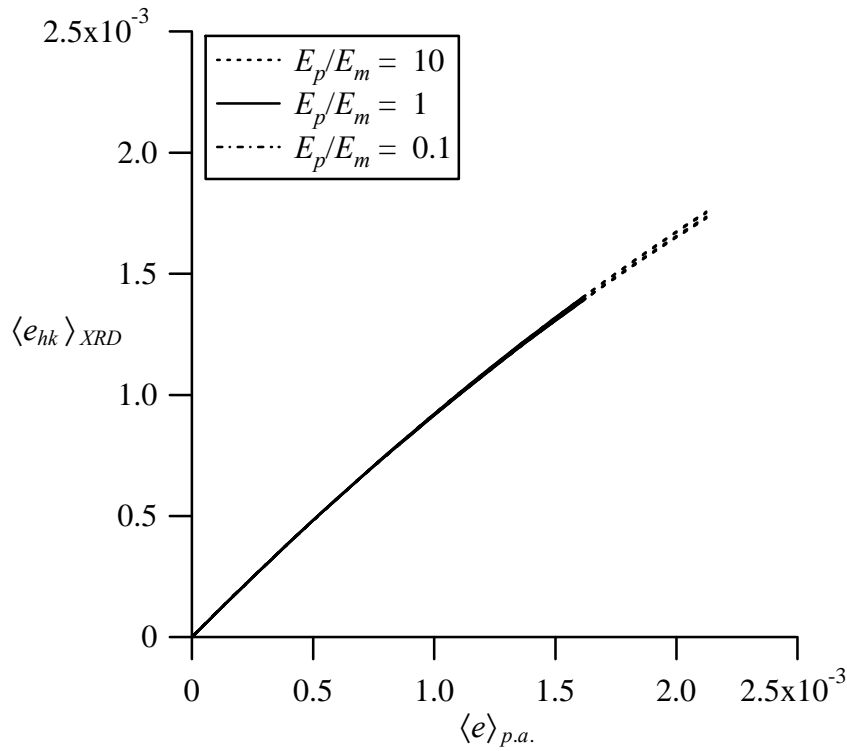


**Fig. 8b.** The average matrix strains derived from the line profiles,  $\langle e_{hk} \rangle_{XRD}$ , versus the average matrix strain, according to the p.a.-unit cell description,  $\langle e \rangle_{p.a.}$ .

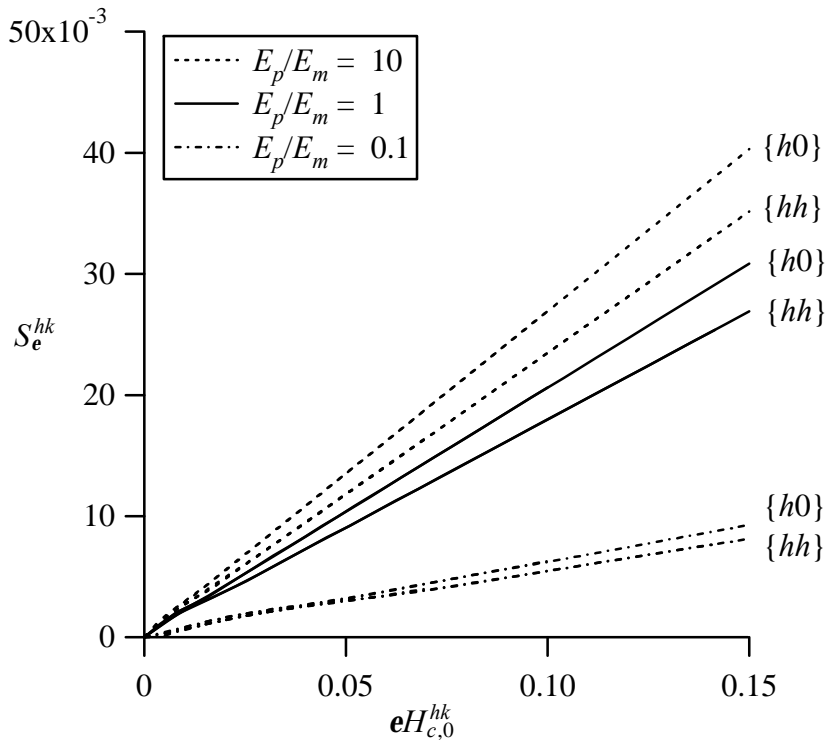


**Fig. 8c.** The standard deviation of the strain contribution to the broadening of the  $\{hk\}$  reflection,  $S_e^{hk}$ , as a function of  $eH_{c,0}^{hk}$ .

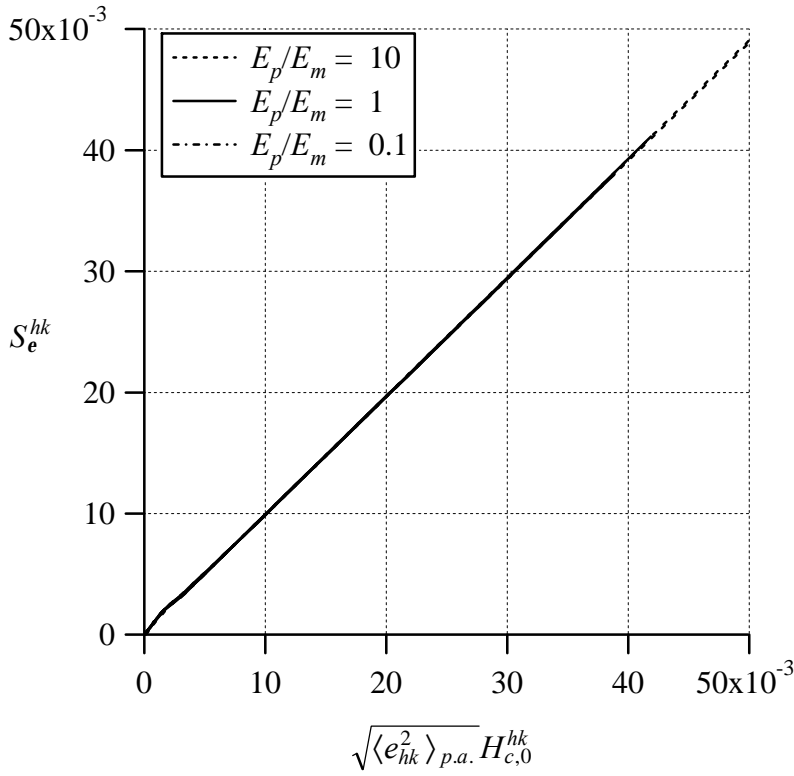


**Fig. 8d.** The standard deviation of the strain contribution to the broadening of the  $\{hk\}$  reflection,  $S_e^{hk}$ , as function of  $\sqrt{\langle e_{hk}^2 \rangle_{p.a.}} H_{c,0}^{hk}$ .

The variation of  $\langle e_{hk} \rangle_{XRD}$  with  $\mathbf{e}$  is shown in Fig. 8a, together with corresponding curves for  $\langle e \rangle_{p.a.}$  and  $\langle e \rangle_{Esh}$  calculated according to Section 3.1. Clearly, for all cases,  $\langle e_{hk} \rangle_{XRD}$  increases with  $\mathbf{e}$  in a nonlinear fashion while  $\langle e \rangle_{p.a.}$  and  $\langle e \rangle_{Esh}$  scale linearly with  $\mathbf{e}$ . The  $\langle hk \rangle$  dependence of  $\langle e_{hk} \rangle_{XRD}$ -curves, for a specific value of  $E_p/E_m$ , is weak. Plotting  $\langle e_{hk} \rangle_{XRD}$  versus  $\langle e \rangle_{p.a.}$  for all sets of  $\langle e_{hk} \rangle_{XRD}$ -curves (see Fig. 8b) shows that  $\langle e_{hk} \rangle_{XRD} / \langle e \rangle_{p.a.}$  is practically independent of  $E_p/E_m$ . The systematic difference between  $\langle e_{hk} \rangle_{XRD}$  and  $\langle e \rangle_{p.a.}$  will be discussed in Section 5.5.

The variation of  $S_e^{hk}$  with  $\mathbf{e}H_{c,0}^{hk}$  is shown in Fig. 8c. As compared to Fig. 8a,  $\mathbf{e}H_{c,0}^{hk}$  is used as abscissa instead of  $\mathbf{e}$ , to account for the dependence on the order of reflection (cf. Eq. (5)). An almost linear dependence of  $S_e^{hk}$  on  $\mathbf{e}H_{c,0}^{hk}$  is observed<sup>5</sup>. The strain broadening strongly depends on the diffraction direction  $\langle hk \rangle$  and on  $E_p/E_m$ . Since  $\sqrt{\langle e_{hk}^2 \rangle_{p.a.}}$  scales with  $\mathbf{e}$  and  $E_p/E_m$  (cf. Section 4.2), the linear dependence of  $S_e^{hk}$  on  $\mathbf{e}H_{c,0}^{hk}$  in Fig. 8c suggests that  $S_e^{hk}$  is roughly proportional with

<sup>5</sup> Small deviations of linearity observed for  $0 \leq \mathbf{e}H_{centr,0}^{hk} \leq 0.02$ , and in particular for small  $2N \times 2N$  (not shown here), are attributed to truncation of tails of the intensity distribution: overlap with neighbouring reflections is more pronounced.

$\sqrt{\langle e_{hk}^2 \rangle_{p.a.}}$ . As shown in Fig. 8d, this holds indeed:  $S_e^{hk}$  is proportional with  $\sqrt{\langle e_{hk}^2 \rangle_{p.a.}} H_{c,0}^{hk}$ , for all values of  $E_p/E_m$  (see discussion in Section 5.5).

## 5.2 Role of particle fraction

The dependences of  $\langle e_{hk} \rangle_{XRD}$  and  $S_e^{hk}$  on  $\mathbf{e}$  have been studied for various values of the particle fraction  $c$  for  $E_p/E_m = 10$  and  $N_R = 40$ . In order that the particle size  $N_R$  remains constant, while  $c$  is varied, the number of atoms within a p.a.-unit cell,  $2N \times 2N$ , has been changed accordingly.

The results of the line profile calculations are presented in Figs. 9a and 9b. Obviously, the slope of each set of  $\langle e_{hk} \rangle_{XRD}$  vs  $\mathbf{e}$  lines and each set of  $S_e^{hk}$  vs  $\mathbf{e}H_{c,0}^{hk}$  lines increases with  $c$ , because the number of particles per unit area and thus the deformation of the matrix increases with  $c$ , while the particle size remains constant. Similar increases with  $c$  have been observed for  $\langle e_{hk} \rangle_{p.a.}$  and  $\sqrt{\langle e_{hk}^2 \rangle_{p.a.}}$  in Figs. 1 and 2, respectively. Indeed, plotting of  $\langle e_{hk} \rangle_{XRD}$  vs  $\langle e_{hk} \rangle_{p.a.}$  and  $S_e^{hk}$  vs  $\sqrt{\langle e_{hk}^2 \rangle_{p.a.}} H_{c,0}^{hk}$  for various values of  $c$  the same relations are observed as in Figs. 8b and 8d, respectively.

## 5.3 Role of p.a.-unit cell size

The influence of the p.a.-unit cell size on  $\langle e_{hk} \rangle_{XRD}$  and  $S_e^{hk}$  is studied as a function of  $\mathbf{e}$  for the {11} reflection and with  $E_p/E_m = 1$  and  $c = 0.087$ . An increase in the p.a.-unit cell size  $2L \times 2L$  at constant  $a$  and  $c$  implies an enlargement of  $2N \times 2N$  and  $2N_R$ .

The results of this series of line profile calculations are presented in Figs. 10a and 10b. It is important to note that since the displacements are sampled from a continuum displacement field, the differences in position and width of the intensity distribution for different  $2L$  are a result of the diffraction process only.

However, it has been shown in part I that "size" broadening of a line profile (as observed at  $\mathbf{e} = 0$ ) depends on the distances in the matrix between the particles, which at constant  $c$  are proportional to  $2N$  (part I; Section 3.4). Therefore  $S_e^{hk}$  at  $\mathbf{e} = 0$  is distinctly different for different  $2N$  (see Fig. 10b). Thus, it can be expected that the influence of the number of atoms in the p.a.-unit cell on the mean matrix strain as function of  $\mathbf{e}$  and on the slope of the strain standard deviation as function of  $\mathbf{e}H_{c,0}^{hk}$  is small. This is confirmed by the results in Figs. 10a and 10b. As, for increasing  $2N$ , the strain field within the p.a.-unit cell is sampled at an increasing number of locations, minor differences in  $\langle e_{hk} \rangle_{XRD}$  and  $S_e^{hk}$  can occur as a consequence of differences in the sampling density.

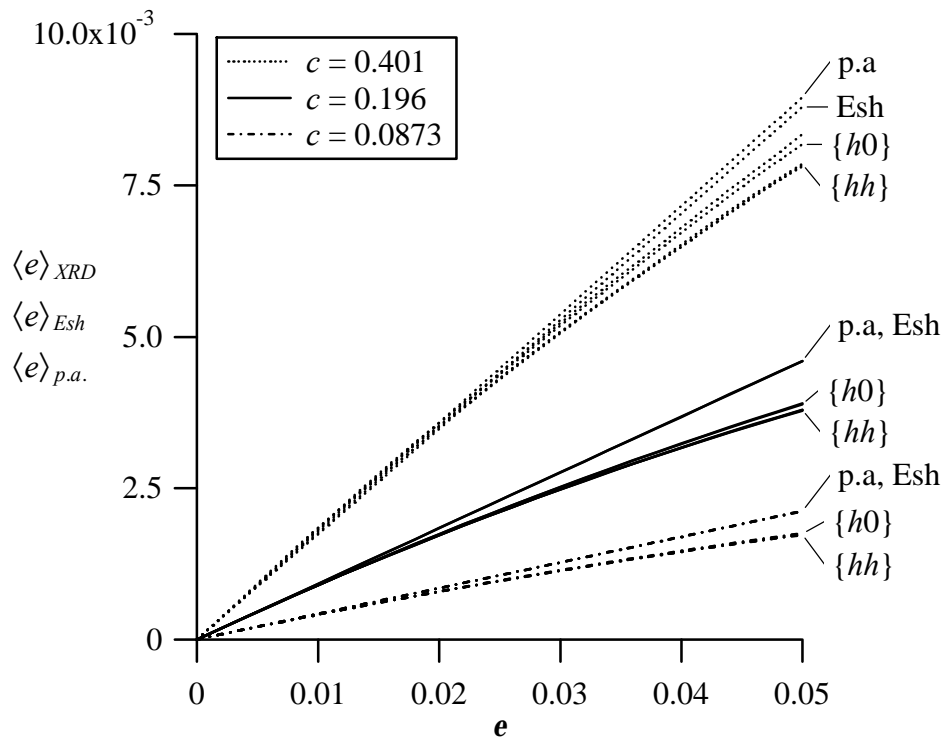


**Fig. 9a.** The average matrix strains,  $\langle e_{hk} \rangle_{XRD}$ ,  $\langle e \rangle_{p.a.}$  and  $\langle e \rangle_{Esh}$ , as a function of  $e$  for the three values of  $c$  for  $E_p/E_m = 10$  and  $N_R = 40$ . See also caption of Fig. 8.

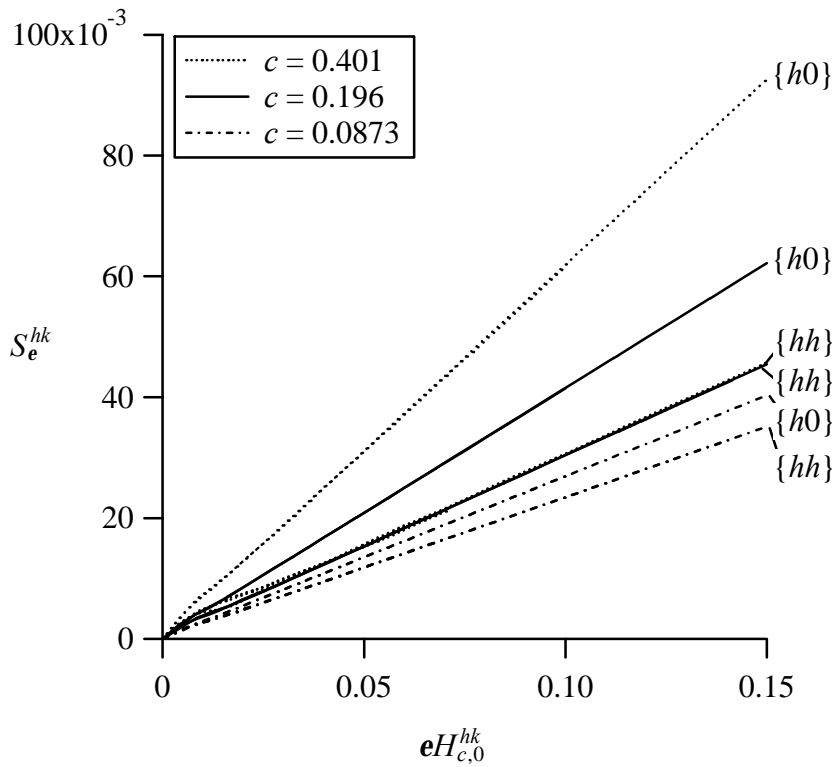


**Fig. 9b.** The standard deviation of the strain contribution to the broadening of the  $\{hk\}$  reflection,  $S_e^{hk}$ , for three values of  $c$  for  $E_p/E_m = 10$  and  $N_R = 40$  as a function of  $eH_{c,0}^{hk}$ .

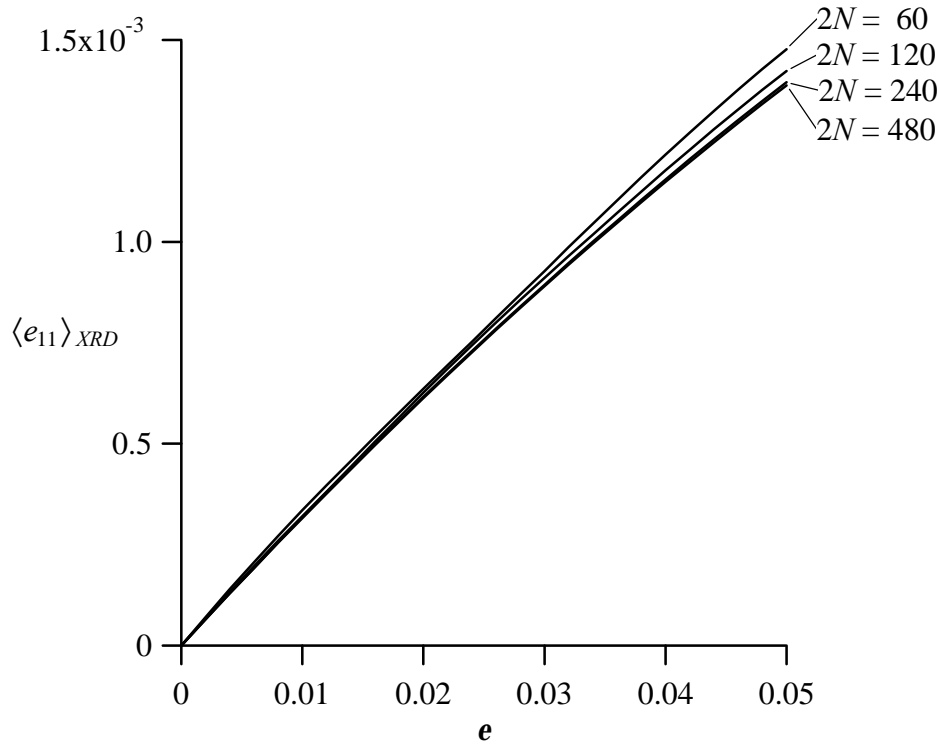


**Fig. 10a.** The average matrix strain,  $\langle e_{11} \rangle_{XRD}$  as a function of  $e$  for four values of  $2N \times 2N$  for  $c = 0.0873$ . See also caption of Fig. 8.

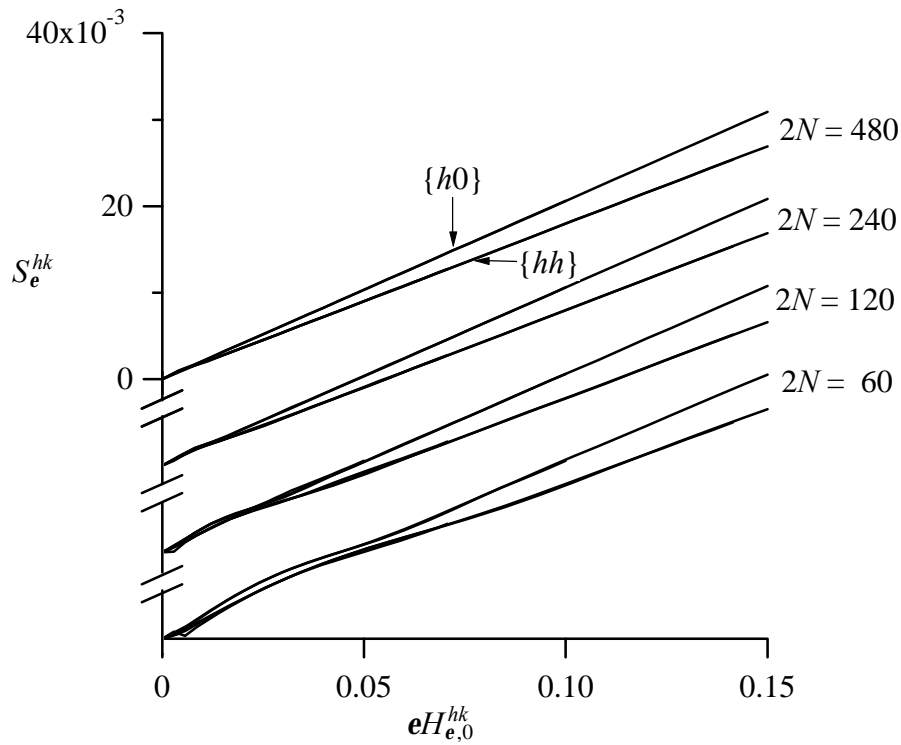


**Fig. 10b.** The standard deviation of the strain contribution to the broadening of the  $\{hk\}$  reflection,  $S_e^{hk}$ , for four values of  $2N \times 2N$  as a function of  $eH_{e,0}^{hk}$  for  $c = 0.0873$ . The dependence of  $S_e^{hk}$  on  $\{hk\}$  is the same for all values of  $2N$ .



#### 5.4 Role of clustering

The influence of clustering of the particles on  $\langle e_{hk} \rangle_{XRD}$  is very small. Only in the most clustered state considered with  $C_f = 0.5$  and with  $E_p/E_m = 10$ ,  $c = 0.087$  and  $4N \times 4N = 240 \times 240$  a difference of about 1.1 % is observed in  $\langle e_{11} \rangle_{XRD}$ .

The effect of clustering becomes clearly visible, however, in  $S_e^{hk}$ . For example, it follows from Fig. 11a that  $S_{strain}^{33}$  decreases significantly due to clustering. Yet, again plotting  $S_e^{33}$  vs  $\sqrt{\langle e_{33}^2 \rangle_{p.a.}} H_{c,0}^{33}$  yields a straight line (cf. Figs. 8d and 11b), also in the present clustered state.

#### 5.5 Concluding remarks on line profile centroid and variance

The relation between line width and  $\sqrt{\langle e_{hk}^2 \rangle_{p.a.}} H_{c,0}^{hk}$  (cf. Eq. 5) has been studied extensively in Ref. [11] for a material containing a distribution of defects, such as dislocations or misfitting particles. It was shown that the type and the distribution of defects within a material determine this relation. In case of a periodic distribution of defects, each associated with the same type of strain field (Cauchy-type:  $e \sim 1/r^2$ , with  $r$  the distance from the defect, a possible approximative model for screw dislocations) it followed that there was a linear relation between the integral breadth, as a measure of line-profile width, and  $\sqrt{\langle e_{hk}^2 \rangle_{p.a.}} H_{c,0}^{hk}$ . The present work demonstrates that a similar result holds for misfitting particles (based on an exact elaboration of the misfit-strain fields).

Minor effects such as (i) the nonlinear dependence of  $\langle e_{hk} \rangle_{XRD}$  on  $\langle e \rangle_{p.a.}$  and (ii) the departure of the slope of  $S_e^{hk}$  vs  $\sqrt{\langle e_{hk}^2 \rangle_{p.a.}} H_{c,0}^{hk}$ -lines from unity (cf. Eqs. 4 and 5) can be understood as true effects made visible here due to the exact calculation of the diffracted intensity, thereby avoiding approximations that are usually made (e.g. [1, 12]).

In diffraction calculations two simplifications are commonly made<sup>6</sup>:

(i) The inner product of the diffraction vector  $\mathbf{H}$  with the vector indicating the displacement of each atom ( $mn$ ) is approximated by the length of the diffraction vector indicating the Bragg reflection of the reflection considered,  $\mathbf{H}_B$ , and the component of the displacement field of atom  $mn$  in the direction of  $\mathbf{H}_B$ .

(ii) The usual procedure to obtain a powder diffraction line profile from the intensity distribution in reciprocal space of a single powder particle employs the so-

<sup>6</sup> In textbooks on X-ray diffraction (e.g. Warren [1]) this approximation is carried out by replacing the continuous variable in reciprocal space,  $h_3$ , by the order of reflection,  $l$ , of a  $\{00l\}$ -type reflection and taking the component of the displacement of unit cell  $m$  along the  $h_3$ -axis,  $Z_m$ .

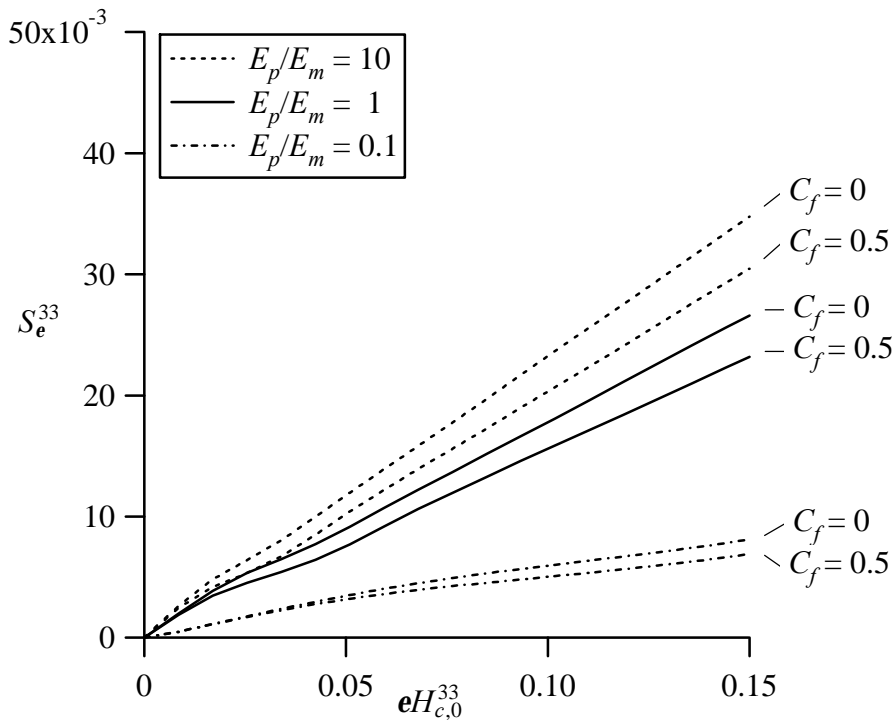


**Fig. 11a.** The standard deviation of the strain contribution to the broadening of the  $\{33\}$  reflection,  $S_e^{33}$ , for two values of  $C_f$  as a function of  $eH_{c,0}^{33}$  for  $c = 0.0873$ .

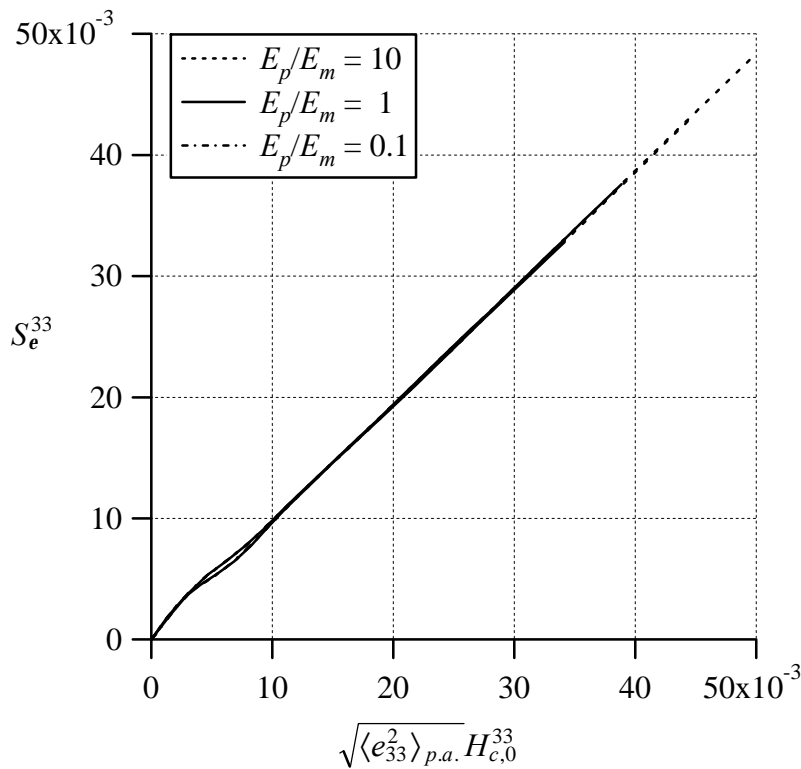


**Fig. 11b.** The standard deviation of the strain contribution to the broadening of the  $\{33\}$  reflection,  $S_e^{33}$ , as a function of  $\sqrt{\langle e_{33}^2 \rangle_{p.a.}} H_{c,0}^{33}$  for  $c = 0.0873$  with  $C_f = 0$  or  $C_f = 0.5$ .

called tangent plane approximation instead of the rotation procedure as used in this work (see Section 2.2.3 in part I).

These effects are illustrated in Figs. 12a and 12b showing exact and approximate results for  $\langle e_{hk} \rangle_{XRD}$  and  $S_e^{hk}$  of a  $\{33\}$  reflection, calculated for the case of an unclustered p.a.-unit cell with  $E_p/E_m = 1$ ,  $c = 0.087$ ,  $2N \times 2N = 60 \times 60$  and  $\mathbf{e} = 0$  to  $0.05$ . The intensity distribution calculated using the approximation (i) deviates from the exact one far away from the position of the matrix Bragg reflection in reciprocal space. The exact calculation of the diffracted intensity shows a slight asymmetry for the tails of the powder diffraction line profile, in particular for increasing values of  $\mathbf{e}$ . This causes  $\langle e_{hk} \rangle_{XRD}$  to be nonlinearly dependent on  $\mathbf{e}$  and thus  $\langle e_{hk} \rangle_{p.a.}$  (see Figs. 8b, 9b, 10a).

The consequence of the use of the tangent plane approximation (i.e. approximation (ii)) is visible also in Fig. 12a. The larger the broadening the larger the influence of this approximation (see also discussion in part I).

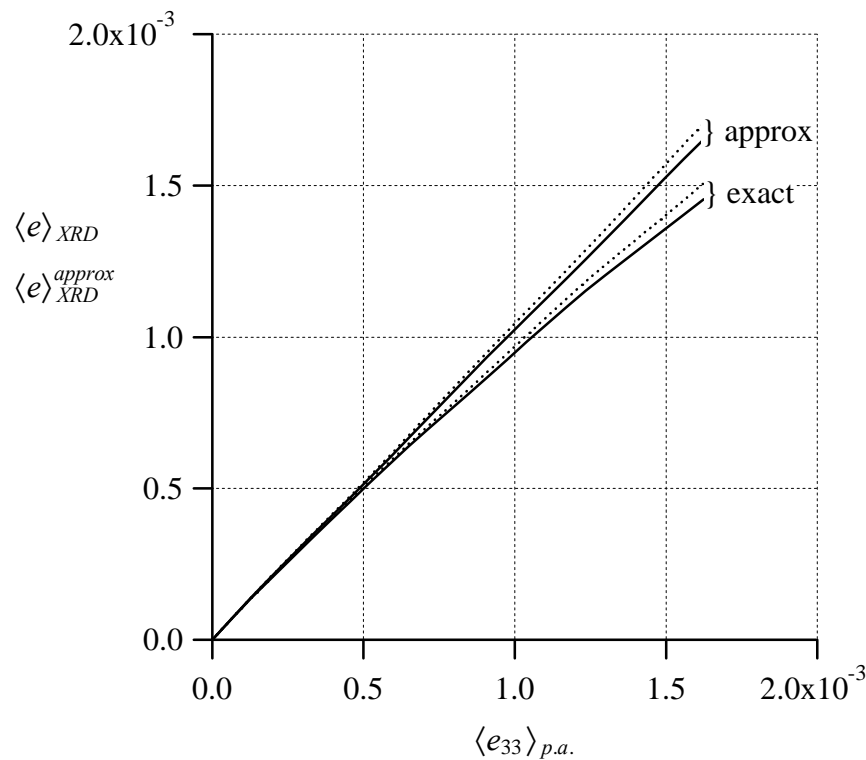


**Fig. 12a.** Average matrix strains calculated from  $\{33\}$  diffraction-line profiles as a function of the average matrix strain according to the p.a.-unit cell description,  $\langle e_{33} \rangle_{p.a.}$  for  $E_p/E_m = 1$ ,  $c = 0.087$ ,  $2N \times 2N = 60 \times 60$  and  $\mathbf{e} = 0 - 0.05$ . The  $\{33\}$  line profiles have been calculated applying either the exact formulae leading to,  $\langle e_{33} \rangle_{XRD}$ , or the approximate formulae for the intensity distribution in reciprocal space, leading to  $\langle e_{33} \rangle_{XRD}^{approx}$  (see text); these intensity distributions have been subsequently projected on the diffraction vector either by the tangent procedure (dashed line) or the rotation procedure (solid line).

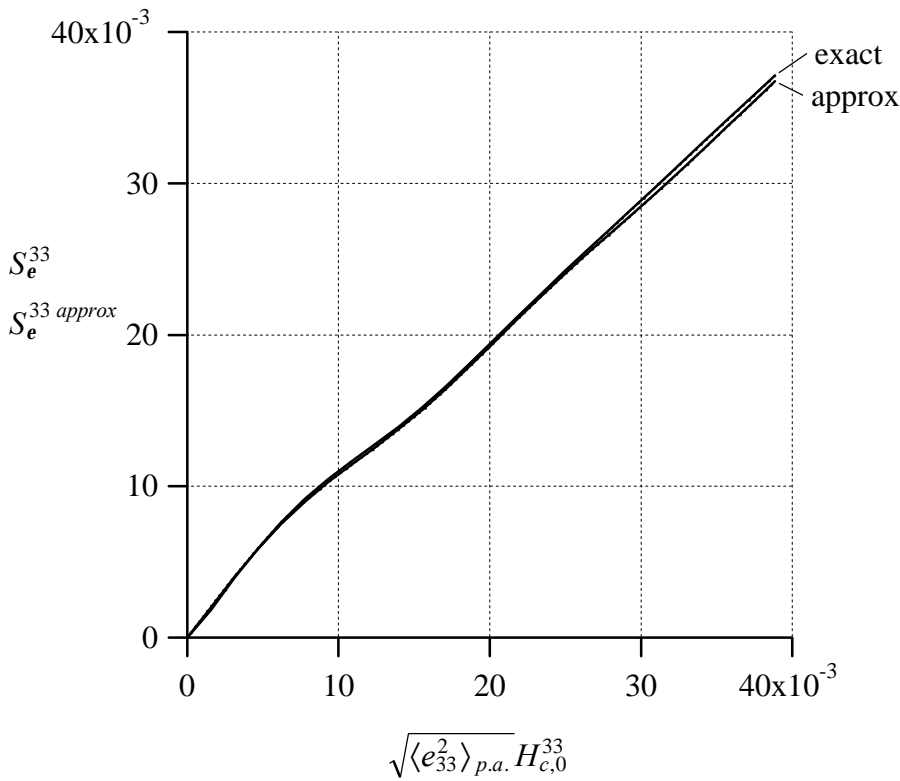


**Fig. 12b.**  $S_e^{33}$  and  $S_e^{33 \text{ approx}}$  as a function of  $\sqrt{\langle e_{33}^2 \rangle_{p.a.}} H_{c,0}^{33}$ . See caption of analogous Fig. 12 a.

As both approximations influence in particular the asymmetry in the observed intensity distribution, albeit slightly, the effect on the centroid is larger than on the variance. This can be understood as follows. If the intensity distribution is divided into an even part and an uneven part with respect to the position of the Bragg reflection considered, then it follows from Eqs. (2) and (3) that the centroid is sensitive to the uneven part of the intensity distribution, whereas the variance is, to a large extent, sensitive to the even part of the intensity distribution; a small effect of the uneven part on the variance remains since the variance is determined with respect to the centroid, cf. Eq. (3). Therefore, the influence of the approximations used is most clearly visible in the centroid of the intensity distribution.

## 6. Conclusions

(i) The mean strain of, and the centroid of a diffraction line profile from, an isotropic matrix containing circular misfitting inclusions, that are not severely clustered, can be well calculated adopting an Eshelby-type description for the strain field of a single

misfitting particle, i.e. ignoring particle misfit-strain field interaction and using an effective radius for the matrix surrounding the single particle.

(ii) The probability distribution of matrix strains and the diffraction-line broadening due to strain cannot be calculated reliably from an Eshelby-type approach. More accurate calculations of the strain field in the matrix may be required, for example using a finite element analysis.

(iii) The centroid of a diffraction line profile of the matrix is practically linearly related to the mean strain of the matrix.

(iv) The strain broadening in reciprocal space of a diffraction-line profile of the matrix is practically linearly related to the product of the linear misfit of particle and matrix and the order of reflection. The standard deviation of the only strain broadened part of the intensity distribution (in reciprocal space), as a measure of line profile width, equals, to a high degree of accuracy, the product of the mean square strain in the direction of the diffraction vector and the centroid of the intensity distribution.

(vi) Clustering of particles enhances the direction dependence of the root mean square strain and the diffraction-line broadening significantly, but the mean strain and the centroid of the diffraction line profile are hardly affected.

### ***Acknowledgement***

This work has been part of the research program of the Foundation for Fundamental Research on Matter (Stichting FOM), The Netherlands.

### *Appendix A*

#### ***Directional independence of mean matrix strain $\langle e_{hk} \rangle_{p.a.}$***

The mean strain in the matrix in the direction of an arbitrary vector  $\mathbf{n} = (\cos \mathbf{f}, \sin \mathbf{f})$ , determined by the angle  $\mathbf{f}$ , as defined in Fig. A. 1, is equal to

$$\langle e_{\mathbf{n}} \rangle = \frac{\iint_{A_m} e_{\mathbf{n}}(x,y) dx dy}{\iint_{A_m} dx dy} \tag{A. 1}$$

with  $A_m$  the matrix part of the p.a.-unit cell and with  $e_{\mathbf{n}}(x,y)$  the strain in the direction of  $\mathbf{n}$  at location  $(x,y)$ , which is related to the components  $e_{ij}$  of the strain tensor by

$$\mathbf{e}_n = \mathbf{e}_{11} \cos^2 \mathbf{f} + 2\mathbf{e}_{12} \cos \mathbf{f} \sin \mathbf{f} + \mathbf{e}_{22} \sin^2 \mathbf{f} . \quad (\text{A. } 2)$$

If the strain tensor at every position in the matrix is known, the mean strain is readily calculated from Eqs. (A. 1) and (A. 2). However, using the symmetry properties of the p.a.-unit cell it can be shown that the mean matrix strain is independent of the direction of  $\mathbf{n}$  and equal to the hydrostatic strain of the matrix. Therefore, the mean matrix strain is now calculated by separating the calculation into (i) the determination of the average strain of a set of selected points and (ii) the integration over all such sets. An example of a set of selected points A, B, C and D is shown schematically in Fig. A.1. If the strain tensor is known at A, the strain tensors in points B, C and D (cf. Fig. A.1), located symmetrically with respect to the symmetry lines  $x = 0$  and  $x = |y|$ , are related to the strain tensor in point A by

$$\begin{aligned} B: \mathbf{e}_{11}^B &= \mathbf{e}_{22}^A; \mathbf{e}_{22}^B = \mathbf{e}_{11}^A; \mathbf{e}_{12}^B = \mathbf{e}_{12}^A \\ C: \mathbf{e}_{11}^C &= \mathbf{e}_{22}^A; \mathbf{e}_{22}^C = \mathbf{e}_{11}^A; \mathbf{e}_{12}^C = -\mathbf{e}_{12}^A \\ D: \mathbf{e}_{11}^D &= \mathbf{e}_{22}^A; \mathbf{e}_{22}^D = \mathbf{e}_{11}^A; \mathbf{e}_{12}^D = -\mathbf{e}_{12}^A \end{aligned} \quad (\text{A. } 3)$$

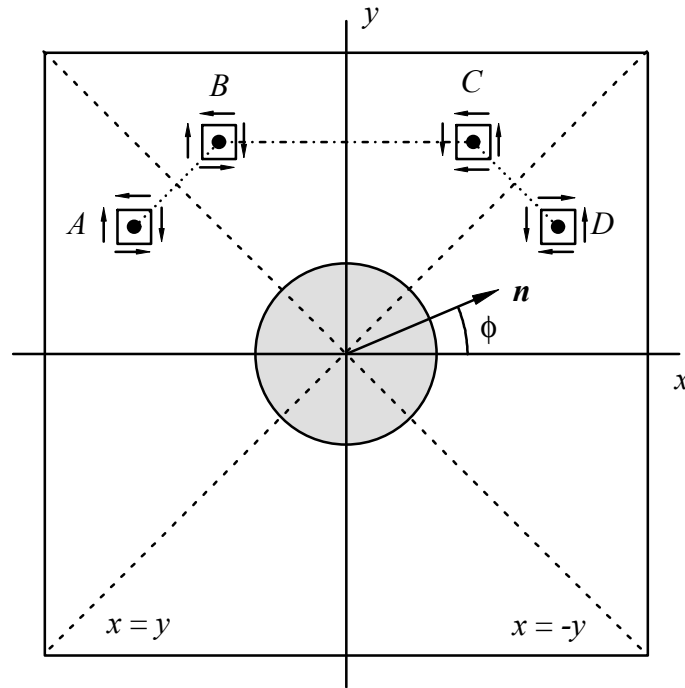


**Fig. A.1.** Schematic drawing of the p.a.-unit cell and symmetry lines  $x = 0$ ,  $y = 0$  and  $x = |y|$ . Point B is located symmetrically to A with respect to  $x = -y$ . Points C and D are located symmetrically to B and A, respectively, with respect to  $x = 0$ . The angle between the x-axis and an arbitrary unit vector  $\mathbf{n}$  is defined as  $\mathbf{f}$ . The directions of the shear components of the strain tensors in the points A, B, C and D are indicated.

The average strain of this set of points in the direction of  $\mathbf{n}$  is equal to:

$$\langle e_{\mathbf{n}} \rangle_{ABCD} = \frac{1}{2}(\mathbf{e}_{11}^A + \mathbf{e}_{22}^A) \quad (\text{A. 4})$$

which is equal to the hydrostatic strain in A, B, C and D.

Subsequently, the mean matrix strain follows from averaging over the results of all sets of points such that the entire matrix of the p.a.-unit cell is covered. Since for all other sets the average strain is also independent of  $\mathbf{n}$  and equal to the hydrostatic strain in the points considered, the mean matrix strain  $\langle e \rangle$  is (i) independent of the direction of  $\mathbf{n}$ , and thus independent of the diffraction direction  $\langle hk \rangle$  and (ii) equal to the hydrostatic strain of the entire matrix of the p.a.-unit cell.

### *Appendix B*

#### ***Strain field for circular inclusion in circular matrix***

The components of the rotationally symmetric strain field in particle and matrix,  $\mathbf{e}_r$ ,  $\mathbf{e}_t$ ,  $\mathbf{e}_{rt} = \mathbf{e}_{tr} = 0$  ( $r$  and  $t$  denoting the radial and tangential directions, respectively) pertaining to a misfitting circular particle (radius  $R_p$ , Young's modulus  $E_p$ , Poisson's ratio  $\mathbf{n}_p$ ) placed centrally in a circular matrix (radius  $R_m > R_p$ , Young's modulus  $E_m$ , Poisson's ratio  $\mathbf{n}_m$ ) are given in Ref. [13]. The derivation is limited to the case where  $\mathbf{n}_m = \mathbf{n}_p = \mathbf{n}$ .

The strain field in the precipitate ( $r \leq R_p$ ) is uniform and can be written as

$$\mathbf{e}_r^p = \mathbf{e}_t^p = \mathbf{e}Q(E_p/E_m, c), \quad (\text{B. 1})$$

where  $c = R_p^2/R_m^2$  and  $\mathbf{e}$  denotes the linear misfit at the particle/matrix interface and where

$$Q\left(\frac{E_p}{E_m}, c\right) = \frac{1}{2} \frac{1+\mathbf{n}}{1-\mathbf{n}} \left[ 1 + (1-2\mathbf{n}) \frac{E_p/E_m (c\{1-2\mathbf{n}\} + 1) + c - 1}{E_p/E_m (c\{1-2\mathbf{n}\} + 1) - (1-2\mathbf{n})(c-1)} \right]. \quad (\text{B. 2})$$

The strain components in the matrix read ( $R_p < r \leq R_m$ )

$$\mathbf{e}_r^m(r) = \mathbf{e}_r^p \frac{c(1-2\mathbf{n}) - R_p^2/r^2}{c(1-2\mathbf{n}) + 1}, \quad (\text{B. 3})$$

$$\mathbf{e}_t^m(r) = \mathbf{e}_r^p \frac{c(1-2\mathbf{n}) + R_p^2/r^2}{c(1-2\mathbf{n}) + 1}. \quad (\text{B. 4})$$

The strain components in the matrix depend linearly on  $\mathbf{e}$  through the precipitate strain  $\mathbf{e}_r^p$  given in Eq. (B. 1). Therefore, an effective linear misfit parameter  $\mathbf{e}_{eff}$  can be defined as follows

$$\mathbf{e}_{eff} = \mathbf{e}_r^p = \mathbf{e}_t^p = \mathbf{e}Q(E_p/E_m, c). \quad (\text{B.5})$$

## References

- [1] B.E. Warren, X-ray Diffraction, Reading, Massachusetts: Addison-Wesley, 1969.
- [2] M.A. Krivoglaz, X-ray and Neutron Diffraction in Nonideal Crystals, Springer, 1996.
- [3] E.J. Mittemeijer, P. van Mourik, Th.H. de Keijser, Phil. Mag. **43** (5), (1981), 1157 - 1164.
- [4] T.C. Bor, R. Delhez, E.J. Mittemeijer, E. Van der Giessen, Mat. Sci. & Eng. **A234-236** (1997) 896 - 899.
- [5] T.C. Bor, R. Delhez, E.J. Mittemeijer, E. Van der Giessen, in Proc. 5th Int. Conf. Residual Stresses, Eds. T. Ericsson, M. Odén, A. Andersson, Linköping University, (1997) 592 - 597.
- [6] J.D. Eshelby, Solid State Phys. **3** (1956), 79 - 144.
- [7] O.C. Zienkiewics, The Finite Element Method in Engineering Science, McGraw-Hill, London, 1971.
- [8] A.J.C. Wilson, Proc. Phys. Soc. **80**, 286 - 294, 1962.
- [9] A.J.C. Wilson, Proc. Phys. Soc. **81**, 41 - 46, 1963.
- [10] J.I. Langford, A.J.C. Wilson, In: Crystallography and Crystal Perfection, ed. G.N. Ramachandran, Academic Press, London, 207 - 222 (1963).
- [11] J.G.M. van Berkum, R. Delhez, Th.H. de Keijser, E.J. Mittemeijer, Acta Cryst. **A52** (1996) 730 - 747.
- [12] A.J.C. Wilson, Elements of X-ray Crystallography, Addison-Wesley, Reading, Massachusetts (1970).
- [13] S.P. Timoshenko and J.N. Goodier, Theory of Elasticity, 3<sup>rd</sup> edn., McGraw-Hill, New York (1970).



## Chapter 4

# Diffraction Contrast Analysis of Misfit Strains around Inclusions in a Matrix *VN Particles in $\alpha$ -Fe*

T.C. Bor<sup>1,3</sup>, A.T.W. Kempen<sup>2</sup>, F.D. Tichelaar<sup>1</sup>,  
E.J. Mittemeijer<sup>1,2</sup> and E. Van der Giessen<sup>3</sup>

<sup>1</sup>Laboratory of Materials Science, Delft University of Technology,  
Rotterdamseweg 137, 2628 AL Delft, The Netherlands

<sup>2</sup>Max Planck Institute for Metals Research,  
Seestraße 92, 70174 Stuttgart, Germany

<sup>3</sup>Koiter Institute Delft, Delft University of Technology,  
Mekelweg 2, 2628 CD Delft, The Netherlands

### ***Abstract***

A new method has been developed to determine the misfit of disc-shaped precipitates in a matrix using Transmission Electron Microscopy (TEM). The method is applicable to specimens containing a high precipitate density, where the classical TEM method, based on the extent of the precipitate diffraction contrast cannot be applied. The new method is based on evaluation of the positions of extrema in the intensity distribution due to misfitting precipitates both in bright field and dark field. A model system, consisting of a single disc-shaped misfitting precipitate placed centrally in a thin specimen, has been studied first. The dynamical theory of electron diffraction has been adopted for a four beam case. The contrast lobes in bright and dark field images have been calculated as a function of, in particular, the particle radius, the foil thickness and the particle thickness. Simultaneous fitting of calculated bright and dark field diffraction contrast images to the experimental ones leads to determination of the precipitate misfit, and the local thickness of the specimen foil. The method has been illustrated for a nitrided Fe-2 at. % V alloy with small disc-shaped VN precipitates and has led to a consistent interpretation in terms of particle size and misfit upon precipitation. The extent of elastic accommodation of misfit has been verified using High Resolution Electron Microscopy (HREM). The foil thickness values determined by diffraction contrast analysis agree well with independently obtained corresponding data. In addition X-Ray Diffraction (XRD) line profiles of the specimens have been recorded. The observed shifts and broadenings of the XRD profiles support the results obtained using TEM.

## 1. Introduction

Small misfitting particles/precipitates in a matrix can enhance the mechanical properties to a large extent. The increases of, for example, the yield strength and hardness are dependent on the size and shape of the precipitate particles and, in particular, on the (volume) misfit between the matrix and the particle [1]. This particle-matrix misfit causes a strain field in both the particle and the matrix that influences the motion of dislocations. To understand material behaviour it is therefore important to obtain quantitative information about the size, the shape and the misfit of the particles introduced.

Several experimental techniques exist that enable the study of small misfitting particles in a matrix, from which Transmission Electron Microscopy (TEM) and X-Ray Diffraction (XRD) are the most important ones. The particle-matrix strain field causes deformation of the matrix lattice which in TEM gives rise to the appearance of contrast lobes around the misfitting particle both in bright field (BF) and dark field (DF) images [2,3]. In the case of XRD the position, the shape and the width of an  $\{hkl\}$  line profile change [4, 5].

The classical method to obtain a quantitative estimate of the particle-matrix misfit of spherical or disc-like particles using TEM is due to Ashby and Brown [2,3]. This method is based on measurement of the width of the contrast image with respect to the intensity of the background. However, this method is unreliable, as shown in this paper, for the determination of the particle-matrix misfit of particles located in thin foils if (i) a foil thickness occurs smaller than approximately four to five times the extinction distance (for such foils the influence of the foil thickness on the image width cannot be neglected; see also Fig. 2) and/or if (ii) significant overlap occurs of the contrast lobes of neighbouring misfitting particles and the intensity of the background cannot be measured accurately.

The present work proposes and tests an alternative method that does not have the limitations of the Ashby and Brown method. The strain contrast is characterized by the distance of the maximum or minimum intensity of the contrast lobes in BF and DF to the centre of the misfitting particle. Full BF and DF contrast images are calculated and compared with experimental ones. Further, since it is often difficult to realize a “two-beam” case of electron diffraction for thin specimen foils (as in the earlier method), a more general “four-beam” case is adopted here.

The method has been applied to the case of a nitrated Fe-2 at.% V alloy containing a high number density of small disc-shaped VN precipitate particles exhibiting large misfit with the ferrite ( $\alpha$ -Fe) matrix.

## 2. Calculated BF and DF diffraction contrast images

### 2.1 Theoretical background

The calculation of the diffraction contrast of misfitting particles is carried out using the following assumptions. (i) The strain field contrast can be adequately calculated using the dynamical theory of electron diffraction considering a four beam case (cf. Section 4.1). The theory is briefly presented in Section 2.1.1. (ii) The disc-like or penny shaped particles are embedded in an elastically isotropic matrix with a misfit in the direction perpendicular to the disc plane only; there is no misfit in the direction parallel to the disc plane. (iii) It is assumed that the displacement field of one misfitting particle in an infinitely large matrix is a sufficiently accurate description of the displacement field *close to* a misfitting particle in a matrix having a high number density of such particles. The displacement field is briefly presented in Section 2.1.2.

#### 2.1.1 Dynamical theory of electron diffraction

The basis of the computation of the images in BF and DF is the dynamical theory of diffraction contrast in the form developed by Howie and Whelan [6]. A specimen of thickness  $t$  is divided into columns along the  $z$ -axis of an orthogonal  $xyz$ -coordinate system, see Fig. 1. A four beam case is considered:  $F_0$ ,  $F_{-g}$ ,  $F_g$  and  $F_{2g}$  indicate the amplitudes of the direct beam and three diffracted beams. The diffraction vectors  $\mathbf{g}$ ,  $-\mathbf{g}$  and  $2\mathbf{g}$  are perpendicular to the  $z$ -axis. The coupling of  $F_0$ ,  $F_{-g}$ ,  $F_g$  and  $F_{2g}$  as a function of depth  $z$  in the crystal is described by the following coupled differential equations [6, 7]

$$\frac{d\Phi_{\mathbf{g}_k}}{dz} = \sum_{\mathbf{g}_j} \frac{\mathbf{p}i}{\mathbf{x}_{\mathbf{g}_j - \mathbf{g}_k}} \Phi_{\mathbf{g}_j} \exp(2\mathbf{p}i[(s_{\mathbf{g}_j} - s_{\mathbf{g}_k})z + (\mathbf{g}_j - \mathbf{g}_k) \cdot \mathbf{u}]). \quad (1)$$

The change of each amplitude  $\Phi_{\mathbf{g}_k}$  in a thin slab of thickness  $dz$ ,  $d\Phi_{\mathbf{g}_k}/dz$  with  $\mathbf{g}_k = -\mathbf{g}$ ,  $\mathbf{0}$ ,  $\mathbf{g}$  and  $2\mathbf{g}$  for  $k = 1, 2, 3$  and  $4$ , consists of the sum of the contributions of all four amplitudes. For each amplitude a phase factor depending on the deviations from the Bragg positions,  $s_{-g}$ ,  $s_0$ ,  $s_g$ ,  $s_{2g}$ , and on the displacement field caused by the misfitting particle,  $\mathbf{u}$  (see next Section), is taken into account. In these equations  $\mathbf{x}_{\mathbf{g}_j - \mathbf{g}_k}$  represents the complex extinction distance of  $\mathbf{g}_j - \mathbf{g}_k$ , i.e. of the "incident" beam  $\mathbf{g}_k$  that diffracts towards the diffracted beam  $\mathbf{g}_j$ . The effect of inelastic scattering is incorporated by replacing  $1/\mathbf{x}_{\mathbf{g}}$  by  $1/\mathbf{x}_{\mathbf{g}} + i/\mathbf{x}'_{\mathbf{g}}$  where  $\mathbf{g} = \mathbf{g}_j - \mathbf{g}_k$  [2, 3, 7].

The amplitudes at the bottom of the specimen are obtained by solving this set of differential equations with the boundary conditions  $F_0 = 1$  and  $F_{-g} = F_g = F_{2g} = 0$  at the top of the specimen. Subsequently, the amplitudes of each beam are multiplied with their corresponding complex conjugates to yield the intensities.

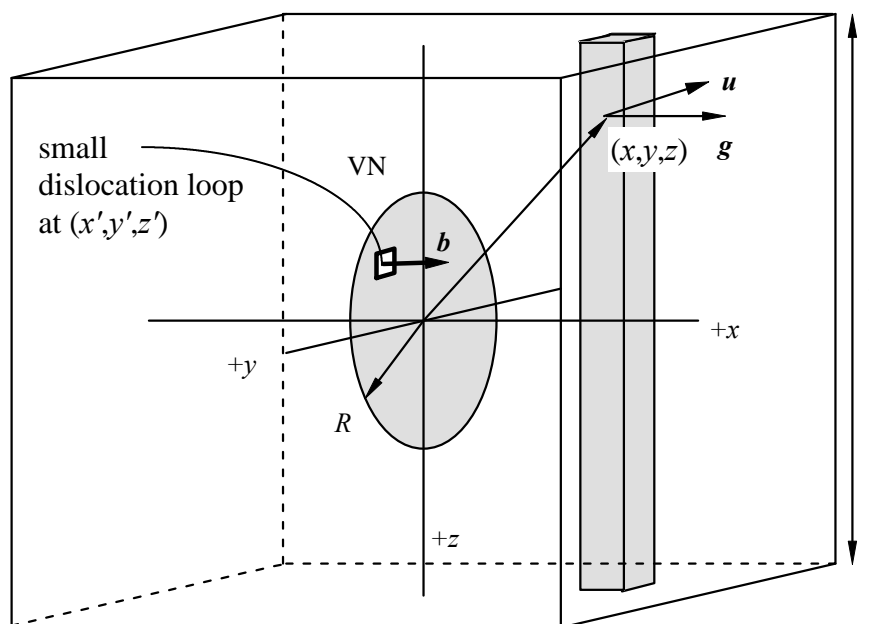


**Fig. 1.** Schematic drawing of a misfitting particle of radius  $R$  in the middle of a foil of thickness  $t$  and located at the origin of an  $xyz$ -coordinate system. The misfitting particle is represented by a collection of small prismatic dislocation loops with Burgers vector  $\mathbf{b}$  normal to the dislocation plane  $dy'dz'$ . Each such dislocation causes a displacement field  $d\mathbf{u}$  within the matrix. The total displacement field at a point  $(x, y, z)$  is equal to the sum of the contributions of all dislocation loops making up the particle. The diffraction contrast images have been calculated dividing the specimen into independently diffracting columns parallel to the  $z$ -axis. Each column represents one pixel of the simulated image. Diffraction vector  $\mathbf{g}$  is oriented perpendicularly to the misfitting particle.

In order to simplify the calculation a location in the (distorted, experimental) specimen is chosen within a bright bend contour in the dark field image obtained with diffraction vector  $\mathbf{g}$ . There,  $s_g = 0$  and  $s_0 = 0$  and  $s_{-g} = s_{2g} = s$ , where  $s$  follows from straightforward geometric analysis in reciprocal space

$$s = \sqrt{\frac{1}{\mathbf{I}^2} - \left(\frac{1}{2}g\right)^2} - \sqrt{\frac{1}{\mathbf{I}^2} - \left(\frac{3}{2}g\right)^2} \quad (2)$$

with  $\mathbf{I}$  the electron wavelength and  $g = |\mathbf{g}|$ .

### 2.1.2 Displacement field of a misfitting particle

The displacement field induced in the matrix by a misfitting disc-shaped particle can be calculated by representation of the particle by a collection of prismatic dislocation loops placed parallel in the plane of the disc at the location of the disc in an infinitely large matrix as shown schematically in Fig. 1 [2, 3] (matrix assumed to be elastically isotropic; misfit only perpendicular to the disc). Each dislocation loop has an area  $dy'dz'$  (disc parallel to  $z$ - and  $y$ - axes) and a Burgers vector  $\mathbf{b}$  parallel to the loop normal. Note that the operating diffraction vector is oriented perpendicularly to the disc-shaped particle. This Burgers vector can be interpreted as follows: if the particle (disc) consists of  $n$  lattice planes with interplanar distance  $d_{part}^{hkl}$  and the matrix at the location of the particle in its hypothetical absence would consist of an equal number of lattice planes with interplanar distance  $d_{matr}^{h'k'l'}$  parallel to the lattice planes of the particle/disc, then, if a coherent interface exists between the matrix and the particle, the length of  $\mathbf{b}$  equals

$$b = n(d_{part}^{hkl} - d_{matr}^{h'k'l'}) \quad (3a)$$

The thickness of the disc-shaped particle,  $t_{part}$ , is defined as  $t_{part} \equiv nd_{part}^{hkl}$ . The relation between  $t_{part}$  and  $b$  is then given by

$$t_{part} = \frac{d_{part}^{hkl}}{(d_{part}^{hkl} - d_{matr}^{h'k'l'})} b. \quad (3b)$$

The interplanar distances of the lattice planes of the particle and the matrix,  $d_{part}^{hkl}$  and  $d_{matr}^{h'k'l'}$ , respectively, are calculated straightforwardly from the respective lattice constants of the particle and the matrix.

The elastic displacement field at a point  $(x,y,z)$  due to a single prismatic dislocation loop located at  $(x',y',z')$  in an isotropic, infinitely large matrix with the Burgers vector parallel to the  $x$ -axis is given by [8]

$$\begin{aligned}
du_x &= \frac{bdy'dz'}{8\mathbf{p}(1-\mathbf{n})r^2} \left\{ (1-2\mathbf{n}) \frac{(x-x')}{r} + 3 \frac{(x-x')^3}{r^3} \right\} \\
du_y &= \frac{bdy'dz'}{8\mathbf{p}(1-\mathbf{n})r^2} \left\{ (1-2\mathbf{n}) \frac{(y-y')}{r} - 3 \frac{(x-x')^2(y-y')}{r^3} \right\} \\
du_z &= \frac{bdy'dz'}{8\mathbf{p}(1-\mathbf{n})r^2} \left\{ (1-2\mathbf{n}) \frac{(z-z')}{r} - 3 \frac{(x-x')^2(z-z')}{r^3} \right\}
\end{aligned} \tag{4a}$$

with

$$r^2 = (x-x')^2 + (y-y')^2 + (z-z')^2 \tag{4b}$$

and  $\mathbf{n}$  being Poisson's ratio. The total displacement field of the misfitting particle is equal to the sum of the displacement fields of the individual prismatic dislocation loops making up the particle with radius  $R$ ,

$$\mathbf{u} = \int \int_{y'z'} d\mathbf{u} \tag{5}$$

In diffraction contrast calculations the displacement field is usually simplified by splitting it up into a dilatation component and a rotation component [7]. The contribution of the dilatation component to image contrast can be shown to be negligibly small in TEM [7]. Therefore only the contribution of the rotation component to image contrast is considered in this work.

### 2.1.3 Procedures of strain field contrast image calculation

The intensity distribution in a BF or DF image at the bottom of a sample has been calculated using a modified version of the TEM software package SIMCON [9], that has been adapted here to allow calculations for four beam cases. The specimen is subdivided in independently diffracting columns perpendicular to the operating diffraction vectors (cf. Section 2.1.1). Each column represents one pixel of the simulated image. The size of the image (width times height) and the desired resolution of the image, i.e. the number of pixels per nanometer, determine both the total number of columns used for the specimen and the lateral size of each column (i.e. the size of the column in the directions parallel to the  $x$ -axis and  $y$ -axis). For every column Eq. (1) is solved numerically, with the displacement field according to Eqs. (4) and (5), using a fifth-order Runge Kutta scheme [10] with a maximum relative integration error of  $1 \cdot 10^{-6}$ . In analogy with Howie and Whelan [6] the set of equations describing

the coupling of the four beams (i.e. Eq. (1)) is rearranged in order to simplify the numerical integration (see Appendix).

## 2.2 Results of BF and DF diffraction-contrast calculations

### 2.2.1 Characterization of the contrast image; the image width

A misfitting particle/disc is considered which is located in the middle of an 80 nm thick specimen with the plane of disc perpendicular to the surfaces of the foil and parallel to  $(100)_{\alpha\text{-Fe}}$ . A BF and a  $(200)_{\alpha\text{-Fe}}$  centered DF image<sup>7</sup> were calculated for such a misfitting particle with radius  $R = 7.5$  nm and Burgers vector length  $b = 0.35$  nm (see Section 2.1.2). The displacement field caused by the particle is obtained from Eqs. (4) and (5) by discretizing the particle into  $N = 156$  equal dislocation loops and with the Poisson ratio of  $\alpha\text{-Fe}$  equal to  $\nu_{\alpha\text{-Fe}} = 0.3$ . The extinction distances correspond to an acceleration voltage for the electrons of 150 kV in  $\alpha\text{-Fe}$ :  $\mathbf{x}_g = 48.47$  nm,  $\mathbf{x}_{2g} = 152.0$  nm and  $\mathbf{x}_{3g} = 39.59$  nm [11]. The lattice constant of the  $\alpha\text{-Fe}$ -matrix and the VN are  $a_{\alpha\text{-Fe}} = 0.28664$  nm and  $a_{\text{VN}} = 0.41392$  nm, respectively, [12]. The deviation parameter  $w = s\mathbf{x}_g$  of the beams  $-\mathbf{g}$  and  $2\mathbf{g}$  is calculated using Eq. (2) as  $w_{-\mathbf{g}} = w_{2\mathbf{g}} = 8.544$ . The effects of inelastic scattering are included by setting  $\mathbf{x}_g/\mathbf{x}'_0 = \mathbf{x}_g/\mathbf{x}'_g = \mathbf{x}_{2g}/\mathbf{x}'_{2g} = \mathbf{x}_{3g}/\mathbf{x}'_{3g} = 0.1$  [2, 3, 13, 14].

Examples of thus calculated BF and centered DF images are depicted in Figs. 2a and b. Contrast lobes occur at both sides of the particle: bright lobes in BF and dark lobes in centered DF. The finely structured vertical band of alternating dark/light contrast through the centre of the image, precisely at the location of the particle, is an artefact of the calculation procedure: it is caused by the approximation of the particle through a finite number of dislocation loops.

The intensity distributions through the centres of the discs and perpendicular to them are shown in Figs. 2c and 2d. In BF the distances of the maximum intensities in the right-hand and left-hand lobes (bright lobes) to the centre of the particle are indicated as  $d_r^{BF}$  and  $d_l^{BF}$ , respectively. Correspondingly  $d_r^{DF}$  and  $d_l^{DF}$  are used with respect to the minimum intensities in DF (dark lobes) in Fig. 2d. The parameters  $d_r^{BF}$ ,  $d_l^{BF}$ ,  $d_r^{DF}$  and  $d_l^{DF}$  are indicative for the width of the diffraction strain contrast image of the misfitting particle.

<sup>7</sup> A centered dark field image is computed if  $\mathbf{g}$  is replaced by  $-\mathbf{g}$  [7].

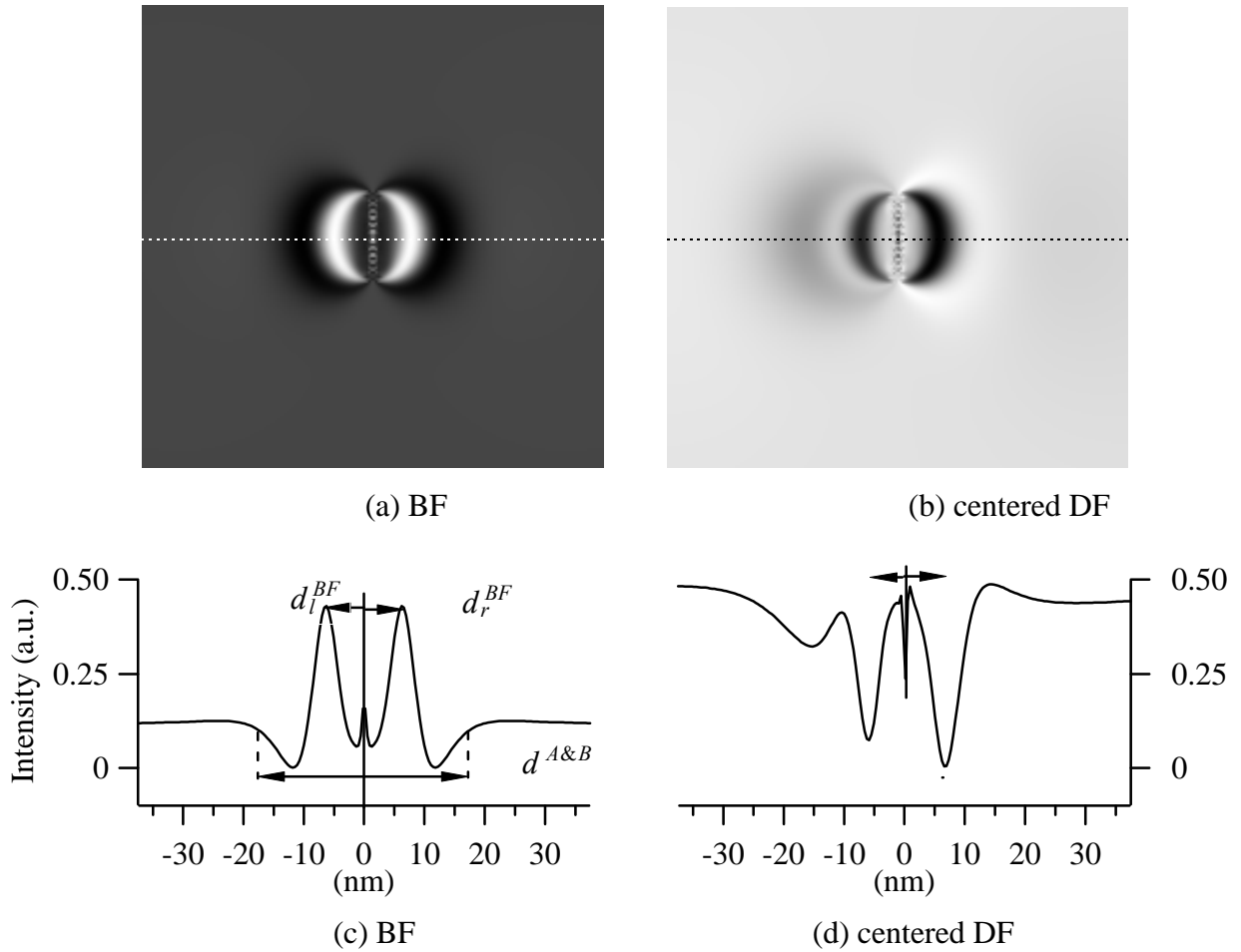


**Fig. 2.** Simulated BF (a) and  $(200)_{\text{a-Fe}}$  centered DF (b) images of a misfitting VN particle (disc) of radius  $R = 7.5 \text{ nm}$  and Burgers vector  $b = 0.35 \text{ nm}$  in the middle of a  $80 \text{ nm}$  thick  $\text{a-Fe}$ -foil with operating reflections  $(\bar{2}00)_{\text{a-Fe}}$ ,  $(000)$ ,  $(200)_{\text{a-Fe}}$  and  $(400)_{\text{a-Fe}}$ . The image size is  $75 \times 75 \text{ nm}^2$ . Below each image the intensity distribution along a horizontal line through the centre of the image is shown for the BF (c) and centered DF (d) images. The particle-lobe distances for BF,  $d_l^{\text{BF}}$  and  $d_r^{\text{BF}}$ , and centered DF,  $d_l^{\text{DF}}$  and  $d_r^{\text{DF}}$ , have been indicated. In addition, the image width in BF, defined according to Ashby and Brown [2, 3] as the distance along the line through the centre of the particle where the intensity differs more than 20 % of the background intensity,  $d^{A\&B}$ , is depicted in Fig. 2c.

### 2.2.2 Parameters determining the image width

A number of simulations was carried out to investigate the influence of several parameters on the DF and the BF images, such as the foil thickness, the particle/disc radius, the effective particle thickness (i.e. the particle Burgers vector, see Section



2.1.2) and the depth location of the particle in the specimen foil. Subsequently, the influence of a neighbouring particle on the image width was studied.

### 2.2.2.1 Foil thickness

The thickness of the foil,  $t$ , was varied from 50 nm to 200 nm in steps of 2.5 nm, while the particle was positioned in the middle of the foil and the Burgers vector length  $b$  and particle radius  $R$  were kept constant:  $b = 0.35$  nm and  $R = 7.5$  nm. The distances  $d^{BF}$  and  $d^{DF}$  to the centre of the particle of each bright lobe in BF and each dark lobe in DF, respectively, are shown in Fig. 3. The so-called 20 % image width in BF, defined by Ashby and Brown [2, 3] as the distance along the line through the centre of the particle where the intensity differs more than 20 % of the background intensity, has also been indicated.

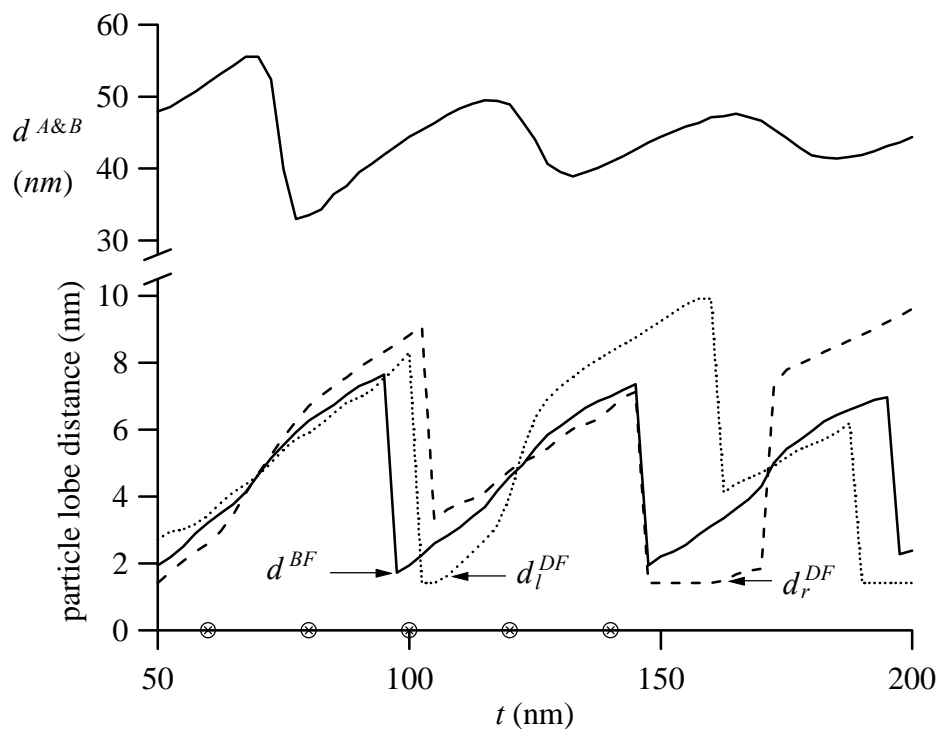


**Fig. 3.** Particle-lobe distance in BF images (bright lobe) and in  $(200)_{\alpha-Fe}$  centered DF images (dark lobe) of a misfitting VN particle of radius  $R = 7.5$  nm and Burgers vector  $b = 3.5$  nm, in the middle of an  $\alpha$ -Fe foil as a function of foil thickness,  $t$ . Full BF and centered DF images at each specimen thickness marked by the cross filled circles on the abscissa are shown in Fig. 4. The image width, defined according to Ashby and Brown [2, 3] as the distance along the line through the centre of the particle where the intensity differs more than 20 % of the background intensity,  $d^{A\&B}$ , is depicted as a function of the specimen thickness in the upper part.

Clearly, the 20%-image width depends on the specimen/foil thickness, especially for  $t < 100 \text{ nm} \approx 2\mathbf{x}_g$ . Ashby and Brown did not consider the influence of the specimen/foil thickness on the image width for foils with a foil thickness  $t < 3.5\mathbf{x}_g$ . Application of the Ashby and Brown method for cases with  $t < 4\mathbf{x}_g$  ( $\approx 200 \text{ nm}$ ; note that electron transparent foils are usually very much thinner), without more ado, will lead to erroneous results in the determination of the particle Burgers vector.

The results of the particle-lobe distance parameters  $d^{BF}$  and  $d^{DF}$  show a zig-zag dependence as a function of the foil thickness, which can be understood considering the series of BF and corresponding centered DF images shown in Figs. 4a-e. These series correspond to the abscis values indicated with  $\otimes$  in Fig. 3. Starting at  $t = 50 \text{ nm}$  the lobes move away from the particle centre for increasing  $t$ , cf. for instance Fig. 4a with Fig. 4b. At some thickness, approximately  $t = 100 \text{ nm}$  in this case, a second bright lobe in BF and a second dark lobe in centered DF appears in between the particle and the first lobe, cf. Fig. 4c. The lobe closest to the particle has been used to determine  $d^{BF}$  and  $d^{DF}$  and therefore a step occurs in Fig. 3 (compare Fig. 3 and Figs. 4b, 4c and 4d), etc.

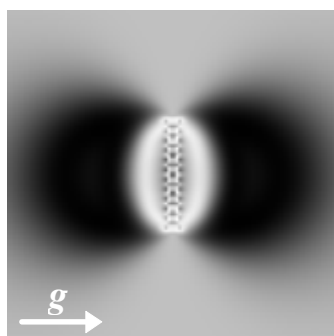
Since the particle is positioned in the middle of the foil and the deviation from the Bragg position of  $\mathbf{g}$  is taken to be zero (cf. Section 2.1.1), the lobes of the BF image are always symmetric:  $d_r^{BF} = d_l^{BF}$ . The centered DF images are usually asymmetric:  $d_r^{DF} \neq d_l^{DF}$ . It depends on the value of  $t$  whether the right or left dark lobe is closest to the particle in the DF image.

### 2.2.2.2 Particle radius

The influence of the particle radius on the extent of the contrast lobes in BF and DF is shown in Fig. 5 for a 80 nm thick specimen. On increasing the particle radius the lobes move away from the particle. Below  $R = 2.5 \text{ nm}$  it is difficult or impossible to find a bright lobe for the BF images and a dark lobe for the centered DF images on either side of the particle.

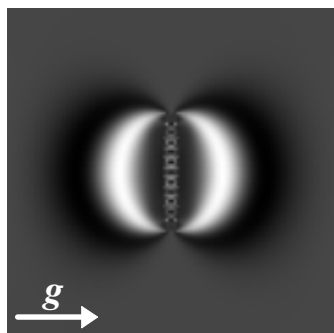
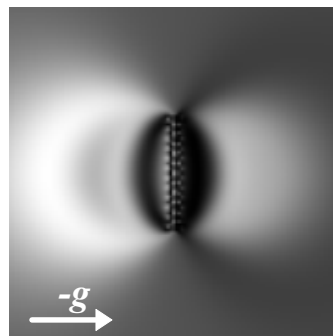
### 2.2.2.3 Particle Burgers vector

The Burgers vector in Eq. (4) represents the misfit of the particle relative to the matrix (cf. Section 2.1.2). The change of the lobe extent for a range of Burgers-vector lengths is shown in Fig. 6. With increasing Burgers-vector length the lobes move away from the particle. For a Burgers vector-length between 0.45 nm and 0.5 nm a second lobe develops for both the centered DF and BF images in between the particle and the first lobe, and this explains the step in Fig. 6.



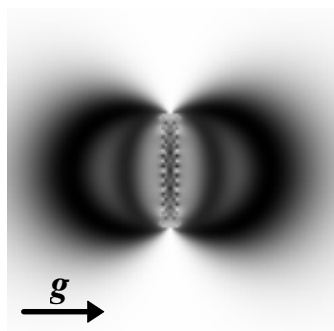
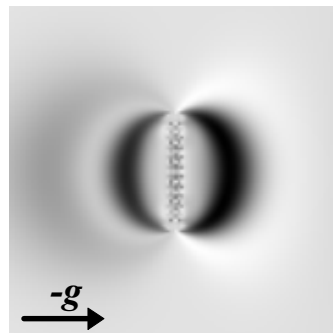
a)  $t = 60 \text{ nm}$

$x_g/t = 1.24$



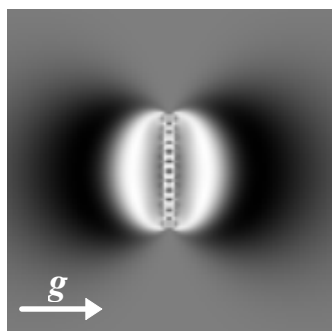
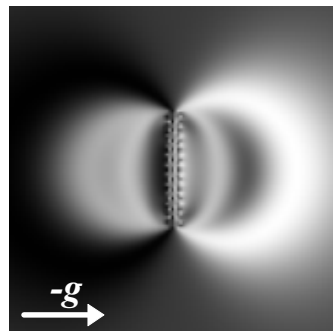
b)  $t = 80 \text{ nm}$

$x_g/t = 1.65$



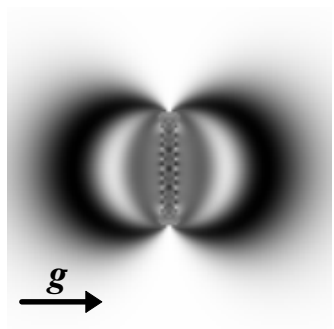
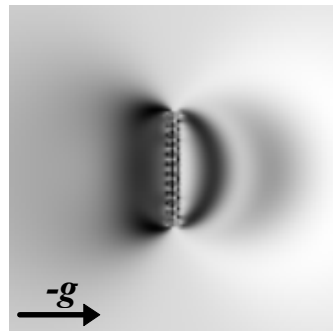
c)  $t = 100 \text{ nm}$

$x_g/t = 2.06$



d)  $t = 120 \text{ nm}$

$x_g/t = 2.48$



e)  $t = 140 \text{ nm}$

$x_g/t = 2.89$

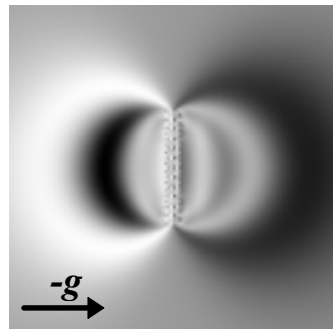


**Fig. 4.** Influence of specimen thickness on BF (left column) and  $(200)_{\alpha\text{-Fe}}$  centered DF images (right column) of a misfitting VN particle of radius  $R = 7.5$  nm and Burgers vector  $b = 0.35$  nm in the middle of an  $\alpha\text{-Fe}$  foil. Thickness  $t$  relative to  $\mathbf{x}_g$ ,  $t/\mathbf{x}_g$  has been indicated. See also Fig. 3.

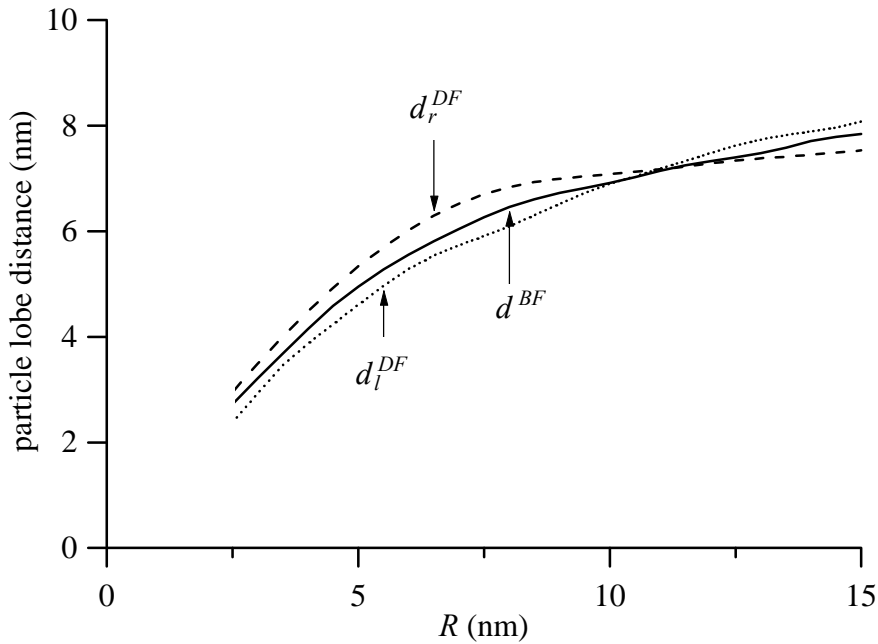


**Fig. 5.** Influence of the particle radius  $R$  on the particle-lobe distances in BF and  $(200)_{\alpha\text{-Fe}}$  centered DF images of a misfitting VN particle with Burgers vector  $b = 0.35$  nm located in the middle of an 80 nm thick  $\alpha\text{-Fe}$  foil.

#### 2.2.2.4 Particle position

The influence of the vertical position (depth beneath the foil surface) of a particle in the foil is shown in Fig. 7. The parameter  $Dh$  indicates the vertical position with respect to the middle of the foil ( $Dh = 0$ ). The particle-lobe distances of the bright lobes in BF and the dark lobes in centered DF are practically independent of  $Dh$ , although the full BF and centered DF images indicate a clear dependence on  $Dh$ ; only if  $Dh = 0$  the full BF image is symmetric. For  $Dh < 0$ , the same kind of results as for  $Dh > 0$  are obtained but the results of the BF left-hand lobe and the BF right-hand lobe would have to be interchanged; the centered DF images are not dependent on the direction of the particle shift (sign of  $Dh$ ).

It is concluded, when comparing full images of simulations and experiments that as long as the experimental image in BF of the particle concerned is symmetric it is justified in the simulation to assume that the particle is located in the middle of the

foil; for an analysis based on  $d^{BF}$  and  $d^{DF}$  only, small deviations of the location/depth of the particle from the middle of the foil are irrelevant.

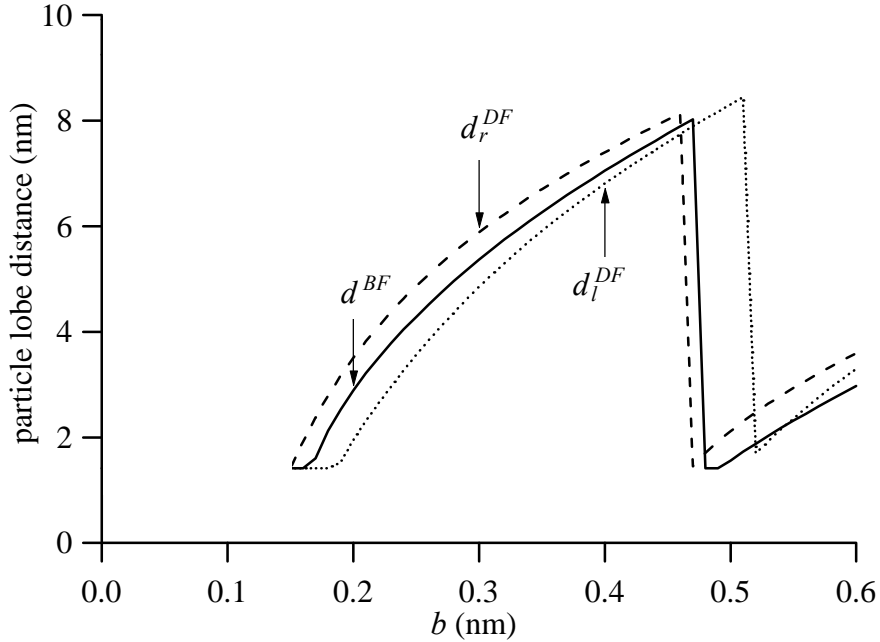


**Fig. 6.** Influence of the particle Burgers vector  $b$  on the particle-lobe distances in BF and  $(200)_{\alpha\text{-Fe}}$  centered DF images of a misfitting VN particle of radius  $R = 7.5$  nm located in the middle of an 80 nm thick  $\alpha\text{-Fe}$  foil.

#### 2.2.2.5 Neighbouring particle; overlapping strain fields

Consider a two-particle system with one particle located at  $(0,0,0)$  and the other one at  $(L,0,0)$ . The particle discs of equal particle radius,  $R = 7.5$  nm, and particle Burgers vector,  $b = 0.35$  nm are parallel and located in the middle of a 80 nm thick foil. The change of the image width for a change of the interparticle distance  $L$  from 10 nm to 150 nm is shown in Fig. 8. Obviously, for small  $L$  distinct effects on  $d^{BF}$  and  $d^{DF}$  occur. Note that  $d_r^{BF}$  is affected more than  $d_l^{BF}$  since the right lobe is located closer to the neighbouring particle than the left lobe. A similar statement holds for the corresponding DF lobes. For  $L > 30$  nm, i.e.  $L$  larger than about 1.5 times the particle diameter, the influence of the neighbouring particle has become negligible and the particle lobe distances are equal to those of a single misfitting particle of equal radius and particle Burgers vector (cf. Fig. 7 at  $Dh = 0$ ).

Thus, comparing images simulated on the basis of a single particle model with experimental contrast images of systems containing a high number density of misfitting particles, in the experimental images particles should be selected that (i) are

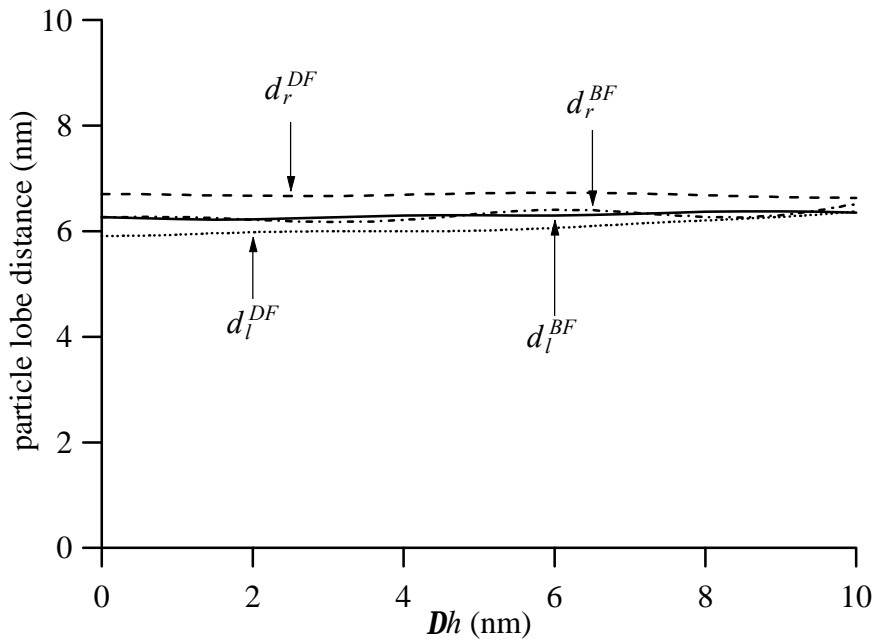


**Fig. 7.** Influence of the particle location on the particle-lobe distances in BF and  $(200)_{\alpha-Fe}$  centered DF images of a misfitting VN particle of radius  $R = 7.5$  nm and Burgers vector  $b = 0.35$  nm located in an 80 nm thick  $\alpha$ -Fe foil. The particle is displaced upwards against the direction of electron motion by an amount  $Dh$  (nm);  $Dh = 0$  corresponds to the middle of the foil.

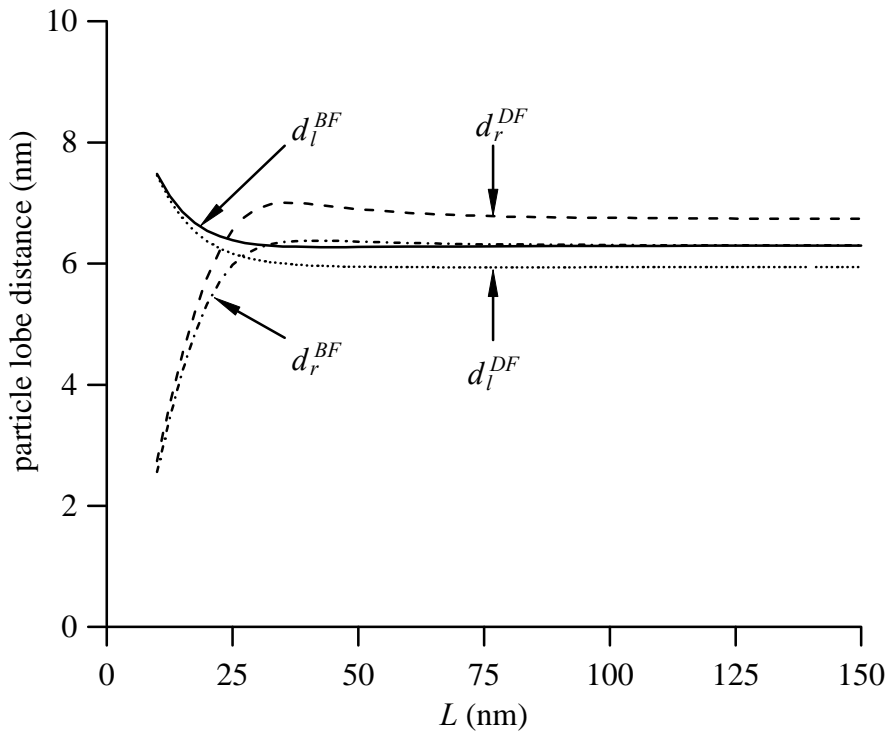


**Fig. 8.** Influence of the distance  $L$  of a second particle (disc) located at  $(L,0,0)$  on the particle-lobe distances in BF and  $(200)_{\alpha-Fe}$  centered DF images of a misfitting VN particle at  $(0,0,0)$ . The particle radius,  $R = 7.5$  nm, and the Burgers vector,  $b = 0.35$  nm, of both particles are equal. The  $\alpha$ -Fe foil is 80 nm thick.

located at about 1.5, or more, times the particle diameter away from neighbouring particles, and (ii) additionally, exhibit symmetric contrast lobes in BF. The latter criterion means that, additionally,  $Dh = 0$ . When the (projected) interparticle distance is smaller, the influence of neighbouring particles can still be negligible if these particles are situated at another height in the foil. Also for this case it holds that occurrence of a symmetrical BF image of a single particle can be considered in general as indicative of negligible influence of strain field overlap with neighbouring particles.

If the second particle at  $(L,0,0)$  is oriented perpendicularly with respect to the first one at  $(0,0,0)$  (while remaining perpendicular to the foil surfaces), then the displacements in the matrix caused by the second particle are directed perpendicularly with respect to the displacements in the matrix from the first particle and also with respect to the diffraction vector employed and therefore the effect of such a second particle is negligible (cf. Eq. 1).

### 3. Specimen preparation

An  $\alpha$ -Fe-2.2 at.% V solid solution was made through arc melting of 99.998 wt.% pure  $\alpha$ -Fe and 99.999 wt.% pure V in the correct ratio and subsequent annealing for 5 days at 1225 °C in an Ar-filled quartz ampul. The alloy composition was checked with Electron Prope Micro Analysis: 0.4 at. % V is present as VO that developed during the alloy production. In all further production steps the amount of VO remained constant and therefore 1.8 at.% V is considered to be present initially in solid solution and as VN after completed nitriding (see below).

A series of rolling and recrystallisation steps was applied to produce elongated sheets of 200  $\mu\text{m}$  thickness with crystallite sizes (optical microscopy) between 10  $\mu\text{m}$  and 60  $\mu\text{m}$ . Small rectangular parts of size 1 cm  $\times$  2 cm cut from the sheet were polished and thinned to about 100  $\mu\text{m}$  thickness using Kawamura's reagent [15]. Next, these pieces, suspended with a thin Ni wire, were through nitrided in a vertical quartz tube furnace at 793 K, 853 K or 913 K for 25 hours. A gas mixture consisting of 99 vol.%  $\text{H}_2$  (99.95 % purity) and 1 vol.%  $\text{NH}_3$  (99.90 % purity) was used, yielding a constant nitriding potential of  $0.0102 \text{ atm}^{-1/2}$  during the time of nitriding [16]. Micro-Vickers hardness measurements at cross sections of the nitrided specimens confirmed that through nitriding had occurred.

X-ray diffraction analysis of the nitrided specimens was performed on a Siemens 500 B diffractometer equipped with Cu-K $\alpha$  radiation and a graphite monochromator in the diffracted beam to select Cu-K $\alpha$  radiation. The specimens were attached magnetically onto a Si- $\langle 510 \rangle$  single crystal substrate. The diffracted intensities in the diffraction angle range of 20 -160  $^\circ 2\mathbf{q}$  were recorded applying a 0.05

$^{\circ}2q$  stepsize and a 28 (s) counting time per step (yielding 15000 to 25000 counts at {110} peak maximum depending on the specimen). During the measurement the specimens were rotated about the specimen's surface normal.

From the nitrated material small circular discs of 3 mm diameter were drilled that were polished with diamond paste (successively 3, 1 and 0.25  $\mu\text{m}$ ) to a thickness of 20  $\mu\text{m}$ . Subsequently, the specimens were jet-electrolytically polished in an acid electrolyt (90 vol.% acetic acid, 10 vol.% perchloric acid) until perforation.

Transmission Electron Microscopy (TEM) was performed in a Philips CM30T microscope operating at 150 kV. The low voltage of 150 kV (300kV is maximally possible on the CM30T) was chosen to reduce the intensity of other than indicated reflections in the systematic row  $\dots, -\mathbf{g}, \mathbf{0}, \mathbf{g}, 2\mathbf{g}, \dots$ , as a low acceleration voltage corresponds to a relatively large electron wavelength and a correspondingly relatively small radius of Ewald's sphere. Selected Area Diffraction Patterns (SADP) as well as BF's and centered DF's employing a  $(200)_{\alpha\text{-Fe}}$  reflection were recorded. At the SADP's spots were observed at the location of the (forbidden)  $(100)_{\alpha\text{-Fe}}$  spots, which originated most likely from the presence of  $\text{Fe}_3\text{O}_4$  at the foil surface as grown after foil preparation; see for a more elaborate discussion Ref. [17].

High Resolution Election Microscopy (HREM) images from the thin parts of the foil were taken at 300 kV with the electron beam direction a few degrees away from the  $[001]_{\alpha\text{-Fe}}$  zone axis, in such a way that a  $(110)_{\alpha\text{-Fe}}$  reflection was precisely in the Bragg orientation. The objective aperture included the first-order reflections and the transmitted beam.

All images and SADP's were recorded on photo negatives; for further interpretation these were scanned using a commercially available scanning device employing 600 dots per inch (dpi).

The thickness of the specimen foil was measured locally with the contamination-spot separation method [18]. To this end, the vacuum of the microscope was deteriorated deliberately by removing the cold trap, such that contamination spots could be formed on both sides of the foil. The separation of the spots was measured in projection for a series of different foil tilts leading to accurate determination of the foil thickness at the location of the contamination spots.



## ***4. Fitting calculated diffraction contrast images to experimental diffraction contrast images of VN in $\alpha$ -Fe***

### **4.1 Selection of experimental diffraction contrast images of misfitting particles**

An overview of the distribution of VN particles in the  $\alpha$ -Fe-matrix and the strain contrast caused by their displacement fields in the  $\alpha$ -Fe-matrix is shown in the BF and the  $(200)_{\alpha\text{-Fe}}$  centered DF images shown in Figs. 9a and 9b for a specimen nitrated at 913 K. The specimen is oriented with the electron beam almost perpendicular to the specimen foil surface and  $\sim 2^\circ$  out of the  $[001]$ -direction of the parent  $\alpha$ -Fe-lattice and  $\mathbf{g} = (200)_{\alpha\text{-Fe}}$ . This arrangement of the specimen is used throughout this work. The corresponding selected area diffraction pattern is given in Fig. 9c. For the specimens nitrated at 793 K and 853 K the contrast changes in the images were much less distinct; see also discussion in Section 5.

The diffraction pattern of the 913 K specimen shows two very strong spots, the transmitted beam and the  $(200)_{\alpha\text{-Fe}}$ -diffraction spot, and two less strong spots, the  $(400)_{\alpha\text{-Fe}}$  and  $(\bar{2}00)_{\alpha\text{-Fe}}$  diffraction spot. Streaks in the  $[100]_{\alpha\text{-Fe}}$  direction can be found through the location of the  $\{200\}_{\text{VN}}$  diffraction positions indicated by arrows in Fig. 9c. The elongated shape of these spots is caused by the small thickness of the disc-shaped VN particles [19, 20] lying on  $(100)_{\alpha\text{-Fe}}$  lattice planes: measurement of the full width at half maximum of both indicated  $\{200\}_{\text{VN}}$  spots, in a way as usually carried out in XRD [21], leads to an apparent VN particle thickness of 1.4 nm. Also VN particles on other  $\{100\}_{\alpha\text{-Fe}}$  lattice planes (i.e.  $(010)_{\alpha\text{-Fe}}$  and  $(001)_{\alpha\text{-Fe}}$ ) are present, but these are not visible in the BF and the centered DF images since the corresponding disc normals and the main matrix-lattice displacements are perpendicular to the operating diffraction vector(s) (see also Section 2.2.2.5). Therefore, given a statistical distribution of the VN particles over the three habit planes of type  $\{100\}_{\alpha\text{-Fe}}$ , only one third of the total number of VN particles with their contrast lobes is visible in Figs. 9a and 9b.

From the BF and centered DF images it is clear that the number density of VN particles is very large. On the basis of the assumptions made in the model for the image simulations (Section 2.1) and the calculated results (Section 2.2), in the experimental images particles have been selected only when the following requirements are met. (i) The particle should have close-to-symmetrical lobes in BF. (ii) The particle should lie in the bright bend contour in the centered DF of  $\mathbf{g} = (200)_{\alpha\text{-Fe}}$  that corresponds to an exact realisation of the Bragg conditions. A possible deviation from the Bragg position could not be assessed from analysis of Kikuchi

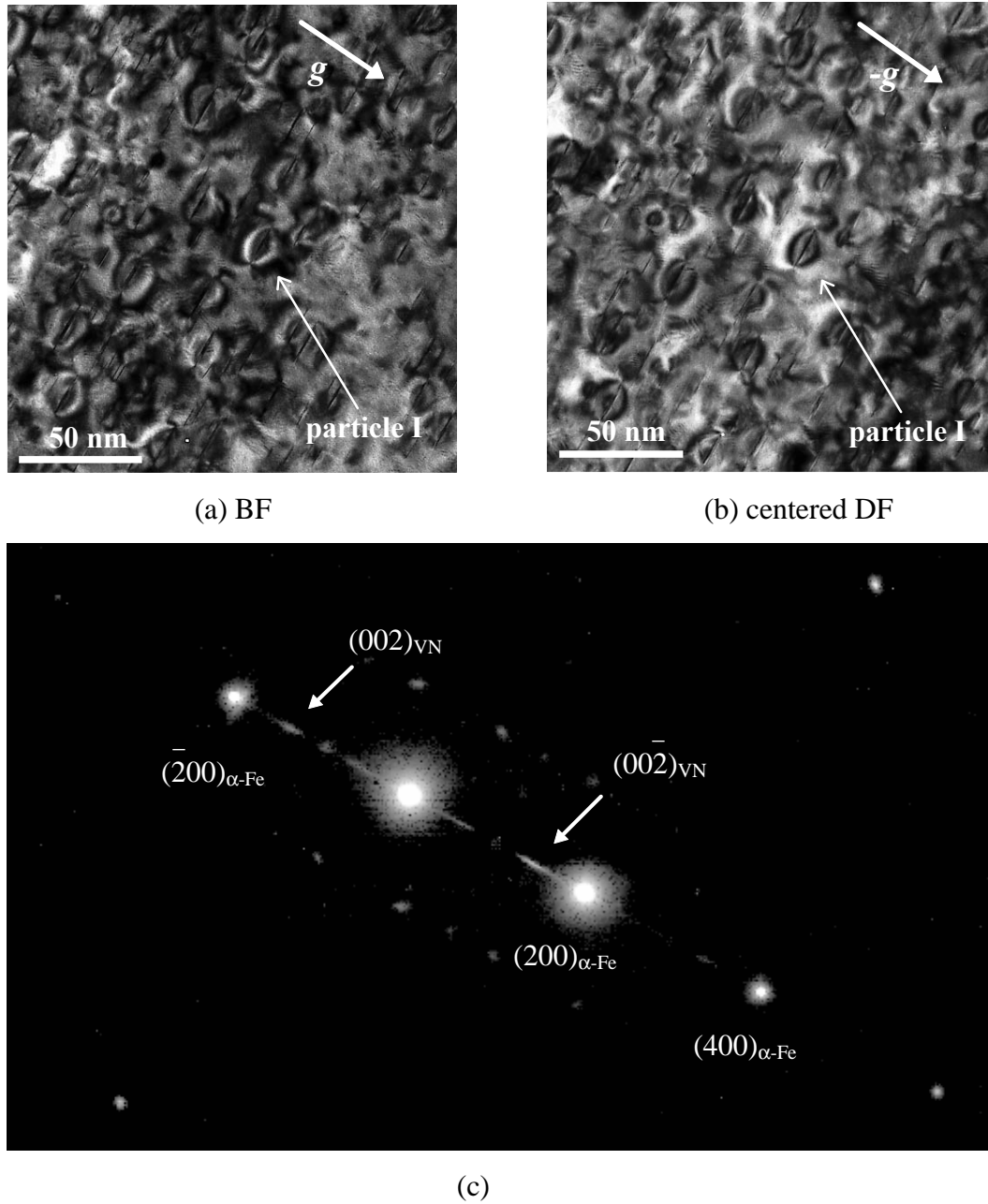


**Fig. 9.** BF image (a) and  $(200)_{\alpha\text{-Fe}}$  centered DF image (b) of Fe-2 at. % V specimen nitrified for 25 hours at 913 K at nitrifying potential of  $0.0102 \text{ atm}^{-1/2}$ . Small VN particles are visible surrounded by contrast lobes. The corresponding diffraction pattern (c), with an orientation that is compatible with Figs. 9a and b, shows the direct beam and the  $(200)_{\alpha\text{-Fe}}$ ,  $(400)_{\alpha\text{-Fe}}$  and  $(\bar{2}00)_{\alpha\text{-Fe}}$  diffraction spots. Some iron oxide reflections from a thin oxide layer on the surface are visible, see also Section 3. Furthermore,  $\{200\}_{\text{VN}}$  streaks in the  $[110]_{\alpha\text{-Fe}}$ -direction are visible as indicated by the arrows. The specimen is oriented with the electron beam almost perpendicular to the specimen foil surface and  $\sim 2^\circ$  out of the  $[001]$ -direction of the parent  $\alpha\text{-Fe}$ -lattice and  $\mathbf{g} = (200)$ .

lines, since these could not be observed, possibly due to the straining of the matrix by the large number of misfitting VN precipitates.

In this way three particles were selected, in the case corresponding to Fig. 9, of which the contrast images are shown in BF and corresponding centered DF in Figs. 10-12. The average intensity distributions along a line perpendicular to the particles and going through the centre of the particles are displayed in Fig. 13a for the BF images and in Fig. 13b for the centered DF ones. The distributions have been averaged over some distance (2.5 nm in total) perpendicular to this line to cancel out intensity fluctuations caused by noise.

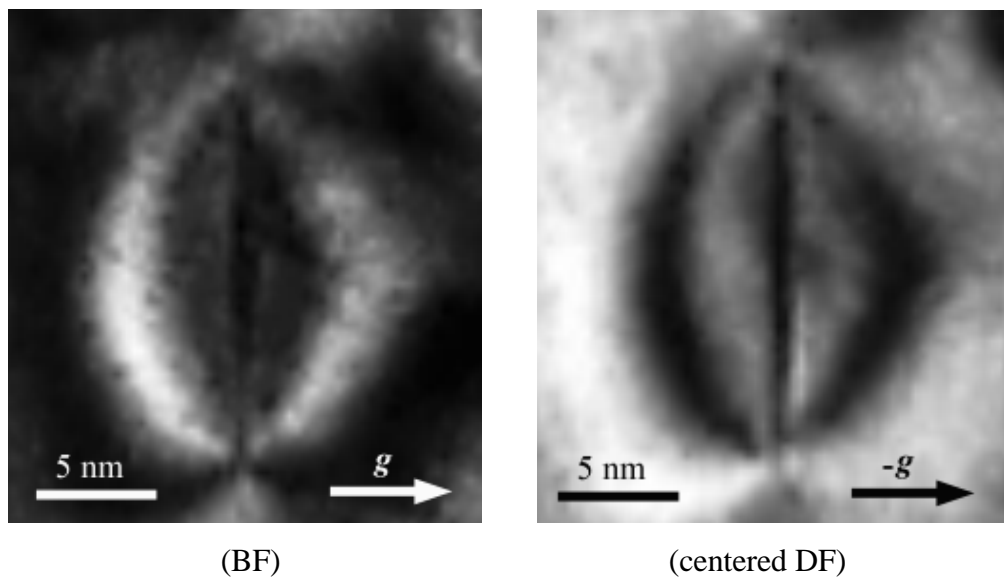


**Fig. 10.** BF and  $(200)_{\alpha\text{-Fe}}$  centered DF image of selected VN particle I.

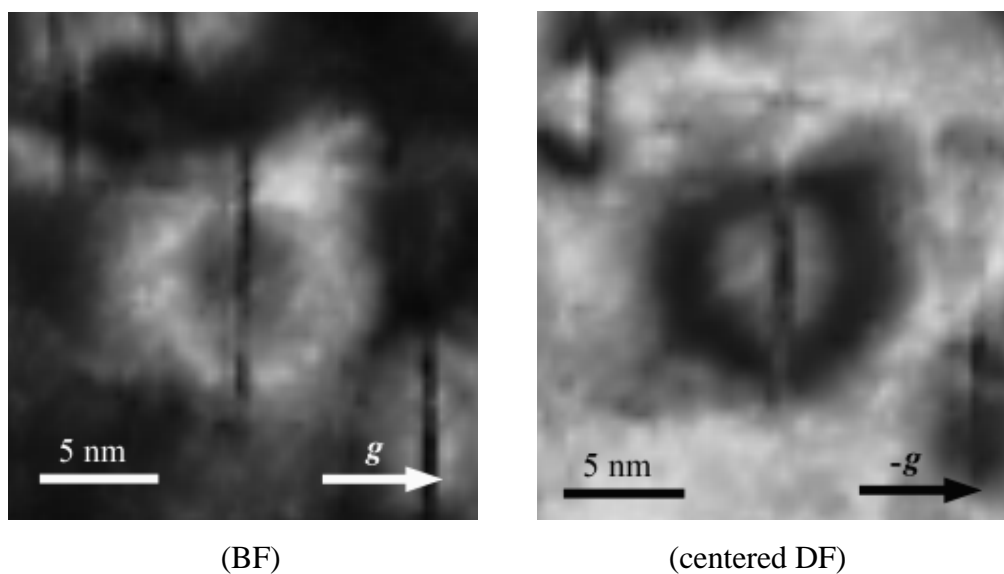


**Fig. 11.** BF and  $(200)_{\alpha\text{-Fe}}$  centered DF image of selected VN particle II.

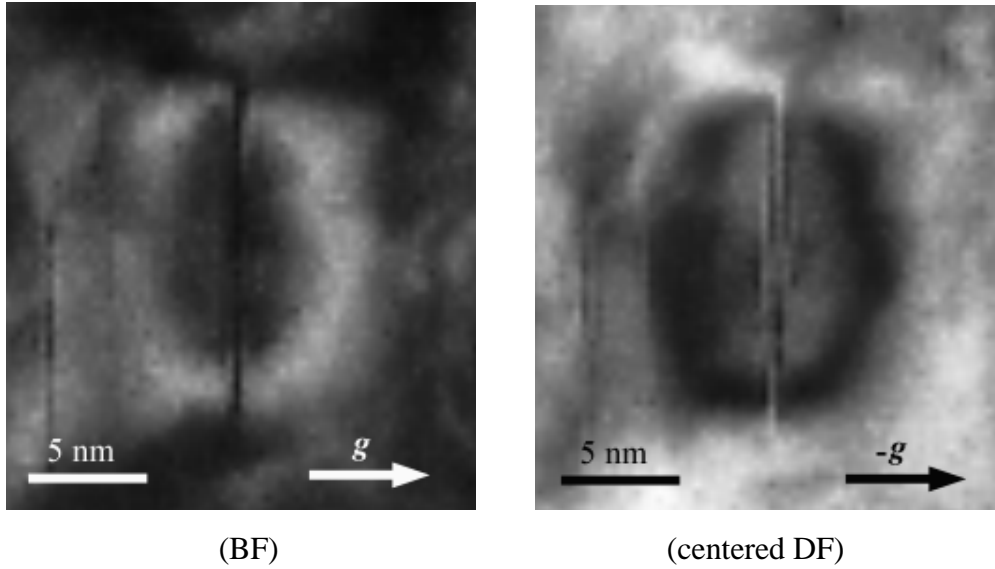


**Fig. 12.** BF and  $(200)_{\alpha-Fe}$  centered DF image of selected VN particle III.

**Table 1:** Particle-lobe distances in BF ( $d_r^{BF}$  and  $d_l^{BF}$ ; see Fig. 2) and corresponding  $(200)_{\alpha-Fe}$  centered DF ( $d_r^{DF}$  and  $d_l^{DF}$ ; see Fig. 2) images with estimates of errors for three selected particles of an Fe-2 at.% V alloy nitrided at 913 K. Particle radii,  $R$ , are measured from the ends of the corresponding contrast lobes in BF and DF and averaged.

particle	$d_l^{BF}$	$d_r^{BF}$	$d_l^{DF}$	$d_r^{DF}$	$R$
	(nm)	(nm)	(nm)	(nm)	(nm)
I	$5.7 \pm 0.2$	$6.3 \pm 0.2$	$5.3 \pm 0.2$	$5.3 \pm 0.2$	$9.0 \pm 0.2$
II	$4.1 \pm 0.2$	$4.1 \pm 0.2$	$4.5 \pm 0.2$	$3.6 \pm 0.2$	$5.3 \pm 0.2$
III	$5.3 \pm 0.4$	$4.9 \pm 0.2$	$4.5 \pm 0.3$	$4.5 \pm 0.2$	$7.5 \pm 0.2$

The distances from the maximum intensity in each bright lobe in BF to the particle,  $d_l^{BF}$ , and from the minimum intensity in each dark lobe in centered DF,  $d_r^{DF}$ , along with an estimate of the measurement errors, are presented in Table 1. Note that in case of particle I and particle III  $d_r^{DF} \approx d_l^{DF}$ , whereas in case of particle II  $d_r^{DF} \neq d_l^{DF}$ . For each particle also the particle radius is given as an average from the measured distances between the ends of the contrast lobes above and below the particle in BF and in centered DF. This distance does not deviate much from the length of the dark line(s) of contrast in the images at the location of the particle (visible particles are perpendicular to the foil).

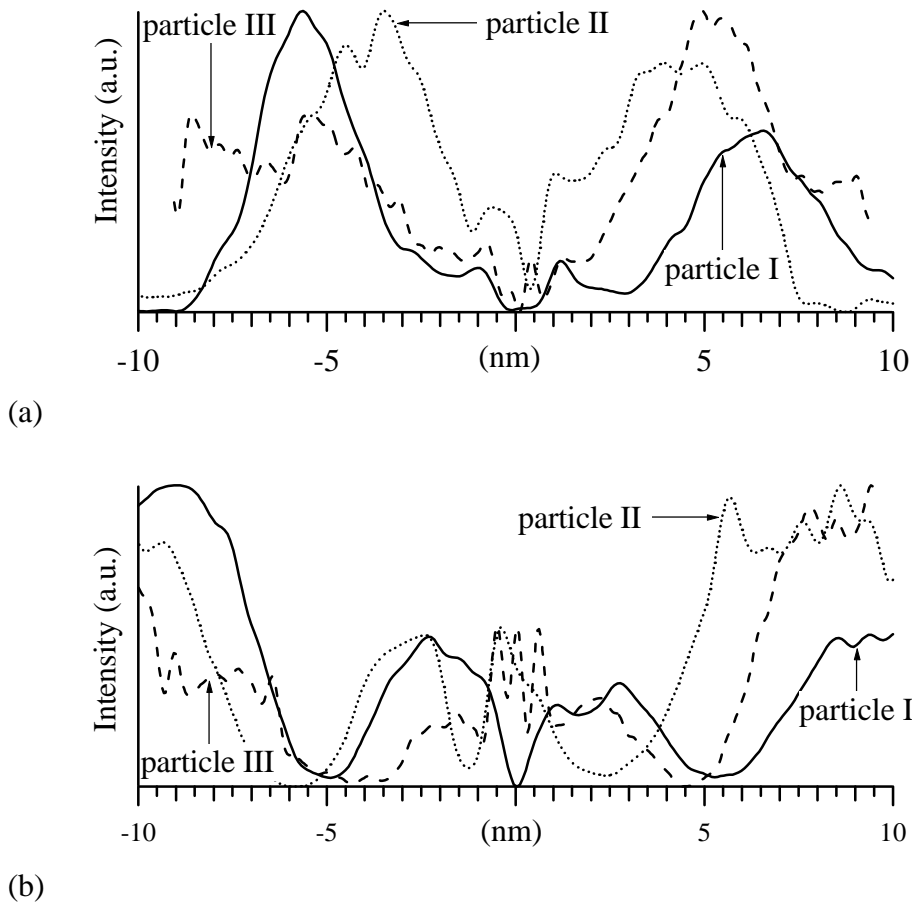


**Fig. 13.** Normalised intensity distributions in BF (a) and  $(200)_{\alpha-Fe}$  centered DF (b) obtained along the line through the centre of the selected particles I, II and III (cf. Figs. 10, 11 and 12) and normalised with respect to the maximum and minimum intensity within the range displayed.

#### 4.2 Fitting of particle Burgers vector and foil thickness

The calculated images were fitted to the experimental ones by varying the values of  $t$  and  $b$ ; the value of  $R$  was set equal to the experimentally measured value (see Table 1). The fitting procedure ran as follows. (i) For wide ranges of values for the particle Burgers vector  $b$  (0.2 nm to 0.5 nm in steps of 0.025 nm) and the specimen foil thickness  $t$  (50 nm to 135 nm in steps of 2.5 nm) the intensity distribution was calculated in BF and centered DF along the line perpendicular to the disc and going through the centre of the disc and, subsequently, the values for the image widths  $d^{BF}$ ,  $d_l^{DF}$  and  $d_r^{DF}$  were determined for each intensity distribution. (ii) Then, contour lines of constant image width in  $(t,b)$  space were constructed for the experimental values of  $d^{BF}$ ,  $d_l^{DF}$ ,  $d_r^{DF}$ . (iii) The intersection of the contour lines for  $d^{BF}$ ,  $d_l^{DF}$  and  $d_r^{DF}$  determined the  $t$  and  $b$  values for the particle concerned. (iv) Finally, full images

were calculated for this combination of  $t$  and  $b$  values and were compared with the experimental images. Only if sufficiently comparable images were obtained, the corresponding values of  $t$  and  $b$  were accepted.

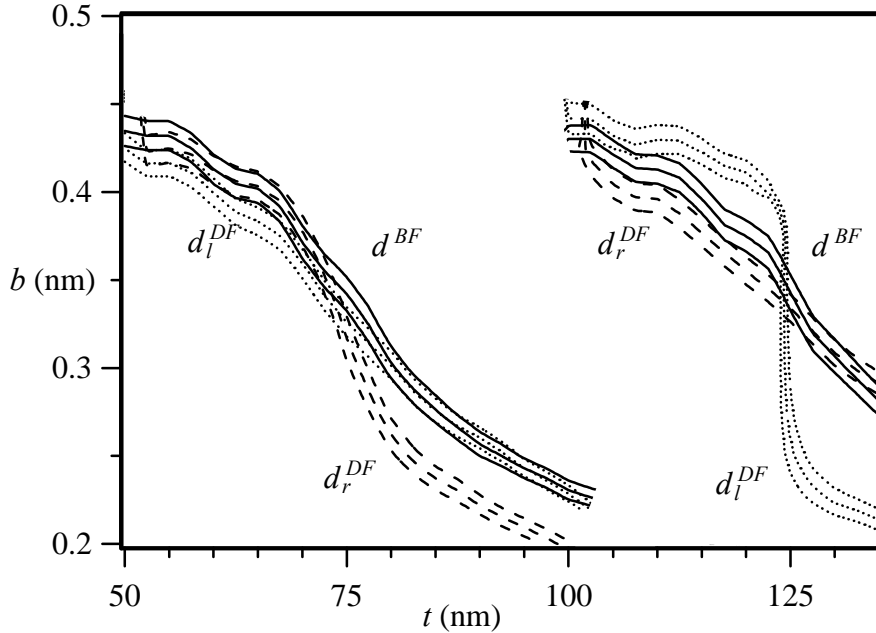


**Fig. 14.** Contour diagram for particle I showing contour plots of the three experimentally measured particle-lobe distances,  $d_{BF}$  ( $5.7 \pm 0.2$  nm),  $d_{DFl}$  ( $5.3 \pm 0.2$  nm) and  $d_{DFr}$  ( $5.3 \pm 0.2$  nm) as a function of the Burgers vector,  $b$ , and specimen thickness,  $t$ , for a simulated VN particle with size  $R = 9.0$  nm. For each particle-lobe distance three lines are drawn: a centre line, corresponding to the mean value of the particle-lobe distance, and two outer lines on either side of the centre line corresponding to the mean value plus or minus the respective error indicated above.

The contour diagram for particle I with  $R = 9.0$  nm, shown in Fig. 14, indicates several regions of intersection for the contour lines of constant image width, i.e.  $(t, b)$  combinations with which values for the particle-lobe distances equal to the experimental ones are observed both in BF and centered DF: (i) a narrow band of overlap between  $(t, b) = (50 \text{ nm}, 0.425 \text{ nm})$  and  $(t, b) = (75 \text{ nm}, 0.325 \text{ nm})$ , (ii) at  $(t, b) = (102.5 \pm 0.5 \text{ nm}, 0.42 \pm 0.02 \text{ nm})$  and (iii) at  $(t, b) = (120 \pm 0.5 \text{ nm}, 0.34 \pm 0.02 \text{ nm})$ . Note that the discontinuities in Fig. 14 for the contrast lines are related to the discontinuities for the particle lobe distance as a function of  $t$  in Fig. 3.

Thus, on the basis of this contour diagram a unique choice of  $(t, b)$  cannot be made. Therefore, a number of full BF and DF images with  $(t, b)$  combinations corresponding to the above indicated regions of intersection were computed and

compared with the experimental ones. Representative results are shown in Fig. 15 for a relatively thin foil (with  $(t,b) = (75.0 \text{ nm}, 0.355 \text{ nm})$ ), and a relatively thick foil (with  $(t,b) = (121.2 \text{ nm}, 0.342 \text{ nm})$ ). Both simulated BF images resemble the experimental image very well<sup>8</sup>. However, distinction can be made on the basis of the centered DF images. The left-hand centered DF lobe for the case of the thick foil (Fig. 15b) does not appear as a curved contrast lobe as observed in the experimental image; it merely shows a wide, diffuse zone without much contrast<sup>9</sup>. It is concluded that the simulation for the case of the thin foil (Fig. 15a) is closer to reality. From a series of simulations for a range of  $(t,b)$  values for the thin foil case, the following estimates were eventually obtained for the foil thickness and the particle Burgers vector of particle I:  $(t,b) = (73 \pm 3 \text{ nm}, 0.34 \pm 0.02 \text{ nm})$ . The value thus obtained for the foil thickness agrees well with the value directly measured according to the contamination spot method at the same location (cf. Section 3):  $t_c = 80 \pm 5 \text{ nm}$ .

The contour diagrams for particle II and III with  $R = 5.3 \text{ nm}$  and  $R = 7.5 \text{ nm}$ , respectively, are presented in Figs. 16 and 18. The same treatment as for particle I has been applied to particles II and III. It was obtained for the foil thickness and the particle Burgers vector of particle II, that  $(t,b) = (61 \pm 3 \text{ nm}, 0.45 \pm 0.02 \text{ nm})$  and of particle III, that  $(t,b) = (70 \pm 3 \text{ nm}, 0.35 \pm 0.02 \text{ nm})$ . Representative simulation results for both particles can be compared with the respective experimental images in Fig. 17 for particle II and in Fig. 19 for particle III. The values thus obtained for the foil thickness agree well with the values directly measured according to the contamination spot method at the same locations: in case of particle II,  $t_c = 62 \pm 10 \text{ nm}$  and in case of particle III,  $t_c = 67 \pm 10 \text{ nm}$ . All results of the fitting procedure have been collected in Table 2.

---

<sup>8</sup> Note, that the comparison of an experimental image with a calculated image is hindered by the different grey scales of both images. Therefore, the exact intensities at a certain point in both images cannot be compared on an absolute basis too strictly. Instead, characteristics of both images that are to a large extent independent of the grey scales used can be compared, such as the extent and the shape of the bright and dark lobes.

<sup>9</sup> Compare also with Figs. 4b and 4d, which display BF and centered DF images for similar thickness and Burgers vector values, albeit for a somewhat larger particle.

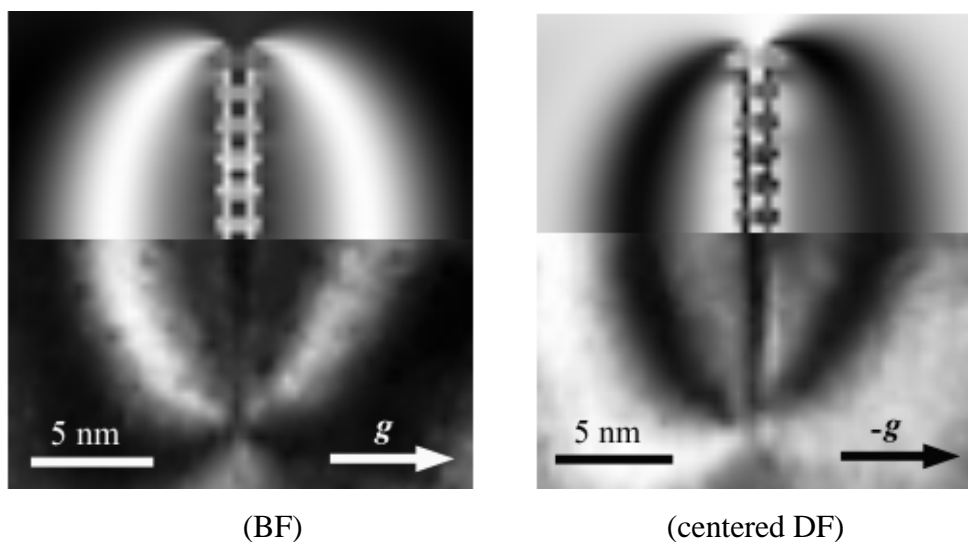


**Fig. 15a.** Comparison of experimental (lower part) and simulated (upper part) BF image and  $(200)_{\text{a-Fe}}$  centered DF image of particle I. Simulation was carried out for a particle of radius  $R = 9.0$  nm and Burgers vector  $b = 0.332$  nm located in the middle of a 75.0 nm thick foil.

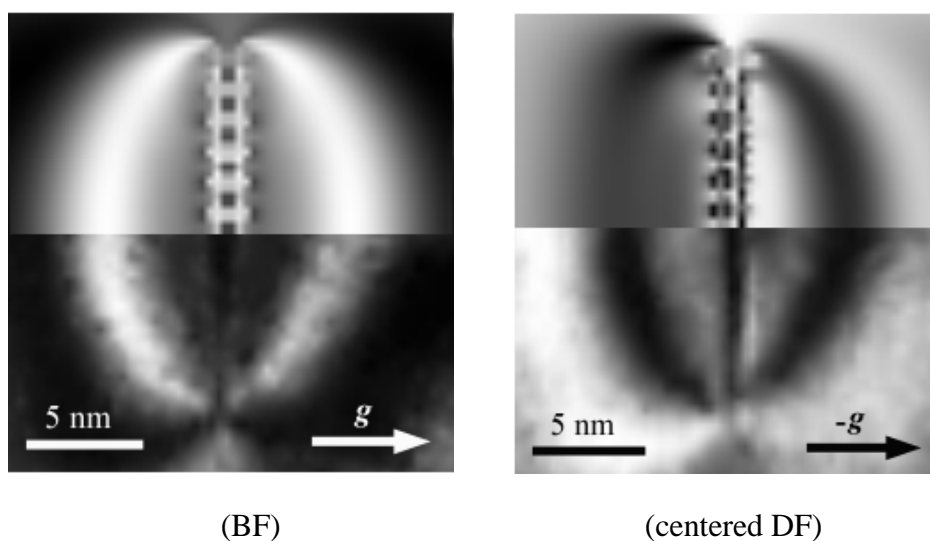


**Fig. 15b.** Comparison of experimental (lower part) and simulated (upper part) BF image and  $(200)_{\text{a-Fe}}$  centered DF image of particle I. Simulation was carried out for a particle of radius  $R = 9.0$  nm and Burgers vector  $b = 0.342$  nm located in the middle of a 124.2 nm thick foil.



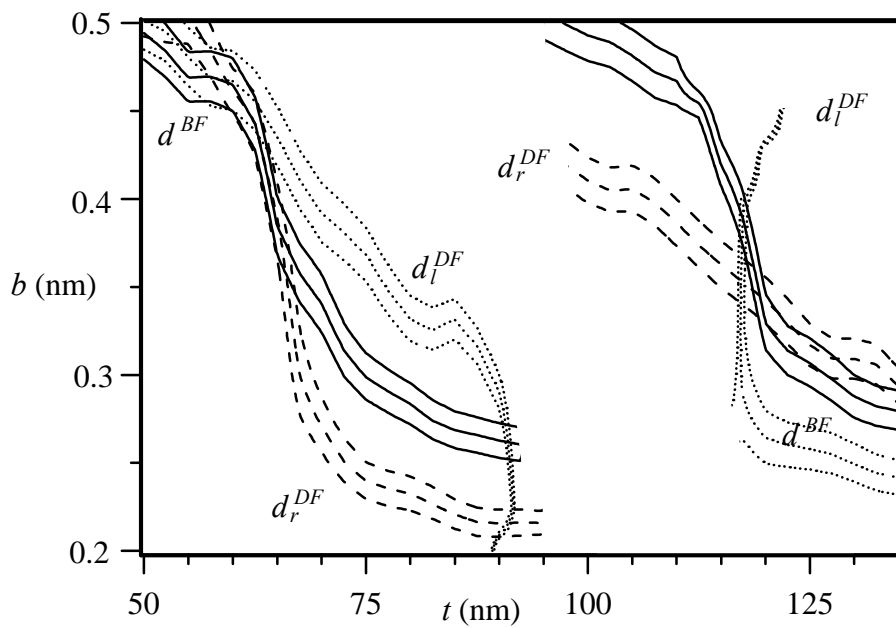


**Fig. 16.** Contour diagram for particle II showing contour plots of the three experimentally measured particle-lobe distances,  $d_{BF}$  ( $4.1 \pm 0.2$  nm),  $d_{DFl}$  ( $4.5 \pm 0.2$  nm) and  $d_{DFr}$  ( $3.6 \pm 0.2$  nm) as a function of the Burgers vector,  $b$ , and specimen thickness,  $t$ , for a simulated VN particle with radius  $R = 5.3$  nm. See also caption of Fig. 14.

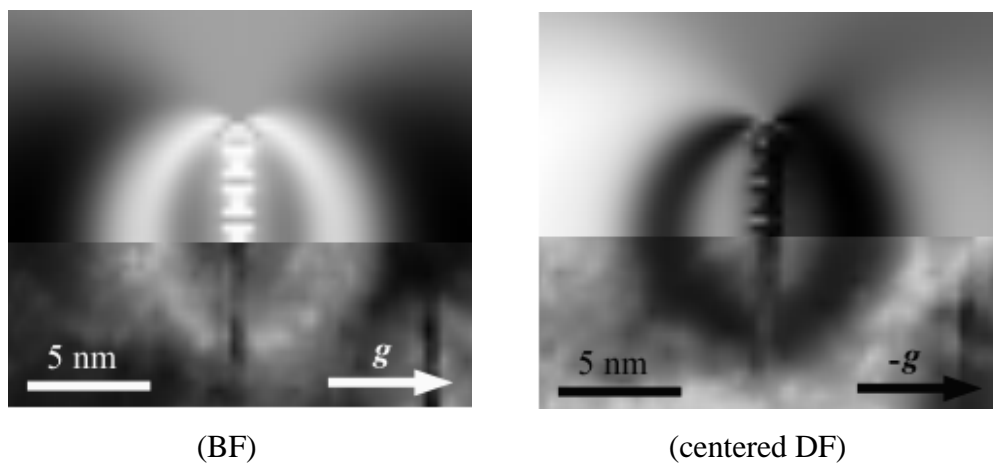


**Fig. 17.** Comparison of experimental (lower part) and simulated (upper part) BF image and  $(200)_{\alpha-Fe}$  centered DF image of particle II. Simulation was carried out for a particle of size  $R = 5.3$  nm and Burgers vector  $b = 0.45$  nm located in the middle of a 62.0 nm thick foil.

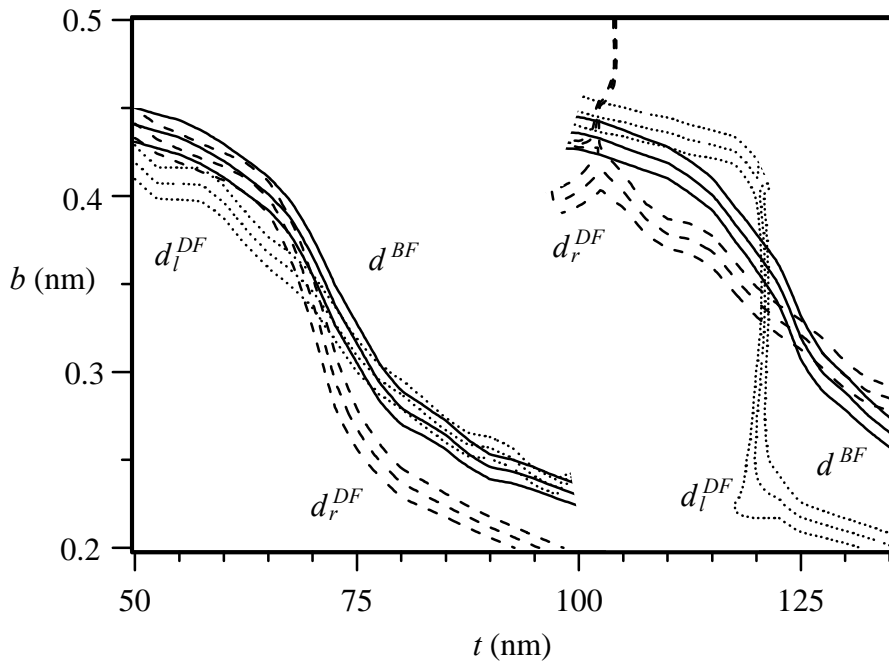


**Fig. 18.** Contour diagram for particle III for the three experimentally measured particle-lobe distances,  $d^{BF}$  ( $4.9 \pm 0.2$  nm),  $d_l^{DF}$  ( $4.5 \pm 0.2$  nm) and  $d_r^{DF}$  ( $4.5 \pm 0.2$  nm) as a function of the Burgers vector  $b$  and specimen thickness  $t$  for a simulated VN particle with radius  $R = 7.5$  nm. See also caption of Fig. 14.

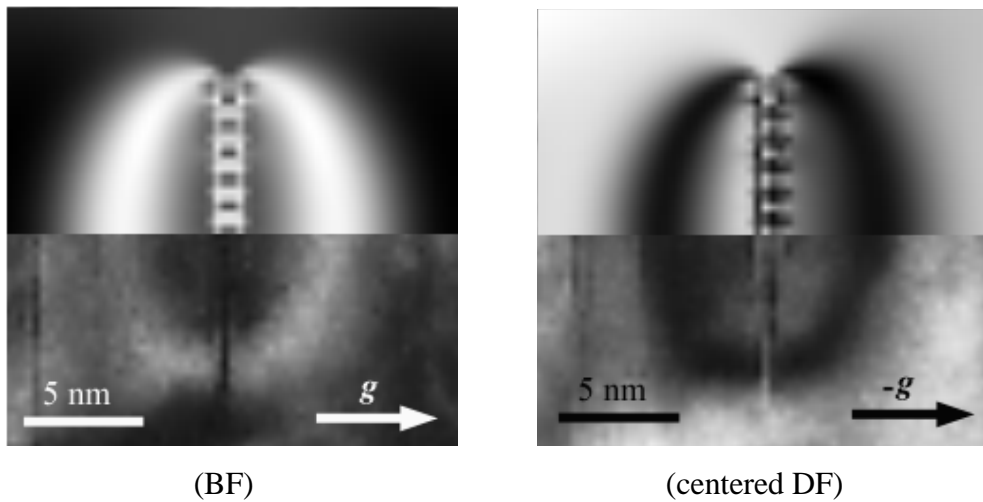


**Fig. 19.** Comparison of experimental (lower part) and simulated (upper part) BF image and  $(200)_{\alpha\text{-Fe}}$  centered DF image of particle III. Simulation was carried out for a particle of size  $R = 7.5$  nm and Burgers vector  $b = 0.35$  nm located in the middle of a 70.0 nm thick foil.

**Table 2:** Burgers vector-length  $b$  and foil thickness  $t$  determined with the fitting procedure for three selected particles of a nitrated Fe-2 at.% V alloy. The specimen/foil thicknesses were also measured locally using the contamination-spot separation method yielding  $t_{cont}$  (see Section 3).  $R$  denotes particle radius.

Particle	$R$	$b$	$t$	$t_{cont}$
	(nm)	(nm)	(nm)	(nm)
I	$9.0 \pm 0.2$	$0.34 \pm 0.02$	$73 \pm 3$	$80 \pm 5$
II	$5.3 \pm 0.2$	$0.45 \pm 0.02$	$61 \pm 3$	$62 \pm 10$
III	$7.5 \pm 0.2$	$0.35 \pm 0.02$	$70 \pm 3$	$67 \pm 10$

## 5. Additional results and discussion

### 5.1 Particle size and visibility of strain contrast

Using  $(200)_{\alpha\text{-Fe}}$  DF images of two different foils prepared from the same specimen nitrated at 913 K, the size distribution of the VN particles was determined; the average VN disc diameter is 13.1 nm, with a standard deviation of 7.6 nm, see Fig. 20. The sizes of the particles investigated detailedly in Section 4 have been indicated. It is concluded that the selected particles are representative for the system investigated.

Similarly the size distribution of the VN particles of specimen nitrated at 853 K was determined. In this case the average VN disc diameter is 5.1 nm, with a standard deviation of 3.6 nm. Specimens nitrated at 793 K contain even smaller VN particles since they could not be made visible in TEM and diffraction contrast lobes could not be detected. This is consistent with the results from the simulations: for particle radii smaller than about 2.5 nm (in a 80 nm thick sample and with a 0.35 nm long Burgers vector) no contrast lobes in the matrix become distinct (see Fig. 5). Even upon nitriding at 853 K contrast lobes can only rarely be observed, although particles with a diameter larger than 5 nm then occur. This may at least partly be ascribed to overlap of displacement fields of neighbouring VN particles. Note that, at constant V content, the number of VN particles per unit of volume is relatively large if the average size of the particles is relatively small.

### 5.2 Platelet thickness

The expected orientation relationship for a VN particle/disc in the  $\alpha\text{-Fe}$  matrix is the so-called Bain orientation relationship [19, 20, 22]

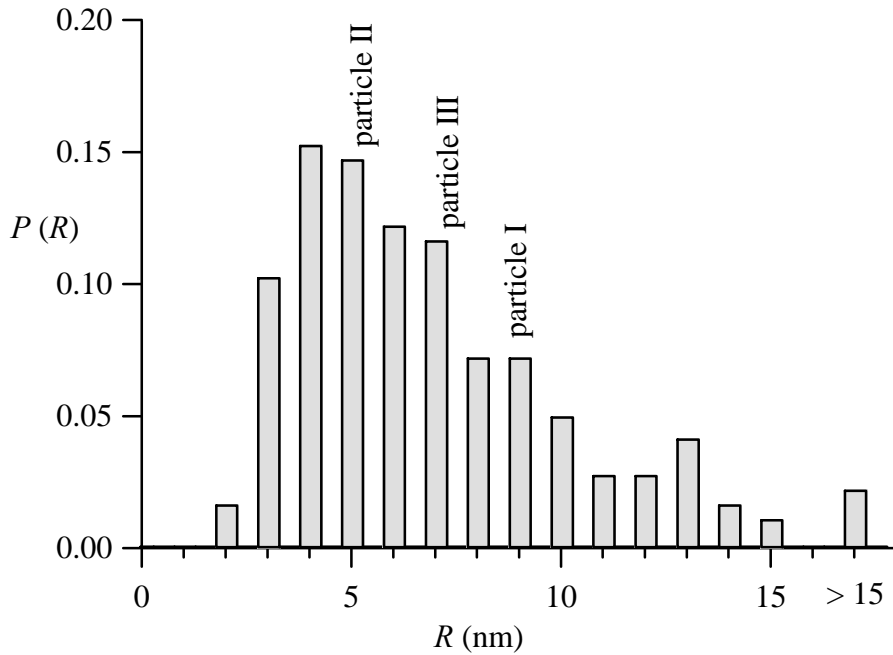


**Fig. 20.** Distribution of VN particle radii after nitriding an Fe-2 at.% V specimen for 25 hours at 913 K at a nitriding potential of  $0.0102 \text{ atm}^{-1/2}$ . Particle radii are measured using  $(200)_{\alpha\text{-Fe}}$  centered DF images of two different specimens. A total amount of 360 particles was considered. Radii of the selected particles I, II and III have been indicated.

$$\{001\}_{\alpha\text{-Fe}} // \{001\}_{\text{VN}}; \langle 100 \rangle_{\alpha\text{-Fe}} // \langle 110 \rangle_{\text{VN}}. \quad (6)$$

The VN particles precipitate as platelets in  $\alpha\text{-Fe}$  because the relative misfit in a direction parallel to the platelet is small (2 %), whereas the relative misfit in the direction perpendicular to the platelet is appreciable (44 %) [22]. The VN platelets consist of a stack of a number of  $\{001\}_{\text{VN}}$  lattice planes parallel with the  $\{001\}_{\alpha\text{-Fe}}$  matrix lattice planes. If it is assumed that a coherent particle-matrix interface occurs such that all misfit is accommodated elastically, it follows from Eq. (3b) that the values of  $b$  obtained for particle I, II and III (see Table 2) correspond to a VN platelet thickness of 1 to 1.4 nm, i.e. about 5 to 7 monolayers of  $\{001\}_{\text{VN}}$  stacked on top of each-other. This value of the thickness agrees very well with the value of 1.4 nm derived from the length of the  $\{200\}_{\text{VN}}$  streaks, as discussed in Section 4.1.

### 5.3 Occurrence of misfit dislocations; lattice plane imaging

For platelets of relatively large thickness it is conceivable that the platelet/matrix misfit can no longer be accommodated fully elastically. If the misfit exceeds a critical

value, it is energetically more favourable to introduce (misfit) dislocations. Then Eqs. (3a) and (3b) do no longer hold and the true particle thickness is larger than derived from the particle-lobe distances using the procedure discussed and used in Section 4.

Evidence for the occurrence of a few misfit dislocations was obtained for relatively large VN precipitates using High Resolution Electron Microscopy (HREM). Contrast of both the  $(110)_{\alpha\text{-Fe}}$  fringes in the matrix and the  $(111)_{\text{VN}}$  fringes in the platelets is shown for a relatively large VN platelet (16 nm long) in  $\alpha\text{-Fe}$  in Fig. 21. Misfit dislocations are revealed near the platelet-matrix interface at the extremities of the projected platelet (see arrows in figure). Note that only a component of  $\mathbf{b}$  in the  $[110]_{\alpha\text{-Fe}}$  direction is directly revealed in the image.

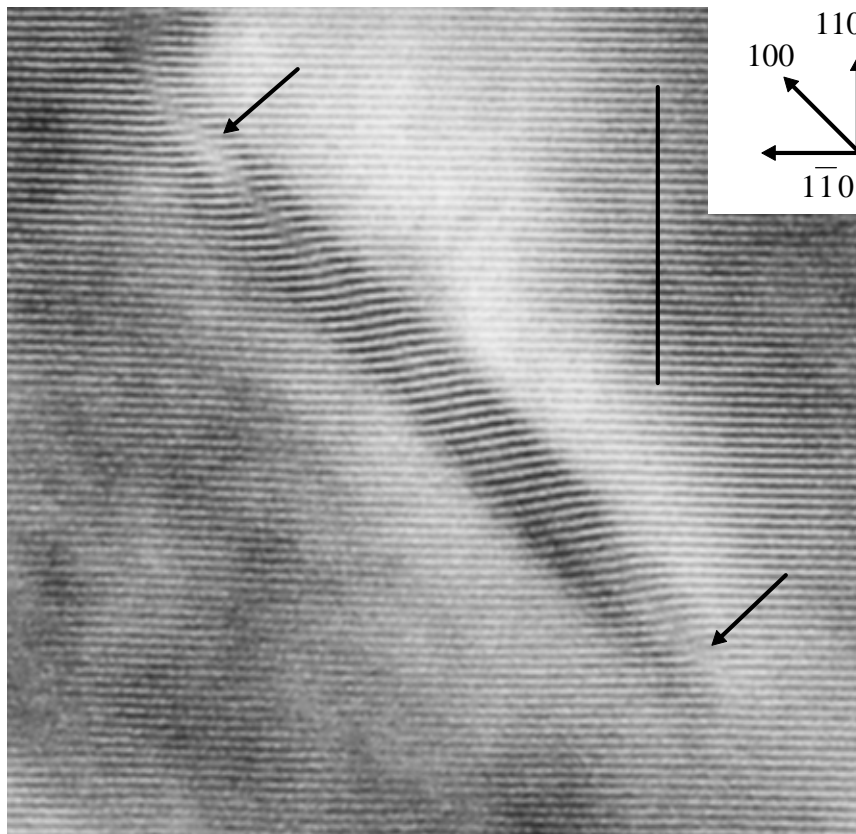


**Fig. 21.** High Resolution Electron Microscopy (HREM) image of an Fe-2 at.% V specimen, nitrided for 25 hours at 913 K at a nitriding potential of  $0.0102 \text{ atm}^{-1/2}$ , and showing the  $(110)$  Fe lattice fringes and the  $(111)$  VN lattice fringes. The electron beam direction was a few degrees away from the  $[001]_{\alpha\text{-Fe}}$  zone axis. The objective aperture included the first order reflections and the transmitted beam. The arrows indicate the locations of two misfit dislocations. The vertical bar corresponds to 6 nm.

#### 5.4 X-ray diffraction line-shift and -broadening

The  $\{222\}_{\alpha\text{-Fe}}$  diffraction line profiles of an unnitrided specimen and of specimens nitrided at 793 K, 853 K and 913 K are presented in Fig. 22 (note the logarithmic intensity scale). Upon nitriding a strong asymmetrical line broadening takes place: the peak maximum shifts appreciably from the peak position of the line profile of the unnitrided specimen and asymmetrical, distinct tails appear. The tail at the high angle side is more pronounced than the one at the low angle side. This type of line broadening is typical for the case of small coherent inclusions in a matrix with elastic accommodation of the misfit [23-27]. Only in case of the specimen nitrided at 913 K a separate  $\{200\}_{\text{VN}}^{\text{XRD}}$  reflection could be observed (near  $43.7^\circ 2\theta$ ), in accordance with the presence of elongated  $\{200\}_{\text{VN}}^{\text{TEM}}$  spots in the selected area diffraction pattern of Fig. 9c.

The shape and the width of the measured line profiles are interpreted now considering their Fourier transforms. In order to remove the broadening due to the wavelength distribution and the instrumental aberrations the  $\{533\}$  line profile of a

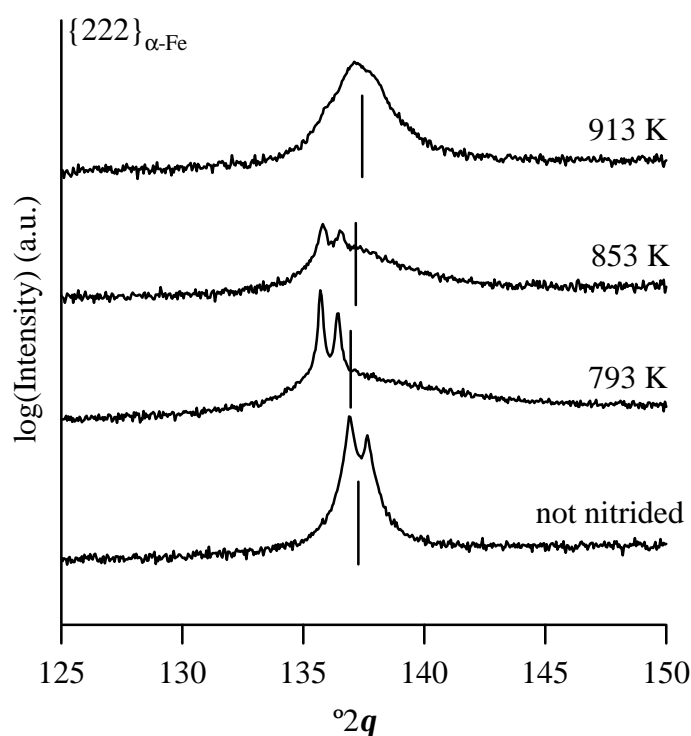


**Fig. 22a.** X-Ray diffraction line profiles recorded for the  $\{222\}_{\alpha\text{-Fe}}$  reflection of different Fe-2 at.% V samples nitrided for 25 hours at 793 K, 853 K or 913 K at a nitriding potential of  $0.0102 \text{ atm}^{-1/2}$  and of a not-nitrided reference sample. Vertical bars indicate the centroid positions of the respective line profiles; see also Table 3.

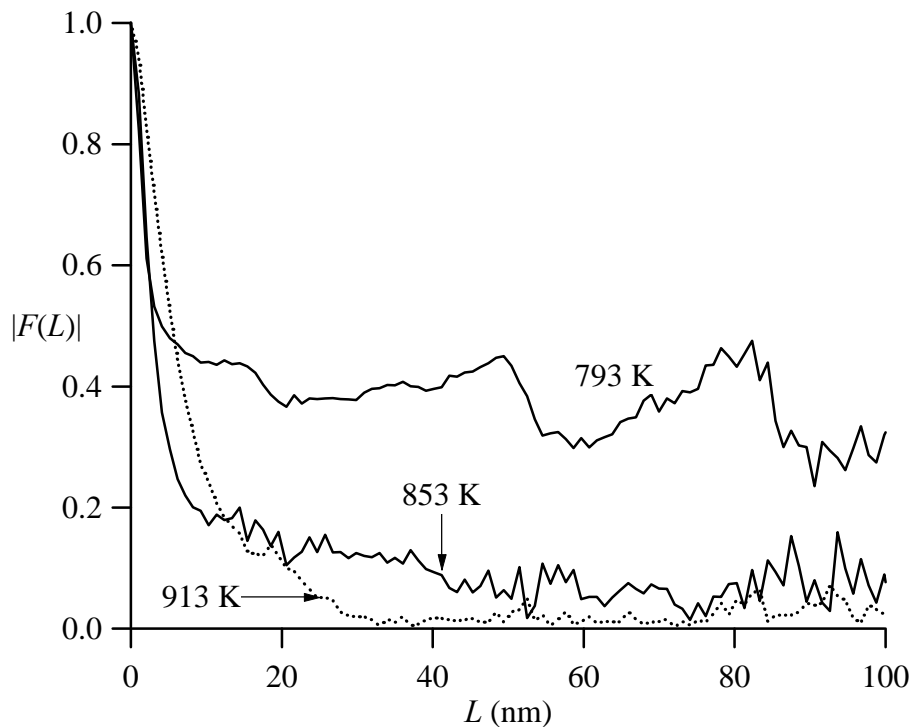


**Fig. 22b.** Modulus of the Fourier transforms of the only structurally broadened  $\{222\}_{\alpha\text{-Fe}}$  reflections of different Fe-2 at.% V samples, nitrided for 25 hours at 793 K, 853 K or 913 K at a nitriding potential of  $0.0102 \text{ atm}^{-1/2}$ .

specially made strain free Si-powder sample [28], with a peak position close to the peak position of the  $\{222\}_{\alpha\text{-Fe}}$  line profile, was used to deconvolute the line profiles measured [4]. The results, in terms of the Fourier transform,  $F(L)$ , with  $L$  as a correlation distance, of the only structurally broadened line profiles, are presented in Fig. 22b. In case of the Fourier transform of the specimen nitrided at 793 K  $F(L)$  decreases for short correlation lengths ( $0 < L < 10 \text{ nm}$  to  $15 \text{ nm}$ ) to a more or less constant value<sup>10</sup>. This more or less constant level of the Fourier transform is equivalent to the presence of a sharp Bragg-like peak in the intensity distribution (cf. Fig. 22a) [31]. This observation is interpreted such that in the specimen nitrided at 793 K (and possibly also in the one nitrided at 853 K) apparently, the lattice distortions brought about by the misfitting particles do not disturb the phase relation between atoms at large correlation distances. In case of the specimen nitrided at 913 K such a non-zero constant level for the Fourier transform of the line profile is not observed: the phase relations between atoms separated by a distance  $L > 30 \text{ nm}$  have become

<sup>10</sup> The more or less periodic ripple observed for  $F(L)$  nitrided at 793 K at approximately  $L = 16, 48$  and  $80 \text{ nm}$  and the slight decrease upon increasing  $L$  for the plateau level of  $F(L)$  for the specimens nitrided at 793 K and 853 K can be ascribed fully to minor shape differences of the instrumental  $\{533\}_{\text{Si}}$  line profile and the  $\{222\}_{\alpha\text{-Fe}}$  line profile due to counting statistics and different measurement conditions (step size and slit size) (see discussion in Refs. 29 and 30).

totally uncorrelated. It has been suggested that this effect occurs for lengths of  $L$  encompassing 2 to 3 interparticle distances [25]. Indeed, it follows from Figs. 9a and 9b in case of the specimen nitrided at 913 K that a distance of 30 nm includes approximately 2 to 3 particles.

The centroid positions of the  $\{222\}_{\alpha\text{-Fe}}$  line profiles, measured for an unnitrided specimen and specimens nitrided at 793 K, 853 K and 913 K, were determined, see Fig. 22a and Table 3. The line profile centroids are shifted towards the low angle side with respect to centroid of the unnitrided specimen; the centroid shifts of the nitrided specimens increase for decreasing nitriding temperature. The following causes for the line profile centroid shifts can be considered.

**Table 3:** Centroids of  $\{222\}_{\alpha\text{-Fe}}$  line profiles,  $1/d_c^{\{222\}}$  or  $2q_c$ , of an unnitrided specimen and specimens nitrided at 793 K, 853 K or 913 K. The centroids were calculated on a  $1/d$ -scale.

Specimens	unnitrided	793 K	853 K	913 K
$1/d_c^{\{222\}}$ (nm <sup>-1</sup> )	12.081	12.067	12.076	12.087
$2q_c$	137.28	136.96	137.18	137.44

Firstly, V depletion of the matrix due to precipitation of the substitutionally dissolved V as VN induces a temperature independent centroid shift. Using Vegard's law [32] and the lattice constant of V,  $a_V = 0.30232$  nm [12], a centroid shift upon precipitation is determined towards the high angle side, which is not observed implying that this effect does not dominate the occurring centroid shift.

Secondly, interstitially dissolved N in the matrix after precipitation leads to centroid shifts that can be shown to be much smaller than the observed ones.

Thirdly, following a model described in Ref. [22], a positive hydrostatic strain emerges upon precipitation of VN in the  $\alpha$ -Fe matrix as a consequence of the elastic accommodation of the precipitate/matrix misfit, which causes the centroid to shift towards the low angle side, as observed. The model assumes the presence of (i) misfitting VN platelets in a *finite*  $\alpha$ -Fe-matrix and of (ii) extra (excess) N atoms adsorbed (and located in octahedral interstices) at the interface of the VN precipitates and the  $\alpha$ -Fe-matrix. The extra N atoms effectively enlarge the misfit of the VN precipitates with respect to the  $\alpha$ -Fe-matrix. The amount of excess N adsorbed at the platelet/matrix interface has been derived from mass measurements before and after the nitriding; these amounts decreased for increasing nitriding temperatures [22]. Then the centroid shift towards lower diffraction angles would decrease for increasing



nitriding temperature, which agrees with the present experimental observation. A quantitative assessment cannot be made as the matrix should diffract fully independently from the VN particles, which, especially for the relatively low nitriding temperatures, appears not to be the case (see above).

## 6. Conclusions

### *Diffraction contrast simulation model*

- The strain field surrounding misfitting inclusions can be characterized quantitatively comparing simulated and measured *full* diffraction-contrast Transmission Electron Microscopy (TEM) images.
- The misfit, as indicated by a "particle Burgers vector", for disc shaped inclusions/precipitates, can be determined unambiguously from the contrast lobes widths ("image widths") as measured in both bright field and dark field.
- For determination of the particle Burgers vector diffraction-contrast image simulations can be based on a system of a single particle in an infinite matrix, as the inner parts of the contrast images are practically unaffected by the presence of neighbouring particles.

### *Misfitting VN particles in $\alpha$ -Fe matrix*

- Upon nitriding of an Fe-2 at.%V alloy small misfitting VN platelets are formed along  $\{001\}_{\alpha\text{-Fe}}$  with  $\{001\}_{\text{VN}}$  parallel to  $\{001\}_{\alpha\text{-Fe}}$ . The platelet/disc radius increases with increasing nitriding temperature from a few nanometers after nitriding at 793 K to  $13 \pm 7$  nm after nitriding at 913 K. After nitriding at 913 K the platelet thickness equals about 1 to 1.4 nm as indicated by both the diffraction strain contrast (simulations) and the extent of the VN precipitate diffraction streaks. The misfit is largely accommodated elastically; only a few misfit dislocations were observed in High Resolution Electron Microscopy images for only the larger VN precipitates
- The observed diffraction contrast images after nitriding at 913 K could be simulated well using the diffraction and strain models.
- On the basis of the contrast lobe widths in bright field and dark field combinations of possible values for the "Burgers vector of the particle",  $b$ , and the thickness of the foil,  $t$ , were obtained. Selection of the correct combination of  $b$  and  $t$  was possible by comparing the full simulated and experimental diffraction-contrast images. The fitted value of the local foil thickness agrees well with the value determined directly by the contamination-spot method at the location of the precipitate.

- The observed shifts and broadenings of the XRD profiles support the results obtained using TEM.

### *Acknowledgements*

This work has been part of the research program of the Foundation for Fundamental Research on Matter (Stichting FOM), The Netherlands. The authors are indebted to Ing. N. Geerlofs for the provision of the nitrating equipment, to Mr. T.R. de Kruijff for assistance with the TEM specimen preparation, to Dr. K.G.F. Janssens for the provision of the SIMCON-simulation program and finally to Dr. R. Delhez for stimulating discussions.

### *Appendix*

#### *Rearrangement of Howie-Whelan equations for a four beam case*

Analogous to the procedure given in Ref. [7] for a two beam case, each amplitude  $\Phi_{g_j}$  of the (four) coupled differential equations of Eq. (1) is multiplied by an additional phase factor such that the term  $(\mathbf{g}_j - \mathbf{g}_k) \cdot \mathbf{u}$  arises only once in every differential equation. This leaves the intensity of each beam at the bottom of the specimen unaffected because any additional phase factor cancels out when the amplitudes are multiplied by their complex conjugates, but the numerical integration of Eq. (1) is accelerated greatly.

The new amplitude equations are written as

$$\frac{d}{dz} \mathbf{F} = A \mathbf{F} \quad (\text{A. 1})$$

where  $\mathbf{F}$  is a column vector containing the real and imaginary parts of the opening beams

$$\mathbf{F} = \begin{bmatrix} \Phi_{-g}^{\text{Re}} \\ \Phi_{-g}^{\text{Im}} \\ \Phi_0^{\text{Re}} \\ \Phi_0^{\text{Im}} \\ \Phi_g^{\text{Re}} \\ \Phi_g^{\text{Im}} \\ \Phi_{2g}^{\text{Re}} \\ \Phi_{2g}^{\text{Im}} \end{bmatrix} \quad (\text{A. 2})$$

and where  $A$  is an 8 by 8 matrix describing the phase relations between the real and imaginary parts of the four beams

$$A = \begin{bmatrix} -n & -2w + 2pb_1 & -a_1 & -1 & -a_2 & -r_2 & -a_3 & -r_3 \\ 2w - 2pb_1 & -n & 1 & -a_1 & r_2 & -a_2 & r_3 & -a_3 \\ -a_1 & -1 & -n & 0 & -a_1 & -a & -a_2 & -r_2 \\ a & -a_1 & 0 & -n & 1 & -a_1 & r_2 & -a_2 \\ -a_2 & -r_2 & -a_1 & -1 & -n & -2pb_3 & -a_1 & -1 \\ r_2 & -a_2 & 1 & -a_1 & 2pb_3 & -n & 1 & -a_1 \\ -a_3 & -r_3 & -a_2 & -r_2 & -a_1 & -1 & -n & -2w - 4pb_4 \\ r_3 & -a_3 & r_2 & -a_2 & 1 & -a_1 & 2w + 4pb_4 & -n \end{bmatrix} \quad (\text{A. 3})$$

The symbols in the above  $A$  matrix represent the following. The deviation of the Bragg position of the beams  $-g$  and  $2g$  is indicated by the deviation parameter  $w$

$$w = s\mathbf{x}_g \quad (\text{A. 4})$$

with  $s$  according to Eq. (2) in Section 2.1.1. The influence of the displacement field of the misfitting particle is represented by  $\mathbf{b}_i$ , defined as

$$\mathbf{b}_i = \frac{d}{dz} \mathbf{g}_i \cdot \mathbf{u} \quad (\text{A. 5})$$

with  $\mathbf{g}_i$  one of the beams considered,  $\mathbf{g}_i = -\mathbf{g}, \mathbf{0}, \mathbf{g}$  or  $2\mathbf{g}$  for  $i = 1, 2, 3$  or  $4$ , and  $\mathbf{u}$  the displacement field as described in Section 2.2.3. Absorption effects were incorporated into Eq. (1) by replacing  $1/\mathbf{x}_g$  by  $1/\mathbf{x}_g + i/\mathbf{x}'_g$  where  $\mathbf{g} = \mathbf{g}_j - \mathbf{g}_k$ . They are subdivided into normal absorption effects, described by  $n$ , and anomalous absorption effects,

described by  $a_1$ ,  $a_2$  and  $a_3$ . The ratios between the extinction distances used are given by  $r_1$ ,  $r_2$  and  $r_3$ :

$$\begin{aligned}
 n &= \frac{\mathbf{X}_g}{\mathbf{X}_0} \\
 a_1 &= \frac{\mathbf{X}_g}{\mathbf{X}_g}, \quad a_2 = \frac{\mathbf{X}_g}{\mathbf{X}_{2g}}, \quad a_3 = \frac{\mathbf{X}_g}{\mathbf{X}_{3g}} \\
 r_1 &= \frac{\mathbf{X}_g}{\mathbf{X}_g} = 1, \quad r_2 = \frac{\mathbf{X}_g}{\mathbf{X}_{2g}}, \quad r_3 = \frac{\mathbf{X}_g}{\mathbf{X}_{3g}}
 \end{aligned}
 \tag{A. 6}$$

## References

- [1] G.E. Dieter, Mechanical Metallurgy, McGraw-Hill, Singapore, 1987.
- [2] M.F. Ashby and L.M. Brown, Phil. Mag. **8** (1963), 1083.
- [3] M.F. Ashby and L.M. Brown, Phil. Mag. **8**, (1963), 1649.
- [4] E.J. Mittemeijer, P. van Mourik, Th.H. de Keijser, Phil. Mag. **A43** (5), (1981), 1157.
- [5] J.G.M. van Berkum, R. Delhez, Th.H. de Keijser, E.J. Mittemeijer, P. van Mourik, Scripta Metall. et Mater. **25**, (1991), 2255.
- [6] A. Howie, M.J. Whelan, Proc. Roy. Soc. A **263** (1961), 217.
- [7] P.B. Hirsch, A. Howie, R.B. Nicholson, D.W. Pashley, Electron microscopy of thin crystals, Butterworths, London, 1967.
- [8] J.D. Eshelby, Proc. Roy. Soc. A **241** (1957) 376.
- [9] K.G.F. Janssens, Localized strain characterization using electron diffraction contrast imaging, Ph.D. thesis, KU Leuven, 1995.
- [10] W.H. Press, S.A. Teukolsky, W.T. Vetterling, B.P. Flannery, Numerical Recipes in Fortran, Cambridge University Press, 1986.
- [11] P. Stadelmann, Ecole Polytechnique Fédérale de Lausanne, EMS OnLine, "http://cimesg1.epfle.ch/EMS/", 05-09-1997.
- [12] Powder Diffraction File, International Centre for Diffraction Data, Swarthmore, PA, 1988.
- [13] H. Hashimoto, A. Howie, M.J. Whelan, Phil. Mag. **5** (1960), 967.
- [14] H. Hashimoto, A. Howie, M.J. Whelan, Proc. Roy. Soc. A **269** (1962) 80.
- [15] K. Kawamura, J. Japan Inst. Metals **24** (1960), 710.
- [16] E.J. Mittemeijer, J.T. Slycke, Härterei Tech. Mit. **50** (1995), 2.
- [17] M.H. Biglari, C.M. Brakman, E.J. Mittemeijer, Phil. Mag. A **72** (5) (1995), 1281.
- [18] D.B. Williams, C.B. Carter, Transmission Electron Microscopy, a Textbook for Materials Science, Plenum Press, New York, 1996.
- [19] M. Pope, P. Grieveson, K.H. Jack, Scan. J. of Metallurgy **2**, (1973), 29.
- [20] M.M. Yang, A.D. Krawitz, Metall. Trans. A. **15A** (1984), 1545.
- [21] B.E. Warren, X-Ray Diffraction, Reading, Massachusetts: Addison-Wesley, 1969.

- 
- [22] M.A.J. Somers, R.M. Lankreijer, E.J. Mittemeijer, *Phil. Mag. A* **59**, (1989), 353.
- [23] M.A. Krivoglaz, *X-Ray and Neutron Diffraction in Nonideal Crystals*, Springer, Berlin, 1996.
- [24] C.R. Houska, *Acta Cryst.* **A49**, (1993), 771.
- [25] R. Kuzel, B. He, C.R. Houska, *J. Mat. Sci.* **32** (1997), 2451.
- [26] T.C. Bor, R. Delhez, E.J. Mittemeijer, E. Van der Giessen, to be published (Chapters 2 and 3).
- [27] L. Velterop, R. Delhez, Th.H. de Keijser, E.J. Mittemeijer, to be published.
- [28] J.G.M. van Berkum, G.J.M. Sprong, Th.H. de Keijser, R. Delhez, E.J. Sonneveld, *Powder Diffraction* **10** (2), (1991), 129.
- [29] T.C. Bor, M.C. Huisman, R. Delhez, E.J. Mittemeijer, *Mat. Sci. For.* **278-281** (1998), 145.
- [30] T.C. Bor, M.C. Huisman, J.-D. Kamminga, E.J. Mittemeijer, E. Van der Giessen, to be published (Chapter 6)
- [31] R.N. Bracewell, *The Fourier Transform and its Applications*, McGraw-Hill, Tokyo, 1978.
- [32] J.W. Christian, *The Theory of Transformations in Metals and Alloys*, Pergamon, Oxford, 1965.



## Chapter 5

# A Method to Determine the Volume Fraction of a Separate Component in a Diffracting Volume

T.C. Bor<sup>1</sup>, M.C. Huisman<sup>2</sup>, R. Delhez<sup>1</sup> and E.J. Mittemeijer<sup>1, 3</sup>

<sup>1</sup>Laboratory of Materials Science, Delft University of Technology,  
Rotterdamseweg 137, 2628 AL Delft, The Netherlands

<sup>2</sup>Faculty of Sciences, Division of Physics and Astronomy,  
vrije Universiteit Amsterdam

De Boelelaan 1081, 1081 HV Amsterdam, The Netherlands

<sup>3</sup>Max Planck Institute for Metals Research,  
Seestraße 92, 70174 Stuttgart, Germany

### *Abstract*

An (X-ray) diffraction line-profile analysis method has been proposed to determine the volume fraction of a component with a “homogeneous” microstructure that forms part of a sample that is, overall, microstructurally non-homogeneous. The method is based on deconvolution of a measured line profile of the sample to be analysed with a line profile separately measured from material that is microstructurally identical to the homogeneous component in the mixture. Consequences of counting statistical variations for the application of the method have been analysed. The method has been applied to ball milled Mo powder to determine the volume fraction of the undeformed powder present in the ball-milled powder.

### *1. Introduction*

The analysis of X-ray diffraction (XRD) line broadening enables the determination of quantities such as the “size” of and the “microstrain” within the crystallites contained in the diffracting volume [1]. The results of an XRD measurement have to be interpreted as a volume weighted average of these quantities over the diffracting crystallites in the volume irradiated. Hence, straightforward interpretation of the broadening of XRD line profiles measured from microstructurally *non-homogeneous* materials is impossible. However, if one separate microstructurally *homogeneous* component can be identified in this non-homogeneous diffracting volume, the volume fraction of the homogeneous component and the line broadening due to only the

remaining material in the diffracting volume can be determined. To this end a deconvolution method is presented here. The effect of counting statistics is analysed quantitatively, leading to a procedure for application of the method proposed.

The diffraction analysis of an initial stage of the deformation process of Mo powder in a ball mill will be given as an example for the procedure proposed.

## 2. Theoretical basis

The result of an XRD measurement can be given in the form of a line profile: i.e. the measured diffracted intensity  $I$  as a function of the diffraction angle  $2\mathbf{q}$  or the length of the diffraction vector. A measured line profile ( $h$ -profile) can be described as the convolution of the structural line profile ( $f$ -profile) with the instrumental line profile ( $g$ -profile). Convolution of two functions in real space is equivalent to the multiplication of their respective Fourier transforms in Fourier (reciprocal) space [2]. The Discrete Fourier Transform (DFT) of a function  $h(t)$  given by  $N$  equidistant sample values ( $t = 0, 1, 2, \dots, (N-1)$ ) is given by:

$$H(n) = \sum_{t=0}^{N-1} h(t) \exp(2\pi i n t / N), \quad (1)$$

where  $n$  denotes the harmonic number,  $n = 0, 1, 2, \dots, (N - 1)$ , and  $N$  can be written as  $p/Dt$ , with  $Dt$  as the sampling distance in real space and  $p$  as the period of the function in real space.

Consider the situation in which a separate component  $A$  can be identified in the total *diffracting* volume composed of (homogeneous) component  $A$  and the rest of the (inhomogeneous) diffracting volume, component  $B$ . According to the kinematical diffraction theory the total intensity diffracted by a volume of material for a  $\{HKL\}$  reflection,  $I_{tot}^{HKL}(2\mathbf{q})$ , is equal to the sum of the diffracted  $\{HKL\}$  intensities from the individually (i.e. incoherently) diffracting crystallites. Hence,  $I_{tot}^{HKL}(2\mathbf{q})$  can be written as the volume weighted sum of the intensity diffracted by crystallites belonging to component  $A$ ,  $I_A^{HKL}(2\mathbf{q})$ , and the intensity diffracted by crystallites belonging to component  $B$ ,  $I_B^{HKL}(2\mathbf{q})$ :

$$I_{tot}^{HKL}(2\mathbf{q}) = \mathbf{a} I_A^{HKL}(2\mathbf{q}) + (1 - \mathbf{a}) I_B^{HKL}(2\mathbf{q}), \quad (2)$$

where  $\mathbf{a}$  denotes the volume fraction of diffracting crystallites of component  $A$ .



Using the additivity of DFT's, it follows from Eq. (2):

$$H_{tot}^{HKL}(n) = \mathbf{a} H_A^{HKL}(n) + (1 - \mathbf{a}) H_B^{HKL}(n), \quad (3)$$

where  $H_{tot}^{HKL}(n)$ ,  $H_A^{HKL}(n)$  and  $H_B^{HKL}(n)$  are the DFT's of the corresponding line profiles, normalised such that  $H_{tot}^{HKL}(0) = H_A^{HKL}(0) = H_B^{HKL}(0) = 1$ .

Now, to determine  $\mathbf{a}$  and  $I_B^{HKL}(2\mathbf{q})$ , it will be supposed that  $I_A^{HKL}(2\mathbf{q})$  can be recorded from a material that has a microstructure identical to that of component  $A$  in the sample to be analysed. For this line profile, to be denoted by  $I_s^{HKL}(2\mathbf{q})$ , it thus holds:

$$I_s^{HKL}(2\mathbf{q}) = I_A^{HKL}(2\mathbf{q}) \text{ and } H_s^{HKL}(n) = H_A^{HKL}(n). \quad (4)$$

Deconvolution of  $I_{tot}^{HKL}(2\mathbf{q})$  with  $I_s^{HKL}(2\mathbf{q})$  can be carried out according to:

$$D^{HKL}(n) \equiv A_D^{HKL}(n) + iB_D^{HKL}(n) \equiv \frac{H_{tot}^{HKL}(n)}{H_s^{HKL}(n)} = \mathbf{a} + (1 - \mathbf{a}) \frac{H_B^{HKL}(n)}{H_A^{HKL}(n)}, \quad (5)$$

with  $D^{HKL}(0) = 1$ ;  $A_D^{HKL}(n)$  and  $B_D^{HKL}(n)$  represent the real and the imaginary parts of  $D^{HKL}(n)$ .

Note that the line profile  $I_s^{HKL}(2\mathbf{q})$ , acting as a "g-profile" in the deconvolution, need not have as little structural broadening as possible. If the line profile resulting from the crystallites belonging to component  $A$  is less broad on a  $2\mathbf{q}$  axis than the line profile resulting from the rest of the crystallites, i.e. component  $B$ , then the second term at the right-hand side of Eq. (5) vanishes for sufficiently large  $n$ . Then  $D^{HKL}(n)$  becomes equal to  $\mathbf{a}$ . Thereby not only the volume fraction  $\mathbf{a}$  of component  $A$  can be determined in principle, but subsequently  $H_B^{HKL}(n)$  (and  $I_B^{HKL}(2\mathbf{q})$ ) can be obtained as well. Obviously, as in "normal" deconvolution procedures (cf. Ref. 3), the accuracy in the values obtained for the desired parameters, here  $\mathbf{a}$  (and  $H_B^{HKL}(n)$ ), is strongly determined by counting statistical variations in the values of  $H_{tot}^{HKL}(n)$  and  $H_s^{HKL}(n)$ . This effect will be discussed in section 4.

### 3. Experimental

Mo powder (Alpha, 99.9 wt-% pure, almost spherical particles with diameter 1 - 7  $\mu\text{m}$ ) was ball milled in vacuum for 30 minutes in a low energy ball mill. This ball mill

is an evacuated vibrating cylindrical vessel with a bottom plate of WC - whereupon the Mo powder is deposited - and that contains a ferritic stainless steel ball. Scanning Electron Microscopy analysis (see [4] for more experimental details and results) of undeformed starting powder (further denoted  $Mo_0$ ) and deformed powder (further denoted  $Mo_{30}$ ) suggested, from the shape of the powder particles, that the  $Mo_{30}$  powder consists of deformed (crushed) particles as well as undeformed particles ( $Mo_0$ ).

To enable a study of the kinetics of the deformation process of Mo in the ball mill it is imperative to determine the volume fraction of the remaining undeformed component as function of ball milling parameters. To this end the procedure proposed in section 2 was applied where the undeformed component is taken as component  $A$ . Small volumes of the  $Mo_0$  powder and of the  $Mo_{30}$  powder were deposited onto Si $\langle 510 \rangle$ -single crystal wafers to enable XRD-measurements [5]. These measurements were performed on a Siemens F- $\omega$  diffractometer equipped with a curved graphite monochromator in the diffracted beam. From both specimens the  $\{110\}$  reflections were measured in the same way using Cu-K $\alpha$  radiation within the  $2\theta$ -range  $32.5^\circ 2q$  to  $51.0^\circ 2q$  using a  $0.01^\circ 2q$  stepsize and a 2 (s) counting time. Each specimen was measured five times consecutively to study the reproducibility of the measurements and the influence of counting statistical errors.

#### 4. Results and discussion

The as-measured line profiles corresponding to the  $\{110\}$ -reflections of both the  $Mo_0$  specimen and the  $Mo_{30}$  specimen are shown in Fig. 1. The line profiles have been normalised by division by their integral intensities. Clearly, the  $\{110\}$  line profile of the  $Mo_{30}$  powder is broader than that of the  $Mo_0$  powder (see in particular the lower intensity maxima for the  $Mo_{30}$  powder).

A linear background determined by a least-squares fit through the first and last 5 % of the data points was subtracted from the line profiles measured. Identifying the  $\{110\}$  profile of the  $Mo_{30}$  powder as  $I_{tot}^{HKL}(2q)$  and the  $\{110\}$  profile of the  $Mo_0$  powder as  $I_s^{HKL}(2q)$ , Eq. (5) was applied. To avoid effects on  $A^{110}(n)$  and  $B^{110}(n)$  due to non-coincidence of centroid and origin of the abscissa in real space, the modulus of  $D^{110}(n)$ ,  $|D^{110}(n)|$ , is considered (Fig. 2a).

From Fig. 2a it follows that with increasing value of the harmonic number  $n$ ,  $|D^{110}(n)|$  decreases from  $|D^{110}(n)| = 1$  to a more or less constant value of approximately  $a = 0.76$  for  $150 \leq n \leq 220$ , indicating that the ball milled powder contains a certain volume fraction of undeformed particles. For still higher values of  $n$ ,  $|D^{110}(n)|$  starts to

oscillate severely and  $\mathbf{a}$ -determination is impossible. This effect can be ascribed to counting statistics as discussed next.

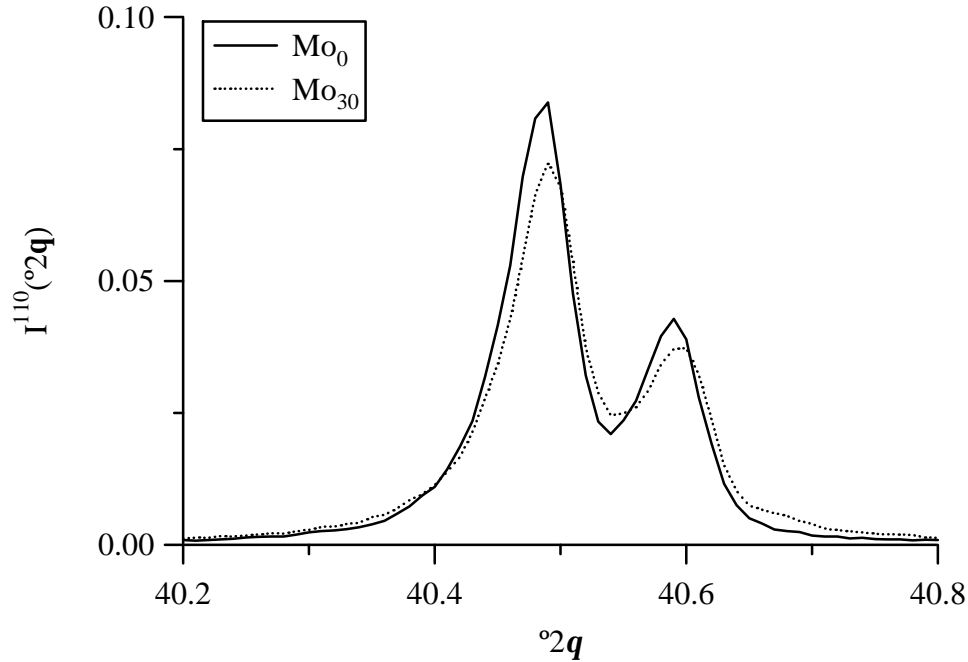


**Fig. 1.** Part of the Cu-K $\alpha$  {110} line profiles recorded from the Mo<sub>0</sub> and Mo<sub>30</sub> powders. No background correction has been applied; both line profiles have been normalised by division of the intensity values by the corresponding integral intensities.

To obtain an indication of the influence of counting statistical errors on the  $|D^{110}(n)|$ -curve results given in Refs. 3 and 6 for the counting statistical variance of deconvoluted Fourier coefficients, here  $\mathbf{s}^2(A_{|D|})$  and  $\mathbf{s}^2(B_{|D|})$ , can be used. Neglecting the covariances, it follows:

$$\mathbf{s}^2(|D(n)|) = \left( \frac{A_{|D|}(n)}{|D(n)|} \right)^2 \mathbf{s}^2(A_{|D|}) + \left( \frac{B_{|D|}(n)}{|D(n)|} \right)^2 \mathbf{s}^2(B_{|D|}). \quad (6)$$

The standard deviations  $\mathbf{s}(|D^{110}(n)|)$  calculated using this equation are shown in Fig. 2b. Obviously the standard deviations increase with increasing  $n$ , but only beyond  $n \approx 400$   $\mathbf{s}(|D^{110}(n)|)$  becomes really large, i.e. of the same magnitude as  $|D^{110}(n)|$  itself (cf. Fig 2a and 2b). This supports the above interpretation that the oscillations in  $|D^{110}(n)|$  for  $n > 400$  are caused by counting statistics. Further, it is remarkable that the standard deviation appears to show a periodic occurrence of maxima (see at  $n \approx 90 - 100$ ,  $260 - 280$  and  $430 - 470$  in Fig. 2b). The maxima are caused by small differences

between the  $I_A^{110}(2\mathbf{q})$  component profile of the  $I_{tot}^{110}(2\mathbf{q})$  line profile, and the separately measured  $I_s^{110}(2\mathbf{q})$  profile, due to occurrence of counting statistical variations in the intensity values. In the absence of counting statistics both profiles would be equal, as implied by Eq. (4). The shape differences are most pronounced at  $2\mathbf{q}$  locations where the intensities are large, i.e. at and around peak maxima. Consequently the  $\mathbf{Ka}_1$ - $\mathbf{Ka}_2$  doublet nature reveals itself in the occurrences of periodic maxima in  $\mathbf{s}(|D^{110}(n)|)$  as will be shown below (see also Ref. 7).

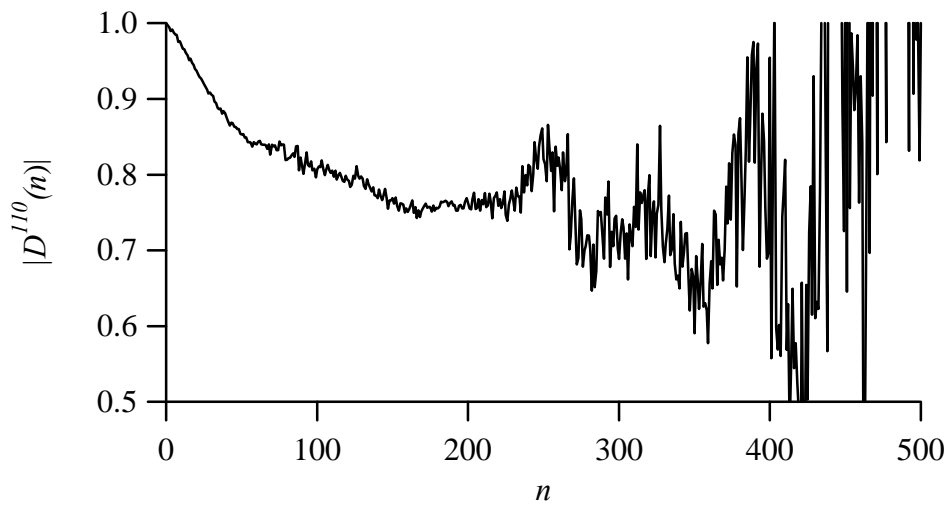


**Fig. 2a.** The modulus of  $D^{110}(n)$  (cf. Eq. (5)) as obtained from the profiles shown in Fig. 1.

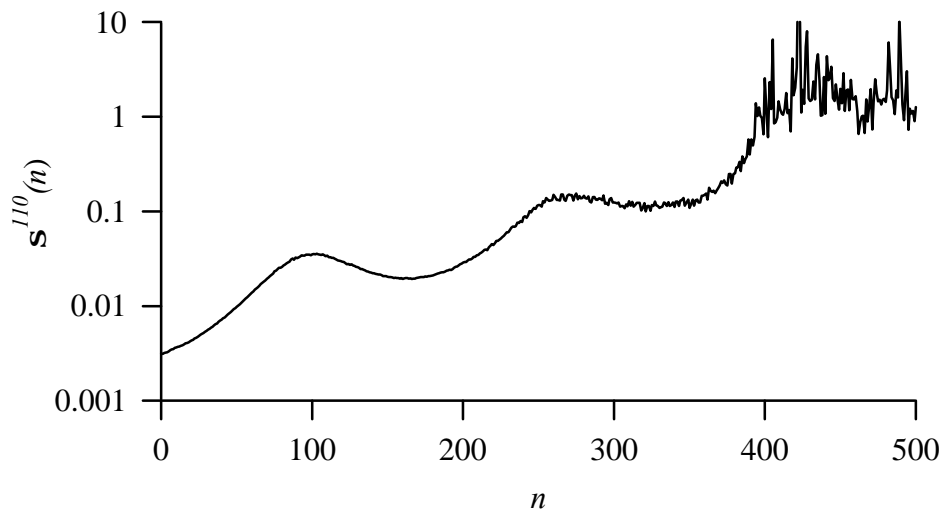


**Fig. 2b.** The counting statistical variance of the modulus of the Fourier coefficients of  $D^{110}(n)$  shown in Fig. 2a (cf. Eq. (6)) (logarithmic ordinate!).

Suppose the  $\mathbf{Ka}_1$ - $\mathbf{Ka}_2$  doublet (of component  $A$ ) consists of the sum of a single peaked function,  $I(2\mathbf{q})$ , with its top at the origin of the  $2\mathbf{q}$ -axis and a scaled

( $R = 0.5$ ) and displaced ( $\mathbf{D} \circ 2\mathbf{q}$ ) version of the same function,  $RI(2\mathbf{q} - \Delta)$ , and thus  $I_{a1/a2}(2\mathbf{q}) = I(2\mathbf{q}) + RI(2\mathbf{q} - \Delta)$ . To illustrate the effects of counting statistical shape differences a second doublet is constructed that is equal to the first doublet but in addition a “delta” peak with area  $I_c$  is added at the top position of the  $\mathbf{Ka}_1$ -peak and thus  $I_{a1/a2}^d(2\mathbf{q}) = I(2\mathbf{q}) + RI(2\mathbf{q} - \Delta) + I_c d(2\mathbf{q}_{a1}^{\max})$ . If the Fourier transform of this affected, second doublet is divided by the Fourier transform of the unaffected, first doublet (similar to the procedure outlined in section 2 with  $I_{a1/a2}^d(2\mathbf{q})$  as  $I_{tot}(2\mathbf{q})$  and  $I_{a1/a2}(2\mathbf{q})$  as  $I_s(2\mathbf{q})$ ) the result is:

$$|D(n)| = \sqrt{1 + \frac{2I_c A_H(n)(1 + R \cos(2pn\Delta/N) + 2B_H(n)(R \sin(2pn\Delta/N) + I_c^2)}{|H(n)|^2 (1 + 2R \cos(2pn\Delta/N) + R^2)}, \quad (7)$$

with  $H(n)$  as the Fourier transform of  $I_{a1/a2}(2\mathbf{q})$  and with  $\mathbf{D}$  expressed as a number of steps;  $A_H(n)$  and  $B_H(n)$  represent the real and the imaginary parts of  $D(n)$ . In the case of a Lorentzian shape function for  $I(2\mathbf{q})$ , with maximum intensity  $I_0$  and full width at half maximum  $2w$ , Eq. (7) becomes approximately:

$$|D(n)| \approx 1 + \frac{I_c}{2pwI_0} e^{2pwn} \left( 1 + \frac{3/4}{5/4 + \cos(2pn\Delta/N)} \right). \quad (8)$$

If a deconvolution procedure like the one described by Eq. (5) is performed, it follows simply from Eq. (8) that the intensity aberration at the top of a  $\mathbf{Ka}_1$  peak leads to effects in Fourier space such that local error maxima occur at approximately  $n = N/2\Delta, 3N/2\Delta, \dots$  and local error minima at  $n = 0, N/\Delta, 2N/\Delta, \dots$ . For the case shown in Fig. 2 it holds that  $N = 1851$  and  $\mathbf{D} = 10$  and therefore the spacing between the local maxima and between the local minima in Fig. 2b should be  $N/\mathbf{D} \approx 185$ , which agrees well with the experimental observation reported above.

From the above analysis it follows that the value of  $\mathbf{a}$  can best be determined from  $|D^{110}(n)|$  where  $n$  is sufficiently large and the estimated standard deviation show a local minimum; i.e. within the range of Fourier numbers  $160 \leq n \leq 190$  (cf. Fig. 2). The corresponding results of the proposed deconvolution method as obtained for five consecutive measurements performed under similar conditions are given in Table 1. Clearly good reproducibility has been achieved. The remaining small differences in the  $\mathbf{a}$  values are ascribed to the effect of counting statistics (for  $n \approx 200$   $\mathbf{s} \approx 0.02$ , cf. Fig. 2b).

For the determination of  $\mathbf{a}$  it is recommended *not* to apply profile unraveling methods based on fitting specific profile-shape functions such as by application of PROFIT [8]. Fitting of specific, presupposed profile functions for components  $A$  and  $B$  leads to *systematic* differences between the measured total profile and the fitted total profile function [9]. It can be shown that these differences yield pronounced effects on the value determined for  $\mathbf{a}$ .

**Table 1.** Results of  $\mathbf{a}$ -determination using the  $\{110\}$  line profiles recorded from the  $Mo_{30}$  powder and the  $Mo_0$  powder according to the deconvolution method proposed in section 2.

measurement number	1	2	3	4	5
volume fraction $\mathbf{a}$	0.74	0.76	0.76	0.77	0.76

## 5. Conclusions

Both (i) the volume fraction of a separate, homogeneous component ( $A$ ) contained in a (microstructurally) non-homogeneous specimen and (ii) the diffraction-line broadening due to the rest of the diffracting volume (component  $B$ ) can be determined by application of a special deconvolution procedure of an (X-ray) diffraction-line profile recorded from the mixture. The method requires that the line profile of the component  $A$  is less broad than the line profile of component  $B$ .

The accuracy of the results obtained is largely determined by the effect of counting statistics. A region in Fourier space can be indicated where the determination of the parameters sought for is optimal.

## Acknowledgement

We are indebted to Dr. H. Bakker for providing the ball milling facilities, and to Dr. G. Rixecker for performing the ball milling experiments.

## References

- [1] B.E. Warren, X-Ray Diffraction, Addison Wesley, Reading, Mass. (1969), 265 -275.
- [2] E.O. Brigham, The Fast Fourier Transform, Englewood Cliffs, NJ, U.S.A.: Prentice-Hall (1974).

- 
- [3] R. Delhez, Th.H. de Keijser and E.J. Mittemeijer, In: Block S, ed. C.R. Hubbard, Accuracy in Powder Diffraction (NBS Special Publication 567), National Bureau of Standards, Washington (1980), 213 - 253.
- [4] T.C. Bor, M.C. Huisman, J.-D. Kamminga, R. Delhez and E.J. Mittemeijer, to be published (Chapter 6 of this thesis).
- [5] J.G.M. van Berkum, G.J.M. Sprong, Th.H. de Keijser, R. Delhez and E.J. Sonneveld, Powder Diffraction **10** (1995), 129 - 139.
- [6] A.J.C. Wilson, Acta Cryst. **23** (1967), 888 - 898.
- [7] R. Delhez and E.J. Mittemeijer, J. Appl. Cryst. **8** (1975), 612 - 614.
- [8] Commercially available software package of Philips Analytical, Almelo, The Netherlands.
- [9] E.J. Sonneveld, R. Delhez, Th.H. de Keijser and E.J. Mittemeijer, Mat. Sci. Forum. **79 - 82** (1991), 85 - 90.





## *Chapter 6*

# **Analysis of Ball Milled Mo Powder using X-ray Diffraction**

T.C. Bor<sup>1</sup>, M.C. Huisman<sup>2</sup>, J.-D. Kamminga<sup>3</sup>, R. Delhez<sup>1</sup> and E.J. Mittemeijer<sup>1,4</sup>

<sup>1</sup>Laboratory of Materials Science, Delft University of Technology,  
Rotterdamseweg 137, 2628 AL Delft, The Netherlands

<sup>2</sup>Faculty of Sciences, Division of Physics and Astronomy,  
vrije Universiteit Amsterdam,

De Boelelaan 1081, 1081 HV Amsterdam, The Netherlands

<sup>3</sup>Netherlands Institute for Metals Research,  
Rotterdamseweg 137, 2628 AL Delft, The Netherlands

<sup>4</sup>Max Planck Institute for Metals Research,  
Seestraße 92, 70174 Stuttgart, Germany

### ***Abstract***

X-ray diffraction measurements and analysis were carried out on ball milled Mo powder. During the ball milling of Mo powder several stages of deformation could be identified. After short durations of ball milling still undeformed starting powder was present of which the volume fraction was determined. The initial aggregates of deformed powder particles exhibited a deformation texture. On prolonged ball milling the particle size decreased, the deformation texture disappeared and internal strains built up. By simulation and matching of the corresponding line profiles using a new Monte-Carlo-type of line-profile simulation based on a simple three dimensional model of the distribution of straight dislocations, an estimate of the dislocation density in the ball milled particles was obtained.

### ***1. Introduction***

In recent years ball milling of powders, in case of starting with a mixture of elemental powders also called mechanical alloying, has become an area of large interest. The milling of elemental and/or alloyed powders provides a route for the production of non-equilibrium materials that may possess unusual chemical and physical properties. Examples are the production of amorphous materials [1], nanostructured materials [2] and intermetallic phases [3].

Little is known yet about processes as welding, fracture, recovery and recrystallisation that can take place at the interfaces of and within the powder particles during ball milling. X-Ray Diffraction (XRD) is a versatile, non-destructive, experimental technique that enables the quantitative determination of (i) the average size of coherently diffracting particles, of (ii) "macroscopic" strains, i.e. strains on the length scale of a grain in the specimen, and of (iii) "microscopic" strains, i.e. strains varying over atomic distances. Therefore, XRD is particularly suited for a quantitative study on the deformation of powder particles upon ball milling.

In this work the emphasis has been on the study of the first stages of the ball milling process of Mo powder in a low-energy ball mill. From preliminary explorative work [4] it followed that Mo powder milled during a relatively short time consists of a mixture of deformed and undeformed powder particles, at least for the type of ball milling applied here. XRD measurements of such mixtures have been carried out to determine the evolution of the volume fractions of the undeformed and the deformed parts of the powder and to evaluate from the diffraction-line broadening the structural changes that occurred in the deformed Mo powder particles.

## 2. Theoretical basis

### 2.1 Description of diffraction-line profiles in real space and Fourier space

The result of an XRD measurement can be given in the form of a line profile: i.e. the measured diffracted intensity  $I$  as a function of the diffraction angle  $2\mathbf{q}$  or the length of the diffraction vector. A measured line profile ( $h$ -profile) can be described as the convolution of the structural line profile ( $f$ -profile) with the instrumental line profile ( $g$ -profile). Convolution of two functions in real space is equivalent to the multiplication of their respective Fourier transforms in Fourier (reciprocal) space [5]. The Discrete Fourier Transform (DFT) of a function  $h(t)$  given by  $N$  equidistant sample values ( $t = 0, 1, 2, \dots, (N-1)$ ) is given by:

$$H(n) = \frac{1}{N} \sum_{t=0}^{N-1} h(t) \exp(2\mathbf{p}int/N), \quad (1)$$

where  $n$  denotes the (harmonic) number,  $n = 0, 1, 2, \dots, (N - 1)$ , and  $N$  can be written as  $p/Dt$ , with  $Dt$  as the sampling distance in real space and  $p$  as the period of the function in real space.

The diffracting volume pertaining to the  $\{HKL\}$  reflection can consist of a mixture of undeformed powder particles of total volume  $V_{undef}^{HKL}$  and deformed powder particles of total volume  $V_{def}^{HKL}$ . According to the kinematical diffraction theory the total intensity diffracted by a volume of material for a  $\{HKL\}$  reflection,  $I_{tot}^{HKL}(2\mathbf{q})$ , is equal to the sum of the diffracted  $\{HKL\}$  intensities from the individually (i.e. incoherently) diffracting crystallites [6]. Hence,  $I_{tot}^{HKL}(2\mathbf{q})$  can be written as the volume weighted sum of the intensity distributions diffracted by the undeformed powder particles,  $\bar{I}_{undef}^{HKL}(2\mathbf{q})$ , and the deformed powder particles,  $\bar{I}_{def}^{HKL}(2\mathbf{q})$ , respectively,

$$I_{tot}^{HKL}(2\mathbf{q}) = V_{undef}^{HKL} \bar{I}_{undef}^{HKL}(2\mathbf{q}) + V_{def}^{HKL} \bar{I}_{def}^{HKL}(2\mathbf{q}). \quad (2)$$

where  $\bar{I}_{undef}^{HKL}(2\mathbf{q})$  indicates the diffracted intensity per unit volume undeformed material and  $\bar{I}_{def}^{HKL}(2\mathbf{q})$  indicates the diffracted intensities per unit of volume deformed material.

Using the additivity of DFT's, it follows from Eq. (2):

$$H_{tot}^{HKL}(n) = V_{undef}^{HKL} \bar{H}_{undef}^{HKL}(n) + V_{def}^{HKL} \bar{H}_{def}^{HKL}(n), \quad (3)$$

where  $H_{tot}^{HKL}(n)$ ,  $\bar{H}_{undef}^{HKL}(n)$  and  $\bar{H}_{def}^{HKL}(n)$  are the DFT's of the corresponding line profiles. Thus

$$\bar{H}_{tot}^{HKL}(n) = \mathbf{a}^{HKL} \bar{H}_{undef}^{HKL}(n) + (1 - \mathbf{a}^{HKL}) \bar{H}_{def}^{HKL}(n) \quad (4)$$

where  $\mathbf{a}^{HKL}$  denotes the volume fraction of undeformed powder in the mixture of undeformed and deformed powder particles for the reflection considered

$$\mathbf{a}^{HKL} \equiv V_{undef}^{HKL} / (V_{undef}^{HKL} + V_{def}^{HKL}). \quad (5)$$

To determine  $\mathbf{a}^{HKL}$  a route is given in Section 2.2. To determine the  $\{HKL\}$  independent fraction of undeformed material in the powder, i.e.  $\mathbf{a} = V_{undef} / (V_{undef} + V_{def})$ , a ratio concerning all powder particles irradiated and not just the powder particles with diffracting  $\{HKL\}$  lattice planes, a direct route is given in Section 2.3. Evidently, if  $\mathbf{a}^{HKL}$  is independent of  $HKL$ , i.e.

$\mathbf{a}^{HKL} = V_{undef}^{HKL} / (V_{undef}^{HKL} + V_{def}^{HKL}) = V_{undef} / (V_{undef} + V_{def}) \equiv \mathbf{a}$ , then  $\mathbf{a}$  follows directly from the route given in Section 2.2.

## 2.2 Deconvolution with prior normalization

To determine  $\mathbf{a}^{HKL}$  and  $\bar{I}_{def}^{HKL}(2\mathbf{q})$  or equivalently  $\bar{H}_{def}^{HKL}(n)$ , it will be supposed that  $\bar{I}_{undef}^{HKL}(2\mathbf{q})$  for the undeformed powder particles in the mixture can be measured separately from a separate, reference specimen of undeformed powder particles yielding  $\bar{I}_{ref}^{HKL}(2\mathbf{q}) = \bar{I}_{undef}^{HKL}(2\mathbf{q})$ . Deconvolution of  $\bar{I}_{tot}^{HKL}(2\mathbf{q})$  ( $= I_{tot}^{HKL}(2\mathbf{q})$  per unit of volume), acting as the "h"-profile, with  $\bar{I}_{ref}^{HKL}(2\mathbf{q})$ , acting as the "g"-profile, through division of  $\bar{H}_{tot}^{HKL}(n)$  with  $\bar{H}_{ref}^{HKL}(n)$  leads to (cf. Eq. (4))

$$D_{nor}^{HKL}(n) \equiv A_D^{HKL}(n) + iB_D^{HKL}(n) \equiv \frac{\bar{H}_{tot}^{HKL}(n)}{\bar{H}_{ref}^{HKL}(n)} = \mathbf{a}^{HKL} + (1 - \mathbf{a}^{HKL}) \frac{\bar{H}_{def}^{HKL}(n)}{\bar{H}_{ref}^{HKL}(n)} \quad (6)$$

with  $A_D^{HKL}(n)$  and  $B_D^{HKL}(n)$  as the real and the imaginary parts of  $D_{nor}^{HKL}(n)$ . The quotient  $\bar{H}_{tot}^{HKL}(n) / \bar{H}_{ref}^{HKL}(n)$  in Eq. (6) equals the quotient of  $H_{tot,nor}^{HKL}(n)$  ( $\equiv H_{tot}^{HKL}(n) / H_{tot}^{HKL}(n=0)$ ) and  $H_{ref,nor}^{HKL}(n)$  ( $\equiv H_{ref}^{HKL}(n) / H_{ref}^{HKL}(n=0)$ ), because  $H_{tot}^{HKL}(n=0) = c_{tot} \cdot V_{tot}^{HKL}$  and  $H_{ref}^{HKL}(n=0) = c_{ref} \cdot V_{ref}^{HKL}$ , with  $c_{tot} = c_{ref}$ , recognizing that the integrated intensity (per unit volume) is independent of the state of deformation. Thus:  $D_{nor}^{HKL}(n=0) = 1$ .

Note that the line profile of the reference specimen acting as a "g-profile" in the deconvolution should contain (only) the same broadening as due to the undeformed particles in the milled powder and thus it need not necessarily have as little structural broadening as possible.

As the line profile resulting from the undeformed powder particles is less broad on a  $2\mathbf{q}$  axis than the line profile resulting from the deformed powder particles, the second term at the right-hand side of Eq. (6) vanishes for sufficiently large  $n$ . Then  $D_{nor}^{HKL}(n)$  becomes equal to  $\mathbf{a}^{HKL}$ . Thereby in principle not only the volume fraction  $\mathbf{a}^{HKL}$  of the undeformed powder is determined, but, using Eq. (6), subsequently the Fourier transform of the line profile of the deformed part of the ball milled powder deconvolved with the reference powder, i.e.  $\bar{H}_{def}^{HKL}(n) / \bar{H}_{ref}^{HKL}(n)$ , is obtained as well.

Note that  $\mathbf{a}^{HKL}$  can depend on  $HKL$  since  $V_{def}^{HKL}$  can depend on  $HKL$  (see discussion at the end of Section 2.1). In practical cases the determination of  $\mathbf{a}^{HKL}$  (and  $\bar{I}_{def}^{HKL}(2\mathbf{q})$ ) is hindered by effects due to measurement errors and counting statistical variations in the measured intensity [6 - 8]. A procedure is given in Ref. 4 to

determine  $\mathbf{a}^{HKL}$  accurately from "h" and "g" line profiles affected by counting statistical errors.

### 2.3 Deconvolution without prior normalization

Clearly, if  $V_{def}^{HKL}$  depends on  $HKL$  (as due to the occurrence of preferred orientation), then  $\mathbf{a}^{HKL}$  depends on  $HKL$  (Eq. (5)). However, the fraction of undeformed powder particles in the mixture of undeformed and deformed powder particles,  $\mathbf{a} = V_{undef} / (V_{undef} + V_{def})$ , is in principle thought to be independent of  $HKL$ . This volume fraction can be determined if the deconvolution procedure (cf. Section 2.2) is performed without prior normalization. Then, deconvolution of the non-normalised  $I_{tot}^{HKL}(2\mathbf{q})$  with the non-normalised  $I_{ref}^{HKL}(2\mathbf{q})$  through division of the corresponding Fourier transforms gives

$$D_{non-nor}^{HKL}(n) = \frac{H_{tot}^{HKL}(n)}{V_{ref}^{HKL} \overline{H}_{ref}^{HKL}(n)} = \frac{V_{undef}^{HKL}}{V_{ref}^{HKL}} + \frac{V_{def}^{HKL} \overline{H}_{def}^{HKL}(n)}{V_{ref}^{HKL} \overline{H}_{ref}^{HKL}(n)} \quad (7)$$

with now  $D_{non-nor}^{HKL}(0) \neq 1$ . For sufficiently large  $n$  the second term at the right-hand side of Eq. (7) vanishes, analogous to the normalised case considered above, and  $D_{non-nor}^{HKL}(n)$  becomes equal to  $V_{undef}^{HKL} / V_{ref}^{HKL}$ . It can be supposed that the undeformed part of the powder that has been ball milled is equal to the powder of the reference specimen (the same morphology, microstructure and texture; implying the same procedure for (diffraction) specimen preparation for both specimens). Then  $V_{undef}^{HKL} / V_{ref}^{HKL}$  must be independent of the  $\{HKL\}$  reflection considered and thus

$$\frac{V_{undef}^{HKL}}{V_{ref}^{HKL}} = \frac{V_{undef}}{V_{ref}}. \quad (8)$$

From this ratio the true,  $HKL$  independent, fraction of undeformed powder in the mixture of deformed and undeformed powder particles of the ball milled specimen, can be determined through

$$\mathbf{a} = \frac{V_{undef}}{V_{undef} + V_{def}} = \frac{V_{undef}}{V_{ref}} \frac{V_{ref}}{V_{undef} + V_{def}} = \frac{V_{undef}}{V_{ref}} \frac{V_{ref}}{V_{tot}} \quad (9)$$

if, in addition to  $V_{undef}/V_{ref}$  (see above),  $V_{ref}/V_{tot}$  is known. The ratio  $V_{ref}/V_{tot}$  is given by the known mass ratio of the reference (diffraction) specimen and the (diffraction) specimen investigated if the diffraction experiments for both specimens are carried out identically, i.e. the irradiated volumes for both experiments are equal.

The Fourier transform of the line profile of the deformed part of the ball milled powder deconvolved with the reference profile, i.e.  $\bar{H}_{def}^{HKL}(n)/\bar{H}_{ref}^{HKL}(n)$ , can be obtained using Eq. (7) with  $V_{undef}^{HKL}/V_{ref}^{HKL}$  ( $= V_{undef}/V_{ref}$ ; cf. Eq. (8)) as given by the above discussed plateau level (see below Eq. (7)) and with  $V_{def}^{HKL}/V_{ref}^{HKL}$  as determined from  $D_{non-nor}^{HKL}(n=0)$  and  $V_{undef}^{HKL}/V_{ref}^{HKL}$ .

### 3. Experimental

The ball milling experiments were performed in the ball mill depicted schematically in Fig. 1. It consists of a cylindrical vessel (inner diameter of 63 mm) with a WC bottom plate (diameter of 20 mm), whereupon the Mo powder was deposited, and a ferritic stainless steel ball (diameter of 58 mm). The experiments were carried out in vacuum (atmosphere pressure less than  $10^{-4}$  Pa). The cylindrical vessel vibrated with an amplitude of 2 mm at a frequency of approximately 20 Hz.

Three series of ball milling experiments were carried out as function of ball milling time using about 2 g of Mo powder (Alpha, 99.9 wt-% pure, almost spherical particles with diameter 1 - 7  $\mu\text{m}$ ) for each series (see Fig. 3a).

In the first series, denoted series *A*, Mo powder was ball milled for 0.5 h, 1 h, 2 h and 4 h consecutively. After 0.5 h of ball milling the milling experiment was stopped temporarily and the steel ball was taken out. A small amount of 0.1 g Mo powder was taken out both from the middle and the periphery of the deposit of Mo powder in the ball mill as indicated in Fig. 1 by "m" and "p", respectively. Then the ball milling experiment was resumed and the remaining Mo powder was ball milled for another 0.5 h to complete 1 h of ball milling. Again a sample at "m" and a sample at "p" were taken out. Subsequently, such samples of Mo powder were taken out after a total ball milling time of 2 h and 4 h, as well.

In the second and third series Mo powder was ball milled for 2, 4, 8 and 16 h consecutively (series *B*) and 8, 16, 32 and 64 h consecutively (series *C*) in the same way as described above for series *A*. However, samples were taken only from the periphery (at "p") of the Mo powder deposit in the ball mill (differences in degree of milling for locations "m" and "p" become negligible for longer milling times (see results reported in Section 5.2)). Since it appeared difficult to impose a constant milling intensity (dependent on frequency of the vibrating cylindrical vessel and the powder mass to be milled) in each series, the ball milling times of the various series

were chosen to overlap partly. The results of series *C* after 64 h of ball milling were disregarded in this work due to excessive contamination of the ball milled powder with small Fe-rich particles broken out of the vibrating ball.

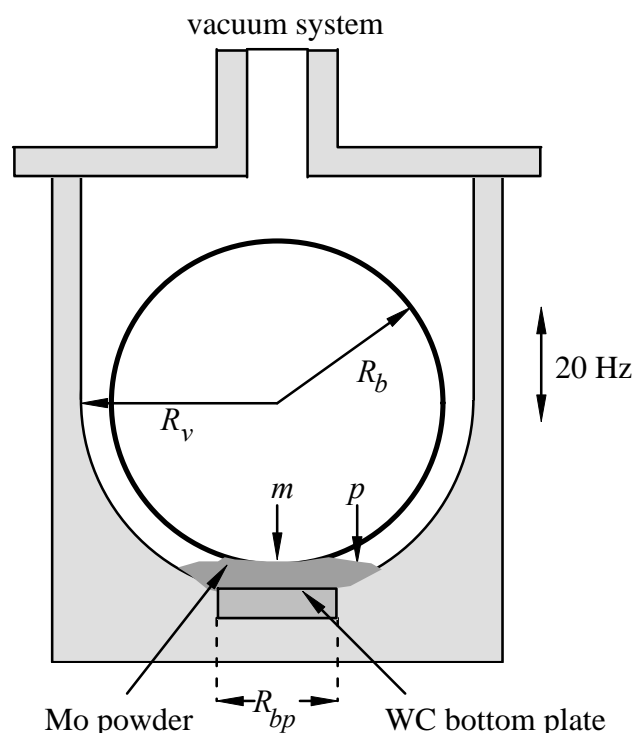


**Fig. 1.** The ball milling equipment consists of a cylindrical vessel (inner diameter of  $R_v = 63$  mm) with a WC bottom plate (diameter of  $R_{bp} = 20$  mm), whereupon the Mo powder is deposited and a ferritic stainless steel ball (diameter of  $R_b = 58$  mm). The experiments are carried out in vacuum with a vibration frequency of the cylindrical vessel of approximately 20 Hz and an amplitude of 2 mm. Regions where after some ball milling time powder was acquired are indicated by "m" and "p".

The specimens for the XRD-measurements were prepared by suspending a small volume of Mo powder in isopropanol directly on a Si  $\langle 510 \rangle$ -single crystal wafer within a specially made support-ring assembly and drying the suspension by evaporating the isopropanol. In general an evenly spread distribution of Mo powder was observed on the Si-wafers.

The XRD measurements were performed in Bragg-Brentano geometry on a Siemens F- $\omega$  diffractometer equipped with a curved graphite monochromator in the

diffracted beam and using Cu-K $\alpha$  radiation. A divergence slit of 1° and receiving slits of 0.018 °2 $q$  for series *A* and of 0.05 °2 $q$  for both series *B* and series *C* were applied, respectively. During the measurement the specimen was spinning around an axis perpendicular to its surface. The line profiles of the {110}, {200}, {211}, {220}, {310} and {321} reflections were recorded with as large as possible measurement ranges taken approximately symmetrically around the peak position of the corresponding line profile but without overlap of neighbouring measurement ranges. The step size was chosen such that at least 10 data points across the full width at half maximum of the K $\alpha_1$  peak were measured and the counting time per step was selected such that at least 10000 counts on the line-profile peak were collected. The step sizes of the {110} and {220} reflection of series *A* were always chosen equal. The background of each line profile was removed by subtracting a straight line fitted to the outermost 5 % of the data points of the line profile on either end of the measurement range.

The morphology of the undeformed and deformed Mo powder particles was analysed employing a JEOL 6400F Scanning Electron Microscope.

#### ***4. Evaluation of X-Ray Diffraction data***

The ball milled powder, in particular after short times of ball milling, can be conceived as composed of a mixture of undeformed and deformed powder particles (see Section 5.1 and Ref. 4). Hence, the deconvolution procedures presented in Section 2 can be applied. The broadened line profiles were deconvolved with the corresponding lines profiles of the undeformed starting powder as reference line profiles using normalised Fourier transforms (cf. Eq. (6)). An example of the results of this procedure for a sample taken from the middle of the ball mill after 0.5 h of ball milling is presented in Fig. 2a. The Fourier transforms of all reflections shown do not fall off to zero for large correlation distances  $L$  ( $L$  is proportional to the Fourier coefficient  $n$ ; cf. Ref. 6), but approach, for increasing  $L$ , a more or less constant plateau level (cf. discussion of Eq. (6)). Surprisingly, this plateau level is dependent on the reflection considered. However, for two orders of the same reflection, {110} and {220}, the plateau level is approximately the same. For correlation distances larger than approximately 150 nm the Fourier transforms become very unreliable as a consequence of superimposed counting statistical errors [4, 7, 8].

The appearance of the plateau levels in Fig. 2a clearly shows the presence of undeformed starting powder in the ball milled powder after short durations of ball milling (cf. Section 2.2). The plateau levels found indicate the value of that volume fraction in the ball milled powder of undeformed starting powder that has the { $HKL$ }



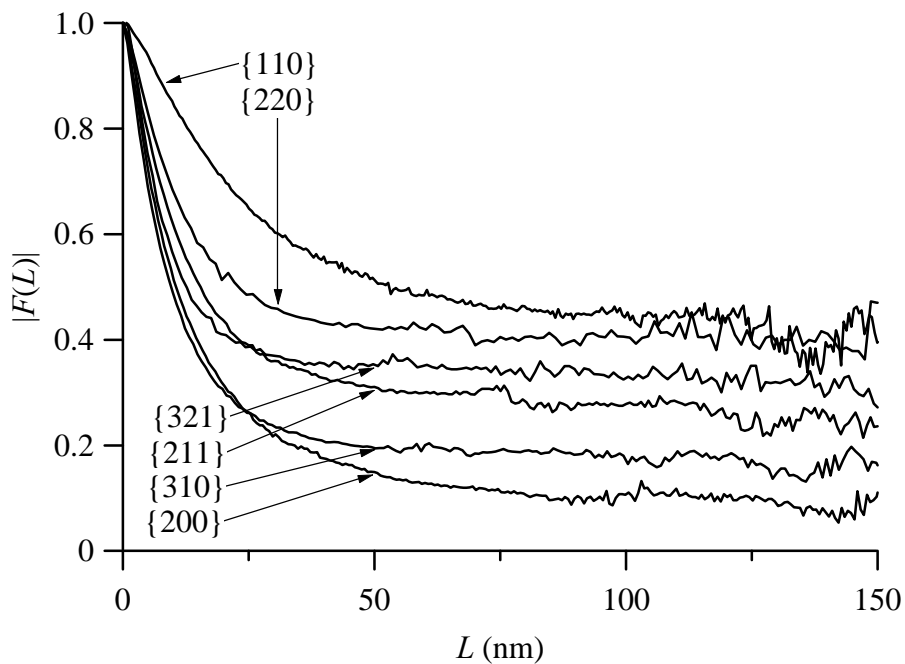


**Fig. 2a.** Deconvoluted Fourier transform (modulus) of several line profiles of 0.5 h ball milled Mo powders of series  $A_m$  using the normalised deconvolution procedure. Note the dependence of the plateau levels on the reflections indicated.

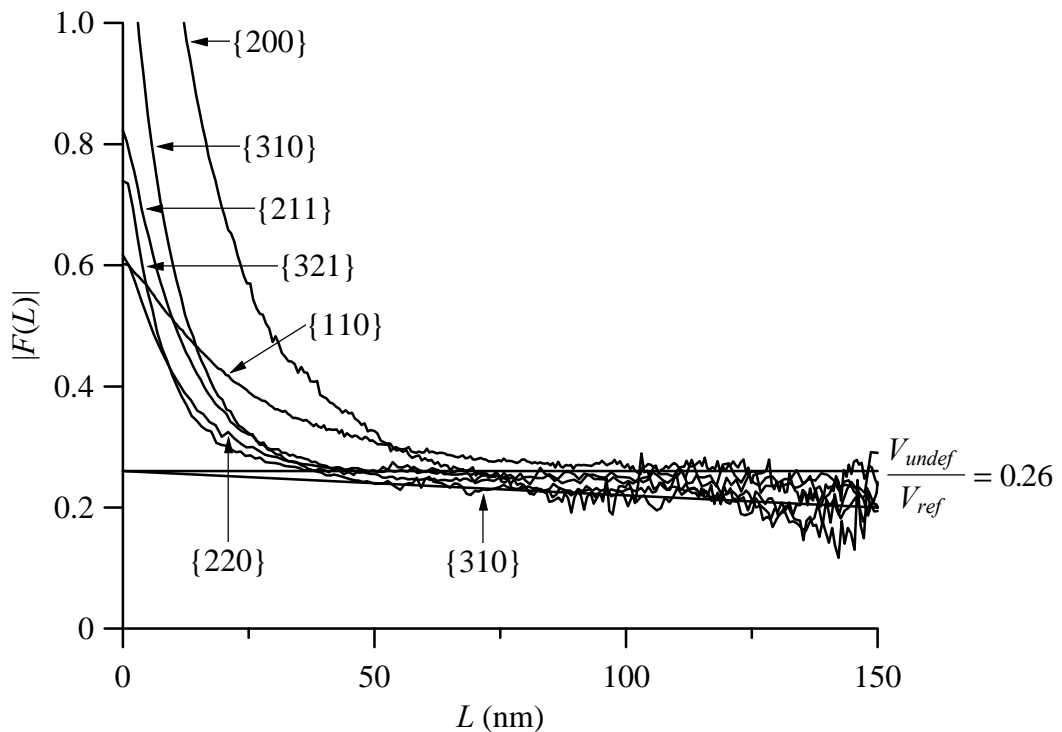


**Fig. 2b.** Deconvoluted Fourier transform (modulus) of several line profiles of 0.5 h ball milled Mo powders of series  $A_m$  using the non-normalised deconvolution procedure.

lattice planes parallel to the sample surface, i.e. perpendicular to the diffraction vector employed (see discussion at end of Section 2.2).

Next, the deconvolution procedure is performed again, but now without prior normalization of the Fourier transforms with respect to the first Fourier coefficient (cf. Eq. (7)). Then, the plateau levels exhibited by the Fourier transforms of all measured reflections practically coincide: see Fig. 2b. Consequently,  $V_{undef}^{HKL} / V_{ref}^{HKL}$  does not depend on  $\{HKL\}$ , as expected (see below Eq. (7) in Section 2.3). Accordingly, the ratio of undeformed starting powder in the ball milled powder and the reference powder, which consists of undeformed starting powder only, in this case equals:  $V_{undef} / V_{ref} = 0.26$ .

On close inspection of the  $\{110\}$  and  $\{220\}$  Fourier transforms a true horizontal plateau level is observed, whereas a minor continuous decrease is observed for the other reflections for the same  $L$ -range. This last effect is ascribed to a minor artefact in the deconvolution procedure, as follows. For the  $\{110\}$  and  $\{220\}$  reflections the step sizes used during the measurement of the line profiles of the ball milled powder, the " $h$ "-profile, and of the reference powder, the " $g$ "-profile, were the same. For the other reflections the step size of the  $h$ -profile was always larger than the step size of the  $g$ -profile. This means that the  $g$ -part in the  $h$ -profile (i.e. the undeformed powder particles in the ball milled powder;  $h = f * g$ ) is also recorded with a larger step size than corresponding to the  $g$ -profile itself, which implies that the  $g$ -part in the  $h$ -profile exhibits in fact a slight additional broadening as compared to the  $g$ -profile used in the deconvolution. This small effect reveals itself only at large values of  $L$  that are not studied normally in line-broadening analysis. However, in this work the large values of  $L$  are of importance (to determine  $\mathbf{a}$ ; cf. Section 2). Recognizing the above, in order to obtain accurate values of  $V_{undef} / V_{ref}$ , the average of only the plateau levels of the Fourier transforms of the  $\{110\}$  and  $\{220\}$  reflections is utilized.

In order to determine the only structurally broadened line profiles of the deformed part of the ball milled powder, the procedure discussed in Section 2.2 (deconvolution with normalization) or the procedure discussed in Section 2.3 (deconvolution without normalization) can be applied. If, because of different step sizes used in the measurements of the corresponding line profiles of the ball milled powder and the reference powder, no truly horizontal plateau level occurs (see above discussion) the following procedure is adopted. In this case  $\bar{H}_{undef}^{HKL}(n)$  is not exactly equal to  $\bar{H}_{ref}^{HKL}(n)$  and thus the first terms on the right hand side of Eqs. (6) and (7) become

$$a^{HKL} \frac{\bar{H}_{undef}^{HKL}(n)}{\bar{H}_{ref}^{HKL}(n)} \quad \text{and} \quad \frac{V_{undef}^{HKL}}{V_{ref}^{HKL}} \frac{\bar{H}_{undef}^{HKL}(n)}{\bar{H}_{ref}^{HKL}(n)}, \text{ respectively.} \quad (10)$$

It is proposed to approximate  $\bar{H}_{undef}^{HKL}(n)/\bar{H}_{ref}^{HKL}(n)$  with  $1 - const \cdot n$  and then the above terms become

$$a^{HKL} - C_1 n \quad \text{and} \quad \frac{V_{undef}^{HKL}}{V_{ref}^{HKL}} - C_2 n, \text{ respectively.} \quad (11)$$

Here,  $a^{HKL}$  and  $C_1$ , or  $V_{undef}^{HKL}/V_{ref}^{HKL}$  and  $C_2$ , follow directly from the straight lines fitted to  $D_{nor}^{HKL}(n)$  or  $D_{non-nor}^{HKL}(n)$  in the range where the "plateau level" occurs. Using this procedure, it followed from the results obtained by deconvolution using non-normalized transforms (cf. Eq. (7)) that  $V_{undef}^{HKL}/V_{ref}^{HKL}$  as determined by fitting straight lines as discussed was independent of  $HKL$ , justifying the above approximate treatment (i.e.  $\bar{H}_{undef}^{HKL}(n=0)/\bar{H}_{ref}^{HKL}(n=0) \cong 1$ ).

## 5. Results and Discussion

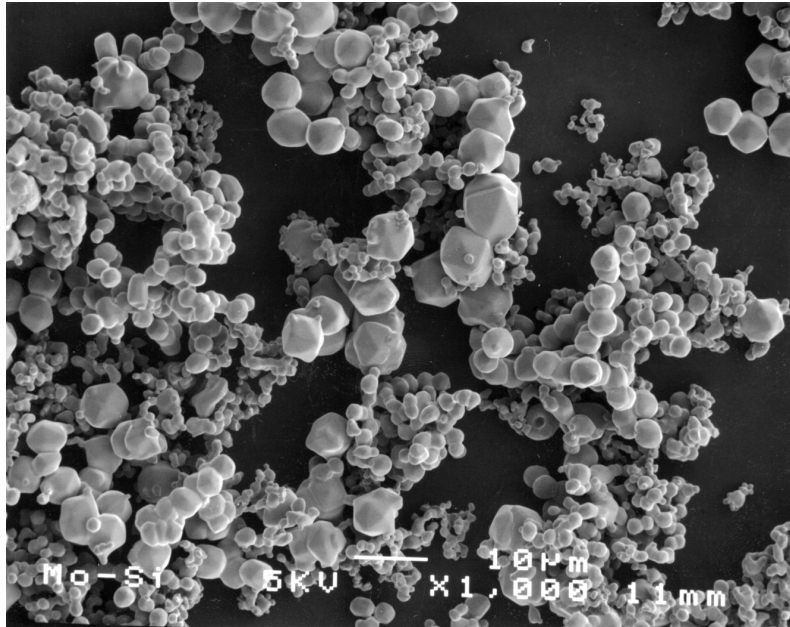
### 5.1 Morphology of ball milled powder

The starting powder consisted of more or less spherical particles with a diameter of 1 to 7  $\mu\text{m}$  and flattened sides (see Fig. 3a). The morphology of the Mo powder particles changed strongly upon ball milling.

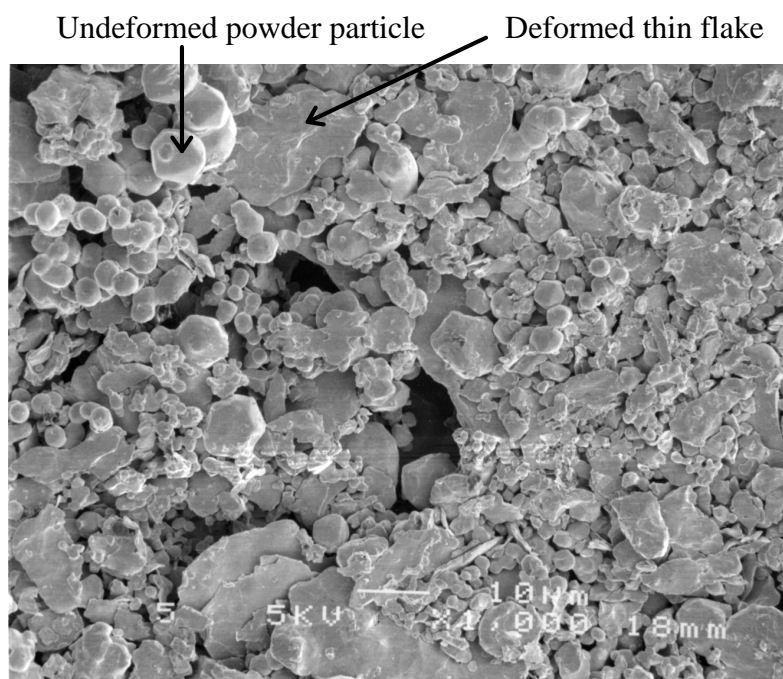
After 1 h of ball milling the ball milled powder consisted of a mixture of powder particles, composed of apparently undeformed starting powder particles and clearly deformed powder particles (see Fig. 3b). The clearly deformed particles were thin flakes, approximately 10 to 20  $\mu\text{m}$  wide and a few micrometers thick.

Longer ball milling caused the amount of apparently undeformed Mo powder to decrease, and the shape of the deformed powder particles to change. An example of the morphology of Mo powder after 8 h of ball milling is given in Fig. 3c. Undeformed Mo powder particles were absent in this sample; large agglomerates of powder particles of approximately 10 to 20  $\mu\text{m}$  diameter and with irregular shapes were observed; each agglomerate consisted of several cold welded and deformed original powder particles. Smaller pieces with a size ranging from 1  $\mu\text{m}$  to 10  $\mu\text{m}$  showed irregularly shaped edges, likely as the result of fracture processes. Some thin flakes, each flake is probably a single deformed original particle, were visible as well.

The amount of these flakes decreased with increasing ball milling time; eventually no flakes were observed anymore and the ball milled powder consisted solely of agglomerates of multiply cold welded and fractured powder particles.



a)



b)

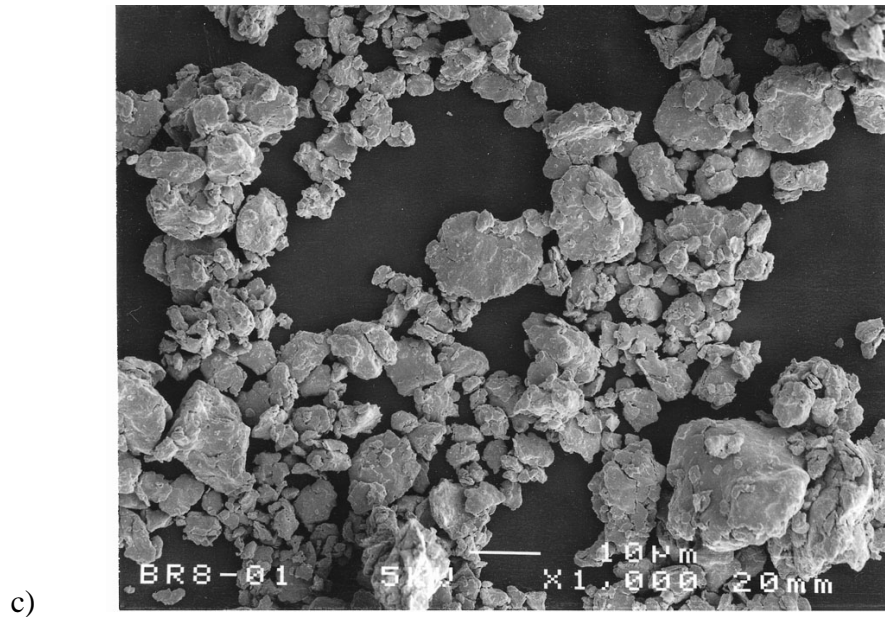


**Fig. 3.** Morphology of Mo powder particles before ball milling (a), after 2 h of ball milling (b) and 8 h of ball milling (c). After 2 h of ball milling apparently undeformed powder particles and deformed thin flakes were present as indicated by the arrows in Fig. (b). After 8 h of ball milling no apparently undeformed powder particles or deformed thin flake-like particles were observed in Fig. (c); solely irregularly shaped agglomerates of particles were recognised.

## 5.2 Volume fraction of undeformed powder particles in ball milled powder

The volume fraction of undeformed powder particles in the ball milled powder,  $\alpha$ , was determined using the procedure outlined in Section 4. The results have been presented in Fig. 4.

In general  $\alpha$  decreased with increasing milling time. After 8 h of ball milling no undeformed starting powder was found in the ball milled powder. For short milling times the influence of the location of sampling ("m" or "p"; see Section 3) of the Mo powder in the ball mill is evident: samples taken from the middle of the bottom plate showed in general a much smaller  $\alpha$ -value than samples taken from the periphery of the bottom plate. Since the spherical stainless steel ball touches predominantly the Mo powder located in the middle of the flat WC bottom plate (cf. Fig. 1), it is understandable that most deformed particles were found at this location. The deformed Mo powder particles at the periphery of the Mo powder in the ball mill appear to have been deformed in the centre region of the bottom plate and have then been moved towards the periphery. The large difference in  $\alpha$  between the middle and

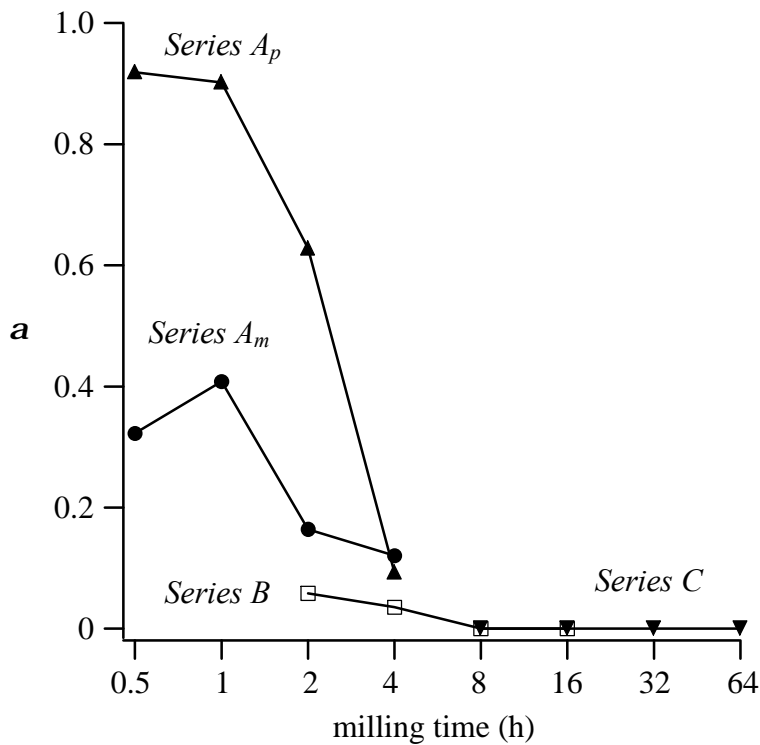


**Fig. 4.** Volume fraction  $a$  of undeformed powder particles in ball milled Mo samples as a function of milling time of series  $A_m$ ,  $A_p$ , B and C determined using the non-normalized deconvolution procedure (Section 2.3).

the periphery of the Mo powder in the ball mill suggests that the transport of Mo powder particles in the ball mill in directions parallel to the surface of the WC bottom plate (cf. Fig. 1), i.e. perpendicular to the movement of the vibrating cylinder of the ball mill, is rather slow as compared to the difference in powder sampling time. This can also explain why, for samples taken from the middle of the bottom plate,  $a$  after 1 h of ball milling is larger than after 0.5 h of ball milling (see Fig. 4), as follows. If powder is taken away from the middle region of the bottom plate then most of the deformed powder particles present at this location are taken out. This follows directly from the geometry of the ball mill. Powder particles will be deformed only if they are located in between the spherical ball and the flat bottom plate. The vibrating ball hits the bottom plate not only at the centre of the bottom plate, but, since the inner radius of the cylindrical vessel,  $R_v$ , is somewhat larger than the radius of the spherical ball,  $R_b$ , the ball can also move somewhat laterally. Therefore, the ball also hits the bottom plate at locations other than the one at the bottom plate that is exactly at the centre line: powder is deformed within a circular region of radius  $R_v - R_b$  around the centre of the bottom plate. Assuming an even distribution of 2 g Mo powder over the surface of the bottom plate (diameter 20 mm) approximately 0.1 g of Mo powder is located

within this circular region. This amount is equal to the amount taken out from the middle of the Mo deposit on the WC bottom plate at every sampling moment (Section 3). It takes time before more or less undeformed powder from the region closely around the centre has moved towards the centre of the bottom plate. Apparently this time is of the order of 0.5 h leading to the observation of a fraction of undeformed starting powder at "*m*" larger after 1 h than after 0.5 h.

After about 4 h of ball milling the fractions of undeformed powder measured from samples taken from the middle and from the periphery of the Mo powder in the ball mill were equal. Therefore, in series *B* and series *C* samples were taken only from the periphery of the deposit of Mo powder in the ball mill (cf. Section 3).

### 5.3 Deformation texture

The texture of the deformed part of the ball milled powders, is revealed by the different plateau levels for the Fourier transforms of the various  $\{HKL\}$  reflections shown in Fig. 2a. The texture has been depicted by the parameter  $T^{HKL}$  which represents the ratio of the relative integrated  $\{HKL\}$  intensity of the ball milled powder and the relative integrated intensity of the reference powder (see Appendix):

$$T^{HKL} \equiv \frac{\int I_{tot}^{HKL} d2\mathbf{q} / \int I_{tot}^{220} d2\mathbf{q}}{\int I_{ref}^{HKL} d2\mathbf{q} / \int I_{ref}^{220} d2\mathbf{q}} \stackrel{a^{HKL} > 0}{=} \frac{a^{220}}{a^{HKL}} \quad (12)$$

with  $\int I d2\mathbf{q}$  as the integrated intensity. To eliminate effects of intensity changes due to differences in mass suspended on the Si-substrates the integrated intensities have been normalised with respect to the, more or less arbitrarily chosen,  $\{220\}$  reflection.

The evolution of the texture of the deformed part of the ball milled powder is shown in Figs. 5a-d. At the beginning of the ball milling process a strong preference for the deformed crystallites occurred to have their  $\{200\}$  and, less strongly, their  $\{310\}$  lattice planes parallel to the specimen surface. On prolonged ball milling this texture became weaker and after approximately 8 h of ball milling no distinct texture was present ( $T^{HKL} \cong 1$ ).

A strong preference for the  $\{200\}$  type of lattice planes to be parallel to the surface was reported for cold rolled polycrystalline Mo [9, 10]. Ball milling and cold rolling imply that material is flattened in between compressing surfaces, i.e. the ball and the bottom plate in the ball milling equipment used here and both rolls in a rolling apparatus. Further, the rolling process flattens material while the material is moving in between the rolls, which causes an additional texture component in the rolling

direction of the rolled material, whereas the ball milling process is not expected to induce any in (surface) plane anisotropy.

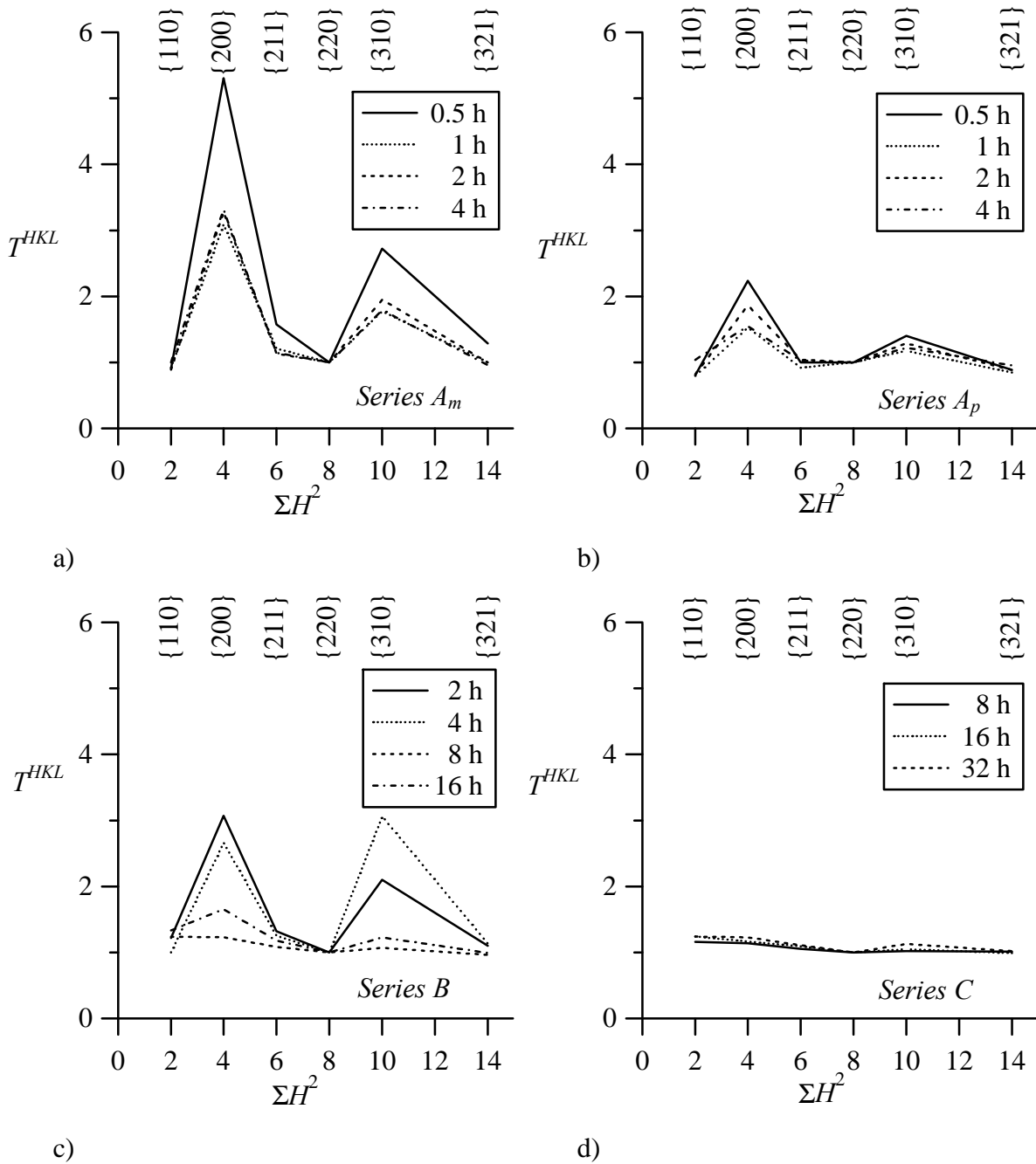


**Fig. 5.** Deformation texture parameter  $T^{HKL}$  as a function of  $\Sigma H^2 = H^2 + K^2 + L^2$  for ball milled Mo powders of series  $A_m$ ,  $A_p$ , B and C determined from the integrated intensities of the line profiles of the ball milled powder and of the reference powder (see Eq. 12).



The evolution of the texture can be explained as follows. In the initial stage of ball milling, most particles that deformed were flattened into flakes (cf. Section 5.1) which after being suspended in isopropanol (in the procedure for specimen preparation for XRD analysis; cf. Section 3) position onto the Si-substrate with a strong tendency for their flat sides to be parallel to the surface of the Si-substrate (cf. Fig. 3b). Upon prolonged ball milling the shape of the deformed powder particles changed due to the multiple cold welding and fracture processes that took place. Then large, irregularly shaped agglomerates of particles (cf. Fig. 3c) occurred and no preferred positioning on the Si-substrate of such particles is expected to take place during preparation of the XRD specimen. This leads to disappearance of the texture, as observed through  $T^{HKL}$ , upon continued ball milling. A similar texture behaviour was observed upon ball milling  $Ni_3Al$  powder [11].

Since the Mo powder particles first deformed into flake-like particles and then, on prolonged ball milling, into irregularly shaped agglomerates of particles, it is understandable that the amount of undeformed, starting powder dropped to zero before the texture (related to the amount of flake-like particles) disappeared (cf. Figs. 4 and 5).

## 5.4 Evolution of structural imperfection

### 5.4.1 Integral breadth as function of ball milling time

The diffraction-line profiles of the Mo powder particles become broadened excessively during the ball milling process. As an example the {220} line profiles of the undeformed starting powder (0 h), also used as reference powder (see Section 4), and a selection of {220} line profiles of deformed powders are shown in Fig. 6 (after removal of the background). For relatively short durations of ball milling (0 to 4 h) the  $K\alpha_1$  and  $K\alpha_2$  peaks are clearly resolved whereas for longer durations of ball milling no separate  $K\alpha_1$  and  $K\alpha_2$  peaks can be observed.

Since the broadenings of the reflections of the undeformed reference powder are very small and comparable with the broadenings of a specially made Si-standard specimen [12], it can be assumed that the line profiles of the reference powder represent the true instrumental line profiles. Consequently, the Fourier transforms of the line profiles of the deformed part of the powder, as obtained by application of a deconvolution procedure, as described in Section 2.2 or 2.3, contain broadening due to structural causes only. These structural broadenings can be characterized by the integral breadth (= integrated intensity of the only structurally broadened line profile divided by its peak height), which, assuming the peak maximum occurs at the origin

chosen in reciprocal space, is equal to the reciprocal value of the area under the corresponding normalized Fourier transforms [5].

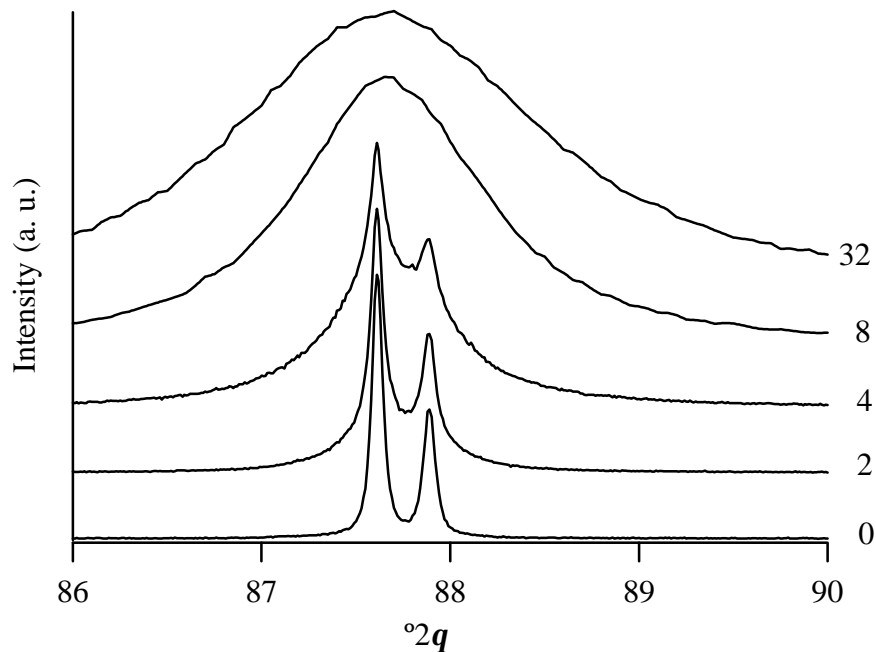


**Fig. 6.** X-ray diffraction line profiles of  $\{220\}$  Mo reflection of undeformed starting powder (0 h), also used as reference powder, and ball milled powder for increasing times of ball milling: 2, 4, 8, 32 h.

The integral breadths of all only structurally broadened line profiles are presented versus the reciprocal of the distance between the corresponding diffracting planes,  $1/d^{HKL}$ , in Figs. 7a-d. In general for a certain reflection the integral breadth increased with ball milling time indicating a more severe lattice deformation if ball milling time increases. The change of the broadenings for series  $A_m$  and  $A_p$  with ball milling time deviates somewhat from the general trend and is comparable with the behaviour of  $\mathbf{a}$  for these series with ball milling time: compare Figs. 7a, b with Fig. 4. Therefore, the same type of reasoning holds to understand the behaviour of the broadening of series  $A_m$  and  $A_p$  with ball milling time (see Section 5.2).

#### 5.4.2 Integral breadth as function of diffraction-vector length

Now consider the results of series  $B$  and series  $C$  in Figs. 7c and 7d, respectively. Ignoring the first period of ball milling, the line broadening of each reflection increased with approximately the same amount if the ball milling time was doubled. This holds for series  $B$  and for series  $C$ , and thus up to at least 32 h of ball milling.

However, the broadenings of the line profiles of series *B* are systematically larger than those of series *C*, which is seen best comparing the results of both series obtained after 8 h and 16 h of ball milling. This is ascribed to the difference in milling intensity (see Section 3).

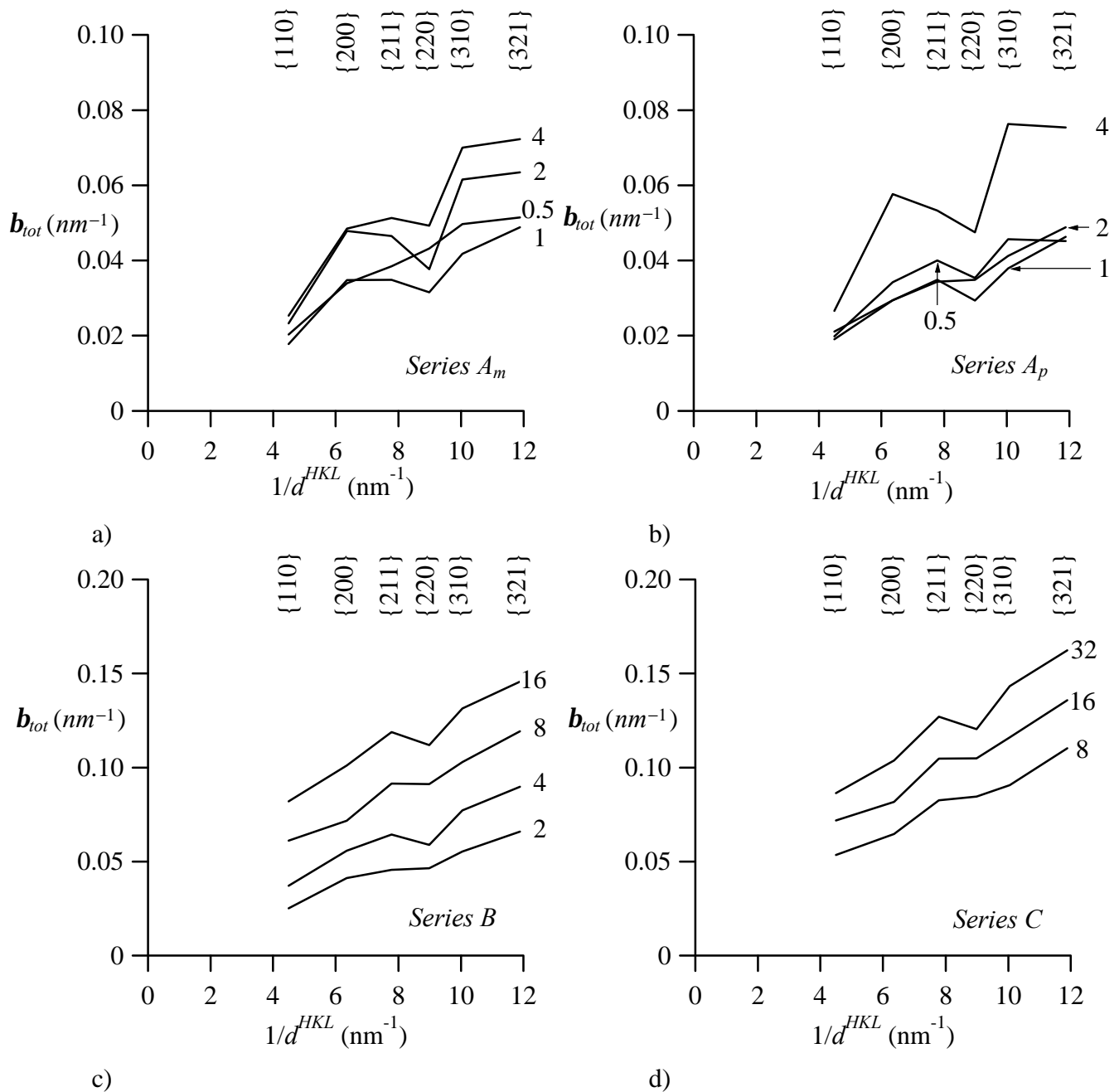


**Fig. 7.** Integral breadths  $b_{tot}$  due to structurally broadening of deformed powder particles versus  $1/d^{HKL}$  of all Mo reflections measured of series *A<sub>m</sub>*, *A<sub>p</sub>*, *B* and *C* after removal of broadening due to undeformed powder particles present and due to the measurement instrument through application of the deconvolution procedures of Sections 2.2 and 2.3.

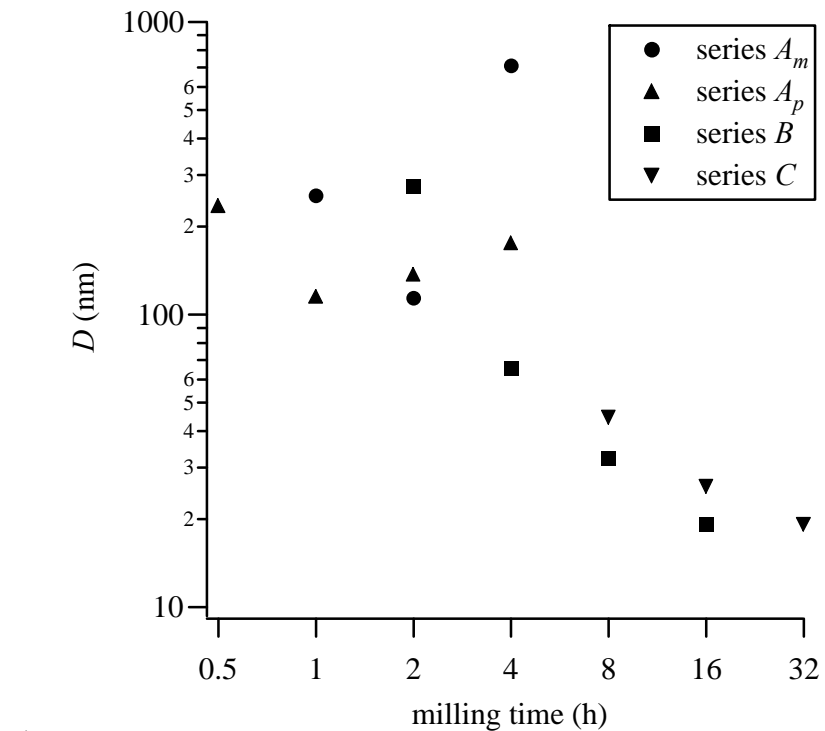
Structural line broadening is usually conceived as the convolution of broadening due to (i) finite size of the diffracting crystallites (size broadening) and (ii) local variations in interplanar distance, as due to the presence of lattice defects inducing strain fields (strain broadening) [6]. If the line profile width is characterized by the integral breadth  $\mathbf{b}$ , then in case of pure size broadening  $\mathbf{b} \equiv \mathbf{b}_S = K/D$  (for  $\mathbf{b}_S$  in reciprocal space) with  $D$  the mean crystallite size and  $K$  a constant close to unity [6], and in case of pure strain broadening  $\mathbf{b} \equiv \mathbf{b}_D = 2\tilde{\epsilon} / d^{HKL}$  (for  $\mathbf{b}_D$  in reciprocal space), with  $\tilde{\epsilon}$  a measure for strain due to the strain fields induced by the lattice distortions [13] and  $d^{HKL}$  as the interplaner distance of lattice planes of the type  $HKL$ .

If both types of broadening occur simultaneously, separation of "size" and "strain" integral breadth components can be performed on the basis of the dependence of the total integral breadth  $\mathbf{b}_{tot}$  on the length of the diffraction vector characterized by  $1/d^{HKL}$  using knowledge of the shape of the corresponding component line profiles. For example, if both component line profiles are assumed to be Cauchy, then the total integral breadth of the measured line profile,  $\mathbf{b}_{tot}$ , equals  $\mathbf{b}_{tot} = \mathbf{b}_S + \mathbf{b}_D$ , whereas if both profiles are assumed to be Gaussian,  $\mathbf{b}_{tot}^2 = \mathbf{b}_S^2 + \mathbf{b}_D^2$ . Then plotting of  $\mathbf{b}_{tot}$  vs  $1/d^{HKL}$  in case of Cauchy component line profiles or of  $\mathbf{b}_{tot}^2$  vs  $1/(d^{HKL})^2$  in case of Gaussian component line profiles yields straight lines with slopes related to  $\tilde{\epsilon}$  and intercepts cut from the ordinate related to  $D$ .

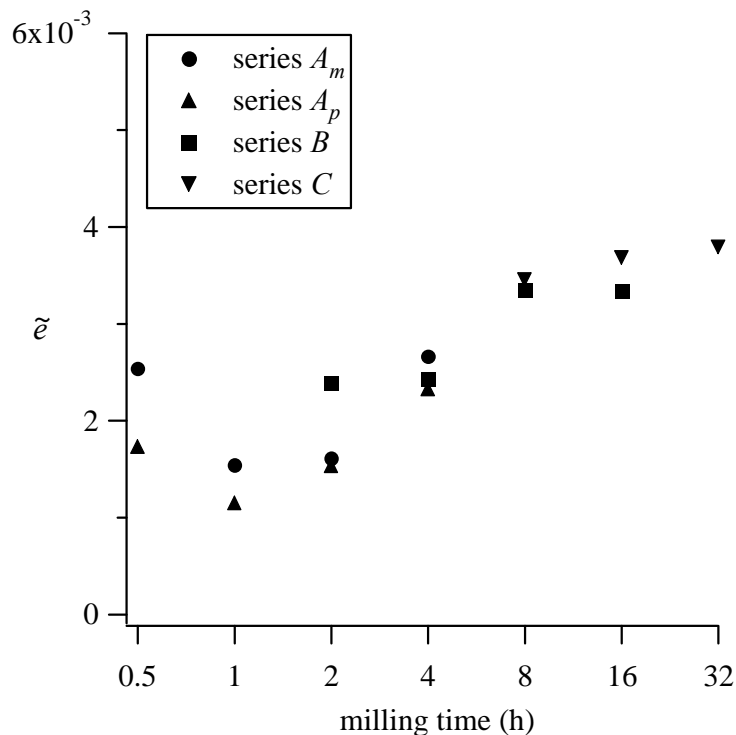
An overall increase of  $\mathbf{b}$  as a function of  $1/d^{HKL}$  occurs for all series shown in Fig. 7. However, systematic deviations of the overall trend occur for specific reflections. For example after short durations of ball milling (0.5 - 4 h) the integral breadths of the {200} and {310} reflections are relatively large. One might suggest that such deviations could be explained by intrinsic anisotropy of the elastic constants of the material considered: a reflection associated with a relatively "weak" crystallographic direction would broaden relatively strongly [14]. However, the anisotropy of the elastic constants of Mo cannot explain the relatively large integral breadths of the {200} and {310} reflections, since these reflections correspond to relatively stiff crystallographic directions [15].

To avoid effects on the line-profile analysis of these  $HKL$  dependent deviations, two orders of the same reflection (i.e. {110} and {220}) are used to separate the contributions due to size and strain. Results obtained assuming Cauchy shaped component (size and strain) line profiles and  $K = 1$  are shown in Fig. 8. The crystallite sizes for series  $A_m$  and  $A_p$  are of the order of 100 - 300 nm after ball milling for 0.5 h to 4 h<sup>11</sup>. Continued ball milling led to a strong decrease of crystallite sizes to

<sup>11</sup> The result of series  $A_m$  after 0.5 h of ball milling has not been shown because the broadening did not comply with the assumed type of size-strain separation: i.e. a negative part cut from the ordinate occurred in the plot of  $\mathbf{b}_{tot}$  vs  $1/d^{HKL}$ .



a)



b)

**Fig. 8.** Results of line-profile analysis assuming Cauchy shaped component (size and strain) line profiles performed on the integral breadth values of the  $\{110\}$  and  $\{220\}$  Mo reflections of series  $A_m$ ,  $A_p$ , B and C depicted in Fig. 7. Particle sizes  $D$  obtained from the intercept of the abscissa are presented in (a) (note the logarithmic scale) and corresponding microstrain values  $\tilde{\epsilon}$  obtained from the slopes in (b).

20 nm after 32 h of ball milling (series C). This decrease of crystallite size is accompanied with an increase of the average microstrain to about 0.4 %. Clearly, both sources of line broadening contribute significantly to the total broadening (see also Fig. 7). Assuming Gaussian shaped component line profiles led to similar results, although the average particle size is somewhat smaller and the average strain is somewhat larger: after 32 h of ball milling a crystallite size of approximately 15 nm and an average strain of 0.6 % were obtained.

The results of series  $A_m$  and  $A_p$  show a relatively large scatter which is ascribed to the relatively large sensitivity of the relatively large values of  $D$  (in these cases) for small deviations of the intercept of the ordinate caused by small errors in  $\mathbf{b}$  and to the effects of sampling of the powder as discussed in Section 5.2. Note also the small but systematic difference between the results of series  $B$  and series  $C$  due to the difference in milling intensities of these series (see Section 3).

It has been observed [14, 16 - 20] that upon ball milling of powders the crystallite size would decrease until a certain saturation level is reached. Such a level could result as a steady state for the competition between grain refinement, due to plastic deformation, and grain growth/relaxation processes, such as recovery and recrystallisation [14, 20]. A saturation level for the average microstrain has sometimes been observed; in other cases the average microstrain reaches a maximum after some ball milling time but decreases upon further ball milling [14, 16 - 20]. From this work it seems probable (see Fig. 8) that on prolonged ball milling, i.e. longer than 32 h, the crystallite size may decrease further and the average microstrain may still increase. Extrapolation of the results obtained suggest a minimum crystallite size of the order of 10 nm and a maximum average microstrain of the order of 0.4 to 0.6 %. Such values have been found for other ball milled bcc materials [14, 17 - 20].

### 5.5 Interpretation of microstrain; determination of dislocation density

It will be shown here that the structural broadening observed can be ascribed to the presence of deformation induced dislocations. To this end line-profile simulation and matching has been performed using a new Monte-Carlo-type approach to line-broadening simulation.

Within a single crystalline sphere of radius  $R$  a number of "infinitely long", straight edge and/or screw dislocations, corresponding to a given dislocation density  $\rho$  is distributed at random in accordance with the operating glide systems of the crystalline material considered [21]. Here, only the strain-broadened parts of the diffraction-line profiles are computed according to the kinematical diffraction theory as follows. A number of pairs of points is selected at random, such that (i) for each

pair the vector connecting both points has length  $L$  and is parallel to the diffraction vector considered ( $L =$  correlation distance; see Section 4) and (ii) the points of each pair are located within the sphere of radius  $R$  considered. The contributions of all pairs of points to the real and imaginary "strain" Fourier coefficients (see Eqs. (13) and (15) in Ref. 13) are calculated taking into account the displacement fields of all dislocations distributed in the crystal considered. The calculated "strain" Fourier coefficients are averaged over the total number of pairs. The process of distributing dislocations on the glide planes and selecting pairs of points is repeated several times for the same value of  $L$  until the average values of the corresponding "strain" Fourier coefficients become independent of continuation of this procedure. Subsequently, this calculation procedure is carried out for increasing values of  $L$ , until for large  $L$  the "strain" Fourier coefficients become negligibly small. The strain broadened line profiles thus calculated were characterized by their integral breadths.

The deformation of a body centered cubic crystal (Mo is bcc) can take place through slip of dislocations along three different glide planes:  $\{110\}$ ,  $\{211\}$  and  $\{321\}$ , with  $\frac{1}{2}a\langle 111 \rangle$  as the possible Burgers vectors [22]. Often the contribution of the  $\{321\}$  glide planes is small and can be neglected [9, 10]. Here, it is assumed that dislocations are present on the  $\{110\}$  and  $\{211\}$  glide planes only.

As an example, the simulation method was carried out for Mo crystals containing either screw dislocations or edge dislocations or both types of dislocations, with in all cases  $r = 10^{14} \text{ m}^{-2}$ . Other parameters were:  $R = 1 \text{ }\mu\text{m}$ , 1000 pairs of points per correlation distance  $L$  and 100 repetitions per correlation distance. The known descriptions for the displacement fields of edge and screw dislocations in an elastically isotropic material were adopted [22] with Poisson's ratio,  $\nu = 0.293$ , and with the lattice constant of Mo,  $a_{\text{Mo}} = 0.31472 \text{ nm}$ . In case of a mixture of edge and screw dislocations the probability of distributing an edge or a screw dislocation is equal. Results are shown in Fig. 9 for the same  $\{HKL\}$  reflections as measured experimentally.

Obviously, the integral breadths of the simulated strain broadened line profiles, show an overall increase upon increasing  $1/d^{HKL}$ . Because size broadening is absent (see above) the lines intersecting the points representing the integral breadths of  $\{110\}$  and  $\{220\}$ , respectively, should go through the origin, as they do. However, systematic deviations from the overall trend occur in case of presence of only screw dislocations, whereas in case of presence of only edge dislocations a more or less linear dependence on  $1/d^{HKL}$  is observed. In case of a mixture of both types of dislocations the integral breadth shows an intermediate behaviour.

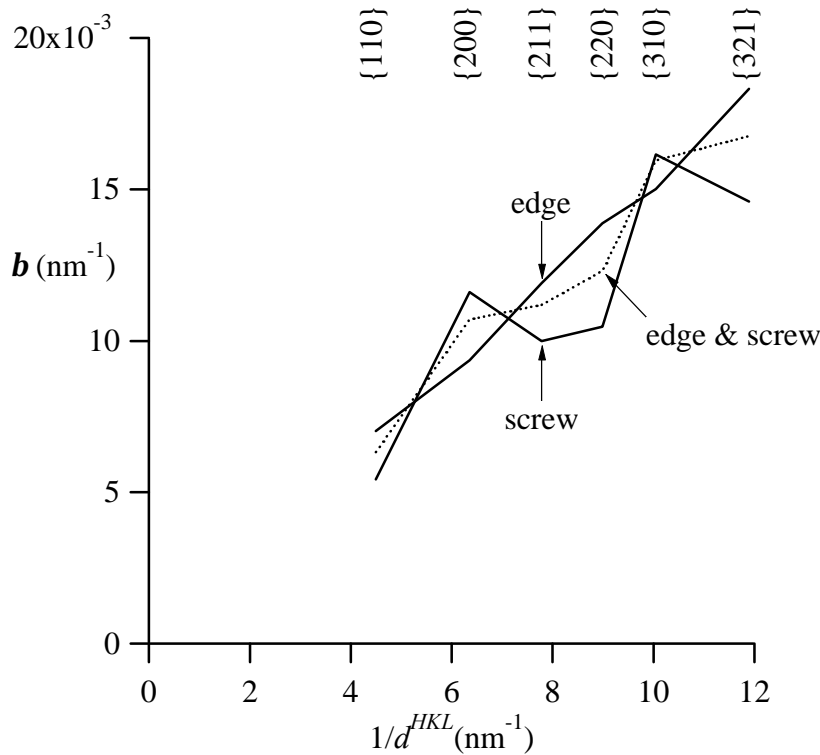


**Fig. 9.** Integral breadths of simulated strain broadened line profiles plotted vs  $1/d^{HKL}$  using either edge dislocations, screw dislocations or a mixture of both types of dislocations with  $\mathbf{r} = 10^{14} \text{ (m}^{-2}\text{)}$  and  $R = 1 \text{ }\mu\text{m}$ . Dislocations are distributed at random compatible with the  $\{110\}$  and  $\{211\}$  glides planes of Mo and with  $\frac{1}{2}a_{\text{Mo}}\langle 111 \rangle$  as the Burgers vector.

The displacement fields used in the calculations for edge and screw dislocations pertain to elastically isotropic material and therefore the  $\{HKL\}$ -dependence of the integral breadth in Fig. 9 in the case of only screw dislocations is solely caused by the crystallographic direction dependence of the displacement and strain fields of the dislocations with respect to the diffraction vectors considered. Thus, possible anisotropy of the elastic constants of the Mo crystal does not play a role here. Corresponding  $\{HKL\}$  dependence has been considered earlier using a different approach [23 -25].

Comparing the simulated integral breadth dependence on  $1/d^{HKL}$  (Fig. 9) with the experimentally obtained results after short durations of ball milling (cf. Figs. 7a and b: 1, 2 and 4 h) similar observations are made: e.g. in both cases the integral breadths of the  $\{200\}$  and  $\{310\}$  are relatively large. This suggests strongly that the presence of dislocations is the cause of the experimentally observed dependence of  $\mathbf{b}$  on  $1/d^{HKL}$ . After longer times of ball milling the integral breadths of the experimentally measured  $\{200\}$  and  $\{310\}$  reflections become relatively less



pronounced, which could be interpreted according to Fig. 9 as that the fraction of screw dislocations becomes smaller and, consequently, the fraction of edge dislocations becomes larger.

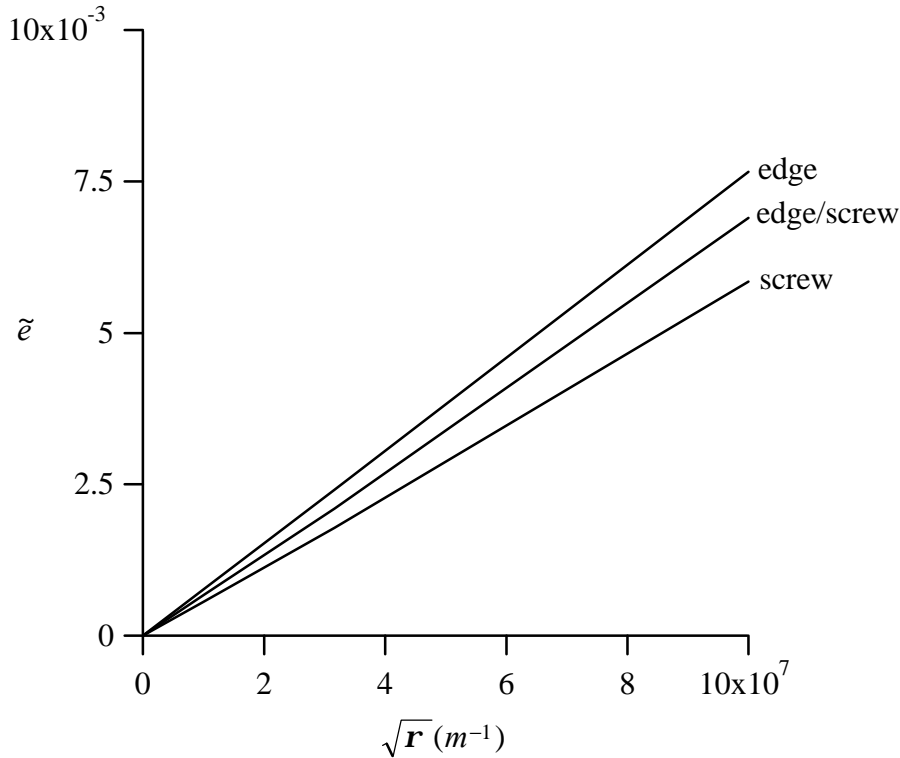


**Fig. 10.** Microstrain estimate  $\tilde{\epsilon}$  versus square root of dislocation density  $\mathbf{r}$  obtained from line-profile analysis assuming Cauchy shaped line profiles of simulated strain broadened  $\{110\}$  and  $\{220\}$  Mo reflections. Dislocations are either of edge type, screw type or a mixture of both types and are distributed at random compatible with the  $\{110\}$  and  $\{211\}$  glide planes of Mo, with  $\frac{1}{2}a_{Mo}\langle 111 \rangle$  as the Burgers vector and with  $R\sqrt{\mathbf{r}} = 10$ .

The simulations [21] show that  $\mathbf{b}_D/\sqrt{\mathbf{r}}$  is practically a univocal function of  $R\sqrt{\mathbf{r}}$ . Variations in the value taken for  $R\sqrt{\mathbf{r}}$  lead to changes in  $\mathbf{b}_D$  at constant  $\mathbf{r}$  of, say, 50 % for  $1 \leq R\sqrt{\mathbf{r}} \leq 10$  and < 10 % for  $10 \leq R\sqrt{\mathbf{r}} \leq 25$ . To arrive at an estimate for the dislocation density in the deformed part of the ball milled powders, for the present simulations  $R\sqrt{\mathbf{r}}$  has been set equal to 10. The strain-broadened diffraction-line profiles were calculated for increasing dislocation densities with either pure edge, pure screw or a mixture of edge and screw dislocations. Then, corresponding average microstrain values  $\tilde{\epsilon}$  were determined assuming Cauchy or Gaussian shaped component lines profiles using the integral breadths of the  $\{110\}$  and  $\{220\}$  only. Results are presented in Fig. 10 for the case of Cauchy shaped component line

profiles. A linear relation between  $\tilde{\epsilon}$  and the square root of the dislocation density is observed. For the same dislocation density, edge dislocations cause a somewhat larger value of  $\tilde{\epsilon}$  than screw dislocations. Estimates of dislocation densities in the deformed part of the ball milled powder were obtained from the experimental average microstrain values  $\tilde{\epsilon}$  (Fig. 8b) and the  $\tilde{\epsilon}$ - $r$  relation shown in Fig. 10. Results are presented in Fig. 11 applying a mixture of edge and screw dislocations for all series. The influence of the type of dislocations on the dislocation densities determined is relatively small. It follows that during the ball milling process the dislocation density increases to values of about  $3 \times 10^{15} \text{ m}^{-2}$  after 32 h of ball milling in case of Cauchy component line profiles (to  $7 \times 10^{15} \text{ m}^{-2}$  in case of Gaussian component line profiles): these values correspond to a severely cold deformed material.

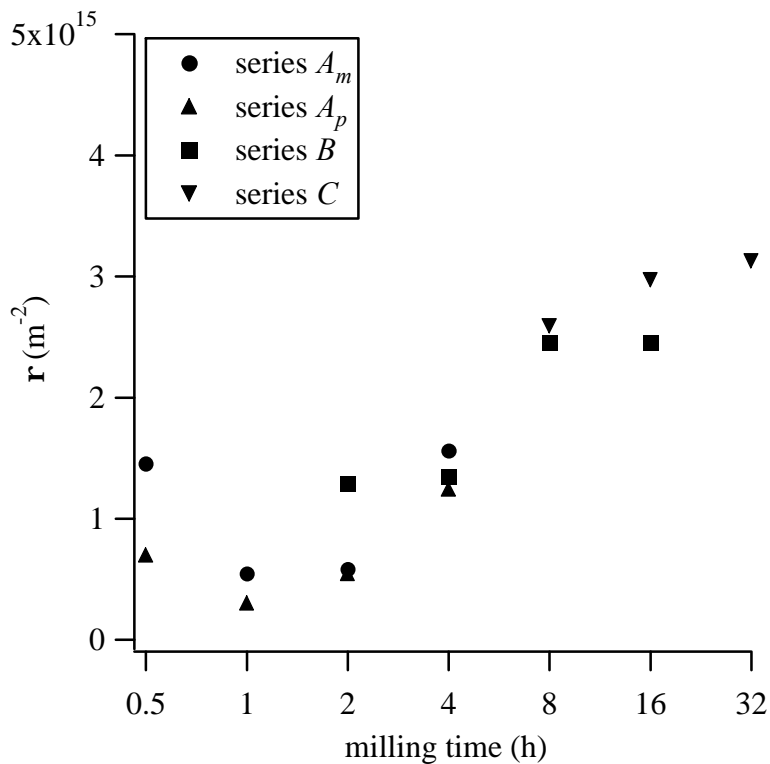


**Fig. 11.** Estimates of dislocation densities  $r$  of series  $A_m$ ,  $A_p$ ,  $B$  and  $C$  using  $\tilde{\epsilon}$  (from Fig. 8b), as obtained from line-profile analysis assuming Cauchy shaped component (size and strain) line profiles performed on the integral breadth values of  $\{110\}$  and  $\{220\}$  Mo reflections (see Fig. 7), and  $\tilde{\epsilon}$  (from Fig. 10), as obtained from the same analysis performed on integral breadth values obtained from simulated  $\{110\}$  and  $\{220\}$  strain broadened Mo reflections.

## **6. Conclusions**

- During ball milling of Mo powder in a low-energy ball mill several stages of deformation can be identified. In a first stage the generally soft, powder particles are flattened due to action of compressive forces. The ball milled powder consists of a mixture of undeformed powder particles and flake-like, deformed powder particles. The flakes have more or less flat faces preferably parallel to {100} planes of the crystal lattice. Continued ball milling causes the amount of flake-like deformed powder particles to decrease, and simultaneously more and more irregularly shaped agglomerates of particles occur, as a result of multiple cold welding and fracturing of powder particles.
- X-ray diffraction methods developed in this study allow quantitative determination of the (still) undeformed part of the ball milled powder from the Fourier transform of reflections from the ball milled powder obtained after deconvolution using corresponding reflections from the initial powder. This analysis is possible also if texture is present in the specimen prepared for diffraction analysis. Such texture can occur due to the presence of the flake-like particles that tend to orient their flat faces, preferably parallel to {100} of the crystal lattice of Mo, parallel to the surface of the diffraction specimen, in dependence on the procedure used for preparation of the specimen for diffraction analysis.
- Analysis of the ball milling induced structural imperfections from the occurring diffraction-line broadening revealed a drastic decrease of the size of the diffracting crystallites upon ball milling down to 10 - 20 nm, i.e. values much smaller than the size of the irregularly shaped agglomerates of particles observed at this advanced state of ball milling. Simultaneously the internal average microstrain increased up to 0.4 - 0.6 %.
- The dominant source of structural line broadening are dislocations generated by ball milling: line-profile simulation and matching revealed a dependence of structural line broadening on the length of the diffraction vector as observed experimentally. The nature of the dislocations becomes less screw-like and more edge-like upon continued ball milling. In an advanced stage of ball milling the dislocation density becomes as large as  $3 - 7 \times 10^{15} \text{ m}^{-2}$ .

## **Acknowledgements**

This work has been part of the research program of the Foundation for Fundamental Research on Matter (Stichting FOM), The Netherlands. Financial support was also provided by the Netherlands Technology Foundation (STW). The authors are indebted

to Dr. H. Bakker for providing the ball milling facilities, to Dr. G. Rixecker for performing the ball milling experiments and to ing. E.J.M. Fakkeldij for operating the SEM.

### *Appendix* **Relation between $T^{HKL}$ and $\mathbf{a}^{HKL}$**

After short times of ball milling the diffracting volume pertaining to the  $\{HKL\}$  reflection consists of a mixture of undeformed powder particles of total volume  $V_{undef}^{HKL}$  and deformed powder particles of total volume  $V_{def}^{HKL}$ . The volume weighted intensity distribution of the line profile of the  $\{HKL\}$  reflection,  $I_{tot}^{HKL}(\mathbf{2q})$ , is described by Eq. (2). The integrated intensity of this reflection,  $\int I_{tot}^{HKL} d\mathbf{2q}$ , can be expressed as

$$\int I_{tot}^{HKL} d\mathbf{2q} = (V_{undef}^{HKL} + V_{def}^{HKL}) \int \bar{I}^{HKL} d\mathbf{2q} \quad (\text{A. 1})$$

with  $\int \bar{I}^{HKL} d\mathbf{2q}$  the integrated intensity of the line profile of the  $\{HKL\}$  reflection *per unit of volume*. It has been assumed that  $\int \bar{I}^{HKL} d\mathbf{2q}$  is independent of the state of deformation of the powder particles, i.e.  $\int \bar{I}_{undef}^{HKL} d\mathbf{2q} = \int \bar{I}_{def}^{HKL} d\mathbf{2q} = \int \bar{I}^{HKL} d\mathbf{2q}$ .

If the integrated intensity of an arbitrary  $\{HKL\}$  reflection is divided by that of the  $\{220\}$  reflection it follows, using Eq. (5), that

$$\frac{\int I_{tot}^{HKL} d\mathbf{2q}}{\int I_{tot}^{220} d\mathbf{2q}} = \frac{V_{und}^{HKL} + V_{def}^{HKL}}{V_{und}^{220} + V_{def}^{220}} \frac{\int \bar{I}^{HKL} d\mathbf{2q}}{\int \bar{I}^{220} d\mathbf{2q}} = \frac{\mathbf{a}^{220}}{\mathbf{a}^{HKL}} \frac{V_{undef}^{HKL}}{V_{undef}^{220}} \frac{\int \bar{I}^{HKL} d\mathbf{2q}}{\int \bar{I}^{220} d\mathbf{2q}}. \quad (\text{A. 2})$$

If the undeformed powder of the ball milled powder is equal to the reference powder (the same morphology, microstructure and texture; implying the same procedure for (diffraction) specimen preparation for both specimens), then, according to Eq. (8)

$$\frac{V_{undef}^{HKL}}{V_{undef}^{220}} = \frac{V_{ref}^{HKL}}{V_{ref}^{220}} \quad (\text{A. 3})$$

and Eq. (A. 2) can be written as

$$\frac{\int I_{tot}^{HKL} d2\mathbf{q}}{\int I_{tot}^{220} d2\mathbf{q}} = \frac{\mathbf{a}^{220} V_{ref}^{HKL}}{\mathbf{a}^{HKL} V_{ref}^{220}} \frac{\int \bar{I}^{HKL} d2\mathbf{q}}{\int \bar{I}^{220} d2\mathbf{q}}. \quad (\text{A. 4})$$

Since  $V_{ref}^{HKL} \int \bar{I}^{HKL} d2\mathbf{q}$  represents the integrated intensity of the  $\{HKL\}$  reflection of the reference specimen,  $V_{ref}^{HKL} \int \bar{I}^{HKL} d2\mathbf{q} = \int I_{ref}^{HKL} d2\mathbf{q}$ , Eq. (A. 4) becomes

$$\frac{\int I_{tot}^{HKL} d2\mathbf{q}}{\int I_{tot}^{220} d2\mathbf{q}} = \frac{\mathbf{a}^{220}}{\mathbf{a}^{HKL}} \frac{\int I_{ref}^{HKL} d2\mathbf{q}}{\int I_{ref}^{220} d2\mathbf{q}}. \quad (\text{A. 5})$$

Recognizing the parameter  $T^{HKL}$  from Eq. (12) it follows from Eq. (A. 5)

$$\frac{\int I_{tot}^{HKL} d2\mathbf{q}}{\int I_{tot}^{220} d2\mathbf{q}} \bigg/ \frac{\int I_{ref}^{HKL} d2\mathbf{q}}{\int I_{ref}^{220} d2\mathbf{q}} = \frac{\mathbf{a}^{220}}{\mathbf{a}^{HKL}} = T^{HKL}. \quad (\text{A. 6})$$

## References

- [1] A.W. Weeber, H. Bakker, *Physica B* **153** (1988) 93.
- [2] E.Hellstern, H.J. Fecht, Z. Fu, W.L. Johnson, *J. Appl. Phys.* **65** (1989), 305.
- [3] E.Hellstern, H.J. Fecht, Z. Fu, W.L. Johnson, *J. Mater. Res.* **4** (1989), 1292.
- [4] T.C. Bor, M.C. Huisman, R. Delhez, E.J. Mittemeijer, *Mat. Sci. For. Vol. 278-281* (1998), 145.
- [5] R.N. Bracewell, *The Fourier Transform and its Applications*, McGraw-Hill, Tokyo, 1978.
- [6] B.E. Warren, *X-Ray Diffraction*, Addison Wesley, Reading, Mass., 1969.
- [7] A.J.C. Wilson, *Acta Cryst.* **23** (1967), 888.
- [8] R. Delhez, E.J. Mittemeijer, *J. Appl. Cryst.* **8** (1975), 612.
- [9] D. Raabe, K. Lücke, *Mat. Sci. For. Vol. 157-162* (1994), 597.
- [10] Y.B. Park, D.N. Lee, G. Gottstein, *Acta. Mat.* **46** (10), (1988), 3371.
- [11] L. Lutterotti, S. Gialanella, *Acta Mater.* **46**, (1), (1998), 101.
- [12] J.G.M. van Berkum, G.J.M. Sprong, Th.H. de Keijser, R. Delhez and E.J. Sonneveld, *Powder Diffraction* **10** (1995), 129.
- [13] R. Delhez, Th.H. de Keijser and E.J. Mittemeijer, *Fresenius Z. anal. Chem.* **312** (1982), 1 - 16.
- [14] I. Börner, J. Eckert, *Mat. Sci. & Eng. A* **226-228** (1997), 541.
- [15] C.J. Smithells (editor), *Metals Reference Book*, 5<sup>th</sup> edition, Butterworths, London, 1976.
- [16] P.S. Gilman, J.S. Benjamin, *Ann. Rev. Mater. Sci.*, Vol. **13**, (1983), 279.
- [17] C.C. Koch, *Nanostruc. Mat.* **2** (1993), 109.
- [18] D. Oleszak, P.H. Shingu, *J. Appl. Phys.* **79** (6), (1996), 2975.

- 
- [19] W.M. Kuschke, R.M. Keller, P. Grahle, R. Mason, E. Arzt, *Z. Metallk.* **86** (1995), 12.
- [20] H.H. Tian, M. Atzmon, *Acta Meta.* **4** (1999), 1255.
- [21] J.-D. Kamminga, R. Delhez, to be published.
- [22] F.R.N. Nabarro, *Theory of Crystal Dislocations*, Oxford University Press, Oxford, 1967.
- [23] M. Wilkens, *Phys. Stat. Sol. (a)* **2** (1970), 359.
- [24] I. Groma, T. Ungár, M. Wilkens, *J. Appl. Cryst.* **21** (1988), 47.
- [25] A.C. Vermeulen, R. Delhez, Th.H. de Keijser, E.J. Mittemeijer, *J. Appl. Phys.* **77** (10), (1995), 5026.

## *Summary*

Lattice imperfections, such as dislocations and misfitting particles, shift and/or broaden X-ray diffraction (XRD) line profiles. Most of the present analysis methods of the shift and broadening of XRD line profiles do not provide the characteristics of lattice imperfections. The main part of this thesis deals with a new approach to the analysis of broadened and shifted XRD line profiles that does not have the limitations of the present analysis methods. The approach is based on micromechanical modelling of the microstructure of the material. A small volume which is representative of the microstructure of the material is used to model and calculate the materials behaviour on a local scale incorporating the (strain fields of the) lattice imperfections. Subsequently, the behaviour of this representative element can be used to calculate the overall materials properties. X-ray diffraction-line profiles are calculated from such model materials and are compared with the measured ones. By adjusting the parameters of the micromechanical model, the calculated line profiles can be matched to the experimental ones. In this way characteristics of the microstructure of the experimental material can be determined and subsequently overall materials properties can be predicted. Hence, a direct link between XRD line-profiles characteristics and materials properties is conceivable.

The new diffraction-line profile calculation approach is developed in chapters 2 and 3 for a two-dimensional model composite material containing a periodic distribution of misfitting particles. The shifts and broadenings of line profiles in absence of particle-matrix misfit are studied in chapter 2. The line-profile broadenings of matrix reflections are caused by finite distances in the matrix between the (non-diffracting) particles ("size" broadening). Relations between the "size" broadening of the matrix line profiles and model parameters, such as the particle fraction, the particle size and the degree of particle clustering, are established. If a misfit between particles and matrix exists the matrix line profiles are also broadened due to the strain field induced by the particles in the matrix ("strain" broadening). A simple method is proposed to separate the "size" and "strain" contributions to the total broadening.

The line-profile shifts and broadenings due to "strain" alone are analyzed in two steps in chapter 3. First, the relations between model parameters, such as the particle size, the particle fraction, the particle-matrix misfit and the degree of particle clustering, and the mean strain of the matrix and root mean square strain of the matrix are studied. Due to the ordering of the particles in the composite material the strain field in the matrix is direction dependent which is reflected in the root mean square strain of the matrix. Then, the relations between the values that characterize the matrix

strain and the shift and width of the calculated line profiles are investigated. The mean matrix strain, calculated on the basis of the shift of the line-profile centroid of the simulated XRD line profile, shows approximately equal behaviour for all values of the model parameters as the mean strain calculated from the strain field in the matrix. The broadening of the simulated XRD line profiles reflects the direction dependence of the strain field in the matrix. This leads to the observation that for all values of the model parameters the line-profile broadenings are proportional to the product of the centroids of the line profiles and the root mean square strains in the specific crystallographic directions (as usually assumed in practice). Thus for the particle-matrix systems studied here the influence of the various model parameters on the line-profile position and width can be explained directly from the influence of these model parameters on the mean strain and root mean square strain of the matrix material.

Verification of the results of the novel simulation approach can be accomplished, for example, by studying the same material employing a different experimental technique, such as Transmission Electron Microscopy. The study of particle/matrix systems using this technique is the topic of chapter 4. The strain field in the matrix due to misfitting particles causes, under certain diffraction conditions, diffraction contrast lobes in bright field and dark field images to appear. Information on the particle-matrix misfit and/or on the particle dimensions can be obtained by an analysis of the extent of the contrast lobes. The classical analysis is unreliable for specimen foils that contain a high number density of misfitting particles and/or that are relatively thin (smaller than five times the extinction distance). An alternative method is proposed here that does not have the limitations of the classical method. The extent of the contrast lobes is characterized by the distance of the maximum or minimum intensity of the contrast lobes in bright field and dark field to the center of the misfitting particle. For the interpretation of the observed contrast lobes a model system, consisting of a single disc-shaped misfitting particle placed centrally in a thin specimen, is considered. The contrast lobes in bright and dark field images are calculated as a function of, in particular, the particle radius, the foil thickness and the particle thickness. Simultaneous fitting of calculated bright and dark field diffraction contrast images to the experimental ones leads to determination of the particle misfit and the local thickness of the specimen foil. The method is illustrated for a nitrided Fe-2 at. % V alloy with small disc-shaped VN precipitates and leads to a consistent interpretation in terms of particle size and misfit upon precipitation. The foil thickness values determined by diffraction contrast analysis agree well with data obtained from an independent thickness measurement technique.



In chapters 5 and 6 attention is paid to powder particles that have been deformed in a ball milling device. Ball milling provides a route for the preparation of non-equilibrium material that may possess unusual chemical and physical properties. In this work the ball milling process in a low energy ball mill is investigated as a function of milling time and using Mo powder as a model material. After relatively short times of ball milling still undeformed Mo powder particles are present in the type of ball mill used. A method is developed, on the basis of line-profile deconvolution, that enables the determination of the volume fraction of undeformed powder particles and the (Fourier transform of the) line profile of the deformed particles. The accuracy of these results are largely determined by the effect of counting statistical intensity variations. A region in Fourier space can be indicated for which the determination of the volume fraction of undeformed Mo powder is optimal.

During the deformation of the Mo powder particles several stages can be identified. First, the particles are flattened due to compressive forces of the bouncing ball in the mill. These flat particles exhibit a deformation texture which is comparable with that of rolled polycrystalline Mo. On prolonged ball milling all powder particles are eventually deformed and agglomerates of particles are formed without exhibiting a specific shape. The crystallite size decreases towards 10 - 20 nm, the apparent texture disappears and internal strains are built up to microstrain levels of the order of 0.4 - 0.6 %.

From the magnitude of the microstrains an estimate of the dislocation density can be calculated using a simple three dimensional model of the distribution of dislocations in deformed Mo powder particles. It assumes that straight edge and/or screw dislocations are distributed at random on the {110} and {211} glide planes of Mo with  $\langle 111 \rangle$  as possible Burgers vector directions. The X-ray diffraction line profiles are obtained using a Monte-Carlo type of line-profile calculation method. A comparison of the integral breadths of several simulated and experimental line profiles clearly indicates the presence of dislocations in the ball milled Mo powder particles. Then the dislocation density is estimated to become as large as  $3-7 \cdot 10^{15} \text{ m}^{-2}$  in an advanced state of ball milling, which indicates a severely cold deformed material.



## *Samenvatting*

Roosterfouten, zoals dislocaties en mispassende deeltjes, verschuiven en/of verbreden röntgendiffractielijnprofielen. De meeste lijnprofiel-analysemethoden zijn niet in staat om uit de gemeten lijnprofielverschuiving en -verbreding roosterfouten goed te karakteriseren. Dit is jammer, omdat roosterfouten een belangrijke rol spelen bij het gedrag en de eigenschappen van kristallijne materialen. Het grootste gedeelte van dit proefschrift gaat daarom over een nieuwe methode voor de analyse van verschoven en verbrede lijnprofielen. De methode is gebaseerd op het berekenen van lijnprofielen op basis van een micromechanisch model van het gemeten materiaal. Dit model beschrijft het gedrag van dit materiaal in een representatief volume-element waarin de betreffende roosterfouten en de, met hun aanwezigheid samenhangende, rekvelden worden opgenomen. Hieruit kunnen bijvoorbeeld ook de overall materiaaleigenschappen berekend worden. Van dit modelmateriaal worden lijnprofielen berekend en deze kunnen vergeleken worden met de gemeten lijnprofielen. Door nu de parameters van het modelmateriaal te variëren, kunnen de berekende lijnprofielen worden gefit aan de gemeten lijnprofielen. Op deze manier kan informatie worden verkregen over de microstructuur van het gemeten materiaal. Dus, een directe relatie tussen karakteristieken van röntgendiffractielijnprofielen en materiaaleigenschappen is denkbaar.

De nieuwe lijnprofielberekeningsmethode wordt beschreven in hoofdstukken 2 en 3 voor een tweedimensionaal model-composietmateriaal dat een periodieke verdeling van mispassende deeltjes bevat. De verschuiving en verbreding van lijnprofielen in afwezigheid van mispassing tussen deeltjes en matrix worden in hoofdstuk 2 bestudeerd. De lijnprofielverbreding van matrixreflecties wordt veroorzaakt door eindige afstanden tussen de (niet-diffracterende) deeltjes ("size"-verbreding). Relaties zijn bepaald tussen deze "size"-verbreding van de matrix lijnprofielen en modelparameters, zoals de deeltjesfractie, de deeltjesgrootte en de mate van deeltjesclustering. Als er een mispassing tussen deeltjes en matrix bestaat, worden de lijnprofielen van de matrixreflecties ook verbreed tengevolge van het rekveld in de matrix veroorzaakt door het mispassende deeltje ("strain"-verbreding). Een eenvoudige methode is voorgesteld om de "size"- en "strain"-bijdragen aan de totale verbreding van elkaar te scheiden.

De lijnprofielverschuiving en -verbreding tengevolge van "strain" zijn in twee stappen geanalyseerd in hoofdstuk 3. Eerst zijn de relaties tussen modelparameters, zoals de deeltjesgrootte, deeltjesfractie, mispassing tussen deeltjes en matrix en de mate van clustering van de deeltjes, en de gemiddelde rek en het gemiddelde van het ordening

van de deeltjes in het composietmateriaal is het rekveld in de matrix richtingsafhankelijk, hetgeen in dit geval alleen tot uiting komt in het gemiddelde kwadraat van de rek in de matrix. Vervolgens zijn de relaties tussen de karakteristieke matrixrekwaarden en de verschuiving en verbreding van de berekende lijnprofielen onderzocht. De gemiddelde rek, berekend op basis van de verschuiving van de centroïde van het lijnprofiel, vertoont een ongeveer gelijk gedrag voor alle onderzochte waarden van de modelparameters als de gemiddelde rek berekend uit het rekveld in de matrix. De verbreding van het berekende lijnprofiel weerspiegelt de richtingsafhankelijkheid van het rekveld in de matrix. Dit leidt tot de waarneming dat voor alle waarden van de modelparameters de lijnprofielverbreding evenredig is aan het produkt van de lijnprofielcentroïde en het gemiddelde kwadraat van de rek in de specifieke kristallografische richting (zoals vaak aangenomen in de praktijk). Dus voor het hier bestudeerde deeltjes/matrix-systeem is de invloed van de verschillende modelparameters op de lijnprofielpositie en -verbreding direct te verklaren vanuit hun invloed op de gemiddelde rek en het gemiddelde kwadraat van de rek in de matrix.

Verificatie van de resultaten van de nieuwe simulatiemethode is mogelijk door hetzelfde materiaal met een andere experimentele techniek te bestuderen, zoals TEM. De studie van deeltje/matrix-systemen met behulp van deze techniek is het onderwerp van hoofdstuk 4. De rekvelden in de matrix, tengevolge van de mispassende deeltjes, veroorzaken onder zekere (diffractie) condities, zogenaamde diffractiecontrastlobben in helderveld- en donkerveldopnamen. Informatie over de deeltjes/matrix-mispassing en/of de deeltjesafmetingen kan worden verkregen door de uitgebreidheid van de lobben te bestuderen. De klassieke methode bleek niet betrouwbaar voor preparaatfolies met een hoge deeltjesdichtheid en/of kleine foliedikte. Vandaar dat een alternatieve methode is voorgesteld. De uitgebreidheid van de contrastlobben is gekarakteriseerd door de afstand tussen de maximum of minimum intensiteit van de contrastlobben in helderveld en donkerveld tot het midden van de mispassende deeltjes. Om de contrastlobben te kunnen interpreteren is een modelsysteem gebruikt, bestaande uit een schijfvormig, mispassend deeltje in het midden van een dun preparaatfolie. De contrastlobben in helder- en donkerveld zijn berekend als functie van, met name, de deeltjesstraal, de foliedikte en de deeltjesdikte. Door nu tegelijkertijd de berekende helderveld- en donkerveldbeelden te fitten op de experimentele beelden kunnen de deeltjesmispassing en de locale preparaatfoliedikte bepaald worden. De methode is geïllustreerd aan de hand van een genitreeerde Fe-2 at.% V legering met kleine schijfvormige VN-precipitaten en leidt tot een consistente interpretatie van de deeltjesgrootte en deeltjes/matrix-mispassing. Bovendien komen

de op deze wijze bepaalde foliediktes goed overeen met waarden die met een andere foliedikte-meettechniek zijn bepaald.

In hoofdstukken 5 en 6 is aandacht besteed aan poederdeeltjes die zijn vervormd in een kogelmolen. Kogelmalen maakt het mogelijk niet-evenwichts-materialen te maken, die buitengewone chemische of fysische eigenschappen bezitten. In dit werk is het kogelmaalproces in een lage-energie kogelmolen bestudeerd als functie van de maalduur en met Mo-poeder als modelmateriaal. Na relatief korte maalduren blijkt er in de door ons gebruikte kogelmolen nog onvervormd Mo-poeder aanwezig te zijn. Er is een methode ontwikkeld, op basis van lijnprofieldeconvolutie, om de volumefractie onvervormd poederdeeltjes en de Fouriertransform van het lijnprofiel van de gedeformeerde deeltjes te bepalen. De nauwkeurigheid van de resultaten blijkt sterk afhankelijk van de invloed van telstatistiek. In de Fourierruimte kan een gebied aangegeven worden waar de volumefractie onvervormd Mo-poeder optimaal bepaald kan worden.

Het deformeren van Mo-poeder verloopt in verschillende stadia. Eerst worden de deeltjes geplet tengevolge van de samendrukkende krachten van de stuiterende bal in de kogelmolen. Deze geplette deeltjes vertonen een deformatietextuur die vergelijkbaar is met die van gewalst polykristallijn Mo. Na langduriger malen worden uiteindelijk alle Mo-deeltjes vervormd en ontstaan agglomeraten van deeltjes zonder voorkeursvorm. De kristallietgrootte neemt af tot 10 - 20 nm, de textuur verdwijnt en microrekenen ontstaan met een grootte tot 0.4 - 0.6 %.

Een schatting van de dislocatiedichtheid op basis van de microrekwaarden kan worden gemaakt met een eenvoudig driedimensionaal model van de distributie van dislocaties in gedeformeerde Mo-poederdeeltjes. Aangenomen wordt dat rechte rand en/of schroef-dislocaties random verdeeld zijn op de {110} en {211} glijvlakken van Mo met  $\langle 111 \rangle$  als mogelijke richtingen van de Burgersvector. De röntgendiffractielijnprofielen worden berekend met een Monte-Carlo-type lijnprofiel-berekeningsmethode. Een vergelijking van de integrale breedte van verschillende gesimuleerde en experimentele lijnprofielen duidt duidelijk op de aanwezigheid van dislocaties in de gekogelmaalde Mo-poederdeeltjes. De dislocatiedichtheid wordt geschat op  $3 - 7 \cdot 10^{15} \text{ m}^{-2}$  in een vergevorderd stadium van kogelmalen, hetgeen duidt op een behoorlijk zwaar koudvervormd materiaal.



## *Nawoord*

De afgelopen jaren heb ik het voorrecht gehad om in twee wetenschappelijke groepen aanwezig te zijn. Dit heeft zo z'n voor- en nadelen. Twee groepen betekent twee professoren met elk hun eigen visie, opvattingen en wijze van schrijven. Het betekent ook ruwweg tweemaal zoveel collega's, vakgroepsvoordrachten en vakgroepsborrels. Twee groepen met elk hun eigen sfeer, maar beide met een grote gedrevenheid voor het doen van onderzoek. Ik heb me er thuis gevoeld en daarvoor dank ik eenieder.

Dit onderzoek kon niet zonder Eric Mittemeijer en Erik van der Giessen met hun niet aflatende inzet en grote betrokkenheid. Het onderzoek kon ook niet zonder Rob Delhez, die de dagelijkse begeleiding op zijn eigen, prettige, wijze vorm gaf. Dit geldt ook voor Staf de Keijser, die echter door omstandigheden gedwongen werd de begeleiding eerder te beëindigen.

Delen van dit proefschrift zijn ontstaan in samenwerking met de afstudeerders Antoine Kempen en Marc Huisman. Hun aanwezigheid en inzet betekende niet alleen een belangrijke bijdrage aan dit proefschrift, maar vooral een zeer prettige tijd van samenwerken en samenouwehoeren.

Dit onderzoek kon ook niet zonder de kennis en kunde van vele collega's en medewerkers binnen en buiten beide vakgroepen. Mensen bedankt! Daarnaast dank ik ook de PCM, de lasgroep en de instrumentmakerij voor de gezelligheid en de "mogelijkheden" buiten het gewone werk om.

Tot slot wil ik mijn ouders en vrienden bedanken voor hun warme belangstelling, steun en begrip in de afgelopen jaren. Als laatste dank ik Jet voor haar liefde en steun, zeker voor die momenten waarop het nodig was.





## *Curriculum Vitae*

### **Teunis Cornelis Bor**

Geboren op 14 december 1969 te Schoonrewoerd

- 1982 - 1988 VWO, Koningin Wilhelmina College te Culemborg
- 1988 - 1994 Studie Materiaalkunde aan de Technische Universiteit Delft.  
Afgestuurd (met lof) in de sectie Lastechnologie en Niet-Destructief Onderzoek onder begeleiding van Prof.dr. G. den Ouden op het onderwerp "*Het diffusielassen van  $Si_3N_4$  met een Ni-tussenlaag*".
- 1994 - 1999 Onderzoeker in Opleiding in de sectie Fysische Chemie van de Vaste Stof, Laboratorium voor Materiaalkunde en de sectie Micromechanica van Materialen, Laboratorium voor Technische Mechanica, Technische Universiteit Delft.  
Promotie-onderzoek onder begeleiding van dr.ir. R. Delhez, dr.ir. Th.H. de Keijser (tot 1997), prof.dr.ir. E. Van der Giessen en prof.dr.ir. E.J. Mittemeijer, op het onderwerp "*Strain Fields in Crystalline Solids, Prediction and Measurement of X-Ray Diffraction Patterns and Electron Diffraction Contrast Images*".
- 1999 - Post-doctoraal onderzoeker in de sectie Fysische Chemie van de Vaste Stof, Laboratorium voor Materiaalkunde en de sectie Micromechanica van Materialen, Laboratorium voor Technische Mechanica, Technische Universiteit Delft. Onderwerp: *Berekening en interpretatie van röntgendiffractielijnverbreding van materialen met dislocaties.*
- 1999 - Research and Development Tricycle Cross